THE K2 & TESS SYNERGY: UNITING NASA'S PLANET HUNTERS

By

Erica A. Thygesen

A DISSERTATION

Submitted to
Michigan State University
in partial fulfillment of the requirements
for the degree of

Astrophysics and Astronomy—Doctor of Philosophy

2025

ABSTRACT

We have entered an era of studying the atmospheres of exoplanets in unprecedented detail, particularly through transmission spectroscopy of transiting planets using the James Webb Space Telescope (JWST). However, most of the 4300+ confirmed transiting planets are not currently accessible to JWST during its mission lifetime. This widespread problem is due mostly to ephemeris degradation: while the transit time and period of the planet may be known to a precision of minutes at discovery, the uncertainties compound with each successive transit, which can culminate in the projected time of future transits being off by hours to days when follow-up observations are being made years later. This costly problem can be alleviated by reobserving transits to greatly narrow down the future transit window before scheduling observations for characterization. Fortunately, NASA's Transiting Exoplanet Survey Satellite (TESS) mission is observing most of the sky for transit signals, providing an efficient and timely avenue for refreshing the ephemerides of hundreds of planets. With this in mind, the K2 & TESS Synergy is a large scale effort to reanalyze planets originally discovered by NASA's K2 mission with new observations from the ongoing TESS mission.

We combine light curves obtained by both NASA missions along with archival radial velocities, Gaia parallaxes, and spectral energy distributions in global fits using `EXOFASTv2`, which not only allows us to update the ephemerides, but also build a self-consistent catalog of parameters for the planets and host stars. We present a reanalysis of 26 single-planet systems reobserved by TESS during its prime mission. For half of the planets, we improve the average 3σ uncertainties by 2030 from the order of tens of hours down to under one hour. As a result of the faintness of some systems, 13 planets do not have transits detectable by TESS. In those cases, we exclude the TESS photometry from the global fits, resulting in a corresponding ephemeris improvement of 43.2 to 35.6 hours.

This systematic approach also provides opportunity to amend ephemerides that were originally incorrect due to problems such as false positive transits in additional photometry used at discovery. We address one such case, that of K2's first planet discovery, K2-2 b, where the period was 28.8

minutes ($\sim 40\sigma$) away from the true value at the time of discovery. In addition to the K2 and TESS light curves, we use a variety of other space- and ground-based photometry to hunt for the transit of K2-2 b. We successfully caught multiple transits of K2-2 b, allowing us to correct and refine the ephemeris such that the transit time uncertainty will be known to within <13 minutes by 2030.

We continue the broader analysis to reanalyze 32 of the top candidates for atmospheric characterization in the K2 catalog to ensure that JWST can be used to obtain transmission spectra for these planets. Most planets in this sample are equally suitable for atmospheric characterization using JWST as other current targets. There are also many targets that would be useful for understanding the formation and evolution processes of sub-Neptunes and giant planets. We improve the average ephemeris uncertainties by 2030 from 9.34 hours to 26 minutes, enabling for future targeted observations to be scheduled.

The culmination of the work in this thesis is updated global parameters for 51 planets. Efforts like the K2 and TESS Synergy will ensure the accessibility of transiting planets for future characterization while leading to a self-consistent catalog of stellar and planetary parameters for future population efforts.

such dedication

A lady doctor? Has science come that far? — Johnny Bravo

ACKNOWLEDGEMENTS

TABLE OF CONTENTS

LIST OF ABBREVIATIONS

C/O	Carbon/Oxygen
HST	Hubble Space Telescope
MC	Monte Carlo
SED	Spectral Energy Distribution
MJD	Modified Julian Date
PI	Principal Investigator
MSU	Michigan State University

CHAPTER 1

INTRODUCTION

1.1 A Brief History of Exoplanet Discovery

The idea that extrasolar planets might exist has been considered since nearly 2000 years ago. However, it was not until the 1990's that the existence of exoplanets was confirmed. The first exoplanet discovery was made in 1992, when two planets were found orbiting the pulsar PSR B1257+12 (Wolszczan & Frail, 1992), perhaps surprisingly in what is now considered an exotic system. Pulsar planets are detected through minuscule variations of the pulsar's rotation, and despite being the first exoplanet discovery, are exceedingly rare, with only eight discovered to date.

Three years later, the first planet around a main sequence star, 51 Pegasi b, was found (Mayor & Queloz, 1995). This discovery was made by monitoring the radial velocities (RVs) of the host star, which had been a technique used for over a decade with the hopes to find an exoplanet signature. As a star and planet orbit their common center of mass, the spectrum of the host star is blue- or red-shifted along our line-of-sight based on the phase of the orbit, inclination of the system, and the mass of the planet in comparison to the star. The shift in wavelength of the spectral lines compared to rest wavelengths can be converted into a velocity as a function of time. A huge advantage of RVs over other exoplanet discovery techniques is that for the most part it does not require the system to be aligned in a particular way in relation to our point of view. A system can be oriented anywhere from perfectly edge-on to nearly face-on for an RV signal to be detectable. Combining Kepler's third law with the measurement of RVs provides a way of measuring the mass of the companion(s) in the system from the semi-amplitude of the velocity in the form,

$$\frac{(M_*^3 \sin^3 i)}{(M_P + M_*)^2} = \frac{P_{\rm orb} K^3}{2\pi G}(1 - e^2)^{3/2} \tag{1.1}$$

where M_* and M_P are the mass of the star and planet, respectively, $P_{\rm orb}$ is the orbital period, K is the RV semi-amplitude, i is the orbital inclination, and e is the orbital eccentricity. In general, M_* can be independently estimated through modeling of the stellar spectral energy distribution (SED) and parallax, from which intrinsic luminosity and stellar mass can be derived. $P_{\rm orb}$ and K

can be directly measured from the RV curve. The eccentricity of the orbit can be inferred from the deviation of the RV signal away from a pure sine wave. This leaves a degeneracy between the inclination of the system with M_P; with RVs alone, only a lower limit on the planetary mass can be found by assuming the system is being viewed edge on. For the most part $M_* >> M_P$, meaning typical values for K are on the order of several to several hundred m/s. The RV community is pushing towards the limit of 10 cm/s, which is the expected signal of an Earth-like planet around a Sun-like star. RVs have been responsible for the direct discovery of hundreds of exoplanets, but even long-term trends in radial velocities can be used to infer the existence of other planets in the system.

Successfully measuring radial velocities is highly dependent on the brightness of the host star and the strength of the spectral lines used in the measurement. The type of star generally determines the signal to noise of these lines, if they exist. RVs are particularly difficult to obtain for fast rotators (O and B type stars, and some M dwarfs) due to the severe line broadening, and for highly active stars (most M dwarfs), where flaring frequently interferes with the measurements. The faintness of M dwarfs can also pose a problem for obtaining high quality spectra.

51 Pegasi b was not only the first exoplanet discovered around a normal star, but, with a mass of $> 0.47 M_J$, was also the first example of a hot Jupiter - a giant planet on a <10 day period around its host star. While the idea that a planet could retain a large atmosphere so close to its host star was confounding at the time, hundreds of hot Jupiters have been discovered since. Whether these planets formed at their current locations or migrated inward through dynamically loud or quiet interactions still remains a highly pursued question in exoplanet formation and evolution.

Radial velocities were the primary exoplanet discovery tool for several years following the discovery of 51 Pegasi b. However, this was to change drastically with the advent of the transit method, which had become possible with improvements on instrumentation. At its core, the transit method is an incredibly simple concept: monitor a star for periodic dips in the amount of light received from said star. The depth of the dip (i.e. transit) tells the ratio of the size of the planet compared to the host star, and the frequency of recurrence is the orbital period. Transits typically

cause a sub-percent level of dimming of the star, meaning the photometric precision of telescopes used for this purpose needs to be on the order of at least ~1000 ppm. On their own, transits provide a measure of the radius of the planet, and can constrain the stellar density, eccentricity, orbital inclination, and the ratio of the semi-major axis to the host star's radius.

The first planet observed using the transit method was HD 209458 b (Charbonneau et al., 2000; Henry et al., 2000; Mazeh et al., 2000), which had previously been discovered through radial velocities cite and found to have a 3.52 day period. This was the first time an exoplanet had been detected through multiple means. By combining the information contained in transit and RV datasets, the orbital eccentricity, argument of periastron, and density of the planet can be derived. HD 209458 b was the first planet for which both a radius and mass was measured ($M_P = 0.63 M_J$, $R_P = 1.27 R_J$), yielding a bulk density of 0.38 g cm^{-3} - roughly half that of Saturn. This confirmed the idea that hot Jupiters can undergo significant inflation due to high levels of irradiation. A couple of years later, the first transiting exoplanet discovery was made using the Optical Gravitational Lensing Experiment (OGLE) (Konacki et al., 2003; Udalski et al., 2002b,a). OGLE-TR-56 b is yet another hot Jupiter ($M_P = 1.3 M_J$, $R_P = 1.3 R_J$) on a short, 1.2 day period.

The transit method was solidified as a viable exoplanet-hunting tool, but it would take nearly a decade for it to rival RVs as the dominant discovery method (Figure 1.1. A major advantage of transits is that they do not require a planet to be tracked for a full orbit, unlike RVs where each peak of the sine curve signature need significant coverage in order for the orbiting object to be confirmed. However, a downside to the transit method is the high rate of false positives. As objects (i.e. giant planet, brown dwarfs, or small stars) with masses from $0.001 \sim 0.1 M_*$ have a near-constant radius of $\sim 0.1 R_*$, a transit alone cannot always distinguish between the cases in the gray area of parameter space. It is therefore common to acquire RV measurements to determine the mass of the companion in order to rule out stellar binaries.

As the transit method requires near perfect alignment of the planet's orbit with respect to Earth, there is a much smaller probability of observing planets than those found through RVs. The

probability of the orbital plane of an exoplanet being oriented such that we could see it transit is

$$P_{\text{transit}} = \frac{R_* + R_P}{a} \tag{1.2}$$

(Johnson, 2016). If the Solar System was being observed from afar, the probability of Earth transiting the Sun is $\sim 0.5\%$.

This only takes into account the geometry of the situation - in reality, the limited sensitivity of our telescopes means we do not detect all planets that are in transit alignment. Furthermore, planets with long orbital periods are even less likely to be seen during transit, meaning the true probability of detecting transiting planets is minuscule. As the chance of serendipitously observing a transit is so low, transit surveys monitoring large swaths of sky - or the entire sky - have become a cornerstone for exoplanet discovery. This began with a series of ground-based facilities and projects from ~2000, the most prolific including the Hungarian Automated Telescope Network (HATNet) and its southern counterpart HATSouth (140 planet discoveries combined), the Kilodegree Extremely Little Telescope (KELT; 21 planets), and the Wide Angle Search for Planets (WASP; 161 planets). The first space-based transit hunter was CoRoT, which operated from 2006 to 2013, discovering 35 planets with more candidates still to be validated. add citations

A new age of exoplanet discovery was born with NASA's space-based Kepler mission. The Kepler telescope was launched in 2009, and used the transit method to search for Earth analogs in the habitable zones of their host stars, located in a single patch of sky over a four-year period. This triggered a gold rush of exoplanet discoveries, and to date Kepler is responsible for 2778 of these, with a further 1982 candidates yet to be confirmed. The leap in known exoplanets allowed for the first population studies of this nature, and uncovered aspects of exoplanet demographics that have rapidly become common knowledge in the field: the radius gap of small planets, the prevalence of super-Earths (and the peculiarity of our own Solar System not hosting one), the existence of hot Jupiters, to name a few. While Kepler was an invaluable resource and discovered hundreds of planets very quickly, follow-up observations of its targets can be difficult, if not impossible, due purely to the distance of the stars.

Unfortunately, in 2013, two of the four reaction wheels on board the spacecraft had degraded to the point of being no longer functional, so Kepler could no longer maintain the stable pointing of the previous four years. As the telescope was otherwise still in working order, a concept to prolong the mission was developed: by aiming Kepler directly away from the Sun (i.e. along the ecliptic plane) and minimizing torque from radiation pressure, the two remaining reaction wheels could keep the telescope sufficiently stable to continue performing science-grade photometry. Thus the K2 mission was created, and ran successfully until 2019, observing in roughly three-month campaigns. K2 has been used to discover 547 planets to date, with a further 975 candidates. The systems observed by K2 were different to those in the original Kepler mission: K2 targets were selected mostly by the community, and are generally closer due to the much shorter observing campaigns.

The age of transits has continued with the successor to Kepler, the Transiting Exoplanet Survey Satellite (TESS), which was launched in 2018. The purpose of TESS was to perform an all-sky survey to look for transiting planets (with a focus on Earth-sized ones) around nearby, bright stars that may be amenable to follow-up with HST and JWST. TESS has a huge 24 by 90 degree field of view, which scans a single patch of sky for ~27 days in an observing 'sector', before moving to the next position. The primary mission lasted for two years, in which it scanned $\sim$ 75% of the sky around the Northern and Southern hemispheres. TESS was approved for an extended mission lasting another two years, which included five sectors dedicated to covering $\sim$ 60% of the ecliptic plane (i.e. overlapping with K2 fields). The chunk of ecliptic that was not able to be targeted was due to the high intensity of moonlight that would be visible in this region at the time. TESS is currently in its second extended mission through to September 2025, which has seen another three sectors revisit the the fields of the previous ecliptic sectors, with planning for a third three-year extended mission in the works.

The transit method has been wildly successful as a discovery tool, especially for blind surveys. The exoplanet community is still heavily invested in it, with many more transit-hunting facilities set to begin operations in the coming decades, including the ESA's PLAnetary Transits and Oscillations

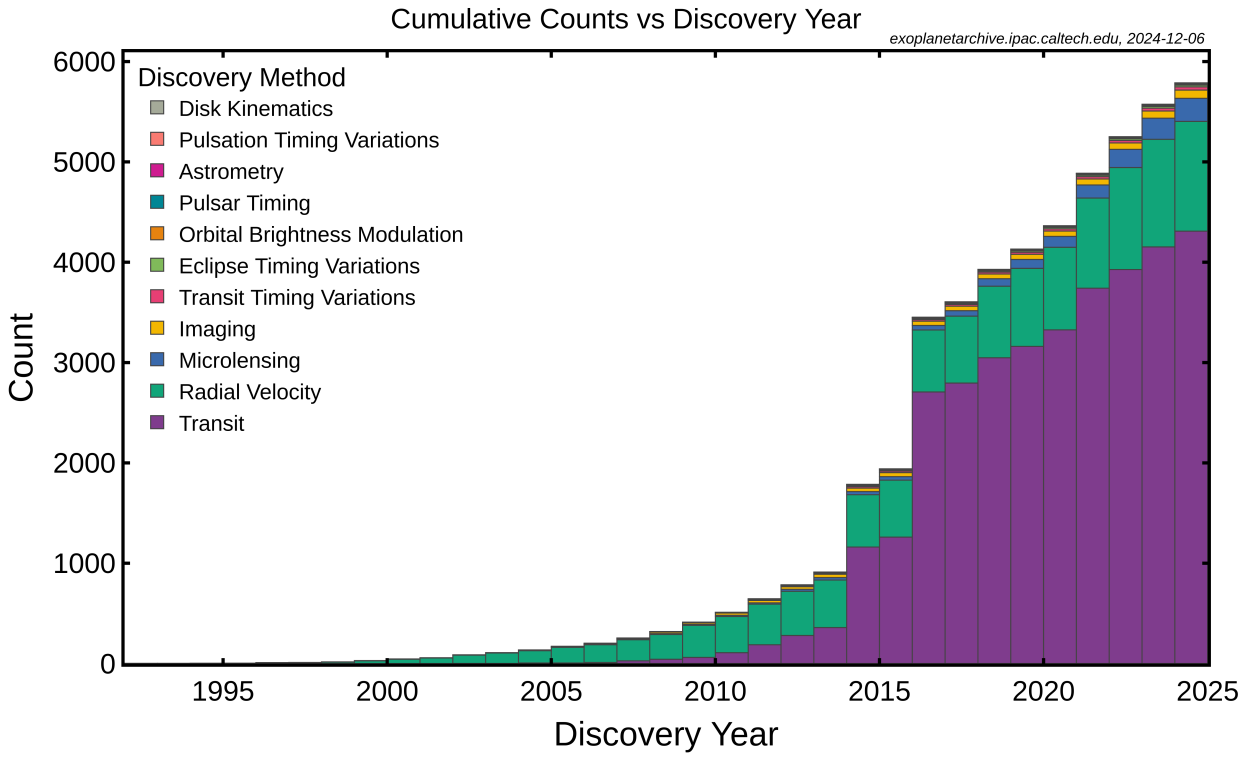

Figure 1.1 Cumulative number of exoplanet discoveries over the past few decades, color-coded by the detection method. RVs (green) were the primary method until 2012, when Kepler started the rapid increase through the transit method (purple).

of stars (PLATO, set to launch 2026), NASA's Nancy Grace Roman Space Telescope (2027 launch), and various Extremely Large Telescope (ELT) class (>20m) ground-based facilities such as ESO's ELT (~2028) and the Giant Magellan Telescope (early 2030s). add citations Until now, we have only seen the tip of the iceberg when it comes to the sheer number of exoplanets, with thousands more expected to be discovered with the aforementioned missions.

1.2 Exoplanet Characterization

With several thousands of exoplanets now confirmed, we have an abundance of worlds to study in more detail to better understand planet formation and evolution - and even search for life. A key observational diagnostic used in these studies is the chemical abundances in the planetary atmosphere. For transiting planets, the primary technique is transit spectroscopy, which involves observing the planet at different stages of its orbit to gain information during transit (transmission spectroscopy) or eclipse (emission spectroscopy). The focus from here on will be transmission

spectroscopy, as the scheduling of these observations is the main motivator for this thesis.

During a transit, light from the host star passes through the atmosphere of the planet, and can be reflected, absorbed, and re-emitted by different amounts depending on the chemical species present. The depth and shape of the transit is measured at many different wavelengths, which is compared to the host star's spectrum and converted into a measure of the amount of stellar light blocked by the planet. By doing this for a band of wavelengths, a transmission spectrum of the planetary atmosphere is revealed.

While transmission spectroscopy (TS) is possible with HST (technically any observation during transit is a form of transmission spectroscopy), it has a very limited wavelength range (0.1-1 microns for STIS, 0.8–1.6 microns for WFC3). The field of atmospheric studies was revolutionized with the much anticipated launch of JWST, which boasts a range of 0.6-27.9 microns across four instruments. TS with JWST has already been abundantly fruitful, uncovering never-before-seen processes in exoplanet atmospheres and unexpected compositions. The major JWST results are discussed further in Chapter 4.

JWST is not the only mission that will be used for precise TS going forward. The European Space Agency is developing the Atmospheric Remote-sensing Infrared Exoplanet Large-survey (Ariel) mission, which has an expected launch during 2029 and nominal mission lifetime of four years. Ariel will be dedicated towards studying ~1000 exoplanets to characterize their atmospheres in the 0.5 to 7.8 micron range.

1.3 Ephemeris Degradation

A key factor in scheduling observations for transit spectroscopy is knowing when in the future a planet will transit its host star. As with any measurement, there is uncertainty associated with the measured transit time of an exoplanet, which depends on the transit midpoint and orbital period of the planet at its discovery. As these uncertainties are typically on the order of minutes to hours, this in itself would not be an issue if it were not for the fact that they compound with each successive transit. The problem lies with error propagation - although a simple equation on the page, this creates a huge obstacle when predicting when a transit will occur in the future. The uncertainty on

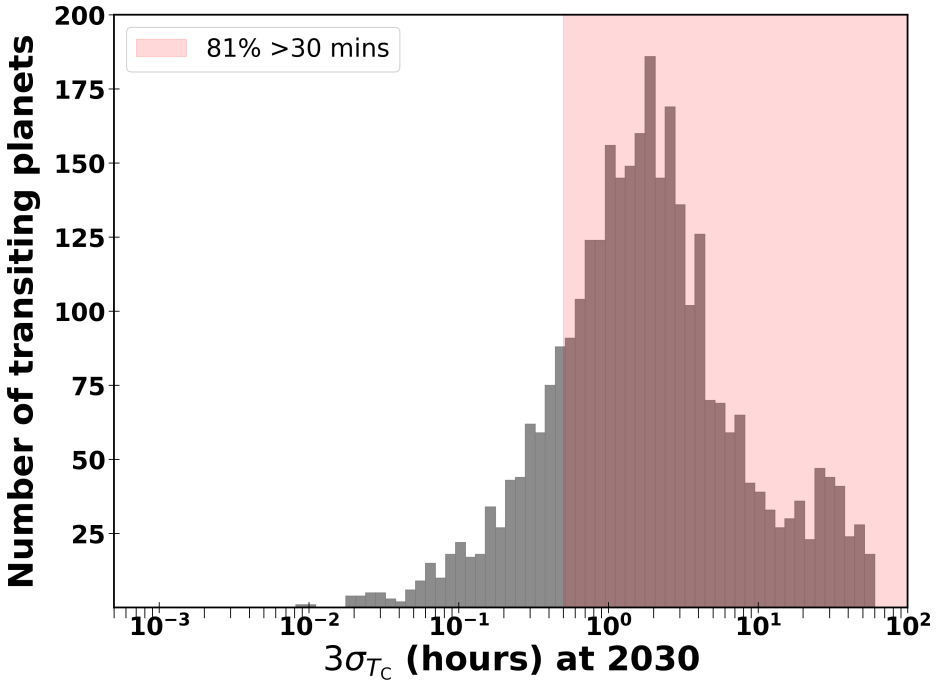

Figure 1.2 3σ uncertainties for all transiting exoplanets by the year 2030.

the transit time is simply

$$\sqrt{(n \times \sigma_P^2) + \sigma_{T_c}^2} \tag{1.3}$$

where n is the number of transits, T_c is the transit midpoint in BJD, and P is the orbital period of the planet. A planet with a 10 day period and an uncertainty of 10 minutes on both P and T_c will have a transit time uncertainty of ~1 hour after a year. This may sound negligible, but most exoplanets were discovered more than eight years ago, and many have much larger uncertainties on P and T_c, so in reality most known transiting planets have futures uncertainties greater than 30 minutes (Figure 1.2).

Facilities like JWST are highly competitive and costly to run[1], and any unnecessary overheads need to be minimized. In order to fully capture the ingress and egress of the planet, it is typical for proposed transmission spectroscopy observations to include around an hour either side of the transit. In practice, this should be added to the uncertainty of the transit time to ensure the observation

[1]The monetary cost of flagship missions is in the ballpark of 10-100k USD per hour to operate when considering the operational costs alone, not including design, construction, launch, etc.

of a complete transit. Alternatively, if the compounded uncertainty is ignored and observations scheduled, it is possible that the transit is only partially captured, or missed altogether. Thus, an uncertainty of a few minutes from the discovery of the planet can quickly become an unsuccessful proposal.

The solution to ephemeris degradation is to reobserve transits to refine the precision on P and T_c. The degree of improvement on the uncertainties increases with the length of the temporal baseline, i.e. number of transits that have occurred between observations. The solution to the ephemeris problem is as simple as the problem itself, but a hidden complication arises when considering the resources needed to perform this on a large scale. Updating individual systems is achievable with targeted observations, but is not feasible to address the hundreds of planets for which this is needed. Fortunately, the TESS mission is observing nearly the entire sky, with some regions of the sky being covered by multiple sectors. While TESS has discovered hundreds of new transiting planets, it is also providing a timely opportunity to update transit times for hundreds, if not thousands, of already-known planets.

Unfortunately, the ephemeris problem is always going to be a part of utilizing the transit method. Even planets discovered by TESS will need to be revisited by future missions to maintain the transit times, as their ephemerides degrade significantly after only a year from discovery (Dragomir et al., 2020). A concerted effort needs to be made to maintain ephemerides of planets that will be characterized in more depth in the future.

1.4 Ephemeris Refinement Projects

Several efforts exist to update transit times for a large number of exoplanets, in some cases utilizing the power of citizen science. ExoClock[2] (Kokori et al., 2021, 2022, 2023) is an open project designed to update ephemerides of most targets of the future Ariel mission. It began in September 2019 and has over 500 members, most of whom are citizen scientists/amateur astronomers, resulting in access to 450 telescopes worldwide. Ephemerides are updated using new data from these observations, as well as from the literature, the Exoplanet Transit Database

[2]https://www.exoclock.space/

(Poddaný et al., 2010), and from space missions (i.e. Kepler, K2, and TESS). Currently, the ephemerides of 450 planets have been updated through this effort.

Exoplanet Watch[3] is a NASA-led project heavily based on citizen science (Zellem et al., 2019, 2020). Similar to ExoClock, amateur astronomers from anywhere in the world can contribute with their own telescopes. This project has not only resulted in updated ephemerides for known planets, but has contributed to the discovery of an eccentric warm Jupiter (Sgro et al., 2024) and been used as part of undergraduate research experience (Hewitt et al., 2023).

The Transit Ephemeris Refinement and Monitoring Survey (TERMS; Kane et al. 2009) is an ongoing effort to update ephemerides and system parameters for planets discovered through RVs. Orbital parameters for each planet are determined through the RV measurements, from which a transit window is calculated. This project highlights the importance of using both RVs and transits to better characterize exoplanets, and shows that observation techniques can be used to inform one another.

All of these efforts will ensure the continued accessibility of hundreds of transiting exoplanets, however, as discussed previously, this will be an ongoing problem needing constant addressing.

1.5 The K2 & TESS Synergy

The K2 & TESS Synergy is a large scale, dedicated effort to reanalyze known planets from the K2 mission with recently acquired TESS observations. The main difference setting it apart from the previously-mentioned projects is that it will result in a self-consistent catalog of not only transit times, but fully updated system parameters (for both the planets and host stars). This highlights another general problem in the field: many population studies to date use measurements made by different teams using various analysis methods, assumptions, and software, meaning trends in the data may be artificially introduced. In this section, we describe how the K2 & TESS Synergy project was started and continued with the work in this thesis.

[3]https://exoplanets.nasa.gov/exoplanet-watch/

1.5.1 Pilot Study

The K2 & TESS Synergy began with a pilot study (predating the work in this thesis) by Ikwut-Ukwa et al. (2020) that considered four single-planet K2 systems (K2-114, K2-167, K2-237 and K2-261) for ephemeris renewal using TESS. This was a proof of concept to show the severity of ephemeris degradation for typical K2 targets, and how TESS would be a powerful tool for combating the problem on a large scale. At this time, TESS was still in its first year of operation and had only clipped the very edges of the K2 campaigns, which meant a single sector of data was available for each of the four planets. By performing global fits including the new TESS light curves, the ephemerides for all four planets were greatly improved: at a 3σ level, the future transit time uncertainty went from 7.6 hours to 8 minutes for K2-114, 40.6 hours to 1.1 hours for K2-167, 55 minutes to 8 minutes for K2-237, and 3.5 hours to 30 minutes for K2-261.

1.5.2 This Work

With the success of the pilot study, the process was proven to be a viable method to achieve significant improvement on the transit times that could be extended to a larger sample as TESS sectors increasingly overlapped with the K2 footprint. It is this extension of the K2 & TESS Synergy that constitutes the work presented in this thesis. Beyond updating stale ephemerides, the systematic reanalysis of all K2 systems allows us to amend any incorrect values in the literature.

The same fundamental method was used going forward: acquire light curves from K2 and TESS, collate RVs from the literature, obtain parallaxes, stellar SEDs, and metallicities, and then run global fits. To handle a much larger sample and ever-increasing number of TESS light curves, a pipeline was created to retrieve and prepare TESS data ready to be fit (include this? will expand if so).

The reason for selecting the K2 catalog specifically for this project is manyfold. As most of the K2 targets were closer and brighter than those from the Kepler field, there are many overlapping targets with TESS. These targets included many M dwarfs, which are increasingly sought-after systems when it comes to finding small planets within their habitable zones. Additionally, many (most? get better estimate) K2 targets have not been reobserved since their original discovery, now

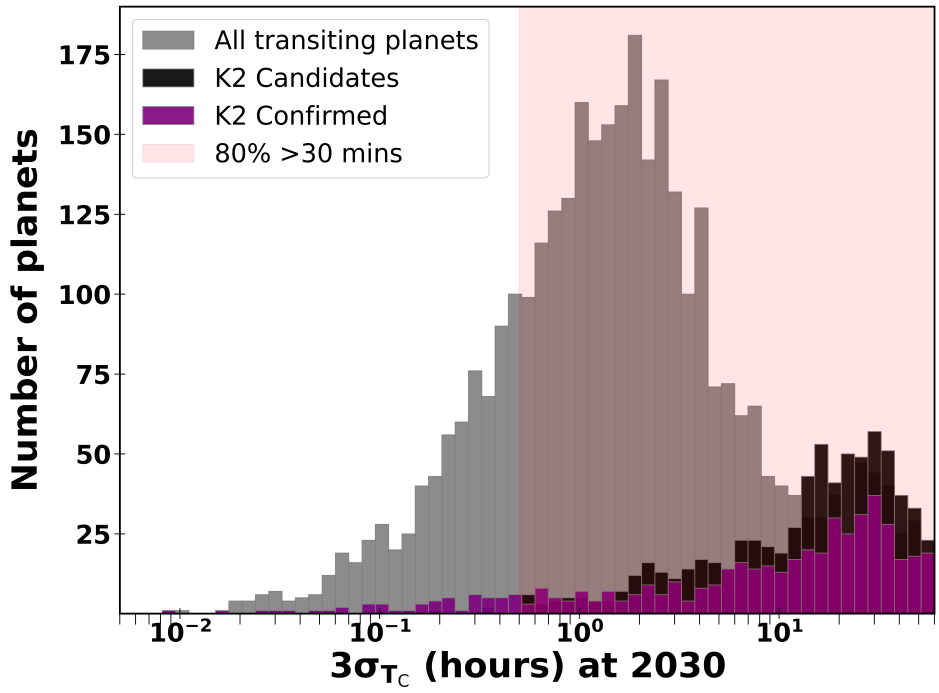

Figure 1.3 3σ uncertainties for all transiting exoplanets by the year 2030 (UPDATE FIGURE). change so it shows only K2. or just show this plot and not the previous one.

6 ~ 10 years ago. The ephemerides for most these systems have uncertainties well beyond the limit for transmission spectroscopy observations (Figure 1.3).

As our goal is to update ephemerides for targets amenable to future atmospheric characterization, we prioritize planets by their transmission spectroscopy metric (TSM), which is an estimate of the expected signal to noise of a transmission spectrum (expand on this?). That way, the targets more likely to be more favorable for JWST observations will be updated first. With the updated global parameters obtained via the same analysis prodecure, we can also perform appropriate population studies within the K2 sample.

1.5.3 EXOFASTv2

The core philosophy of the K2 & TESS Synergy is to produce self-consistent, global parameters for all of the systems that are addressed. This is where the choice of fitting software plays a major role. A plethora of fitting suites exists for exoplanet data. The majority fit either the photometry (e.g. TAP, BATMAN) or radial velocities (e.g. RadVel, Systemic), or both (e.g. Exonailer, the Transit Light Curve Modeller, Pyaneti, exoplanet, Juliet, allesfitter, ellc), and incorporate lower-

level fitting codes to model the data (e.g. BATMAN, dynesty, emcee, ellc, celerite, george, PyMC3). add citations The major differences between these codes are their approach to fitting (nested, mcmc, look all this up), and capabilities for fitting other phenomena present in the data (e.g. star spots, flares, transit timing variations etc.).

The fitting software of choice for the K2 & TESS Synergy is `EXOFASTv2` (Eastman et al., 2013; Eastman, 2017; Eastman et al., 2019), which is, to our understanding, the most complete fitting tool for exoplanets. The major advantage of `EXOFASTv2` compared to other available software is the fact that it simultaneously fits parameters of the planet(s) and host star(s), meaning parameters are concurrently being fit while guiding the direction of the fit for related parameters. This is becoming increasingly pertinent, especially if we heed the popular adage of "know thy star, know thy planet". For example, the transit duration can help constrain the stellar density, and limb darkening can inform $T_{\rm eff}$, $\log(g_*)$, and [Fe/H]. Conversely, the planetary radius and mass are relative to those of the host star.

`EXOFASTv2` uses a Differential Evolution (DE) MCMC to fit for parameters from the given data sets. The DE-MCMC approach allows for multiple chains to be run in parallel and 'learn' from each other. In this case, the number of chains is set to twice the number of dimensions (typically on the order of $\sim$ 40). `EXOFASTv2` has the capability to simultaneously fit many data sets. Along with photometry and spectroscopy, it can fit for stellar parameters if an SED of the star is provided, in conjunction with stellar evolutionary models selected by the user, the default being MIST (torres, parsec and YY also available). Additionally, the limb darkening coefficients are fit for each photometric band. Both additive and multiplicative detrending can be accounted for in the light curve and RV curve, along with dilution of the light curve due to contamination of the photometric aperture. `EXOFASTv2` is able to model systems with multiple planets and/or stars. Other features of `EXOFASTv2` that are not used within this work include modeling Doppler Tomography, and fitting for variations in transit timing, depth and duration. The user is able to provide starting points and/or priors for each parameter that is being fitted. So as not to underestimate uncertainties, we limit the parameters that we place Gaussian priors on (which ones). Convergence criteria are fairly strict

compared to other standards: only when $R_z < 1.01$ and $T_z > 1000$ is a fit considered converged (elaborate).

This is currently the most thorough fitting code for exoplanets, however, it comes with the inevitable high computation cost. While it would certainly be faster to use a simpler fitting suite, or only fit photometry (as with the other large ephemeris projects), the use of `EXOFASTv2` allows us to kill two birds with one stone (find a nicer saying) - updating both the ephemerides and system parameters to build to a self-consistent catalog.

1.6 Outline

Chapter 2 is the published work of Thygesen et al. (2023), which included the first large batch of systems for the K2 & TESS Synergy. In this work, we addressed 26 single-planet systems that were observed by TESS in its primary mission. We were able to significantly improve the ephemerides of half of the systems, from an average 3σ uncertainty by 2030 of 26.7 hours to 35 minutes. The remaining 13 planets did not have transits of high enough signal to noise to be detected in the TESS light curves, but we still ran the global fits with only the K2 light curves, which saw an average improvement of the ephemerides from 43.2 to 35.6 hours.

In chapter 3, we take a detour to investigate the lost ephemeris of K2's first planet discovery, K2-2 b. This is the third installment of the K2 & TESS Synergy, published as Thygesen et al. (2024). A factitious transit in a secondary light curve originally used to confirm this planet meant the period was off by 28.8 minutes ($\sim 40\sigma$), which resulted in the transit being missed during targeted follow-up with HST and Spitzer. We found the true transit time with light curves obtained from ground- and space-based facilities over a seven year span, and uncovered a potential outer planet in the system via a long term trend in the radial velocities.

Chapter 4 consists of the current work on the next installment of the K2 & TESS Synergy. This batch contains the top 31 K2 planets amenable to transmission spectroscopy, which includes eight planets previously analyzed as part of the K2 & TESS Synergy. We improved the average 3σ uncertainties on transit times by 2030 from 9.34 hours to 26 minutes, ensuring these planets can be targeted for future observations.

Finally, the work in this thesis is summarized in Chapter 5, along with potential paths forward for the K2 & TESS Synergy project.

CHAPTER 2

THE K2 & TESS SYNERGY II: REVISITING 26 SYSTEMS IN THE TESS MISSION

This section reviews the published work of Thygesen et al. (2023)

2.1 Abstract

The legacy of NASA's K2 mission has provided hundreds of transiting exoplanets that can be revisited by new and future facilities for further characterization, with a particular focus on studying the atmospheres of these systems. However, the majority of K2-discovered exoplanets have typical uncertainties on future times of transit within the next decade of greater than four hours, making observations less practical for many upcoming facilities. Fortunately, NASA's Transiting Exoplanet Survey Satellite (TESS) mission is reobserving most of the sky, providing the opportunity to update the ephemerides for ~300 K2 systems. In the second paper of this series, we reanalyze 26 single-planet, K2-discovered systems that were observed in the TESS primary mission by globally fitting their K2 and TESS lightcurves (including extended mission data where available), along with any archival radial velocity measurements. As a result of the faintness of the K2 sample, 13 systems studied here do not have transits detectable by TESS. In those cases, we re-fit the K2 lightcurve and provide updated system parameters. For the 23 systems with $M_* \gtrsim 0.6\ M_\odot$, we determine the host star parameters using a combination of Gaia parallaxes, Spectral Energy Distribution (SED) fits, and MESA Isochrones and Stellar Tracks (MIST) stellar evolution models. Given the expectation of future TESS extended missions, efforts like the K2 & TESS Synergy project will ensure the accessibility of transiting planets for future characterization while leading to a self-consistent catalog of stellar and planetary parameters for future population efforts.

2.2 Introduction

The past two decades have been fruitful for exoplanet discovery, with over 5000 exoplanets confirmed to date[1]. While new discoveries are still being made, we are simultaneously venturing into an era of exploring known systems in further detail, with a variety of dedicated efforts for exoplanet characterization. Facilities that are operational or expected to be online in the next

[1] https://exoplanetarchive.ipac.caltech.edu/

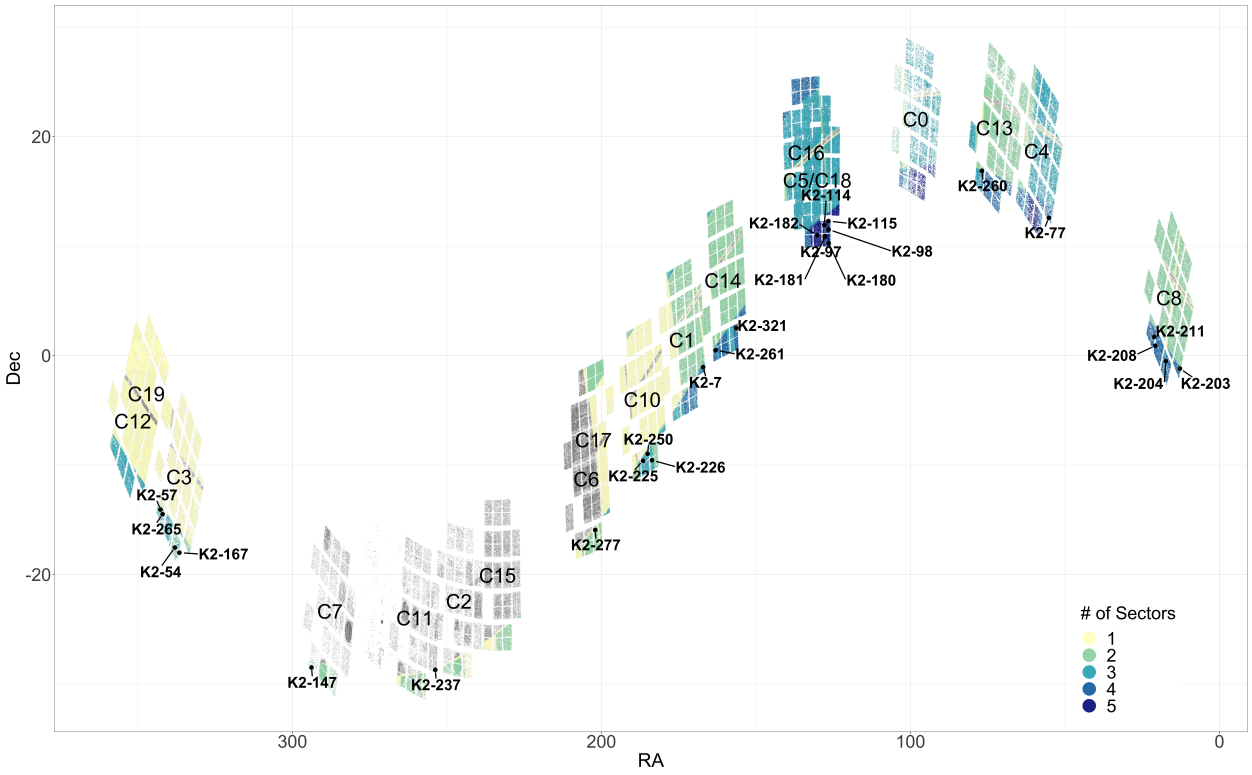

Figure 2.1 Overlap between K2 campaigns and TESS sectors. The number of times each K2 target was observed in TESS sectors is indicated by the color, with gray indicating no TESS overlap as of Sector 46. The systems analyzed in this study are labeled.

decade such as JWST (Gardner et al., 2006; Beichman et al., 2020), 39 m European Southern Observatory Extremely Large Telescope (ELT; Udry et al. 2014), Nancy Grace Roman Space Telescope (e.g. Carrión-González et al. 2021), Giant Magellan Telescope (Johns et al., 2012) and Atmospheric Remote-sensing Infrared Exoplanet Large-survey (ARIEL; Tinetti et al. 2018, 2021) will provide key information about the atmospheres of exoplanets, and insight into their formation and evolutionary processes. However, these ongoing and future endeavors to reobserve known transiting exoplanets heavily rely on precisely knowing the transit time, which is challenged by the degradation of the ephemeris over time.

Most exoplanets and candidates found to date were originally discovered by the Kepler mission (Borucki et al., 2010). Kepler was launched in 2009 with the goal of understanding the demographics of transiting exoplanets. This mission was a success, having discovered ~2700 confirmed planets

with a further ~2000 candidates[2], in addition to advancing our understanding of the host stars they orbit (e.g. Bastien et al. 2013; Berger et al. 2020a,b). However, by May of 2013 two of the four reaction wheels on the spacecraft had failed, severely limiting the pointing of Kepler, threatening to end the mission. A solution was conceived to point the spacecraft at the ecliptic to reduce torque from Solar radiation pressure, so that the remaining two reaction wheels, along with the thrusters, could maintain sufficient stability. This saw Kepler successfully reborn as the K2 mission (Howell et al., 2014). While Kepler continuously pointed at one region of sky, the necessity of K2 being aimed along the ecliptic opened up an opportunity to study different populations of stars. K2 continued on the path of exoplanet discovery, with currently ~500 confirmed planets and another ~1000 candidates found by the time the spacecraft retired in 2018 when fuel for the thrusters ran out (Vanderburg et al., 2016; Zink et al., 2021; Kruse et al., 2019; Pope et al., 2016; Livingston et al., 2018a; Crossfield et al., 2016; Dattilo et al., 2019).

Unfortunately, many of the known planets discovered by the K2 mission have not been reobserved since their discovery, leading to future transit time uncertainties of many hours (Ikwut-Ukwa et al., 2020). This has recently changed with the launch of NASA's *Transiting Exoplanet Survey Satellite* (TESS) mission in 2018 (Ricker et al., 2015), the successor to the Kepler and K2 missions. The two-year primary mission of TESS aimed to observe more than 200,000 stars at two-minute cadence across ~75% of the sky. To date, TESS has found ~280 confirmed planets and another ~6100 candidates[3]. Even though K2 targeted the ecliptic plane and the TESS primary mission only skimmed the edges of some K2 fields, there are ~30 systems that were observed by both (single- and multi-planet systems). This provides an opportunity to begin updating the ephemerides and parameters of K2 systems that have been reobserved by TESS. The first extended mission of TESS began during 2020, and includes sectors dedicated to the ecliptic plane, providing more substantial overlap of a further ~300 systems with the K2 fields[4] (Figure 2.1). With TESS scheduled to reobserve nearly the entire sky during its extended missions, it will be a useful tool

[2]https://exoplanetarchive.ipac.caltech.edu/

[3]https://nexsci.caltech.edu/

[4]https://heasarc.gsfc.nasa.gov/docs/tess/the-tess-extended-mission.html

for refreshing the ephemerides of thousands of transiting exoplanets.

Currently, many known exoplanets do not have sufficiently accurate projected transit times to plan observations with future missions. Even TESS ephemerides will need to be updated as most TESS planets will have transit time uncertainties exceeding 30 minutes in the era of JWST (Dragomir et al., 2020). With the wealth of data coming from ongoing surveys like TESS and the ability to follow up many planets with small aperture (<1 m) telescopes (Collins et al., 2018), many efforts have begun to keep the ephemerides of transiting planets from going stale, like the ExoClock Project (Kokori et al., 2021, 2022) for future ARIEL targets and the K2 & TESS Synergy (Ikwut-Ukwa et al., 2020). Ephemeris refinement programs focused on citizen science (Zellem et al., 2019, 2020) and high-school students (e.g. ORBYTS; Edwards et al. 2019, 2020, 2021) also provide opportunities to actively engage the public while contributing to an essential aspect of future exoplanet characterization. These efforts will be key to making a large number of systems accessible for future facilities.

A continual renewal of ephemerides also presents an opportunity to create self-consistent catalogs of exoplanets and their parameters, which not only helps to plan for future missions, but also allows for appropriate population studies using data that have been uniformly prepared. While the vast amount of data available per system makes this a challenge, the advent of new exoplanet fitting suites to globally analyze large quantities of data, like `Juliet` (Espinoza et al., 2019), `EXOFASTv2` (Eastman et al., 2013; Eastman, 2017; Eastman et al., 2019), `Allesfitter` (Günther & Daylan, 2021) and `exoplanet` (Foreman-Mackey et al., 2021), has made it possible to individually model the available observations for a large sample of exoplanetary systems. These types of studies are necessary to uncover large-scale trends or mechanisms that may play important roles in planet formation and evolution. A renowned example is the radius valley of small planets (Fulton et al., 2017), which was achieved through more accurate and consistent handling of host star parameters for over 2000 planets from the California-Kepler Survey.

A case study for updating K2 ephemerides and system parameters with new TESS data was presented in the first paper of this series (Ikwut-Ukwa et al., 2020), where four K2-discovered

systems (K2-114, K2-167, K2-237 and K2-261) were reanalyzed by performing global fits using K2 and TESS lightcurves. This resulted in the uncertainties for the transit times of all four planets being reduced from multiple hours to between 3-26 minutes (at a one sigma level) throughout the expected span of the JWST primary mission, showcasing the value of combining the K2 and TESS data. We continue this work by reanalyzing a sample of 26 single-planet systems observed with K2 and the primary TESS mission (including refitting the original four systems for consistency), while also making use of archival radial velocities, *Gaia* parallaxes and any currently available lightcurves from the TESS extended mission. We focus on previously-confirmed single-planet systems, but future papers in this series are expected to reanalyze all K2 systems (including multi-planet systems) as part of an ongoing TESS guest investigator program (G04205, PI Rodriguez). Updated transit times will be made available to the community throughout this series through the Exoplanet Follow-up Observing Program for TESS (ExoFOP)[5].

In §2.3 we describe how we obtained and prepared the data used in our global fits. §2.4 outlines how we ran the `EXOFASTv2` analysis, and §2.5 presents our results along with any peculiarities for specific systems. Our conclusions are summarized in §2.6.

2.3 Observations and Archival Data

Given that most known K2-discovered exoplanet systems will have uncertainties larger than 30 minutes (see Figure 2.2), we take advantage of the high-quality data obtained with K2 and TESS, simultaneously fitting the photometry and archival spectroscopy to update system parameters for 26 K2 systems. Here we describe the techniques used to obtain and process K2 and TESS lightcurves, as well as radial velocities from existing literature.

2.3.1 K2 Photometry

Each of these stars was observed by the Kepler spacecraft during its K2 extended mission (Howell et al., 2014). During K2, the spacecraft's roll angle drifted significantly due to the failure of two reaction wheels, which introduced significant systematic errors into its lightcurves[6]. Over

[5]https://exofop.ipac.caltech.edu/tess/

[6]The two remaining reaction wheels onboard K2 could control the position of the telescope's boresight, but the roll angle could only be controlled by occasional firing of the thrusters about every 6 hours as radiation pressure caused

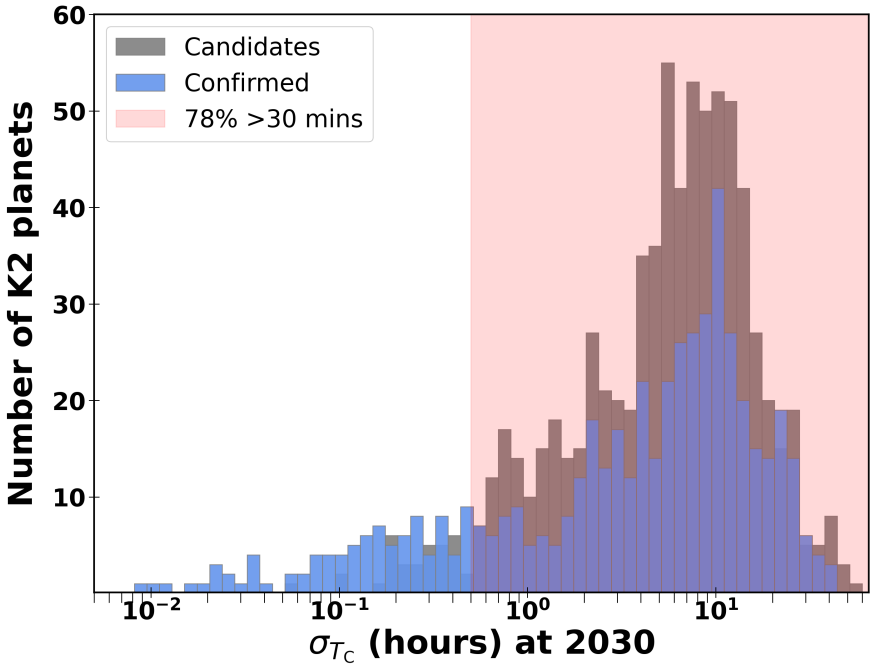

Figure 2.2 Uncertainty of the transit time (σ_{T_c}) for K2 candidate and confirmed planets at the year 2030, based on the discovery ephemeris. The majority of planets have uncertainties greater than 30 minutes (indicated by the red region) in the era of JWST, making these challenging to reobserve. Values taken from the NASA Exoplanet Archive (NEA) default parameter sets.

the course of the mission, a number of different techniques and methods were developed to mitigate these errors (e.g. Aigrain et al. 2016; Barros et al. 2016; Luger et al. 2016; Lund et al. 2015; Pope et al. 2019). In this work, we used the methods of Vanderburg & Johnson (2014) and Vanderburg et al. (2016) to derive a rough systematics correction. In brief, these methods involve extracting raw lightcurves from a series of 20 different photometric apertures, correlating short timescale variations in the raw lightcurves with the spacecraft's roll angle (which changes rapidly due to K2's unstable pointing), and subtracting variability correlated with the spacecraft's roll angle. The process of correlating and subtracting variability correlated with the roll angle is performed iteratively until the only remaining variations in the lightcurve are unrelated to the spacecraft's roll. Finally, we select the aperture that produces the most precise lightcurve among the 20 originally extracted. Then, we refined the systematics correction by simultaneously fitting the transits for each planet along with the systematics correction and low-frequency stellar variability, prior to the

the telescope to slowly roll about its long axis.

final global fit. Most of the data we analyzed were collected in 30-minute long-cadence data, but when available, we analyzed 1-minute short-cadence exposures for better time sampling. For all systems, we only included out-of-transit data from one full transit duration before and after each transit. This is to optimize the balance between having enough data points to establish the baseline flux of the star and lengthening the runtime of the fits due to having more data.

2.3.2 TESS Photometry

While all 26 systems were initially observed by TESS in the primary mission, each was reobserved in at least one sector of the first extended mission. We therefore included TESS lightcurves from the primary and extended missions up to and including Sector 46 (as of February 1, 2022). This was the final sector dedicated to the ecliptic plane for the first extended mission. Future efforts in this series will analyze systems that were first observed by TESS during the first extended mission and beyond.

We used the Python package *Lightkurve* (Lightkurve Collaboration et al., 2018) to retrieve TESS lightcurves from the Mikulski Archive for Space Telescopes (MAST). Three systems within the footprint of the TESS primary mission (K2-42, K2-132/TOI 2643 and K2-267/TOI 2461) did not have corresponding retrievable lightcurves, which is likely due to being too close to the edge of the detector, so we excluded these from the current analysis. For the TESS lightcurves, we used the Pre-search Data Conditioned Simple Aperture Photometry (PDCSAP) flux, which is the target flux within the optimal TESS aperture that has been corrected for systematics with the PDC module (Stumpe et al., 2012, 2014; Smith et al., 2012). Typically, observations for each sector are processed through the Science Processing Operations Center (SPOC) pipeline at the NASA Ames Research Center (Jenkins et al., 2016). The SPOC pipeline takes in the raw data and applies corrections for systematics, runs diagnostic tests and identifies transits, resulting in a calibrated lightcurve that can be used for analysis.

TESS science observations are taken at 20-second and 2-minute cadences (the former only becoming available from the first extended mission), while the Full Frame Images (FFIs) are created every 30 minutes during the primary mission, and every 10 minutes since the first extended

mission. For our global analysis, (see §2.4) we used the shortest cadence available, preferentially using data processed through SPOC (Jenkins et al., 2016; Caldwell et al., 2020). The increased timing precision of short cadence observations is only valuable if there is a significant detection of the transit. For this reason, and since TESS is optimized for targets with brighter magnitudes than those of K2, we binned lightcurves observed at 20-second cadence to two minutes to increase signal-to-noise.

If a TESS-SPOC FFI lightcurve was not available for a particular sector, we extracted the lightcurve using a custom pipeline as described in Vanderburg et al. (2019). The pipeline uses a series of 20 apertures from which lightcurves are extracted and corrected for systematic errors from the spacecraft by decorrelating the flux with the mean and standard deviation of the quaternion time series. Dilution from neighbouring stars within the TIC is corrected for within each aperture, which takes into account the TESS pixel response function. The final aperture used for the lightcurve extraction is selected as the one that minimized the scatter in the photometry. Recent efforts have compared this custom pipeline with other FFI pipelines (Rodriguez et al., 2022a), supporting our adoption of this pipeline. The list of available lightcurves (as of February 1, 2022) is shown in Table 3.2.

After retrieving the TESS lightcurves for our targets, we processed them further for our own analysis, assuming values for transit duration, time of conjunction (T_c) and period from the NASA Exoplanet Archive (NEA). To flatten the out-of-transit lightcurve for fitting, we used `keplerspline`[7], a spline-fitting routine to model and remove any variability from the star or remaining systematics (Vanderburg & Johnson, 2014). Within `keplerspline`, the spacing between breaks in the spline to handle discontinuities is optimized by minimizing the Bayesian Information Criterion (BIC) for different break points (see Shallue & Vanderburg 2018 for further methodology). We applied a constant per-point error for the photometry, calculated as the median absolute deviation of the out-of-transit flattened lightcurve, although this error is optimized within our analysis since `EXOFASTv2` fits a jitter term. If any lightcurve had large outliers or features that may influence our

[7]https://github.com/avanderburg/keplerspline

Table 2.1 Target list and data used in this analysis.

TIC ID	TOI	KID	EPIC ID	K2 Campaign	TESS Sector		RV inst
					(2 min)	(FFI)	
53210555	—	K2-7	201393098	C1	9, 36, 45, 46	—	–
12822545	—	K2-54†	205916793	C3	2, 42	—	–
146799150	—	K2-57	206026136	C3	2, 29	—	–
435339847	4544.01	K2-77	210363145	C4	5′, 42′, 43′, 44′	—	–
366568760	5121.01	K2-97	211351816	C5, C18	7′, 44′, 45′, 46′	—	LEVY[1] (6),
366410512	5101.01	K2-98	211391664	C5, C18	7, 34, 44, 45, 46	—	FIES[3] (4), HARPS[3]
366576758	514.01	K2-114	211418729	C5, C18	7, 44, 45, 46	—	HIRE
7020254	4316.01	K2-115	211442297	C5, C18	7, 34, 45, 46	—	HIRE
398275886	—	K2-147†	213715787	C7	27	13	–
69747919	1407.01	K2-167	205904628	C3	2, 28, 42,	—	–
366411016	5529.01	K2-180	211319617	C5, C18	34, 44, 45, 46	7*	HARPS
366528389	—	K2-181	211355342	C5, C18	7, 44, 45, 46	—	–
366631954	5068.01	K2-182	211359660	C5, C18	34, 44, 45, 46	7	HIRES
333605244	—	K2-203	220170303	C8	30, 42, 43	3	–
248351386	—	K2-204	220186645	C8	30, 42, 43	3	–
399722652	—	K2-208	220225178	C8	30, 42, 43	3	–
399731211	—	K2-211	220256496	C8	30, 42, 43	3	–
98677125	—	K2-225	228734900	C10	36, 46	10	–
176938958	—	K2-226	228736155	C10	36, 46	10	–
16288184	1049.01	K2-237	229426032	C11	12, 39	—	CORALIE[7] (9), HAR
98591691	—	K2-250	228748826	C10	36, 46	10	–
293612446	2466.01	K2-260	246911830	C13	32, 43	5*	FIES[9]
281731203	685.01	K2-261	201498078	C14	9, 35, 45, 46	—	FIES[9] (12), HARPS[9]
146364192	—	K2-265	206011496	C3	29, 42	2	HARPS
404421005	4628.01	K2-277	212357477	C6	10, 37′	—	–
277833995	5524.01	K2-321†	248480671	C14	8′, 45′, 46′	35′ (10min)	–

Notes: TESS lightcurves taken at 20 second cadence were prioritised, and binned to two minutes. Where short cadence observations were not available, FFIs were used. TESS sectors in which transits had SNR≤7 and thus were too shallow to be recovered are colored red. We incorporated previous RV measurements that were taken from the previous studies listed here. The number in parentheses following the RV instrument indicates the number of measurements. K2 references are previous analyses with which we compare our updated ephemerides in §2.5.

† The host stars in these systems were classed as low mass ($\lesssim 0.6\ M_\odot$), so we did not include the SEDs in the global fits. See §2.4 for details.

′ The full lightcurves for these were used to ensure the transit was able to be detected. All other lightcurves were sliced as discussed in §2.3.

* A custom pipeline was used to extract lightcurves for sectors without TESS-SPOC FFIs as discussed in §2.3.2.

References for RV measurements: [1]Grunblatt et al. (2016), [2]Grunblatt et al. (2018), [3]Barragán et al. (2016), [4]Shporer et al. (2017), [5]Korth et al. (2019), [6]Akana Murphy et al. (2021), [7]Soto et al. (2018), [8]Smith et al. (2019), [9]Johnson et al. (2018a), [10]Lam et al. (2018)

K2 references: 1 - Montet et al. (2015), 2 - Crossfield et al. (2016), 3 - Mayo et al. (2018), 4 - Livingston et al. (2018a), 5 - Barragán et al. (2016), 6 - Shporer et al. (2017), 7 - Adams et al. (2021), 8 - Korth et al. (2019), 9 - Akana Murphy et al. (2021), 10 - Soto et al. (2018), 11 - Livingston et al. (2018b), 12 - Johnson et al. (2018b), 13 - Lam et al. (2018), Castro González et al. (2020)

transit fit, we used only the data that had no bad quality flags within *Lightkurve* (this was only the case for K2-250 and K2-260). To reduce the individual runtime for each system, we excluded the out-of-transit baseline of the TESS lightcurves from the `EXOFASTv2` fit other than one full transit duration before and after each transit (as with the K2 lightcurves). However, for systems whose transits were not readily visually identified in the TESS data (K2-77, K2-97, K2-277 and K2-321; see Table 3.2), we included all out-of-transit photometry to account for any large uncertainties in the time of transits during the TESS epochs.

2.3.3 Archival Spectroscopy

We identified spectroscopic observations from the literature for 10 of the 26 total targets (Figure 2.3; K2-97, K2-98, K2-114, K2-115, K2-180, K2-182, K2-237, K2-260, K2-261 and K2-265; Grunblatt et al. 2016, 2018; Barragán et al. 2016; Shporer et al. 2017; Korth et al. 2019; Akana Murphy et al. 2021; Soto et al. 2018; Smith et al. 2019; Johnson et al. 2018a; Lam et al. 2018). We selected data sets with four or more RV measurements to ensure more degrees of freedom in the global fit, thus avoiding overfitting the data. For this reason we do not include RVs for K2-77 (Gaidos et al., 2017) and K2-147 (Hirano et al., 2018). Table 3.2 lists the analyses from which we obtained each set of RVs that we incorporated in the global analysis (see §2.4). All but one of the systems that have RVs also have significant TESS transits (see §2.4), which is an outcome of spectroscopic measurements preferentially targeting brighter stars. The archival RVs were obtained from the following instruments: the Levy spectrometer on the 2.4m Automated Planet Finder at Lick Observatory, the High Resolution Echelle Spectrometer (HIRES) on the Keck-I Telescope (Vogt et al., 1994), the FIbre-fed Echelle Spectrograph (FIES) on the 2.56m Nordic Optical Telescope at Roque de los Muchachos Observatory Frandsen & Lindberg (1999), the High Accuracy Radial velocity Planet Searcher (HARPS) spectrograph on the 3.6m telescope at La Silla Observatory (Mayor et al., 2003), HARPS-N on the 3.58m Telescopio Nazionale Galileo at the Roque de los Muchachos Observatory (Cosentino et al., 2012), and the CORALIE spectrograph on the Swiss 1.2m Leonhard Euler Telescope at La Silla Observatory (Queloz et al., 2000).

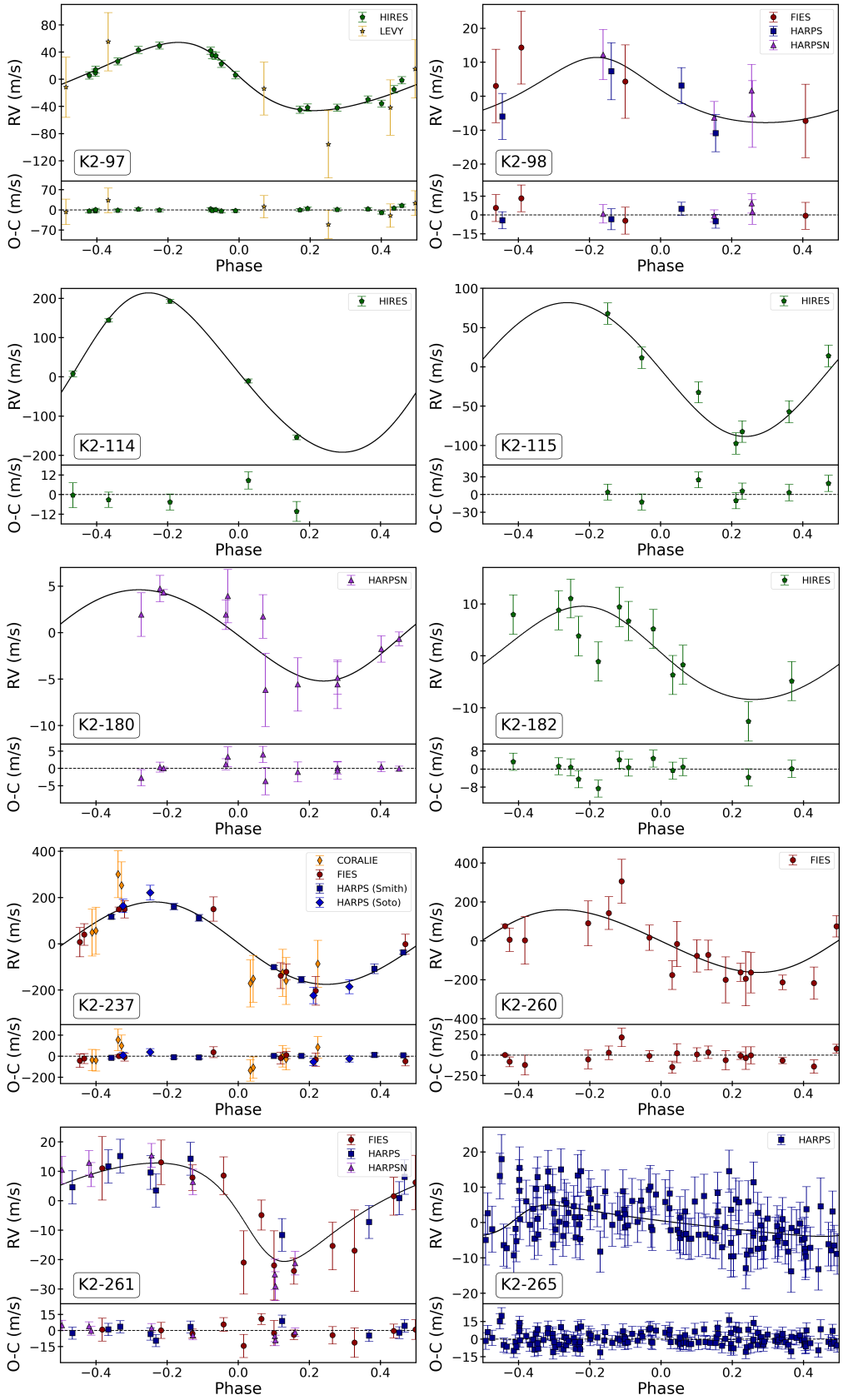

Figure 2.3 Radial velocities for the 10 systems with archival spectroscopic measurements. The best fit model from `EXOFASTv2` is shown in each subplot. Each set of RVs are phased using the best fit period and T_c determined in the fit, and the residuals are shown below each dataset. The references for each set of RVs are listed in Table 3.2.

If any determination for the host star's metallicity ([Fe/H]) was available, we included it as a prior in the fit to better constrain the host star parameters. For consistency, we used metallicity priors for most of the systems from spectra obtained using the Tillinghast Reflector Echelle Spectrograph (TRES; Fűrész 2008) on the 1.5m Tillinghast Reflector at the Fred L. Whipple Observatory (FLWO). Starting points were used for other stellar parameters where available, but no prior constraints were placed on any other values. We assumed the RV extraction and metallicity determination was done correctly in the discovery data. An RV jitter term is fit within the `EXOFASTv2` analysis to ensure the uncertainties are properly estimated. In the cases of five or fewer RVs, we placed conservative uniform bounds on the variance of the jitter. The jitter variance for K2-114 and for the Soto et al. (2018) RVs for K2-237 were bounded to ±300 m/s, and for K2-98 the variance bounds were ±100 m/s for the FIES RVs, and ±4 m/s for HARPS and HARPS-N. For the HARPS RVs of K2-265, we removed three clear outliers that were included in the discovery paper based on visual inspection[8].

2.4 Global Fits

To analyze the wealth of data for these 26 known K2 exoplanet systems, we used `EXOFASTv2` (Eastman et al., 2013, 2019; Eastman, 2017) to perform global fits for our sample. `EXOFASTv2` is an exoplanet fitting software package that uses MCMC sampling to simultaneously fit parameters for both the planets and host star. The K2 and TESS photometric observations (Figures 2.4 and 2.5), along with any archival RVs (Figure 2.3), were jointly analyzed to obtain best-fit parameters for planets and host stars.

2.4.1 Stellar parameters

To characterize the host stars within each fit, we placed a uniform prior from 0 to an upper bound on line-of-sight extinction (A_v) from Schlegel et al. (1998) and Schlafly & Finkbeiner (2011), and Gaussian priors on metallicity ([Fe/H]) and parallax (using Gaia EDR3 and accounting for the small systematic offset reported; Gaia Collaboration et al. 2016, 2021; Lindegren et al. 2021). This also included the spectral energy distribution (SED) photometry as reported by Gaia DR2 (Gaia Collaboration et al., 2018), WISE (Cutri et al., 2012) and 2MASS (Cutri et al., 2003). These

[8] All parameters were within uncertainties when compared to an earlier fit including the outliers.

values are collated in Table 3.1, and all priors are listed in Tables 2A.1-2A.5. We excluded the WISE4 SED values for three systems that had this photometric measurement (K2-115, K2-225 and K2-237) due to the large uncertainties, and as there was a $\gtrsim 2\sigma$ discrepancy with the stellar model. Two other systems (K2-167 and K2-277) had WISE4 measurements that we used in the fits; these are consistent with the stellar models, but still have relatively large uncertainties. Within the `EXOFASTv2` global fit, the MESA Isochrones and Stellar Tracks (MIST) stellar evolution models (Paxton et al., 2011, 2013, 2015; Choi et al., 2016; Dotter, 2016) are used as the base isochrone to better constrain the host star's parameters.

2.4.2 Low-mass stars

Stellar evolutionary models struggle to constrain low-mass stars ($\lesssim 0.6\ M_{\odot}$; Mann et al. 2015) and are thus unreliable. For the three systems that fell into this category (K2-54, K2-147 and K2-321), we used the equations from Mann et al. (2015, 2019) that relate the apparent magnitude in the K_S band (M_{K_s}) to M_* and R_* to set a starting point with wide 5% Gaussian priors for these parameters. We excluded the SEDs from these fits and did not use the MIST models, fitting only the lightcurves (these systems did not have RV measurements). For this reason, we caution that the stellar parameters for these systems are unreliable. We also did not use the limb-darkening tables from Claret (2017) for the low-mass stars, as is the default in `EXOFASTv2` for fitting the u_1 and u_2 coefficients, but rather placed starting points based on tables from Claret & Bloemen (2011) (Eastman et al., 2013) with a conservative Gaussian prior of 0.2 (Patel & Espinoza, 2022).

2.4.3 Contamination

For systems with TESS contamination ratios specified in the TESS input catalog (TICv8, Stassun et al., 2018) and a clear transit detected in both K2 and TESS, we fit for a dilution term[9] on the TESS photometry with a 10% Gaussian prior. This accounts for any nearby sources that may contribute flux to the target aperture that were unknown at the time the TESS Input Catalog was created. Although the TESS PDCSAP lightcurves are corrected for contamination, fitting the dilution allows an independent check on the contamination ratio correction performed by the

[9]The starting point for dilution is calculated as D=C/(1+C).

Table 2.2 Literature Values.

Param	Description	K2-7	K2-54	K2-57	K2-77	K2-97
α_{J2016}	Right ascension (R.A.)	11:08:22.4996	22:32:12.9990	22:50:46.0386	03:40:54.8458	08:31:03.0
δ_{J2016}	Declination (Dec.)	-01:03:57.0898	-17:32:38.6338	-14:04:12.0152	+12:34:20.7938	+10:50:51.2
G	Gaia DR2 G mag	13.057 ± 0.020	—	14.104 ± 0.020	11.920 ± 0.020	12.306 ± 0
G_{Bp}	Gaia DR2 B_P mag	13.404 ± 0.020	—	14.781 ± 0.020	12.485 ± 0.020	12.895 ± 0
G_{Rp}	Gaia DR2 R_P mag	12.552 ± 0.020	—	13.326 ± 0.020	11.236 ± 0.020	11.601 ± 0
T	*TESS* mag	12.612 ± 0.008	—	13.383 ± 0.006	11.287 ± 0.006	11.652 ± 0
J	2MASS J mag	11.952 ± 0.022	—	12.350 ± 0.024	10.384 ± 0.020	10.694 ± 0
H	2MASS H mag	11.628 ± 0.023	—	11.761 ± 0.022	9.910 ± 0.023	10.177 ± 0
K_S	2MASS K_S mag	11.564 ± 0.021	—	11.645 ± 0.023	9.799 ± 0.020	10.035 ± 0
WISE1	WISE1 mag	11.527 ± 0.030	—	11.586 ± 0.030	9.733 ± 0.030	9.990 ± 0.
WISE2	WISE2 mag	11.572 ± 0.030	—	11.639 ± 0.030	9.790 ± 0.030	10.090 ± 0
WISE3	WISE3 mag	11.554 ± 0.233	—	11.506 ± 0.217	9.773 ± 0.054	10.026 ± 0
WISE4	WISE4 mag	—	—	—	—	—
μ_α	Gaia p.m. in R.A.	-4.657 ± 0.016	-5.018 ±0.021	24.311 ± 0.022	22.425 ± 0.025	-1.239 ± 0
μ_δ	Gaia p.m. in Dec.	-23.647± 0.012	-9.804 ± 0.018	-25.298 ± 0.019	-37.908 ± 0.015	-6.694 ±0.
π	Gaia parallax (mas)	1.451 ± 0.028	5.782 ± 0.033	3.818 ± 0.029	7.111 ± 0.043	1.241 ± 0.
Param.	K2-147	K2-167	K2-180	K2-181	K2-182	K2-203
α_{J2016}	19:35:19.9267	22:26:18.2722	08:25:51.4492	08:30:12.9870	08:40:43.2088	00:51:05.6
δ_{J2016}	-28:29:54.5839	-18:00:42.0516	+10:14:47.6330	+10:54:36.5034	+10:58:58.6242	-01:11:45.1
G	—	8.104 ± 0.020	12.404 ± 0.020	12.562 ± 0.020	11.720 ± 0.020	12.122 ± 0
G_{Bp}	—	8.402 ± 0.020	12.817 ± 0.020	12.945 ± 0.020	12.190 ± 0.020	12.614 ± 0
G_{Rp}	—	7.689 ± 0.020	11.839 ± 0.020	12.036 ± 0.020	11.122 ± 0.020	11.493 ± 0
T	—	7.728 ± 0.006	11.896 ± 0.006	12.087 ± 0.006	11.170 ± 0.006	11.547 ± 0
J	—	7.202 ± 0.021	11.146 ± 0.023	11.438 ± 0.022	10.408 ± 0.021	10.773 ± 0
H	—	6.974 ± 0.038	10.747 ± 0.026	11.082 ± 0.021	9.994 ± 0.022	10.281 ± 0
K_S	—	6.887 ± 0.034	10.677 ± 0.026	11.026 ± 0.021	9.913 ± 0.023	10.206 ± 0
WISE1	—	6.810 ± 0.055	10.619 ± 0.030	10.999 ± 0.030	9.845 ± 0.030	10.145 ± 0
WISE2	—	6.866 ± 0.030	10.667 ± 0.030	11.062 ± 0.030	9.917 ± 0.030	10.217 ± 0
WISE3	—	6.906 ± 0.030	10.599 ± 0.099	11.041 ± 0.205	9.896 ± 0.054	10.100 ± 0
WISE4	—	6.917 ± 0.100	—	—	—	—
μ_α	-31.399 ±0.016	73.590±0.028	97.243±0.013	16.936±0.014	-65.130±0.029	-11.103±0
μ_δ	-147.502±0.015	-114.502±0.024	-89.214±0.010	-33.182±0.012	1.544±0.022	0.450±0.0
π	11.027 ± 0.033	12.457 ± 0.071	4.936 ± 0.041	2.805 ± 0.040	6.510 ± 0.052	5.937 ± 0.
Param.	K2-225	K2-226	K2-237	K2-250	K2-260	K2-261
α_{J2016}	12:26:09.8617	12:14:34.9587	16:55:04.5232	12:20:07.5686	05:07:28.1596	10:52:07.7
δ_{J2016}	-09:37:29.3675	-09:33:45.4617	-28:42:38.1039	-08:58:32.6688	+16:52:03.6985	+00:29:35.2
G	11.520 ± 0.020	12.092 ± 0.020	11.467 ± 0.020	13.973 ± 0.020	12.467 ± 0.020	10.459 ± 0
G_{Bp}	11.929 ± 0.020	12.545 ± 0.020	11.776 ± 0.020	14.484 ± 0.020	12.798 ± 0.020	10.872 ± 0
G_{Rp}	10.984 ± 0.020	11.492 ± 0.020	11.013 ± 0.020	13.324 ± 0.020	11.974 ± 0.020	9.917 ± 0.
T	11.028 ± 0.007	11.547 ± 0.006	11.066 ± 0.006	13.379 ± 0.006	12.036 ± 0.007	9.962 ± 0.
J	10.362 ± 0.023	10.697 ± 0.023	10.508 ± 0.023	12.539 ± 0.026	11.400 ± 0.023	9.337 ± 0.
H	10.046 ± 0.021	10.307 ± 0.023	10.268 ± 0.022	12.078 ± 0.022	11.189 ± 0.032	8.920 ± 0.
K_S	9.954 ± 0.023	10.223 ± 0.023	10.217 ± 0.023	12.016 ± 0.024	11.093 ± 0.021	8.890 ± 0.
WISE1	9.915 ± 0.030	10.166 ± 0.030	10.105 ± 0.030	11.878 ± 0.030	11.039 ± 0.030	8.828 ± 0.
WISE2	9.978 ± 0.030	10.204 ± 0.030	10.129 ± 0.030	11.971 ± 0.030	11.036 ± 0.030	8.897 ± 0.

SPOC pipeline. Fitting a dilution term for only the TESS photometry assumes the K2 aperture has been correctly decontaminated or is comparatively uncontaminated, which is based on K2 having a significantly smaller pixel scale than TESS (4" and 21" for K2 and TESS, respectively). However, it is possible that there is still a level of contamination within the K2 aperture that might be identified through high-resolution imaging. We checked the K2 aperture for all of our targets to identify any major sources of contamination from the *Gaia* EDR3 catalog. We define contaminants as having flux ratios with the target star that are much larger than the uncertainties of the transit depth. To correct for the contaminating light, we followed the method from Rampalli et al. (2019) to account for the fraction of the flux within the aperture that belonged to our targets ($F_{\rm star}$) as opposed to the contaminating stars based on the *Gaia* G-band fluxes. We found significant contamination for K2-54 ($F_{\rm star} \approx 0.56$) and K2-237 ($F_{\rm star} \approx 0.98$; the latter was originally discussed in Ikwut-Ukwa et al. 2020). Several other systems had potential faint contaminants, however, the global fit for the system with the next highest level of contamination (K2-250; $F_{\rm star} \approx 0.98$) did not change within uncertainties before and after flux correction, so we did not apply corrections to any systems other than K2-54 and K2-237.

2.4.4 Global fits

We ran a short preliminary fit for each system to identify any potential issues, e.g. particularly shallow transits, and then ran a final fit to convergence. For a fit to be accepted as converged, we adopted the default `EXOFASTv2` criteria of $T_Z > 1000$, where T_Z is the number of independent draws, and a slightly loose Gelman-Rubin value of < 1.02 due to some transits being very shallow in TESS, resulting is long runtimes for the global fits. Within `EXOFASTv2`, we opted to reject all flat and negative transit models, which ensured a more reliable recovery of marginal transits (Eastman et al., 2019). We did not fit for transit timing variations, but plan to explore this in future papers.

Shallow transits clearly detected in K2 were not always evident in the TESS lightcurves as the latter are necessarily noisier due to the smaller collecting area of the telescope (see §2.5.6 for discussion). For these systems we ran a K2-only fit to convergence and a short preliminary fit (Gelman-Rubin of ~ 1.1, $T_z \sim 100$). To assess whether it was advantageous to include the TESS

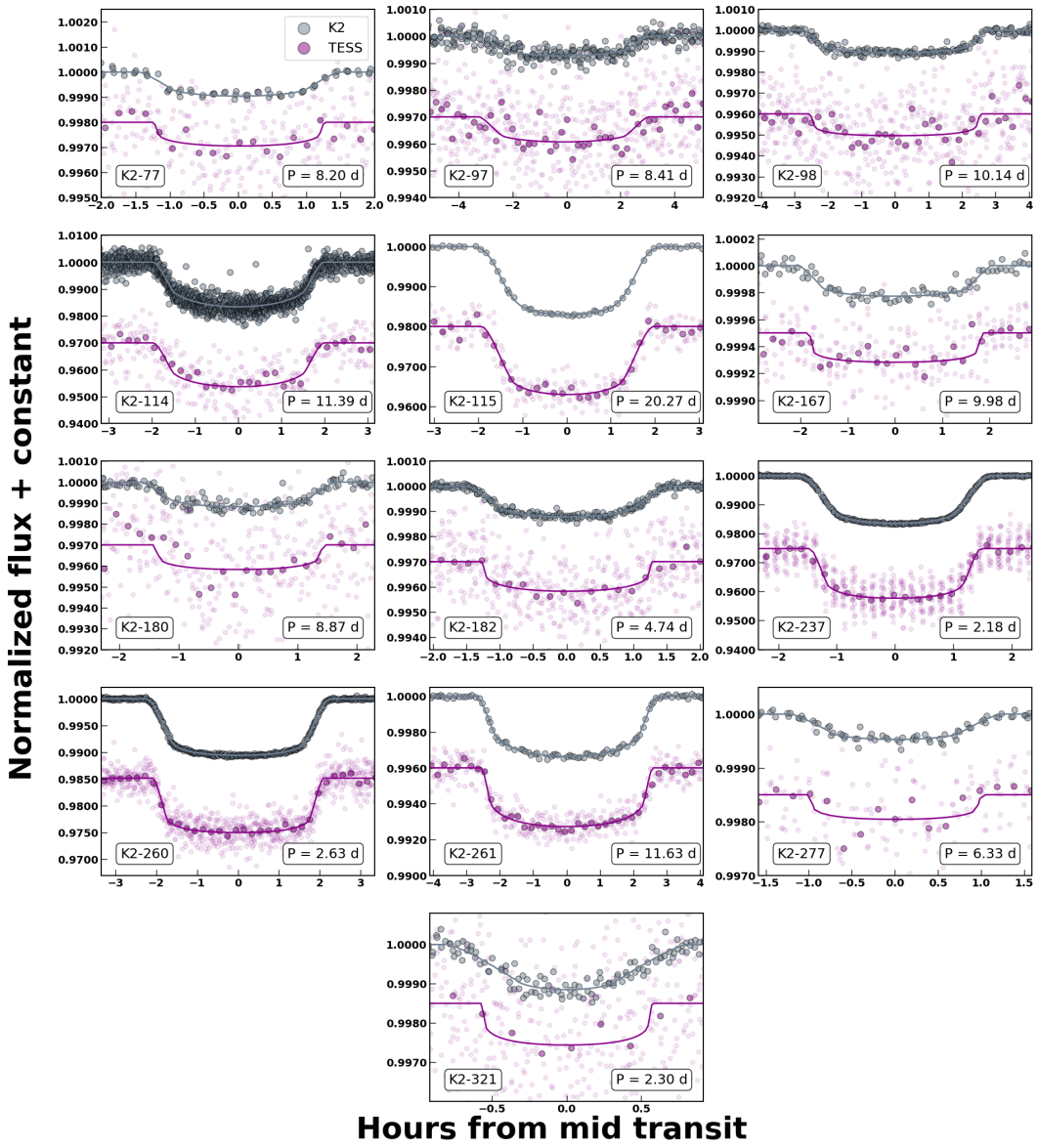

Figure 2.4 K2 (gray) and TESS (purple) transits for all systems where TESS added significant value to the ephemeris projection. The phase-folded lightcurves include all data available across the K2 campaigns and TESS sectors for each system, and have the best-fit model from `EXOFASTv2` overlaid (see Eastman et al. 2013, 2019; Eastman 2017 for how this is calculated). The system K2 identifier and orbital period of the planet are displayed in each subplot. The TESS lightcurves are shown binned to 12 minutes, and the K2 lightcurves are unbinned. For K2-237, the discreteness of the points is likely due to the period being an integer multiple of the exposure time.

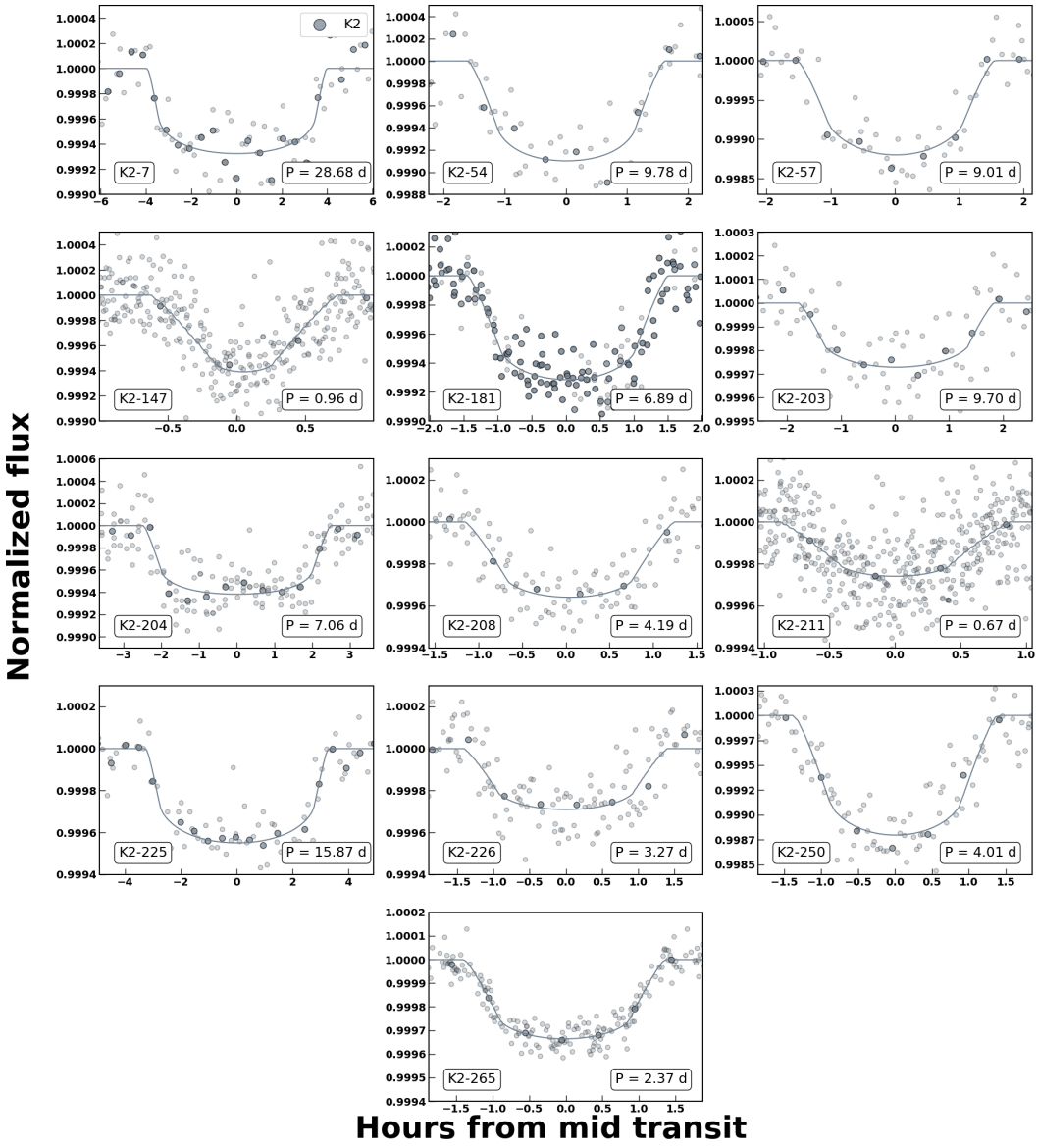

Figure 2.5 K2 transits for systems that were not recoverable in TESS lightcurves. The darker points are binned to 30 minutes, and the `EXOFASTv2` best-fit model is shown.

.

lightcurves, we required certain criteria be met before running the K2 and TESS fit to convergence. Firstly, we compared the improvement on uncertainties for parameters such as period and T_C, and projected these to the year 2030. If the uncertainties were notably smaller when including TESS data, we continued by visually inspecting the transits modelled by `EXOFASTv2`. For extremely marginal transits, we further binned the phased lightcurves to determine whether the transit was indeed visible. If the transit in TESS was still not obvious, we inspected the probability distribution functions (PDFs) output by `EXOFASTv2` for clearly non-Gaussian distributions for key parameters, particularly period. If the period was not well-constrained (e.g. multimodal) even with the increased baseline of TESS, we excluded the TESS lightcurve from the fit. A multimodal period indicates that the MCMC identified different transit solutions based on the TESS data, implying that the TESS transits are not securely enough detected to update the ephemeris.

We ultimately excluded any TESS lightcurves where the transit has SNR $\lesssim 7$. As these are all previously confirmed planets, we adopted a less conservative SNR for bona fide transits in TESS compared to what is required for initial planet verification. This SNR threshold was chosen because the first system below this cut (K2-265, SNR = 6.0) had a multimodal posterior for period, and all other systems with lower SNR exhibited similar issues. Conversely, the system just above this threshold (K2-277, SNR = 8.1) has a broad but Gaussian period posterior, with no other systems above this SNR having unreliable PDFs.

Using this threshold, 13 of the 26 systems did not have recoverable TESS transits, so these were globally fit using only their K2 lightcurves (Figure 2.5). While these systems will not have as significant improvement on their ephemerides, we still provide the updated parameters to include them in our final catalog of self-consistent parameters.

2.5 Results and Discussion

We updated the system parameters for 26 single-planet systems discovered by K2 and reobserved by TESS, four of which were part of the pilot study for the *K2 & TESS* Synergy (K2-114, K2-167, K2-237 and K2-261; Ikwut-Ukwa et al. 2020). Tables 2A.1-3.6 contain parameters from the global fits. Here we address any points of interest for individual systems and for the sample as a whole.

2.5.1 Ephemeris improvement

As addressed in §2.2, a major incentive for refitting all K2 and TESS systems is to update their ephemerides to provide the community with accurate transit times for observing with existing and upcoming facilities. Figures 2.6 and 2.7 show the projected transit timing uncertainties for our sample extrapolated to 2035, with markers indicating the expected launches for ongoing and future missions. The uncertainties on the transit times are calculated by standard error propagation,

$$\sigma_{t_{\rm trans}} = \sqrt{\sigma_{T_0}^2 + (n_{\rm trans} \times \sigma_P)^2} \tag{2.1}$$

where $\sigma_{t_{\rm trans}}$ is the uncertainty on future transit time, σ_{T_0} is the uncertainty on the fitted optimal time of conjunction, $n_{\rm trans}$ is the number of transits that occurred between timestamps and σ_P is uncertainty on the period. For the future transit times using the results of the `EXOFASTv2` global fits, we used the optimal time of conjunction in order to minimize the covariance between T_C and P. However, T_0 is not generally available for the K2 discovery parameters, so for the projected uncertainties on transit times for the original K2 values we used T_C.

As expected, systems for which we excluded the TESS data due to shallow transits were not improved on the same scale as those with significant TESS transits. For the K2 and TESS systems, the updated global fits were able to reduce most uncertainties from hours to minutes within the scope of some of the major facilities in the near future (Figure 2.6). For the 13 systems with detected TESS transits, the average 3σ uncertainty on the future transit time by the year 2030 was reduced from 26.7 to 0.35 hours (Table 2.3).

Systems for which we only included the K2 lightcurves had significantly less improvement on the precision of predicted transit times. However, the ephemeris for K2-181 was considerably refined due to the addition of data from K2 Campaign 18, which was not included in any previous analysis of this system. Excluding K2-181, there was a slight reduction of the average 3σ uncertainty from 43.2 to 35.6 hours (Table 2.4). The small improvement for some systems is likely due to using optimized K2 lightcurves obtained from the pipeline described in §2.3.1, in conjunction with our fits including both the planet and the host star.

Table 2.3 Ephemerides as of discovery compared to our updated values for systems with K2 and TESS transits, with the 3σ uncertainty on future transit time by the year 2030.

	P (days)	T_c (BJD)	$3\sigma_{2030}$	TSM
		K2-77		
Discovery	$8.199814^{+0.000364}_{-0.000367}$	$2457070.806480^{+0.001511}_{-0.001449}$	17.4 hr	
Updated	$8.2000844^{+0.0000086}_{-0.0000073}$	$2457316.80766^{+0.00099}_{-0.00096}$	22 min	27.3
		K2-97		
Discovery	$8.406726^{+0.001863}_{-0.001827}$	$2457142.04977^{+0.00888}_{-0.00854}$	84.8 hr	
Updated	8.407115 ± 0.000023	$2457722.1447^{+0.0027}_{-0.0026}$	58 min	—
		K2-98		
Discovery	10.13675 ± 0.00033	2457145.9807 ± 0.0012	12.6 hr	
Updated	$10.1367349^{+0.0000094}_{-0.0000092}$	$2457662.95321^{+0.00077}_{-0.00074}$	19 min	13.5
		K2-114		
Discovery	$11.39109^{+0.00018}_{-0.00017}$	$2457174.49729 \pm 0.00033$	5.9 hr	
Updated	$11.3909310^{0.0000031}_{-0.0000032}$	$2457687.08869 \pm 0.00016$	6 min	—
		K2-115		
Discovery	$20.273034^{+0.000036}_{-0.000037}$	$2457157.15701 \pm 0.00025$	42 min	
Updated	20.2729914 ± 0.0000050	$2457522.07014 \pm 0.00017$	5 min	—
		K2-167		
Discovery	$9.977481^{+0.001039}_{-0.001007}$	$2456979.936780^{+0.002518}_{-0.002443}$	40.8 hr	
Updated	$9.978541^{+0.000023}_{-0.000019}$	$2457299.2465^{0.0022}_{0.0023}$	48 min	46.1
		K2-180		
Discovery	8.8665 ± 0.0003	2457143.390 ± 0.002	13.0 hr	
Updated	$8.865663^{0.000011}_{0.000010}$	$22457489.15656^{+0.00078}_{-0.00076}$	26 min	15.1
		K2-182		
Discovery	4.7369683 ± 0.0000023	$2457719.11517 \pm 0.00028$	10 min	
Updated	4.7369696 ± 0.0000017	$2457652.79755^{+0.00027}_{-0.00028}$	8 min	15.4
		K2-237		
Discovery	2.18056 ± 0.00002	2457684.8101 ± 0.0001	3.2 hr	
Updated	$2.18053332 \pm 0.00000054$	$2457706.61618^{+0.00003}_{-0.00003}$	5 min	—
		K2-260		
Discovery	2.6266657 ± 0.0000018	$2457820.738135 \pm 0.00009$	14 min	
Updated	$2.62669762 \pm 0.00000066$	$2457894.284876^{+0.000060}_{-0.000059}$	5 min	—
		K2-261		
Discovery	11.63344 ± 0.00012	$2457906.84084^{+0.00054}_{-0.00067}$	3.4 hr	
Updated	11.6334681 ± 0.0000044	$2458151.14394^{+0.00026}_{-0.00030}$	7 min	85.5
		K2-277		
Discovery	$6.326763^{+0.000355}_{-0.000361}$	$2457221.22958^{+0.00221}_{-0.00217}$	21.5 hr	
Updated	$6.326768^{+0.000015}_{-0.000012}$	2457303.4771 ± 0.0010	48 min	35.6
		K2-321		
Discovery	2.298 ± 0.001	2457909.17	144.0 hr	
Updated	$2.2979749^{+0.0000017}_{-0.0000019}$	$2458141.26759^{+0.00064}_{-0.00068}$	15 min	—

NOTES: The discovery values are taken from the K2 references listed in Table 3.2. The T_C for the updated values is T_0 as determined by our global fits.

Table 2.4 Ephemerides as of discovery compared to our updated values for systems with only K2 transits, with the 3σ uncertainty on future transit time by the year 2030.

	P (days)	T_c (BJD)	$3\sigma_{2030}$	TSM
		K2-7		
Discovery	28.67992 ± 0.00947	2456824.6155 ± 0.0149	135.0 hr	
Updated	$28.6781^{+0.0046}_{-0.0051}$	$2456853.2946^{+0.0046}_{-0.0042}$	68.8 hr	5.9
		K2-54		
Discovery	9.7843 ± 0.0014	2456982.9360 ± 0.0053	56.8 hr	
Updated	$9.7833^{+0.0013}_{-0.0012}$	2457002.5042 ± 0.0029	50.6 hr	—
		K2-57		
Discovery	9.0063 ± 0.0013	2456984.3360 ± 0.0048	57.3 hr	
Updated	$9.0073^{+0.0012}_{-0.0011}$	2457011.3568 ± 0.0023	50.4 hr	10.8
		K2-147		
Discovery	0.961918 ± 0.000013	$2457327.91683^{+0.00089}_{-0.00100}$	5.0 hr	
Updated	0.961939 ± 0.000029	$2457343.30907^{+0.00100}_{-0.00099}$	11.2 hr	—
		K2-181		
Discovery	$6.894252^{+0.000430}_{-0.000426}$	$2457143.793550^{+0.002559}_{-0.002528}$	23.9 hr	
Updated	6.893813 ± 0.000011	2457778.0262 ± 0.0012	0.5 hr	14.6
		K2-203		
Discovery	$9.695101^{+0.001285}_{-0.001334}$	$2457396.638780^{+0.005765}_{-0.005844}$	49.7 hr	
Updated	9.6952 ± 0.0014	$2457435.4189^{+0.0037}_{-0.0036}$	52.7 hr	1.3
		K2-204		
Discovery	$7.055784^{+0.000650}_{-0.000641}$	$2457396.50862^{+0.00372}_{-0.00376}$	33.6 hr	
Updated	$7.05576^{+0.00066}_{-0.00064}$	2457431.7872 ± 0.0022	33.6 hr	11.1
		K2-208		
Discovery	$4.190948^{0.000230}_{-0.000248}$	$2457396.51164^{+0.00248}_{-0.00235}$	21.0 hr	
Updated	4.19097 ± 0.00023	2457430.0390 ± 0.0016	20.0 hr	12.9
		K2-211		
Discovery	0.669532 ± 0.000019	$2457395.82322 \pm 0.00160$	10.4 hr	
Updated	$0.669561^{+0.000031}_{-0.000032}$	2457432.6479 ± 0.0013	17.2 hr	2.1
		K2-225		
Discovery	$15.871455^{+0.002113}_{-0.001670}$	$2457587.368230^{+0.004034}_{-0.004872}$	42.2 hr	
Updated	$15.8723^{+0.0021}_{-0.0019}$	$2457619.1111^{+0.0031}_{-0.0030}$	44.3 hr	11.1
		K2-226		
Discovery	$3.271106^{+0.000367}_{-0.000369}$	$2457584.026130^{+0.004436}_{-0.004366}$	39.8 hr	
Updated	$3.27109^{+0.00036}_{-0.00039}$	2457620.0082 ± 0.0020	40.3 hr	14.6
		K2-250		
Discovery	$4.01457^{+0.00062}_{-0.00057}$	$2457584.1212^{+0.0061}_{-0.0066}$	52.5 hr	
Updated	4.01392 ± 0.00029	2457620.2535 ± 0.0015	25.4 hr	13.8
		K2-265		
Discovery	2.369172 ± 0.000089	2456981.6431 ± 0.0016	14.9 hr	
Updated	$2.369020^{+0.000058}_{-0.000059}$	$2457017.18078^{+0.00055}_{-0.00054}$	9.8 hr	15.7

Notes: The discovery values are taken from the K2 references listed in Table 3.2. The T_C for the updated values is T_0 as determined by our global fits.

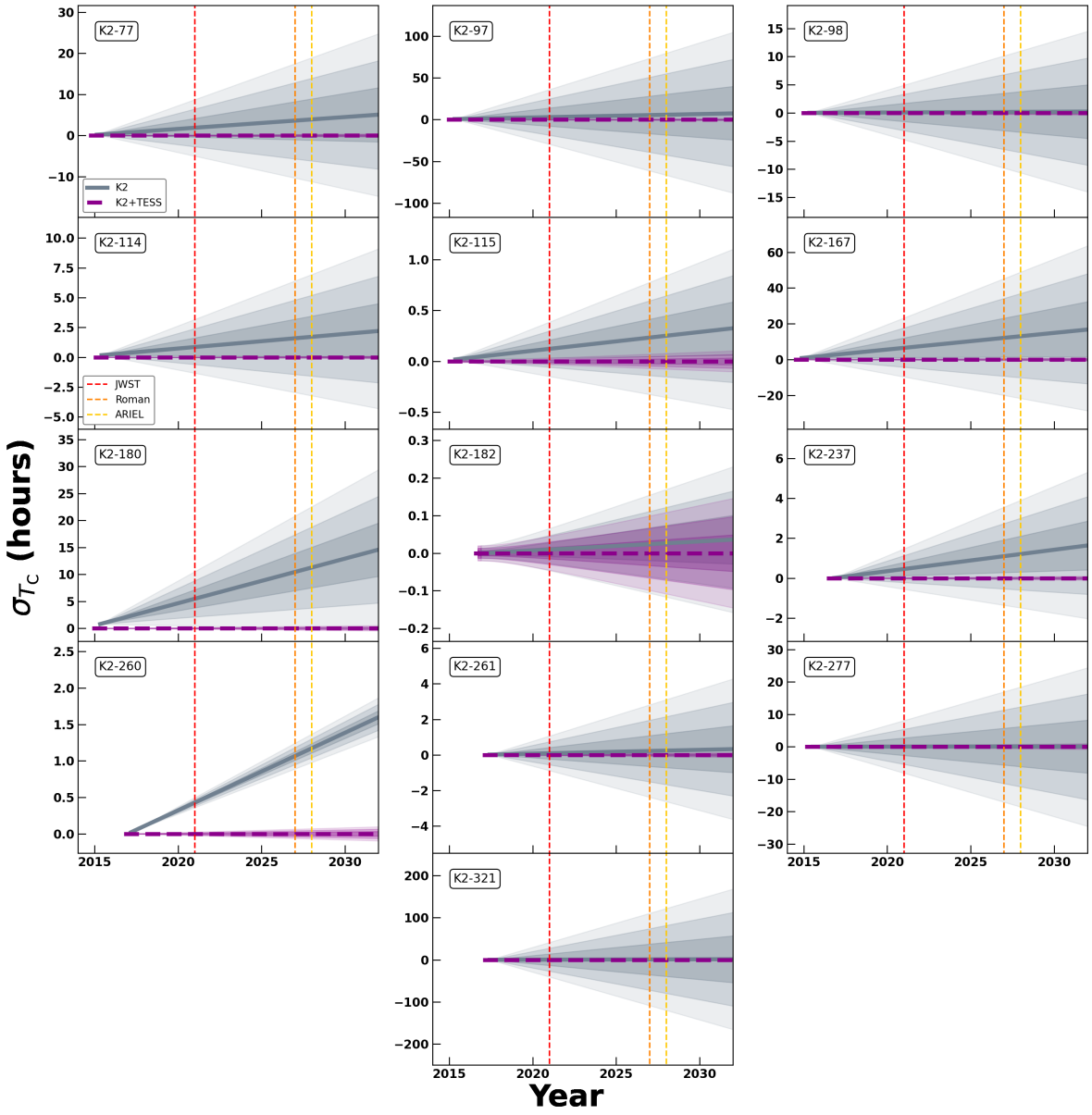

Figure 2.6 Projected uncertainties for transit times (σ_{T_c}) for systems with transits detected in both K2 and TESS. The shaded regions represent the 1, 2 and 3 σ uncertainties, where gray is the uncertainty from the K2 ephemerides listed in Table 3.2 and purple is our updated version using `EXOFASTv2`. The vertical dashed lines show the expected or actual launch years for missions for which these systems would be prospective targets (*JWST*: red, *NGRST*: orange, *ARIEL*: yellow). Note the y-axis scale is different in each subplot.

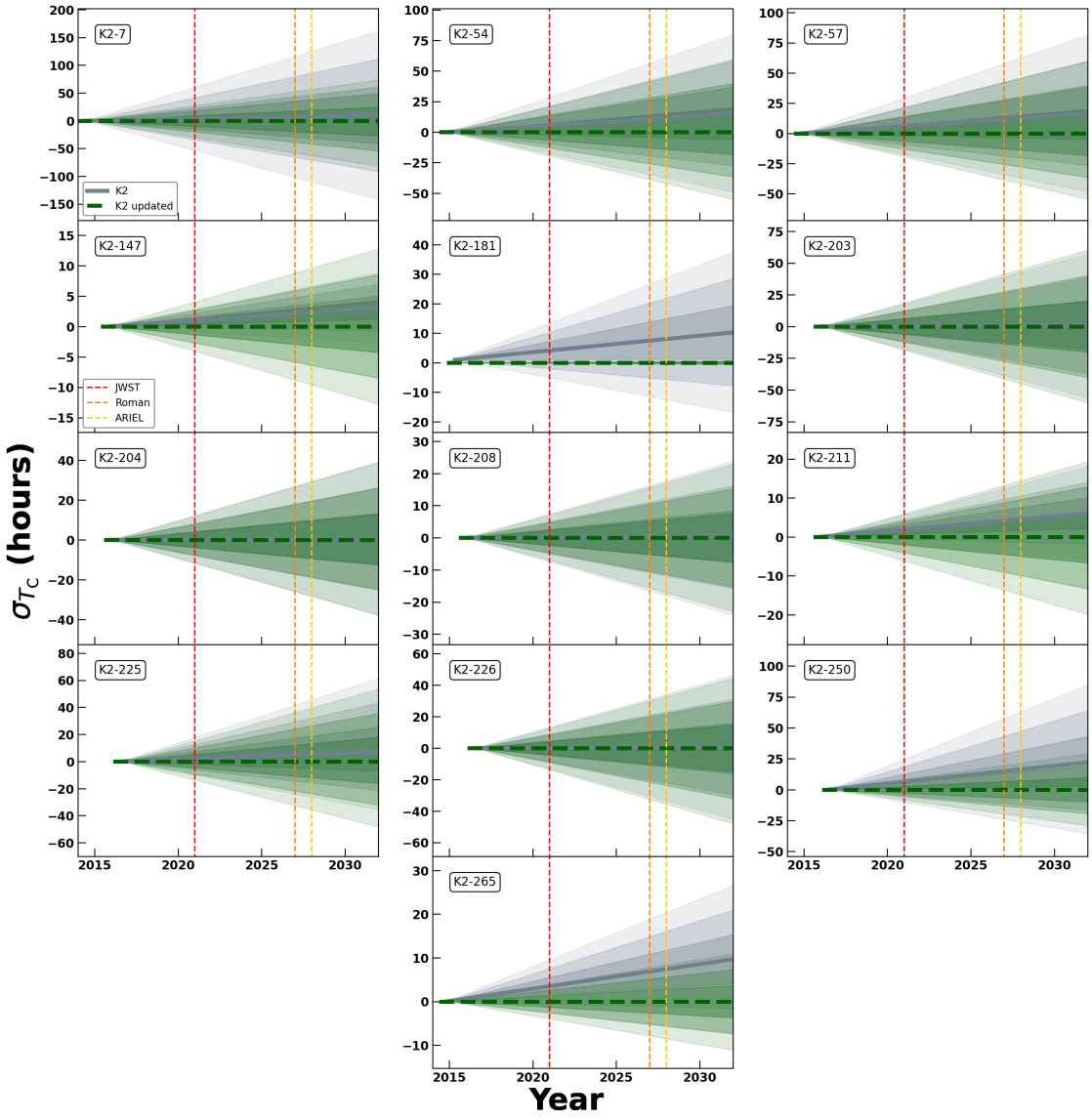

Figure 2.7 Same as Figure 2.6 but for systems with transits only detectable in the K2 lightcurves. The shaded regions represent the 1, 2 and 3 σ uncertainties, where gray is the uncertainty from the K2 ephemerides listed in Table 3.2 and green is our updated version using `EXOFASTv2`. The vertical dashed lines show the expected or actual launch years for missions for which these systems would be prospective targets (*JWST*: red, *NGRST*: orange, *ARIEL*: yellow). The ephemeris for K2-181 is significantly improved due to the inclusion of data from K2 Campaign 18.

For systems with RV measurements, our ephemeris comparison uses uncertainties taken from previous analyses that included the RVs along with the K2 data. The uncertainties for systems without RVs are taken from the most recent study that included lightcurves from K2. There are a handful of exceptions to this rule: for K2-77 we use the values from Mayo et al. (2018) as Gaidos et al. (2017) only has three RV measurements which is insufficient for our `EXOFASTv2` fits; for K2-97, we use the values from Livingston et al. (2018a) as no T_c was presented in the analysis by Grunblatt et al. (2018) that included RVs; for K2-237 we use the less precise values from Soto et al. (2018) which are consistent with our results, rather than from Smith et al. (2019) which have a $\sim 4\sigma$ discrepancy with our findings (this was also found in Paper I; Ikwut-Ukwa et al. 2020).

As mentioned in §2.4.4, half of our sample did not have transits deep enough to be recovered by TESS. This presents a challenge for updating the transit times for these systems. If these systems are observed in future TESS sectors, it is possible that the SNR will increase sufficiently to include in a global fit. We will continue to monitor these and will include them in future releases, if this is the case.

2.5.1.1 K2-167

We note the use of an errant stellar metallicity prior used in the pilot study, where 0.45 instead of -0.45 (as reported by Mayo et al. 2018) was used as the Gaussian center. While this may have affected the solutions of stellar and planetary parameters, it would not have significantly altered the ephemeris.

2.5.1.2 K2-260

There is a clear discrepancy between the previously published ephemeris and our updated version (see Figure 2.6), well beyond a 3σ level. To test whether this was an artifact of our global fit, we ran a fit using only the K2 lightcurves and compared the results to the original and K2 and TESS fits. Our K2-only fit was consistent with our K2 and TESS ephemeris, and still in disagreement with the original results, suggesting that our updated fit provides the optimal ephemeris. It is possible that the original lightcurves introduced systematics in the discovery analysis, or the inclusion of additional follow-up data affected the ephemeris, but this is not clear.

In any case, the consistency between our K2-only and K2 and TESS ephemerides (and no other system showing similar issues) gives us confidence in our results.

2.5.1.3 K2-261

As discussed in the pilot study (Ikwut-Ukwa et al., 2020), the PDFs for some stellar parameters (particularly age and mass) of K2-261 exhibit distinct bimodality that is likely due to the star being at a main sequence transition point (and not associated with the poor fits of shallow transits discussed in §2.4.4), causing difficulties with fitting the MIST isochrones to the data to constrain age. We followed the same procedure from Ikwut-Ukwa et al. (2020), splitting the posterior at the minimum probability for M_* between the two Gaussian peaks (at M_*=1.19 $M_\odot$; see Figure 5 of Ikwut-Ukwa et al. 2020) and extracting two separate solutions for each peak. We list both solutions in Table 2A.5, however, we use the low-mass solution for all figures as this has the higher probability. The different stellar mass solutions do not affect the ephemeris projection for this planet.

2.5.1.4 Comparison to pilot study

The ephemerides were slightly improved for the four systems from the pilot study, the most significant being K2-167 (1.1 hours to 48 minutes) and K2-261 (30 minutes to 7 minutes). We did not expect to see major improvement because the baseline of new TESS sectors is relatively short compared to that of K2 and the TESS primary mission.

2.5.2 TSM

We calculated the transmission spectroscopy metric (TSM; Kempton et al. 2018) for the planets in this sample to gauge the value of atmospheric follow-up (Tables 2.3 & 2.4; Figure 2.8). As the TSM is dependent on stellar parameters, we excluded the three systems for which we did not fit the host star (K2-54, K2-147, K2-321; see §2.4). The TSM is only valid for planets with $R_p < 10\ R_\oplus$, which removes a further five planets from this calculation (K2-97, K2-114, K2-115, K2-237 and K2-260). Only one system, K2-261, has a TSM above the threshold suggested by Kempton et al. (2018), and falls between the second and third quartile for the corresponding mass bin (see Table 1

of Kempton et al. 2018.) Future work in this project to update ephemerides will prioritize planets with high TSMs relative to the entire K2 catalog.

2.5.3 The sample

While the systems in this analysis span a broad range of stellar temperatures and planet masses, most planets have orbital periods $\lesssim$10 days and radii $\lesssim$5 $R_\oplus$ (Figures 2.8 and 2.9). Planet masses range from 2.6 $\sim$ 639 $M_\oplus$ and host stars include M dwarfs to F-type spectral classifications. This demonstrates the diversity of the original K2 sample as largely community-selected targets. Figure 2.9 shows how this sample compares to other known exoplanets.

2.5.4 TTVs

We did not fit for transit timing variations (TTVs) in this study. We would expect these to manifest as a significant change in ephemeris over time, whereas all of the systems studied here have updated ephemerides consistent to within 3σ of the original K2 ephemeris (except K2-260; see §2.5.1.2). Therefore, any TTVs that may be present are currently too small to detect for these systems. Differences in the ephemerides on the $1 \sim 3\sigma$ level are likely due to the addition of the TESS lightcurves.

2.5.5 Candidate planets

We note that a couple of the systems in our analysis have additional candidate planets (K2-203 and K2-211). However, we ignore these for the purpose of updating ephemerides of known exoplanets that are more likely future targets for missions such as JWST, but plan to revisit these in a future paper addressing multi-planet systems.

2.5.6 K2 vs. TESS

It is not surprising that relatively shallow K2 transits were not detected by TESS. Kepler and TESS were designed to observe different stellar demographics, resulting in different photometric capabilities. Kepler was built with the intent to explore the number of near-Earth-sized planets close to their respective habitable zones around distant stars with apparent magnitudes $\lesssim$ 16. The original Kepler mission could reach a precision of $\sim$ 20 parts per million (ppm), which was generally the same for the K2 mission (Vanderburg & Johnson, 2014; Vanderburg et al., 2016).

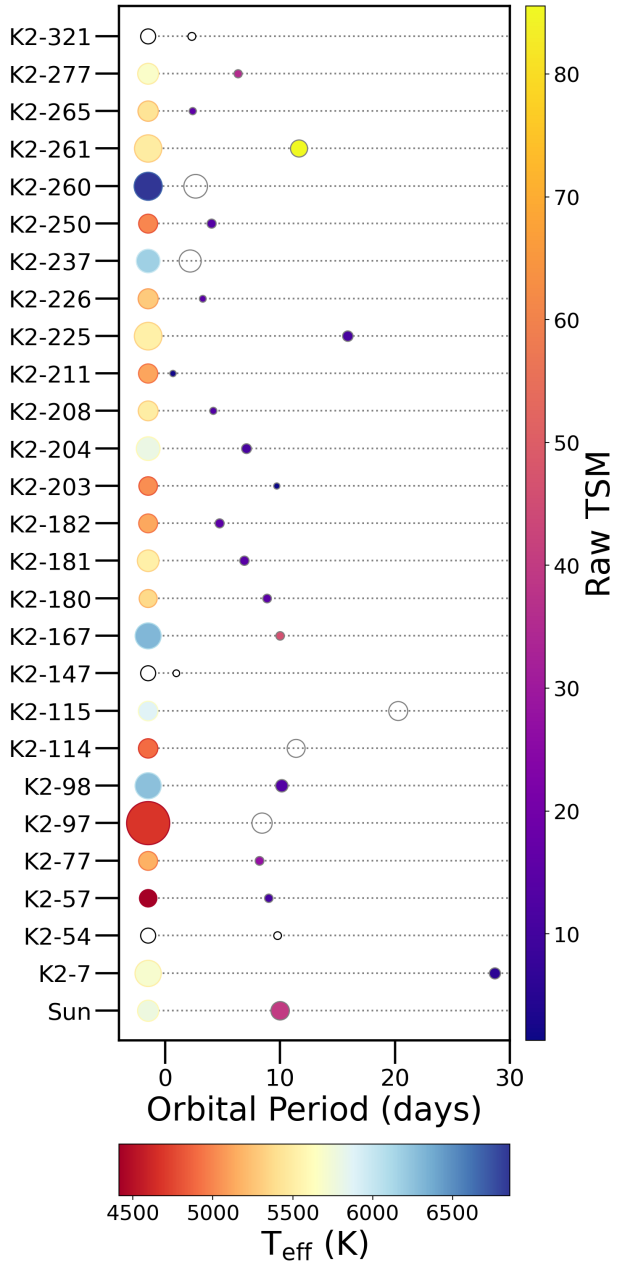

Figure 2.8 Architecture for each system showing the values from the global fits for the 26 systems in this analysis. The host stars are the left-most circles, with their temperatures indicated by color and relative radius shown by size. The right-most circles represent the planets, with size showing relative radius and color indicating their raw Transmission Spectroscopy Metric (TSM). The radius of the star and planet within each system is not scaled to each other. Systems for which we did not fit stellar parameters and planets that do not have a calculated TSM are represented by empty circles (see §2.5.2). An example of the Sun hosting a Jupiter planet with a 10-day period and TSM of 40 is shown.

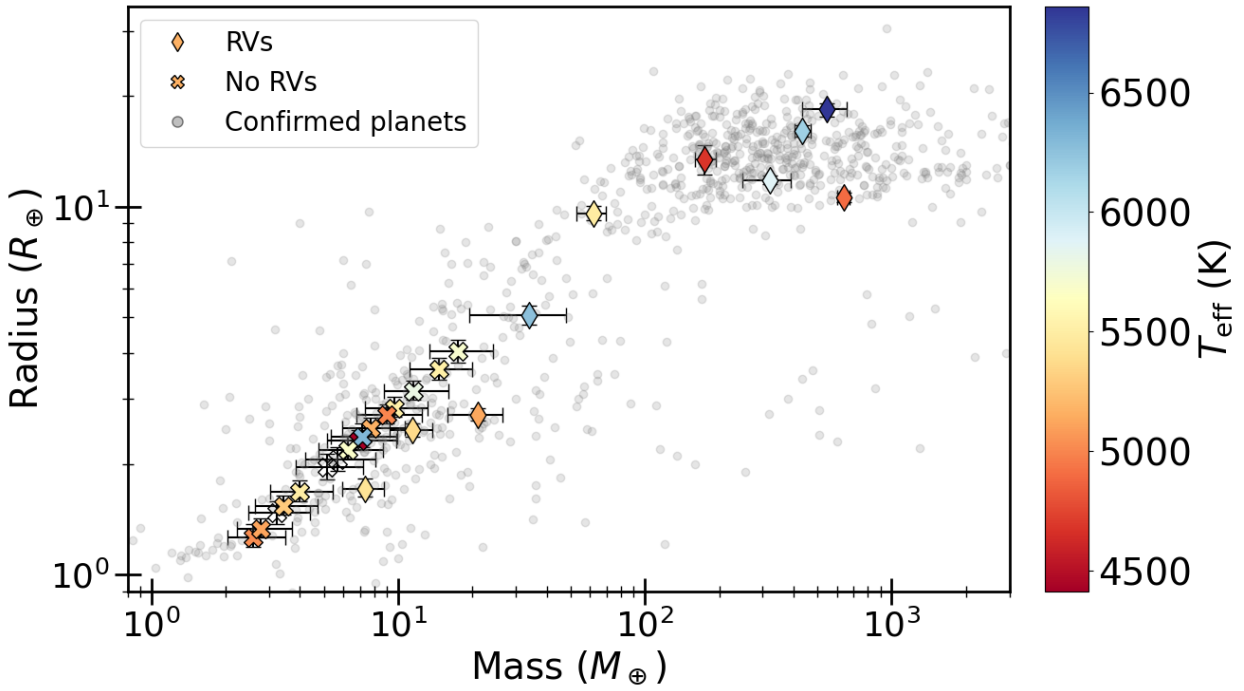

Figure 2.9 Radius versus mass for all confirmed exoplanets (gray; values taken from the NEA) and those in our work (using the median values from the `EXOFASTv2` output). The 10 systems with planetary masses measured through RVs are indicated by diamonds, while the planets without RVs that have masses obtained from the Chen & Kipping (2017) mass-radius relations are shown as crosses. The points are colored by the effective temperature of the host star, and are empty for the three systems without fitted stellar parameters.

On the other hand, TESS is focused on nearby, brighter stars with magnitude $\lesssim$ 12. The precision of TESS has a floor at ~20 ppm at 1 hour for the brightest stars with $T_{\rm mag} < 4$, but is more realistically $\gtrsim$100 ppm for the majority of stars. Due to the all-sky nature of the TESS missions, observing sectors last on average 27 days for efficient sky coverage. K2 campaigns were around 80 days in duration, meaning the same targets may have ~3 times as many transits observed by K2.

While TESS may not be able to recover all K2 systems, the ones it can detect will have vastly improved ephemerides as demonstrated in Figure 2.6. Our analysis indicates TESS transits with SNR $\gtrsim$ 7 are recoverable, and while this places a limit on the scope of this reanalysis, we can potentially gain access for reobservation of at least half of known K2 planets. It is possible that future TESS missions that reobserve the planets with currently marginal transits (SNR $\sim 5-6$) will increase the SNR enough for a significant detection. However, for transits with SNR$\lesssim$ 5, it is

unlikely that more TESS observations will result in recoverable transits.

2.5.7 Future work

With several major facilities able to characterize exoplanets in extensive detail planned to come online within the next decade, not having accurate and precise transit times is a relevant issue. The K2 & TESS Synergy aims to solve the problem of degrading ephemerides for all K2 systems reobserved by TESS (with clearly detectable transits as shown by this effort). Assuming TESS will reobserve all K2 systems throughout its extended missions, we expect to be able to update the ephemerides for around half of K2 planets (~250 planets) with transits deep enough to be detected by TESS, based on this study. Over the next couple of years, we plan to reanalyze the remaining K2 systems with current TESS overlap, providing the updated parameters to the community. In future batches, we will place a focus on systems that are potentially well suited as JWST targets for atmospheric studies based on their TSMs. While we do not see strong evidence for TTVs in the current work, we will make note of this in future for any systems with significant change in ephemeris, particularly for known multi-planet systems where this would be more readily detectable.

2.6 Conclusion

Past efforts to create and analyze homogeneous populations of exoplanet parameters have led to great insight into major questions in planetary formation and evolution (Wang et al., 2014; Fulton et al., 2017; Fulton & Petigura, 2018). The K2 & TESS Synergy is uniting NASA's planet hunting missions, and focuses on extending the scientific output of both telescopes by creating a self-consistent catalog for the K2 and TESS sample while providing the community with updated ephemerides to efficiently schedule future characterization observations with facilities like JWST (Gardner et al., 2006). As well as refreshing stale ephemerides, this provides a uniform way of addressing any inconsistencies between the original K2 ephemeris and the updated value from TESS. In this paper, we have presented updated parameters for 26 single-planet systems originally discovered by K2 and more recently reobserved by TESS during its primary and extended missions. Following from the success of the pilot study (Ikwut-Ukwa et al., 2020), we have significantly

reduced the uncertainties on transit times for the 13 systems with transits detectable in TESS from hours down to minutes through the JWST operations window (~2030). Assuming the current sample is representative of the entire K2 catalog, we expect significant improvement on ephemerides for about half of the systems revisited by TESS, with the goal of a ~250-system catalog of parameters that will be publicly available. As TESS continues to reobserve large portions of the entire sky during its current and possible future extended missions, there will be a well-suited opportunity to conduct this analysis on all known exoplanets, possibly leading to key insights into the evolutionary processes of exoplanets.

APPENDIX

EXOFASTV2 MEDIAN PARAMETER TABLES.

Table 2A.1 Median values and 68% confidence intervals.

Priors:		K2-7	K2-54′	K2-57	K2-77	K2-97	K2
π	Gaia Parallax (mas)	$\mathcal{G}[1.45113, 0.02810]$	—	$\mathcal{G}[3.81841, 0.02910]$	$\mathcal{G}[7.11086, 0.04290]$	$\mathcal{G}[1.24110, 0.06320]$	$\mathcal{G}[1.94998$
[Fe/H]	Metallicity (dex)	$\mathcal{G}[-0.153, 0.24]^*$	—	$\mathcal{G}[-0.01, 0.20]^*$	$\mathcal{G}[0.118, 0.080]$	$\mathcal{G}[0.267, 0.080]$	$\mathcal{G}[-0.10$
A_V	V-band extinction (mag)	$\mathcal{U}[0, 0.12741]$	—	$\mathcal{U}[0, 0.1209]$	$\mathcal{U}[0, 1.11693]$	$\mathcal{U}[0, 0.13733]$	$\mathcal{U}[0, 0.$
$D_T^\star$	Dilution in TESS	$\mathcal{G}[0, 0.00030159]$	—	—	$\mathcal{G}[0, 0.00023943]$	—	$\mathcal{G}[0, 0.0$
Parameter	**Units**	**Values**					
Stellar Parameters:							
M_*	Mass ($M_\odot$)	$1.056^{+0.098}_{-0.068}$	0.615 ± 0.031	$0.699^{+0.034}_{-0.031}$	$0.847^{+0.039}_{-0.038}$	$1.17^{+0.19}_{-0.13}$	1.246
R_*	Radius ($R_\odot$)	$1.533^{+0.082}_{-0.074}$	0.643 ± 0.031	$0.671^{+0.023}_{-0.022}$	$0.792^{+0.027}_{-0.025}$	$4.14^{+0.28}_{-0.26}$	1.518
L_*	Luminosity ($L_\odot$)	$2.24^{+0.12}_{-0.11}$	$0.095^{+0.034}_{-0.026}$	$0.1541^{+0.0053}_{-0.0051}$	$0.401^{+0.04}_{-0.037}$	$7.36^{+0.83}_{-0.72}$	3.19
F_{Bol}	Bolometric Flux (cgs)	$1.504e-10^{+5.1e-12}_{-5.5e-12}$	—	$7.18e-11^{+2.2e-12}_{-2.1e-12}$	$6.47e-10^{+6.3e-11}_{-5.9e-11}$	$3.521e-10^{+9.9e-12}_{-1e-11}$	$3.88e-1$
ρ_*	Density (cgs)	$0.416^{+0.086}_{-0.074}$	$3.25^{+0.54}_{-0.45}$	$3.26^{+0.32}_{-0.29}$	$2.41^{+0.25}_{-0.24}$	$0.0235^{+0.0065}_{-0.0048}$	0.499
$\log g$	Surface gravity (cgs)	$4.092^{+0.065}_{-0.062}$	4.61 ± 0.047	4.629 ± 0.028	$4.569^{+0.03}_{-0.033}$	$3.276^{+0.085}_{-0.077}$	4.169
$T_{\rm eff}$	Effective Temperature (K)	5700.0 ± 140.0	3990.0 ± 300.0	4413.0 ± 76.0	5160.0 ± 130.0	$4673.0^{+95.0}_{-93.0}$	6260.0
[Fe/H]	Metallicity (dex)	$0.049^{+0.120}_{-0.081}$	$-0.02^{+0.95}_{-0.99}$	$0.08^{+0.2}_{-0.14}$	$0.13^{+0.078}_{-0.076}$	$0.328^{+0.079}_{-0.081}$	-0.04
$[Fe/H]_0$	Initial Metallicity[1]	$0.103^{+0.100}_{-0.082}$	—	$0.07^{+0.18}_{-0.13}$	$0.115^{+0.08}_{-0.078}$	$0.261^{+0.074}_{-0.078}$	0.069
Age	Age (Gyr)	$8.6^{+2.5}_{-3.1}$	—	$6.8^{+4.7}_{-4.5}$	$4.7^{+5.2}_{-3.4}$	$7.5^{+4.0}_{-3.2}$	3.4
EEP	Equal Evolutionary Phase[2]	$447.5^{+8.7}_{-24.0}$	—	$327.0^{+14.0}_{-30.0}$	$334.0^{+19.0}_{-37.0}$	$499.6^{+8.7}_{-9.6}$	389.0
A_V	V-band extinction (mag)	$0.087^{+0.029}_{-0.047}$	—	$0.063^{+0.04}_{-0.042}$	$0.59^{+0.14}_{-0.15}$	$0.091^{+0.034}_{-0.051}$	0.088
σ_{SED}	SED photometry error scaling	$0.6^{+0.26}_{-0.15}$	—	$1.45^{+0.73}_{-0.39}$	$0.9^{+0.4}_{-0.24}$	$0.9^{+0.38}_{-0.24}$	1.13
ϖ	Parallax (mas)	1.449 ± 0.028	—	3.818 ± 0.03	7.107 ± 0.043	1.222 ± 0.062	1.951 ±
d	Distance (pc)	$689.0^{+14.0}_{-13.0}$	—	$261.9^{+2.1}_{-2.0}$	$140.71^{+0.85}_{-0.84}$	$818.0^{+44.0}_{-40.0}$	512.0
Planetary Parameters:							
P	Period (days)	$28.6781^{+0.0046}_{-0.0051}$	$9.7833^{+0.0013}_{-0.0012}$	$9.0073^{+0.0012}_{-0.0011}$	$8.2000844^{+8.6e-06}_{-7.3e-06}$	$8.407115 \pm 2.3e-05$	10.136734
R_P	Radius (R_J)	$0.360^{+0.027}_{-0.023}$	$0.233^{+0.019}_{-0.017}$	$0.206^{+0.015}_{-0.012}$	$0.223^{+0.015}_{-0.011}$	1.2 ± 0.11	0.452
M_P	Mass (M_J)	$0.055^{+0.021}_{-0.013}$	$0.0264^{+0.0100}_{-0.0066}$	$0.0217^{+0.0091}_{-0.0055}$	$0.0244^{+0.0091}_{-0.0058}$	$0.549^{+0.059}_{-0.046}$	0.107
T_C	Time of conjunction[3] (BJD_{TDB})	$2456824.6164^{+0.0079}_{-0.0067}$	$2456982.9376^{+0.0044}_{-0.0045}$	$2456984.335^{+0.0037}_{-0.0039}$	2457070.8051 ± 0.001	2457142.0537 ± 0.0031	2457145.97
T_T	Time of minimum projected separation[4] (BJD_{TDB})	$2456824.6164^{+0.0076}_{-0.0064}$	$2456982.9376^{+0.0043}_{-0.0044}$	$2456984.335^{+0.0036}_{-0.0038}$	2457070.80511 ± 0.0008	2457142.05 ± 0.0027	2457145.979
T_0	Optimal conjunction Time[5] (BJD_{TDB})	$2456853.2946^{+0.0046}_{-0.0042}$	$2457012.2875^{+0.0028}_{-0.0027}$	2457011.3568 ± 0.0023	$2457316.80766^{+0.00099}_{-0.00096}$	$2457722.1447^{+0.0027}_{-0.0026}$	2457662.95
a	Semi-major axis (AU)	$0.1867^{+0.0056}_{-0.0041}$	0.0761 ± 0.0013	$0.0752^{+0.0012}_{-0.0011}$	0.0753 ± 0.0011	$0.0854^{+0.0044}_{-0.0033}$	0.0986
i	Inclination (Degrees)	$89.08^{+0.58}_{-0.47}$	$89.08^{+0.59}_{-0.5}$	$88.95^{+0.67}_{-0.46}$	$88.33^{+0.83}_{-0.37}$	$75.5^{+1.6}_{-1.8}$	88.39
e	Eccentricity	$0.24^{+0.40}_{-0.17}$	$0.24^{+0.40}_{-0.18}$	$0.25^{+0.38}_{-0.17}$	$0.29^{+0.37}_{-0.19}$	$0.207^{+0.039}_{-0.038}$	0.119
ω_*	Argument of Periastron (Degrees)	$-30.0^{+110.0}_{-130.0}$	$-43.0^{+93.0}_{-120.0}$	$-20.0^{+110.0}_{-140.0}$	$-40.0^{+100.0}_{-130.0}$	$68.4^{+9.0}_{-11.0}$	14.0
T_{eq}	Equilibrium temperature[6] (K)	$786.0^{+14.0}_{-14.0}$	$560.0^{+45.0}_{-44.0}$	$635.8^{+6.8}_{-6.7}$	806.0 ± 18.0	$1566.0^{+49.0}_{-50.0}$	1185.0
$\tau_{\rm circ}$	Tidal circularization timescale (Gyr)	$28000.0^{+35000.0}_{-27000.0}$	$750.0^{+1000.0}_{-740.0}$	$880.0^{+1000.0}_{-860.0}$	$380.0^{+580.0}_{-380.0}$	$4.5^{+3.2}_{-1.8}$	330.0
K	RV semi-amplitude (m/s)	$3.9^{+2.0}_{-1.1}$	$3.8^{+2.1}_{-1.1}$	$2.98^{+1.7}_{-0.83}$	$3.09^{+1.5}_{-0.83}$	48.7 ± 2.3	8.8
R_P/R_*	Radius of planet in stellar radii	$0.02408^{+0.0011}_{-0.0009}$	$0.0373^{+0.0023}_{-0.0020}$	$0.0315^{+0.0019}_{-0.0014}$	$0.0288^{+0.0016}_{-0.0011}$	0.0298 ± 0.0011	0.03049
a/R_*	Semi-major axis in stellar radii	$26.3^{+1.7}_{-1.6}$	$25.4^{+1.3}_{-1.2}$	$24.09^{+0.76}_{-0.73}$	$20.46^{+0.68}_{-0.69}$	$4.44^{+0.38}_{-0.33}$	13.94
δ	$(R_P/R_*)^2$	$0.00058^{+5.4e-05}_{-4.3e-05}$	$0.00139^{+0.00018}_{-0.00014}$	$0.00099^{+0.00012}_{-8.3e-05}$	$0.000831^{+9.7e-05}_{-6e-05}$	$0.000891^{+6.7e-05}_{-6.2e-05}$	0.00093
$Depth_{\rm K2}$	Flux decrement at mid transit for K2	$0.000693 \pm 4.5e-05$	$0.00169^{+0.00019}_{-0.00017}$	$0.001377^{+9.7e-05}_{-0.0001}$	$0.000995^{+4e-05}_{-4.4e-05}$	$0.000576^{+5.6e-05}_{-6.4e-05}$	0.00108
$Depth_{\rm TESS}$	Flux decrement at mid transit for TESS	—	—	—	$0.00096 \pm 3e-05$	$0.000681^{+3.5e-05}_{-3.9e-05}$	0.001035 ±
τ	Ingress/egress transit duration (days)	$0.0085^{+0.0036}_{-0.0012}$	$0.00476^{+0.0023}_{-0.00066}$	$0.00382^{+0.0017}_{-0.00059}$	$0.0042^{+0.0026}_{-0.0012}$	$0.0348^{+0.0087}_{-0.0073}$	0.00729
T_{14}	Total transit duration (days)	$0.3159^{+0.0096}_{-0.0093}$	$0.1162^{+0.0074}_{-0.0072}$	$0.1075^{+0.0056}_{-0.006}$	$0.106^{+0.0028}_{-0.0023}$	$0.2613^{+0.0077}_{-0.0072}$	0.2134
b	Transit Impact parameter	$0.37^{+0.24}_{-0.25}$	$0.37^{+0.26}_{-0.25}$	$0.39^{+0.24}_{-0.26}$	$0.55^{+0.19}_{-0.33}$	$0.895^{+0.02}_{-0.026}$	0.37
ρ_P	Density (cgs)	$1.45^{+0.53}_{-0.35}$	$2.55^{+0.95}_{-0.62}$	$3.04^{+1.2}_{-0.74}$	$2.69^{+0.97}_{-0.63}$	$0.392^{+0.14}_{-0.1}$	1.4+
$loggP$	Surface gravity	$3.02^{+0.13}_{-0.11}$	$3.08^{+0.13}_{-0.11}$	$3.1^{+0.14}_{-0.12}$	$3.08^{+0.13}_{-0.11}$	$2.974^{+0.095}_{-0.091}$	3.12
T_S	Time of eclipse (BJD_{TDB})	$2456810.3^{+6.7}_{-6.4}$	2456987.8 ± 2.2	2456979.8 ± 2.1	$2457066.7^{+2.1}_{-2.0}$	$2457138.26^{+0.14}_{-0.15}$	2457141

Table 2A.2 Median values and 68% confidence intervals.

Priors:		K2-7	K2-54′	K2-57	K2-77	K2-97
π	Gaia Parallax (mas)	$\mathcal{G}[2.12963, 0.03560]$	$\mathcal{G}[2.49675, 0.02480]$	—	$\mathcal{G}[12.45657, 0.07130]$	$\mathcal{G}[4.93626, 0.04120]$
[Fe/H]	Metallicity (dex)	$\mathcal{G}[0.401, 0.037]^{\dagger}$	$\mathcal{G}[-0.23, 0.04]^{*}$	—	$\mathcal{G}[-0.459, 0.080]$	$\mathcal{G}[-0.588, 0.080]$
A_V	V-band extinction (mag)	$\mathcal{U}[0, 0.08928]$	$\mathcal{U}[0, 1.302]$	—	$\mathcal{U}[0, 0.12431]$	$\mathcal{U}[0, 0.08866]$
D_T^*	Dilution in TESS	—	$\mathcal{G}[0, 1.40623e-05]$	—	$\mathcal{G}[0, 2.69843e-05]$	$\mathcal{G}[0, 0.040635]$
Parameter	Units	Values				
Stellar Parameters:						
M_*	Mass ($M_\odot$)	$0.863^{+0.037}_{-0.031}$	$0.918^{+0.039}_{-0.046}$	0.563 ± 0.028	$1.084^{+0.1}_{-0.097}$	$0.735^{+0.035}_{-0.029}$
R_*	Radius ($R_\odot$)	$0.832^{+0.022}_{-0.021}$	$0.855^{+0.024}_{-0.021}$	0.578 ± 0.028	$1.499^{+0.077}_{-0.071}$	$0.719^{+0.025}_{-0.023}$
L_*	Luminosity ($L_\odot$)	0.36 ± 0.015	$0.78^{+0.1}_{-0.071}$	$0.056^{+0.022}_{-0.017}$	3.21 ± 0.14	0.386 ± 0.014
F_{Bol}	Bolometric Flux (cgs)	$5.18e-11 \pm 1.4e-12$	$1.55e-10^{+2e-11}_{-1.4e-11}$	—	$1.594e-08^{+6.6e-10}_{-6.7e-10}$	$3.011e-10^{+9.6e-12}_{-9.7e-12}$
ρ_*	Density (cgs)	$2.11^{+0.18}_{-0.17}$	$2.08^{+0.16}_{-0.19}$	$4.11^{+0.71}_{-0.58}$	$0.454^{+0.098}_{-0.086}$	$2.79^{+0.31}_{-0.28}$
$\log g$	Surface gravity (cgs)	$4.534^{+0.027}_{-0.026}$	$4.538^{+0.024}_{-0.033}$	4.665 ± 0.048	$4.122^{+0.066}_{-0.072}$	$4.591^{+0.034}_{-0.033}$
$T_{\rm eff}$	Effective Temperature (K)	$4899.0^{+59.0}_{-58.0}$	$5870.0^{+170.0}_{-150.0}$	3690.0 ± 300.0	6310.0 ± 170.0	$5365.0 \pm +92.0$
[Fe/H]	Metallicity (dex)	$0.42^{+0.036}_{-0.037}$	$-0.198^{+0.043}_{-0.049}$	$-0.02^{+0.96}_{-1.0}$	-0.456 ± 0.081	$-0.578^{+0.079}_{-0.080}$
$[Fe/H]_0$	Initial Metallicity[1]	0.39 ± 0.046	$-0.202^{+0.056}_{-0.058}$	—	$-0.253^{+0.075}_{-0.088}$	$-0.531^{+0.085}_{-0.086}$
Age	Age (Gyr)	$7.6^{+4.2}_{-4.6}$	$2.2^{+3.5}_{-1.6}$	—	$5.3^{+2.5}_{-2.0}$	$7.5^{+4.4}_{-4.7}$
EEP	Equal Evolutionary Phase[2]	$348.0^{+23.0}_{-26.0}$	$325.0^{+24.0}_{-39.0}$	—	$431.0^{+16.0}_{-39.0}$	$345.0^{+16.0}_{-25.0}$
A_V	V-band extinction (mag)	$0.05^{+0.027}_{-0.032}$	$0.17^{+0.13}_{-0.11}$	—	$0.07^{+0.038}_{-0.045}$	$0.051^{+0.027}_{-0.032}$
σ_{SED}	SED photometry error scaling	$1.09^{+0.48}_{-0.29}$	$1.13^{+0.5}_{-0.32}$	—	$1.65^{+0.59}_{-0.37}$	$1.48^{+0.58}_{-0.35}$
ϖ	Parallax (mas)	$2.122^{+0.035}_{-0.034}$	2.496 ± 0.025	—	12.456 ± 0.071	$4.937^{+0.042}_{-0.041}$
d	Distance (pc)	$471.2^{+7.8}_{-7.6}$	$400.7^{+4.0}_{-3.9}$	—	80.29 ± 0.46	202.6 ± 1.7
Planetary Parameters:						
P	Period (days)	$11.390931^{+3.1e-06}_{-3.2e-06}$	$20.2729914 \pm 5e-06$	$0.961939 \pm 2.9e-05$	$9.978541^{+2.3e-05}_{-1.9e-05}$	$8.865663^{+1.1e-05}_{-1e-05}$
R_P	Radius (R_J)	$0.945^{+0.029}_{-0.028}$	$1.053^{+0.03}_{-0.028}$	$0.1314^{+0.0099}_{-0.0088}$	$0.211^{+0.019}_{-0.013}$	$0.2200^{+0.0098}_{-0.0086}$
M_P	Mass (M_J)	2.01 ± 0.12	$1.01^{+0.22}_{-0.23}$	$0.0101^{+0.0037}_{-0.0023}$	$0.0224^{+0.0088}_{-0.0056}$	$0.0359^{+0.0075}_{-0.0068}$
T_C	Time of conjunction[3] (BJD_{TDB})	$2457140.324^{+0.00023}_{-0.00022}$	2458495.17373 ± 0.0003	$2457301.9457^{+0.0016}_{-0.0017}$	2456979.9331 ± 0.0024	$2457143.3957^{+0.00089}_{-0.00088}$
T_T	Time of minimum projected separation[4] (BJD_{TDB})	$2457140.32397^{+0.00023}_{-0.00022}$	$2458495.17376 \pm 0.00028$	$2457301.9457^{+0.0014}_{-0.0015}$	$2456979.9331^{+0.0016}_{-0.0015}$	$2457143.3957^{+0.00089}_{-0.00088}$
T_0	Optimal conjunction Time[5] (BJD_{TDB})	$2457687.08869 \pm 0.00016$	$2457522.07014 \pm 0.00017$	$2457343.30907^{+0.001}_{-0.00099}$	$2457299.2465^{+0.0022}_{-0.0023}$	$2457489.1566^{+0.00078}_{-0.00076}$
a	Semi-major axis (AU)	$0.0944^{+0.0013}_{-0.0011}$	$0.1415^{+0.002}_{-0.0024}$	$0.01575^{+0.00026}_{-0.00027}$	$0.0932^{+0.0028}_{-0.0029}$	$0.0756^{+0.0012}_{-0.001}$
i	Inclination (Degrees)	$89.16^{+0.18}_{-0.13}$	$88.912^{+0.057}_{-0.075}$	$83.6^{+3.6}_{-1.8}$	$86.8^{+1.6}_{-1.1}$	$89.15^{+0.51}_{-0.38}$
e	Eccentricity	0.079 ± 0.03	$0.063^{+0.061}_{-0.042}$	$0.38^{+0.26}_{-0.22}$	0.48 ± 0.26	$0.075^{+0.080}_{-0.051}$
ω_*	Argument of Periastron (Degrees)	$-50.0^{+22.0}_{-13.0}$	$137.0^{+46.0}_{-87.0}$	$40.0^{+100.0}_{-150.0}$	$140.0^{+120.0}_{-100.0}$	$130.0^{+120.0}_{-110.0}$
T_{eq}	Equilibrium temperature[6] (K)	$701.4^{+7.6}_{-7.7}$	$696.0^{+19.0}_{-15.0}$	$1077.0^{+93.0}_{-92.0}$	$1220.0^{+20.0}_{-19.0}$	$797.5^{+8.4}_{-8.5}$
$\tau_{\rm circ}$	Tidal circularization timescale (Gyr)	$256.0^{+45.0}_{-37.0}$	$960.0^{+310.0}_{-330.0}$	$0.089^{+0.24}_{-0.084}$	$270.0^{+1600.0}_{-270.0}$	$1950.0^{+750.0}_{-690.0}$
K	RV semi-amplitude (m/s)	200.0 ± 10.0	$80.0^{+17.0}_{-18.0}$	$3.44^{+1.4}_{-0.86}$	$2.44^{+1.3}_{-0.72}$	$4.36^{+0.90}_{-0.82}$
R_P/R_*	Radius of planet in stellar radii	$0.1167^{+0.0013}_{-0.0014}$	$0.12659^{+0.00075}_{-0.00084}$	$0.0234^{+0.0012}_{-0.0011}$	$0.01436^{+0.0011}_{-0.0005}$	$0.03141^{+0.00069}_{-0.00055}$
a/R_*	Semi-major axis in stellar radii	$24.4^{+0.67}_{-0.66}$	$35.62^{+0.91}_{-1.1}$	$5.86^{+0.32}_{-0.29}$	13.37 ± 0.9	$22.63^{+0.82}_{-0.79}$
δ	$(R_P/R_*)^2$	$0.01361^{+0.00031}_{-0.00033}$	$0.01603^{+0.00019}_{-0.00021}$	$0.000545^{+5.9e-05}_{-4.8e-05}$	$0.000206^{+3.1e-05}_{-1.4e-05}$	$0.000987^{+4.4e-05}_{-3.4e-05}$
$Depth_{\rm K2}$	Flux decrement at mid transit for K2	$0.01856^{+0.00028}_{-0.00027}$	$0.01732^{+0.00018}_{-0.00016}$	$0.0006^{+4.7e-05}_{-4.3e-05}$	$0.0002287^{+8.7e-06}_{-8.6e-06}$	$0.00121^{+3.5e-05}_{-3.4e-05}$
$Depth_{\rm TESS}$	Flux decrement at mid transit for TESS	$0.0171^{+0.00029}_{-0.0003}$	0.01695 ± 0.00015	—	$0.0002225^{+1.2e-05}_{-1e-05}$	$0.001152 \pm 3.4e-05$
τ	Ingress/egress transit duration (days)	0.0199 ± 0.0014	$0.0299^{+0.0014}_{-0.0015}$	$0.00114^{+0.00083}_{-0.00028}$	$0.00301^{+0.0035}_{-0.00089}$	$0.00403^{+0.00081}_{-0.00041}$
T_{14}	Total transit duration (days)	0.1654 ± 0.0012	0.1614 ± 0.0011	0.0376 ± 0.0025	$0.15^{+0.0045}_{-0.0042}$	$0.1187^{+0.0020}_{-0.0019}$
b	Transit Impact parameter	$0.378^{+0.061}_{-0.085}$	$0.655^{+0.018}_{-0.021}$	$0.5^{+0.24}_{-0.34}$	$0.55^{+0.26}_{-0.36}$	$0.33^{+0.17}_{-0.20}$
ρ_P	Density (cgs)	$2.96^{+0.34}_{-0.31}$	$1.07^{+0.26}_{-0.27}$	$5.5^{+1.9}_{-1.3}$	$2.89^{+1.1}_{-0.69}$	$4.16^{+1.10}_{-0.92}$
$loggP$	Surface gravity	$3.748^{+0.03}_{-0.038}$	$3.356^{+0.088}_{-0.12}$	$3.16^{+0.13}_{-0.1}$	$3.09^{+0.13}_{-0.11}$	$3.263^{+0.089}_{-0.099}$
T_S	Time of eclipse (BJD_{TDB})	$2457134.99^{+0.11}_{-0.12}$	$2458505.03^{+0.62}_{-0.89}$	2457301.47 ± 0.26	$2456974.9^{+3.2}_{-3.3}$	$2457147.81^{+0.43}_{-0.36}$
$T_{S,14}$	Total eclipse duration (days)	$0.1493^{+0.009}_{-0.0079}$	$0.165^{+0.0043}_{-0.0038}$	$0.0399^{+0.019}_{-0.0073}$	$0.151^{+0.094}_{-0.054}$	$0.121^{+0.014}_{-0.011}$
$e\cos\omega_*$		$0.049^{+0.015}_{-0.017}$	$-0.022^{+0.048}_{-0.069}$	0.0 ± 0.43	$-0.0^{+0.5}_{-0.52}$	$-0.003^{+0.076}_{-0.063}$

Table 2A.3 Median values and 68% confidence intervals.

Priors:		K2-7	K2-54′	K2-57	K2-77	K2-97	K2
π	Gaia Parallax (mas)	$\mathcal{G}[2.80448, 0.04020]$	$\mathcal{G}[6.50953, 0.05160]$	$\mathcal{G}[5.93701, 0.05600]$	$\mathcal{G}[1.83974, 0.05160]$	$\mathcal{G}[3.85946, 0.04790]$	
[Fe/H]	Metallicity (dex)	$\mathcal{G}[0.416, 0.080]$	$\mathcal{G}[-0.006, 0.080]$	$\mathcal{G}[-0.073, 0.080]$	$\mathcal{G}[0.064, 0.080]$	$\mathcal{G}[-0.116, 0.080]$	
A_V	V-band extinction (mag)	$\mathcal{U}[0, 0.10664]$	$\mathcal{U}[0, 0.086490]$	$\mathcal{U}[0, 0.13733]$	$\mathcal{U}[0, 0.10416]$	$\mathcal{U}[0, 0.08556]$	
D_T^*	Dilution in TESS	—	$\mathcal{G}[0, 0.00028648]$	—	—	—	
Parameter	Units	Values					
Stellar Parameters:							
M_*	Mass ($M_\odot$)	$1.022^{+0.060}_{-0.058}$	$0.823^{+0.036}_{-0.033}$	$0.793^{+0.033}_{-0.029}$	$1.076^{+0.092}_{-0.086}$	$0.881^{+0.045}_{-0.042}$	
R_*	Radius ($R_\odot$)	$1.04^{+0.043}_{-0.039}$	$0.789^{+0.025}_{-0.023}$	$0.765^{+0.024}_{-0.023}$	$1.253^{+0.055}_{-0.053}$	$0.872^{+0.033}_{-0.03}$	
L_*	Luminosity ($L_\odot$)	$0.903^{+0.038}_{-0.036}$	$0.388^{+0.013}_{-0.012}$	0.337 ± 0.013	$1.58^{+0.11}_{-0.1}$	$0.629^{+0.027}_{-0.026}$	
F_{Bol}	Bolometric Flux (cgs)	$2.267e-10^{+6.9e-12}_{-6.4e-12}$	$5.26e-10 \pm 1.5e-11$	$3.79e-10 \pm 1.3e-11$	$1.692e-10^{+6.2e-12}_{-5.7e-12}$	$2.992e-10^{+1.1e-11}_{-9.9e-12}$	
ρ_*	Density (cgs)	$1.28^{+0.19}_{-0.18}$	$2.37^{+0.23}_{-0.22}$	$2.5^{+0.26}_{-0.23}$	$0.77^{+0.14}_{-0.11}$	$1.88^{+0.24}_{-0.23}$	
$\log g$	Surface gravity (cgs)	$4.413^{+0.047}_{-0.050}$	$4.56^{+0.029}_{-0.032}$	4.57 ± 0.031	$4.273^{+0.056}_{-0.054}$	$4.503^{+0.04}_{-0.042}$	
$T_{\rm eff}$	Effective Temperature (K)	$5520.0^{+100.0}_{-110.0}$	$5128.0^{+79.0}_{-80.0}$	$5026.0^{+82.0}_{-81.0}$	$5783.0^{+100.0}_{-98.0}$	5500.0 ± 100.0	
[Fe/H]	Metallicity (dex)	0.385 ± 0.057	$0.022^{+0.077}_{-0.066}$	$-0.021^{+0.064}_{-0.041}$	$0.21^{+0.18}_{-0.19}$	-0.064 ± 0.054	
$[Fe/H]_0$	Initial Metallicity[1]	$0.366^{+0.058}_{-0.060}$	$0.025^{+0.077}_{-0.071}$	$-0.01^{+0.063}_{-0.057}$	$0.23^{+0.15}_{-0.16}$	-0.048 ± 0.063	
Age	Age (Gyr)	$5.9^{+4.5}_{-3.8}$	$6.2^{+4.9}_{-4.2}$	$6.9^{+4.6}_{-4.5}$	$6.5^{+3.7}_{-3.1}$	$6.1^{+4.8}_{-4.1}$	
EEP	Equal Evolutionary Phase[2]	$374.0^{+36.0}_{-43.0}$	$341.0^{+19.0}_{-31.0}$	$341.0^{+15.0}_{-29.0}$	$413.0^{+20.0}_{-44.0}$	$349.0^{+35.0}_{-30.0}$	
A_V	V-band extinction (mag)	$0.046^{+0.036}_{-0.030}$	$0.05^{+0.026}_{-0.032}$	$0.073^{+0.044}_{-0.047}$	$0.063^{+0.029}_{-0.038}$	$0.049^{+0.025}_{-0.032}$	
σ_{SED}	SED photometry error scaling	$0.341^{+0.140}_{-0.085}$	$1.1^{+0.45}_{-0.27}$	$0.8^{+0.33}_{-0.2}$	$1.01^{+0.46}_{-0.27}$	$0.97^{+0.41}_{-0.25}$	
ϖ	Parallax (mas)	2.802 ± 0.04	6.508 ± 0.052	$5.935^{+0.055}_{-0.056}$	1.83 ± 0.052	3.857 ± 0.048	
d	Distance (pc)	$356.9^{+5.2}_{-5.1}$	153.7 ± 1.2	168.5 ± 1.6	$546.0^{+16.0}_{-15.0}$	259.3 ± 3.2	
Planetary Parameters:							
P	Period (days)	$6.893813 \pm 1.1e-05$	$4.7369696 \pm 1.7e-06$	9.6952 ± 0.0014	$7.055908^{+5.8e-05}_{-7.4e-05}$	4.19097 ± 0.00023	
R_P	Radius (R_J)	$0.253^{+0.019}_{-0.014}$	$0.242^{+0.0099}_{-0.0081}$	$0.1129^{+0.0091}_{-0.0071}$	$0.283^{+0.016}_{-0.014}$	$0.1494^{+0.011}_{-0.0082}$	
M_P	Mass (M_J)	$0.0304^{+0.0110}_{-0.0073}$	$0.066^{+0.017}_{-0.016}$	$0.0081^{+0.0029}_{-0.0017}$	$0.0365^{+0.014}_{-0.0089}$	$0.0125^{+0.0046}_{-0.003}$	
T_C	Time of conjunction[3] (BJD_{TDB})	$2457143.7954^{0.0017}_{0.0016}$	2457145.9418 ± 0.00033	$2457396.6382^{+0.0067}_{-0.0065}$	$2457396.5078^{+0.0022}_{-0.0023}$	2457396.5113 ± 0.0026	
T_T	Time of minimum projected separation[4] (BJD_{TDB})	2457143.7954 ± 0.0014	$2457145.94181 \pm 0.00032$	$2457396.6382^{+0.0066}_{-0.0064}$	2457396.5078 ± 0.002	$2457396.5113^{+0.0024}_{-0.0023}$	
T_0	Optimal conjunction Time[5] (BJD_{TDB})	2457778.0262 ± 0.0012	$2457652.79755^{+0.00027}_{-0.00028}$	$2457435.4189^{+0.0037}_{-0.0036}$	2457452.955 ± 0.0022	2457430.039 ± 0.0016	
a	Semi-major axis (AU)	0.0714 ± 0.0014	$0.05174^{+0.00075}_{-0.0007}$	$0.0824^{+0.0011}_{-0.001}$	0.0738 ± 0.002	$0.04878^{+0.00082}_{-0.00079}$	
i	Inclination (Degrees)	$87.4^{+1.5}_{-0.71}$	$88.91^{+0.71}_{-0.69}$	$89.12^{+0.59}_{-0.57}$	$88.76^{+0.86}_{-1.0}$	$86.94^{+1.8}_{-0.76}$	
e	Eccentricity	$0.40^{+0.30}_{-0.22}$	$0.071^{+0.11}_{-0.051}$	$0.23^{+0.42}_{-0.18}$	$0.28^{+0.37}_{-0.19}$	$0.37^{+0.31}_{-0.21}$	
ω_*	Argument of Periastron (Degrees)	$20.0^{+110.0}_{-180.0}$	$-160.0^{+110.0}_{-130.0}$	$-124.0^{+100.0}_{-74.0}$	$-88.0^{+61.0}_{-63.0}$	$-210.0^{+160.0}_{-110.0}$	
T_{eq}	Equilibrium temperature[6] (K)	1015.0 ± 13.0	$965.8^{+10.0}_{-9.8}$	$738.4^{+8.0}_{-7.9}$	$1148.0^{+25.0}_{-24.0}$	$1122.0^{+15.0}_{-14.0}$	
$\tau_{\rm circ}$	Tidal circularization timescale (Gyr)	$61.0^{+170.0}_{-60.0}$	$153.0^{+64.0}_{-62.0}$	$11000.0^{+12000.0}_{-11000.0}$	$120.0^{+160.0}_{-120.0}$	$49.0^{+110.0}_{-48.0}$	
K	RV semi-amplitude (m/s)	$3.7^{+1.8}_{-1.0}$	9.1 ± 2.3	$0.99^{+0.52}_{-0.25}$	$4.1^{+2.0}_{-1.1}$	$1.96^{+0.9}_{-0.52}$	
R_P/R_*	Radius of planet in stellar radii	$0.02485^{+0.00160}_{-0.00085}$	$0.03143^{+0.00068}_{-0.00036}$	$0.01518^{+0.001}_{-0.00084}$	$0.02319^{+0.00077}_{-0.00063}$	$0.01757^{+0.0011}_{-0.00073}$	
a/R_*	Semi-major axis in stellar radii	$14.76^{+0.71}_{-0.72}$	$14.11^{+0.44}_{-0.46}$	$23.16^{+0.76}_{-0.75}$	$12.64^{+0.73}_{-0.63}$	$12.03^{+0.5}_{-0.51}$	
δ	$(R_P/R_*)^2$	$0.000618^{+8.3e-05}_{-4.1e-05}$	$0.000988^{+4.3e-05}_{-2.3e-05}$	$0.00023^{+3.3e-05}_{-2.5e-05}$	$0.000538^{+3.6e-05}_{-2.9e-05}$	$0.000309^{+3.9e-05}_{-2.5e-05}$	
$Depth_{\rm K2}$	Flux decrement at mid transit for K2	$0.000747^{+2.9e-05}_{-3.0-05}$	$0.001308 \pm 2.5e-05$	$0.0003 \pm 3e-05$	$0.000645^{+3.2e-05}_{-3e-05}$	$0.000365 \pm 2.1e-05$	
$Depth_{\rm TESS}$	Flux decrement at mid transit for TESS	—	$0.001226^{+2.3e-05}_{-2.4e-05}$	—	$0.000623 \pm 2.9e-05$	—	
τ	Ingress/egress transit duration (days)	$0.00329^{+0.0025}_{-0.00077}$	$0.0035^{+0.00071}_{-0.00025}$	$0.00216^{+0.001}_{-0.00027}$	$0.00462^{+0.0016}_{-0.00035}$	$0.00183^{+0.0013}_{-0.00044}$	
T_{14}	Total transit duration (days)	$0.105^{+0.0028}_{-0.0026}$	$0.10693^{+0.001}_{-0.00088}$	$0.1293^{+0.0078}_{-0.008}$	$0.1904^{+0.005}_{-0.0046}$	$0.081^{+0.0036}_{-0.0035}$	
b	Transit Impact parameter	$0.48^{+0.25}_{-0.33}$	$0.27^{+0.19}_{-0.18}$	$0.33^{+0.29}_{-0.23}$	$0.27^{+0.27}_{-0.19}$	$0.49^{+0.24}_{-0.33}$	
ρ_P	Density (cgs)	$2.28^{+0.83}_{-0.54}$	$5.7^{+1.6}_{-1.5}$	$6.7^{+2.4}_{-1.3}$	$1.98^{+0.75}_{-0.46}$	$4.5^{+1.6}_{-1.1}$	
$logg_P$	Surface gravity	$3.06^{+0.13}_{-0.11}$	$3.44^{+0.1}_{-0.13}$	$3.187^{+0.12}_{-0.095}$	$3.05^{+0.14}_{-0.11}$	$3.13^{+0.13}_{-0.11}$	
T_S	Time of eclipse (BJD_{TDB})	2457140.4 ± 2.1	$2457148.3^{+0.22}_{-0.29}$	$2457401.5^{+2.0}_{-2.1}$	$2457400.0^{+1.5}_{-1.6}$	$2457398.6^{+1.1}_{-1.2}$	
$T_{S,14}$	Total eclipse duration (days)	$0.109^{+0.058}_{-0.022}$	$0.105^{+0.0072}_{-0.012}$	$0.114^{+0.02}_{-0.041}$	$0.144^{+0.032}_{-0.047}$	$0.084^{+0.039}_{-0.017}$	
$e\cos\omega_*$		$-0.0^{+0.50}_{-0.48}$	$-0.003^{+0.074}_{-0.095}$	$-0.0^{+0.32}_{-0.34}$	$-0.0^{+0.33}_{-0.34}$	$-0.0^{+0.43}_{-0.47}$	

Table 2A.4 Median values and 68% confidence intervals.

Priors:		K2-7	K2-54′	K2-57	K2-77	K2-97
Priors:		K2-211	K2-225	K2-226	K2-237	K2-250
π	Gaia Parallax (mas)	$\mathcal{G}[3.60379, 0.05510]$	$\mathcal{G}[2.79562, 0.04500]$	$\mathcal{G}[4.80729, 0.07400]$	$\mathcal{G}[3.29816, 0.07060]$	$\mathcal{G}[2.47572, 0.03610]$
[Fe/H]	Metallicity (dex)	$\mathcal{G}[0.115, 0.080]$	$\mathcal{G}[0.471, 0.080]$	$\mathcal{G}[-0.082, 0.080]$	$\mathcal{G}[0.357, 0.080]$	$\mathcal{G}[-0.227, 0.280]^{\dagger}$
A_V	V-band extinction (mag)	$\mathcal{U}[0, 0.08618]$	$\mathcal{U}[0, 0.11997]$	$\mathcal{U}[0, 0.21266]$	$\mathcal{U}[0, 0.58342]$	$\mathcal{U}[0, 0.11997]$
D_T^*	Dilution in TESS	—	—	—	$\mathcal{G}[0, 0.079682]$	—
D_K	Dilution in K2	—	—	—	$\mathcal{G}[0, 0.050]$	—
Parameter	Units	Values				
Stellar Parameters:						
M_*	Mass ($M_\odot$)	$0.851^{+0.039}_{-0.035}$	$1.482^{+0.11}_{-0.096}$	$0.856^{+0.042}_{-0.03}$	$1.256^{+0.055}_{-0.062}$	$0.809^{+0.044}_{-0.036}$
R_*	Radius ($R_\odot$)	$0.818^{+0.029}_{-0.027}$	$1.700^{+0.094}_{-0.087}$	$0.889^{+0.034}_{-0.032}$	$1.236^{+0.043}_{-0.036}$	$0.797^{+0.029}_{-0.027}$
L_*	Luminosity ($L_\odot$)	$0.414^{+0.017}_{-0.016}$	2.41 ± 0.11	0.558 ± 0.029	$2.01^{+0.27}_{-0.21}$	$0.359^{+0.017}_{-0.016}$
F_{Bol}	Bolometric Flux (cgs)	$1.715e-10 \pm 4.6e-12$	$6.01e-10^{+1.8e-11}_{-2e-11}$	$4.14e-10^{+1.6e-11}_{-1.9e-11}$	$7e-10^{+9.1e-11}_{-7e-11}$	$7.04e-11^{+2.6e-12}_{-2.4e-12}$
ρ_*	Density (cgs)	$2.19^{+0.25}_{-0.23}$	$0.425^{+0.047}_{-0.043}$	$1.72^{+0.22}_{-0.19}$	$0.937^{+0.073}_{-0.085}$	$2.26^{+0.24}_{-0.22}$
$\log g$	Surface gravity (cgs)	$4.543^{+0.033}_{-0.034}$	4.148 ± 0.025	$4.473^{+0.04}_{-0.034}$	$4.353^{+0.022}_{-0.029}$	$4.544^{+0.033}_{-0.032}$
$T_{\rm eff}$	Effective Temperature (K)	$5117.0^{+85.0}_{-86.0}$	5520.0 ± 140.0	5288.0 ± 99.0	$6180.0^{+160.0}_{-140.0}$	5003.0 ± 94.0
[Fe/H]	Metallicity (dex)	$0.134^{+0.077}_{-0.078}$	$0.486^{+0.061}_{-0.072}$	$-0.05^{+0.068}_{-0.052}$	0.337 ± 0.076	$-0.02^{+0.24}_{-0.098}$
$[Fe/H]_0$	Initial Metallicity[1]	$0.13^{+0.078}_{-0.079}$	$0.405^{+0.057}_{-0.067}$	$-0.013^{+0.066}_{-0.06}$	$0.309^{+0.069}_{-0.07}$	$0.01^{+0.21}_{-0.1}$
Age	Age (Gyr)	$6.5^{+4.8}_{-4.3}$	$0.0121^{+0.0039}_{-0.0032}$	$9.6^{+3.0}_{-4.7}$	$1.09^{+1.5}_{-0.78}$	$8.2^{+4.0}_{-5.0}$
EEP	Equal Evolutionary Phase[2]	$344.0^{+24.0}_{-31.0}$	$188.0^{+4.3}_{-4.8}$	$373.0^{+20.0}_{-30.0}$	$324.0^{+28.0}_{-40.0}$	$347.0^{+19.0}_{-25.0}$
A_V	V-band extinction (mag)	$0.05^{+0.026}_{-0.032}$	$0.08^{+0.029}_{-0.046}$	$0.164^{+0.037}_{-0.07}$	$0.24^{+0.15}_{-0.14}$	$0.071^{+0.035}_{-0.045}$
σ_{SED}	SED photometry error scaling	$1.0^{+0.4}_{-0.25}$	$0.78^{+0.32}_{-0.19}$	$1.18^{+0.5}_{-0.29}$	$1.81^{+0.73}_{-0.46}$	$1.6^{+0.66}_{-0.4}$
ϖ	Parallax (mas)	3.599 ± 0.054	2.792 ± 0.045	$4.812^{+0.073}_{-0.074}$	$3.304^{+0.067}_{-0.068}$	2.478 ± 0.036
d	Distance (pc)	$277.9^{+4.2}_{-4.1}$	$358.1^{+5.8}_{-5.7}$	$207.8^{+3.3}_{-3.1}$	$302.7^{+6.3}_{-6.0}$	$403.6^{+6.0}_{-5.8}$
Planetary Parameters:						
P	Period (days)	$0.669561^{+3.1e-05}_{-3.2e-05}$	$15.8723^{+0.0021}_{-0.0019}$	$3.27109^{+0.00036}_{-0.00039}$	$2.18053332 \pm 5.4e-07$	4.01392 ± 0.00029
R_P	Radius ($R_{\rm J}$)	$0.1188^{+0.0078}_{-0.0064}$	$0.322^{+0.025}_{-0.020}$	$0.1373^{+0.0092}_{-0.0077}$	$1.433^{+0.056}_{-0.049}$	$0.242^{+0.016}_{-0.012}$
M_P	Mass ($M_{\rm J}$)	$0.0087^{+0.003}_{-0.0017}$	$0.046^{+0.017}_{-0.011}$	$0.0108^{+0.004}_{-0.0025}$	$1.366^{+0.11}_{-0.092}$	$0.0282^{+0.011}_{-0.0068}$
T_C	Time of conjunction[3] ($\rm BJD_{TDB}$)	2457393.8134 ± 0.0023	$2457587.3665^{+0.0049}_{-0.0055}$	$2457584.0262^{+0.0049}_{-0.0046}$	$2457656.463914 \pm 3.3e-05$	2457584.1282 ± 0.0031
T_T	Time of minimum projected separation[4] ($\rm BJD_{TDB}$)	2457393.8134 ± 0.0021	$2457587.3665^{+0.0046}_{-0.0051}$	$2457584.0262^{+0.0048}_{-0.0044}$	$2457656.463912 \pm 3.1e-05$	$2457584.1281^{+0.003}_{-0.0029}$
T_0	Optimal conjunction Time[5] ($\rm BJD_{TDB}$)	2457432.6479 ± 0.0013	$2457619.1111^{+0.0031}_{-0.0030}$	2457620.0082 ± 0.002	$2457706.61618 \pm 3e-05$	2457620.2535 ± 0.0015
a	Semi-major axis (AU)	$0.01419^{+0.00021}_{-0.0002}$	$0.1409^{+0.0033}_{-0.0031}$	$0.04095^{+0.00066}_{-0.00049}$	$0.03552^{+0.00051}_{-0.0006}$	$0.04606^{+0.00082}_{-0.00068}$
i	Inclination (Degrees)	$84.1^{+3.8}_{-3.0}$	$88.64^{+0.85}_{-0.60}$	$87.6^{+1.5}_{-1.1}$	$88.37^{+1.0}_{-0.88}$	$88.26^{+1.1}_{-0.94}$
e	Eccentricity	$0.19^{+0.3}_{-0.14}$	$0.23^{+0.39}_{-0.16}$	$0.22^{+0.37}_{-0.16}$	$0.03^{+0.033}_{-0.021}$	$0.21^{+0.39}_{-0.16}$
ω_*	Argument of Periastron (Degrees)	$-150.0^{+130.0}_{-110.0}$	$-160.0^{+130.0}_{-120.0}$	$-33.0^{+99.0}_{-130.0}$	$73.0^{+57.0}_{-58.0}$	$-40.0^{+92.0}_{-120.0}$
T_{eq}	Equilibrium temperature[6] (K)	$1873.0^{+22.0}_{-21.0}$	$923.0^{+13.0}_{-14.0}$	$1187.0^{+16.0}_{-17.0}$	$1759.0^{+49.0}_{-42.0}$	1003.0 ± 14.0
$\tau_{\rm circ}$	Tidal circularization timescale (Gyr)	$0.107^{+0.087}_{-0.095}$	$4000.0^{+4500.0}_{-3900.0}$	$53.0^{+57.0}_{-51.0}$	$0.0231^{+0.0044}_{-0.0043}$	$19.0^{+20.0}_{-19.0}$
K	RV semi-amplitude (m/s)	$2.38^{+0.89}_{-0.5}$	$3.13^{+1.5}_{-0.83}$	$1.79^{+0.81}_{-0.46}$	$184.0^{+14.0}_{-11.0}$	$4.5^{+2.2}_{-1.2}$
R_P/R_*	Radius of planet in stellar radii	$0.01489^{+0.00079}_{-0.00059}$	$0.01942^{+0.00091}_{-0.00064}$	$0.01586^{+0.00082}_{-0.00068}$	$0.119^{+0.0024}_{-0.0023}$	$0.0311^{+0.0016}_{-0.001}$
a/R_*	Semi-major axis in stellar radii	3.73 ± 0.13	$17.82^{+0.64}_{-0.62}$	$9.91^{+0.41}_{-0.37}$	$6.18^{+0.16}_{-0.19}$	$12.44^{+0.43}_{-0.42}$
δ	$(R_P/R_*)^2$	$0.000222^{+2.4e-05}_{-1.7e-05}$	$0.000377^{+3.6e-05}_{-2.4e-05}$	$0.000252^{+2.7e-05}_{-2.1e-05}$	$0.01416^{+0.00058}_{-0.00053}$	$0.00097^{+0.0001}_{-6.2e-05}$
$Depth_{\rm K2}$	Flux decrement at mid transit for K2	$0.000287 \pm 1.9e-05$	$0.000465 \pm 2.6e-05$	$0.000314 \pm 2.3e-05$	$0.0169^{+0.00072}_{-0.00067}$	$0.001284^{+7e-05}_{-7.2e-05}$
$Depth_{\rm TESS}$	Flux decrement at mid transit for TESS	—	—	—	$0.01624^{+0.00072}_{-0.00068}$	—
τ	Ingress/egress transit duration (days)	$0.00092^{+0.00037}_{-0.00012}$	$0.00572^{+0.0026}_{-0.00082}$	$0.00176^{+0.00076}_{-0.00025}$	$0.01347^{+0.00054}_{-0.00041}$	$0.00336^{+0.0014}_{-0.00041}$
T_{14}	Total transit duration (days)	$0.0538^{+0.003}_{-0.0031}$	$0.258^{+0.0073}_{-0.0064}$	$0.0968^{+0.0046}_{-0.0047}$	$0.12197^{+0.00038}_{-0.00034}$	0.0986 ± 0.0037
b	Transit Impact parameter	0.36 ± 0.24	$0.38^{+0.24}_{-0.25}$	$0.38^{+0.24}_{-0.25}$	$0.171^{+0.091}_{-0.11}$	$0.35^{+0.25}_{-0.23}$
ρ_P	Density (cgs)	$6.4^{+2.2}_{-1.3}$	$1.67^{+0.61}_{-0.4}$	$5.1^{+1.9}_{-1.2}$	$0.577^{+0.069}_{-0.064}$	$2.41^{+0.88}_{-0.56}$
$loggg_P$	Surface gravity	$3.182^{+0.12}_{-0.09}$	$3.03^{+0.13}_{-0.11}$	$3.15^{+0.13}_{-0.1}$	3.218 ± 0.039	$3.07^{+0.13}_{-0.11}$

Table 2A.5 Median values and 68% confidence intervals.

Priors:		K2-7	K2-54′	K2-57	K2-77	K2-97
Priors:		K2-260	K2-261[†]		K2-265	K2-277
π	Gaia Parallax (mas)	$\mathcal{G}[1.49761, 0.04250]$	$\mathcal{G}[4.68526, 0.04270]$		$\mathcal{G}[7.18885, 0.05050]$	$\mathcal{G}[8.84150, 0.061$
[Fe/H]	Metallicity (dex)	$\mathcal{G}[0.386, 0.080]$	$\mathcal{G}[0.382, 0.080]$		$\mathcal{G}[0.08, 0.08]$	$\mathcal{G}[0.064, 0.080$
A_V	V-band extinction (mag)	$\mathcal{U}[0, 0.82243]$	$\mathcal{U}[0, 0.12679]$		$\mathcal{U}[0, 0.11408]$	$\mathcal{U}[0, 0.19933]$
D_T^*	Dilution in TESS	$\mathcal{G}[0, 0.036733]$	$\mathcal{G}[0, 0.0021478]$		—	$\mathcal{G}[0, 0.0020849$
Parameter	Units	Values				
Stellar Parameters:						
M_*	Mass ($M_\odot$)	$1.637^{+0.065}_{-0.069}$	$1.107^{+0.042}_{-0.047}$	1.264 ± 0.041	$0.901^{+0.051}_{-0.042}$	$0.974^{+0.053}_{-0.058}$
R_*	Radius ($R_\odot$)	$1.755^{+0.061}_{-0.078}$	$1.663^{+0.071}_{-0.068}$	$1.609^{+0.061}_{-0.057}$	$0.92^{+0.034}_{-0.032}$	$0.973^{+0.038}_{-0.035}$
L_*	Luminosity ($L_\odot$)	$6.14^{+0.48}_{-0.52}$	$2.259^{+0.087}_{-0.083}$	$2.275^{+0.085}_{-0.084}$	0.657 ± 0.024	$0.89^{+0.048}_{-0.044}$
F_{Bol}	Bolometric Flux (cgs)	$4.36e-10^{+1.9e-11}_{-3e-11}$	$1.588e-09^{+5.5e-11}_{-5.1e-11}$	$1.599e-09^{+5.2e-11}_{-5.3e-11}$	$1.087e-09 \pm 3.7e-11$	$2.22e-09^{+1.2e-}_{-1.1e-}$
ρ_*	Density (cgs)	$0.424^{+0.067}_{-0.039}$	$0.339^{+0.046}_{-0.042}$	$0.427^{+0.046}_{-0.041}$	$1.63^{+0.22}_{-0.19}$	1.5 ± 0.2
$\log g$	Surface gravity (cgs)	$4.161^{+0.044}_{-0.03}$	$4.040^{+0.038}_{-0.041}$	$4.126^{+0.030}_{-0.028}$	$4.465^{+0.042}_{-0.039}$	$4.452^{+0.041}_{-0.049}$
$T_{\rm eff}$	Effective Temperature (K)	$6860.0^{+150.0}_{-160.0}$	5490 ± 110	5587 ± 100	5420.0 ± 100.0	5680.0 ± 120.0
[Fe/H]	Metallicity (dex)	$0.334^{+0.052}_{-0.061}$	$0.372^{+0.069}_{-0.072}$	$0.401^{+0.064}_{-0.070}$	$0.033^{+0.099}_{-0.1}$	$0.078^{+0.072}_{-0.065}$
$[Fe/H]_0$	Initial Metallicity[1]	$0.44^{+0.04}_{-0.056}$	$0.368^{+0.064}_{-0.068}$	$0.396^{+0.057}_{-0.064}$	$0.051^{+0.096}_{-0.091}$	$0.084^{+0.072}_{-0.069}$
Age	Age (Gyr)	$0.65^{+0.43}_{-0.37}$	$8.8^{+1.7}_{-1.2}$	$4.78^{+0.72}_{-0.78}$	$7.8^{+4.0}_{-4.6}$	$4.9^{+4.8}_{-3.4}$
EEP	Equal Evolutionary Phase[2]	$327.0^{+13.0}_{-26.0}$	$455.4^{+4.6}_{-5.7}$	$413.3^{+9.4}_{-15}$	$366.0^{+29.0}_{-32.0}$	$350.0^{+45.0}_{-32.0}$
A_V	V-band extinction (mag)	$0.766^{+0.041}_{-0.079}$	$0.060^{+0.045}_{-0.041}$	$0.074^{+0.037}_{-0.047}$	$0.071^{+0.031}_{-0.042}$	$0.099^{+0.065}_{-0.066}$
σ_{SED}	SED photometry error scaling	$0.56^{+0.24}_{-0.14}$	$0.81^{+0.32}_{-0.20}$	$0.82^{+0.33}_{-0.20}$	$0.95^{+0.41}_{-0.26}$	$0.75^{+0.27}_{-0.17}$
ϖ	Parallax (mas)	1.486 ± 0.041	4.688 ± 0.043	4.687 ± 0.042	$7.19^{+0.051}_{-0.05}$	8.838 ± 0.062
d	Distance (pc)	$672.0^{+19.0}_{-18.0}$	$213.3^{+2.0}_{-1.9}$	213.3 ± 1.9	$139.08^{+0.98}_{-0.97}$	$113.14^{+0.8}_{-0.78}$
Planetary Parameters:						
P	Period (days)	$2.62669762 \pm 6.6e-07$	$11.6334681 \pm 4.4e-06$	$11.6334681 \pm 4.4e-06$	$2.36902^{+5.8e-05}_{-5.9e-05}$	$6.326768^{+1.5e-0}_{-1.2e-0}$
R_P	Radius (R_J)	$1.643^{+0.058}_{-0.073}$	$0.856^{+0.038}_{-0.036}$	$0.827^{+0.033}_{-0.030}$	$0.1524^{+0.01}_{-0.0072}$	$0.195^{+0.018}_{-0.011}$
M_P	Mass (M_J)	$1.72^{+0.34}_{-0.35}$	$0.194^{+0.024}_{-0.028}$	$0.217^{+0.025}_{-0.029}$	$0.0231^{+0.0045}_{-0.0044}$	$0.0197^{+0.0076}_{-0.0048}$
T_C	Time of conjunction[3] (BJD_{TDB})	$2457820.737343 \pm 6.3e-05$	$2457906.84110^{+0.00028}_{-0.00033}$	$2457906.84108^{+0.00026}_{-0.00029}$	$2456981.6455^{+0.0011}_{-0.001}$	2457221.2291 ± 0.0
T_T	Time of minimum projected separation[4] (BJD_{TDB})	$2457820.737341 \pm 6e-05$	$2457906.84130 \pm 0.00022$	$2457906.84124 \pm 0.00022$	$2456981.64531^{+0.00099}_{-0.00098}$	$2457221.22914^{+0.0}_{-0.0}$
T_0	Optimal conjunction Time[5] (BJD_{TDB})	$2457894.284876^{+6e-05}_{-5.9e-05}$	$2458151.14394^{+0.00027}_{-0.00032}$	$2458151.14392^{+0.00024}_{-0.00027}$	$2457017.18078^{+0.00055}_{-0.00054}$	$2457303.4771 \pm 0.$
a	Semi-major axis (AU)	$0.04392^{+0.00057}_{-0.00063}$	$0.1040^{+0.0013}_{-0.0015}$	0.1086 ± 0.0012	$0.03359^{+0.00062}_{-0.00053}$	$0.0664^{+0.0012}_{-0.0013}$
i	Inclination (Degrees)	$89.18^{+0.58}_{-0.83}$	$88.24^{+1.0}_{-0.67}$	$88.58^{+0.85}_{-0.57}$	$87.01^{+1.8}_{-1.0}$	$86.83^{+1.6}_{-0.96}$
e	Eccentricity	$0.053^{+0.051}_{-0.036}$	$0.331^{+0.063}_{-0.066}$	$0.274^{+0.065}_{-0.061}$	$0.16^{+0.16}_{-0.11}$	$0.52^{+0.24}_{-0.26}$
ω_*	Argument of Periastron (Degrees)	$-72.0^{+74.0}_{-79.0}$	137^{+13}_{-16}	145^{+13}_{-15}	$-57.0^{+52.0}_{-27.0}$	$46.0^{+96.0}_{-120.0}$
T_{eq}	Equilibrium temperature[6] (K)	$2090.0^{+35.0}_{-39.0}$	1058 ± 11	$1036 \pm 10.$	1366.0 ± 17.0	1049.0 ± 15.0
$\tau_{\rm circ}$	Tidal circularization timescale (Gyr)	$0.0381^{+0.011}_{-0.0099}$	$15.8^{+12}_{-7.3}$	33^{+19}_{-14}	$23.0^{+14.0}_{-15.0}$	$31.0^{+210.0}_{-31.0}$
K	RV semi-amplitude (m/s)	$182.0^{+36.0}_{-37.0}$	$17.3^{+2.1}_{-2.5}$	$17.4^{+1.9}_{-2.3}$	$3.87^{+0.77}_{-0.75}$	$2.73^{+1.3}_{-0.75}$
R_P/R_*	Radius of planet in stellar radii	$0.09617^{+0.00024}_{-0.00019}$	$0.05279^{+0.00079}_{-0.00054}$	$0.05274^{+0.00076}_{-0.00049}$	$0.01695^{+0.00095}_{-0.00045}$	$0.02045^{+0.0019}_{-0.0007}$
a/R_*	Semi-major axis in stellar radii	$5.37^{+0.27}_{-0.17}$	13.43 ± 0.58	$14.51^{+0.51}_{-0.47}$	$7.86^{+0.33}_{-0.31}$	$14.68^{+0.64}_{-0.7}$
δ	$(R_P/R_*)^2$	$0.00925^{+4.5e-05}_{-3.7e-05}$	$0.002787^{+8.5e-05}_{-5.6e-05}$	$0.002781^{+8.1e-05}_{-5.6e-05}$	$0.000287^{+3.3e-05}_{-1.5e-05}$	$0.000418^{+7.9e-0}_{-3e-05}$
$Depth_{\rm K2}$	Flux decrement at mid transit for K2	0.01042 ± 0.00011	$0.003571^{+6.7e-05}_{-6.4e-05}$	$0.003553^{+6.5e-05}_{-6.2e-05}$	$0.00035 \pm 1.1e-05$	$0.000482^{+1.7e-0}_{-1.9e-0}$
$Depth_{\rm TESS}$	Flux decrement at mid transit for TESS	0.01007 ± 0.00014	$0.003353 \pm 5.2e-05$	$0.003332 \pm 5.0e-05$	—	$0.000469^{+1.6e-0}_{-1.7e-0}$
τ	Ingress/egress transit duration (days)	$0.015594^{+0.00033}_{-9.5e-05}$	$0.0117^{+0.0016}_{-0.0010}$	$0.01163^{+0.0016}_{-0.00092}$	$0.00198^{+0.0013}_{-0.00037}$	$0.00227^{+0.003}_{-0.0006}$
T_{14}	Total transit duration (days)	$0.17496^{+0.00035}_{-0.00032}$	$0.2138^{+0.0015}_{-0.0011}$	$0.2137^{+0.0014}_{-0.0011}$	$0.0962^{+0.0018}_{-0.0016}$	$0.0819^{+0.0028}_{-0.0023}$
b	Transit Impact parameter	$0.08^{+0.08}_{-0.056}$	$0.30^{+0.14}_{-0.18}$	$0.29^{+0.14}_{-0.18}$	$0.44^{+0.26}_{-0.28}$	$0.53^{+0.28}_{-0.36}$
ρ_P	Density (cgs)	$0.48^{+0.12}_{-0.11}$	$0.381^{+0.078}_{-0.072}$	$0.473^{+0.082}_{-0.079}$	$7.9^{+2.1}_{-1.9}$	$3.18^{+1.2}_{-0.76}$
$loggP$	Surface gravity	$3.199^{+0.085}_{-0.1}$	$2.815^{+0.066}_{-0.080}$	$2.895^{+0.058}_{-0.070}$	$3.385^{+0.09}_{-0.1}$	$3.1^{+0.13}_{-0.11}$
T_S	Time of eclipse (BJD_{TDB})	$2457819.432^{+0.082}_{-0.063}$	$2457910.91^{+0.61}_{-0.62}$	$2457911.04^{+0.51}_{-0.55}$	2456980.58 ± 0.1	$2457218.1 \pm 2.$

Table 2A.6 Median values and 68% confidence intervals for the global models for K2 fits only.

System	K2 Campaign	Wavelength Parameters		Transit Parameters	
		$u_1^\dagger$	$u_2^\ddagger$	$\sigma^{2\star}$	F_0^*
K2-7	C1	0.394 ± 0.054	0.261 ± 0.051	$-0.0000000095^{+0.0000000051}_{-0.0000000045}$	$0.999998^{+0.000018}_{-0.000019}$
K2-54	C3	0.44 ± 0.17	$0.24^{+0.17}_{-0.18}$	$0.0000000087^{+0.000000011}_{-0.0000000097}$	1.000000 ± 0.000029
K2-57	C3	0.677 ± 0.054	$0.076^{+0.053}_{-0.054}$	$0.000000001^{+0.000000013}_{-0.000000010}$	1.000021 ± 0.000031
K2-147	C7	$0.28^{+0.17}_{-0.15}$	0.35 ± 0.18	$0.0000000111^{+0.0000000033}_{-0.0000000030}$	$1.0000077^{+0.000010}_{-0.0000100}$
K2-181	C5	$0.480^{+0.042}_{-0.041}$	0.217 ± 0.038	$0.0000000110^{+0.0000000027}_{-0.0000000024}$	$0.999996^{+0.000012}_{-0.000011}$
	C18	$0.480^{+0.042}_{-0.041}$	0.217 ± 0.038	$0.0000000020^{+0.0000000025}_{-0.0000000022}$	1.000010 ± 0.000012
K2-203	C8	0.561 ± 0.054	0.158 ± 0.052	$0.0000000038^{+0.0000000017}_{-0.0000000015}$	0.999997 ± 0.000010
K2-204	C8	$0.372^{+0.055}_{-0.054}$	$0.253^{+0.051}_{-0.052}$	$0.0000000095^{+0.0000000033}_{-0.0000000030}$	0.999995 ± 0.000012
K2-208	C8	0.447 ± 0.055	$0.237^{+0.051}_{-0.053}$	$0.00000000067^{+0.00000000100}_{-0.00000000091}$	$0.9999965^{+0.0000069}_{-0.0000070}$
K2-211	C8	0.548 ± 0.055	0.166 ± 0.052	$0.0000000056 \pm 0.0000000012$	$1.0000020^{+0.0000057}_{-0.0000056}$
K2-225	C10	0.468 ± 0.058	0.210 ± 0.054	$0.0000000029^{+0.0000000014}_{-0.0000000012}$	1.000031 ± 0.000011
K2-226	C10	$0.492^{+0.056}_{-0.055}$	0.203 ± 0.053	$0.0000000019^{+0.0000000013}_{-0.0000000012}$	1.0000034 ± 0.0000081
K2-250	C10	0.576 ± 0.058	0.157 ± 0.054	$0.0000000115^{+0.0000000063}_{-0.0000000057}$	1.000006 ± 0.000015
K2-265	C3	0.466 ± 0.054	0.215 ± 0.052	$-0.00000000033^{+0.00000000015}_{-0.00000000014}$	0.9999979 ± 0.0000025

Notes. †Linear limb-darkening coefficient. ‡Quadratic limb-darkening coefficient. *Added variance. * Baseline flux.

System	Campaign/Sector	Wavelength Parameters		Transit Parameters		Dilution
		$u_1^\dagger$	$u_2^\ddagger$	$\sigma^{2\star}$	F_0^*	A_D
K2-77	K2 C4	0.506 ± 0.059	0.151 ± 0.055	$0.0000000036^{+0.0000000016}_{-0.0000000013}$	1.000009 ± 0.000010	
	TESS S5	$0.411^{+0.034}_{-0.035}$	0.218 ± 0.029	$0.000000178^{+0.000000050}_{-0.000000049}$	0.999994 ± 0.000016	0.00000 ± 0.00024
	TESS S42			$0.000000028^{+0.000000059}_{-0.000000058}$	1.000003 ± 0.000019	
	TESS S43			$0.000000118^{+0.000000054}_{-0.000000053}$	1.000007 ± 0.000017	
	TESS S44			$-0.000000085^{+0.000000050}_{-0.000000049}$	1.000012 ± 0.000017	
K2-97	K2 C5	$0.652^{+0.040}_{-0.041}$	0.098 ± 0.039	$0.0000000070^{+0.0000000031}_{-0.0000000028}$	0.999995 ± 0.000011	
	K2 C18			$0.0000000149^{+0.0000000048}_{-0.0000000043}$	0.999996 ± 0.000014	
	TESS S7	0.488 ± 0.029	0.181 ± 0.026	$0.000000159^{+0.000000070}_{-0.000000069}$	1.000000 ± 0.000020	-0.27 ± 0.12
	TESS S44			$0.000000244^{+0.000000083}_{-0.000000082}$	1.000001 ± 0.000022	
	TESS S45			$-0.000000001^{+0.000000084}_{-0.000000083}$	0.999988 ± 0.000022	
	TESS S46			$0.000000148^{+0.000000072}_{-0.000000070}$	1.000008 ± 0.000020	
K2-98	K2 C5	$0.325^{+0.037}_{-0.036}$	0.305 ± 0.036	$0.0000000017^{+0.0000000012}_{-0.0000000010}$	$1.0000098^{+0.0000075}_{-0.0000074}$	
	K2 C18			$0.0000000044^{+0.0000000020}_{-0.0000000018}$	0.999991 ± 0.000010	
	TESS S7	$0.235^{+0.028}_{-0.027}$	0.304 ± 0.023	$-0.00000003^{+0.00000031}_{-0.00000029}$	1.000088 ± 0.000085	-0.0000 ± 0.0019
	TESS S34			$0.00000057^{+0.00000045}_{-0.00000042}$	1.00015 ± 0.00010	
	TESS S44			$0.00000017^{+0.00000033}_{-0.00000031}$	$0.999879^{+0.000088}_{-0.000087}$	
	TESS S45			$0.00000045^{+0.00000033}_{-0.00000031}$	$0.999931^{+0.000086}_{-0.000085}$	
	TESS S46			$0.00000059^{+0.00000030}_{-0.00000028}$	1.000249 ± 0.000079	
K2-114	K2 C5	$0.611^{+0.025}_{-0.026}$	$0.106^{+0.036}_{-0.035}$	$0.000000012^{+0.000000018}_{-0.000000016}$	1.000034 ± 0.000032	
	K2 C18			$0.00000082 \pm 0.00000013$	$0.999745^{+0.000044}_{-0.000043}$	
	TESS S7	0.473 ± 0.026	$0.189^{+0.026}_{-0.025}$	$-0.0000060^{+0.0000062}_{-0.0000058}$	$0.99980^{+0.00042}_{-0.00043}$	$-0.027^{+0.034}_{-0.035}$
	TESS S44			$-0.0000000^{+0.0000076}_{-0.0000071}$	0.99925 ± 0.00047	
	TESS S45			$0.0000153^{+0.0000093}_{-0.0000088}$	0.99999 ± 0.00051	
	TESS S46			$-0.0000077^{+0.0000068}_{-0.0000064}$	0.99941 ± 0.00044	
K2-115	K2 C5	0.365 ± 0.035	0.278 ± 0.036	$0.0000000117^{+0.0000000070}_{-0.0000000058}$	0.999993 ± 0.000023	
	K2 C18			$0.000000028^{+0.000000016}_{-0.000000013}$	0.999966 ± 0.000037	
	TESS S7	0.274 ± 0.032	0.285 ± 0.026	$0.0000013^{+0.0000015}_{-0.0000014}$	1.00008 ± 0.00018	-0.000000 ± 0.000014
	TESS S34			$0.0000033^{+0.0000033}_{-0.0000030}$	0.99972 ± 0.00034	
	TESS S45			$-0.0000020^{+0.0000016}_{-0.0000015}$	$0.99999^{+0.00020}_{-0.00021}$	
	TESS S46			$-0.0000024^{+0.0000020}_{-0.0000018}$	0.99930 ± 0.00027	
K2-167	K2 C3	0.320 ± 0.050	0.314 ± 0.050	$-0.000000000008^{+0.000000000022}_{-0.000000000018}$	0.9999986 ± 0.0000041	
	TESS S2	0.224 ± 0.031	0.300 ± 0.029	$0.0000000005^{+0.0000000047}_{-0.0000000044}$	0.999982 ± 0.000011	0.000000 ± 0.000027
	TESS S28			$-0.0000015010^{+0.0000000039}_{-0.0000000019}$	$1.000031^{+0.000038}_{-0.000032}$	
	TESS S42			$0.000000017^{+0.000000012}_{-0.000000010}$	1.000000 ± 0.000021	
K2-180	K2 C5	$0.416^{+0.042}_{-0.041}$	$0.253^{+0.038}_{-0.039}$	$0.0000000016^{+0.0000000029}_{-0.0000000025}$	0.999998 ± 0.000013	
	K2 C18			$0.0000000196^{+0.0000000070}_{-0.0000000059}$	1.000017 ± 0.000021	
	TESS S7	$0.323^{+0.030}_{-0.029}$	$0.268^{+0.24}_{-0.025}$	$0.00000007^{+0.00000031}_{-0.00000022}$	0.99953 ± 0.00019	-0.012 ± 0.039
	TESS S34			$0.0000011^{+0.0000011}_{-0.0000010}$	1.00028 ± 0.00016	
	TESS S44			$0.00000045^{+0.0000011}_{-0.00000097}$	0.99981 ± 0.00016	
	TESS S45			$0.00000168^{+0.00000081}_{-0.00000077}$	0.99983 ± 0.00014	
	TESS S46			$-0.00000158^{+0.00000069}_{-0.00000064}$	0.99985 ± 0.00013	
K2-182	K2 C5	0.528 ± 0.035	0.167 ± 0.038	$0.00000000092^{+0.00000000059}_{-0.00000000053}$	$0.9999964^{+0.0000051}_{-0.0000050}$	
	K2 C18			$0.00000000107^{+0.00000000095}_{-0.00000000085}$	1.0000071 ± 0.0000067	
	TESS S7	0.416 ± 0.027	0.219 ± 0.024	$-0.000000031^{+0.000000039}_{-0.000000031}$	1.000089 ± 0.000052	-0.00000 ± 0.00029
	TESS S34			$0.00000022^{+0.00000019}_{-0.00000018}$	$1.000116^{+0.000059}_{-0.000058}$	
	TESS S44			$0.00000002^{+0.00000019}_{-0.00000018}$	0.999984 ± 0.000065	
	TESS S45			$0.00000027^{+0.00000020}_{-0.00000019}$	1.000113 ± 0.000067	
	TESS S46			$0.00000009^{+0.00000018}_{-0.00000017}$	0.999995 ± 0.000063	
K2-237	K2 C11-1	$0.337^{+0.014}_{-0.015}$	0.250 ± 0.034	$0.0000000056^{+0.0000000021}_{-0.0000000018}$	$1.0000000^{+0.0000096}_{-0.0000097}$	$0.006^{+0.039}_{-0.040}$
	K2 C11-2			$0.00000000385^{+0.0000000010}_{-0.00000000092}$	0.9999947 ± 0.0000062	
	TESS S12	0.266 ± 0.033	0.305 ± 0.035	0.0000217 ± 0.0000013	1.00025 ± 0.00015	$-0.050^{+0.042}_{-0.043}$
	TESS S39			$0.0001052^{+0.0000031}_{-0.0000030}$	1.00057 ± 0.00014	
K2-260	K2 C13	0.228 ± 0.017	0.323 ± 0.037	$0.0000000061^{+0.0000000012}_{-0.0000000011}$	$0.9999861^{+0.0000058}_{-0.0000059}$	
	TESS S5	0.164 ± 0.026	0.321 ± 0.028	$-0.00000027^{+0.00000012}_{-0.00000011}$	$1.000021^{+0.000072}_{-0.000073}$	0.027 ± 0.011
	TESS S32			$0.00000086^{+0.00000051}_{-0.00000049}$	$1.000154^{+0.000082}_{-0.000083}$	
	TESS S43			$-0.00000027^{+0.00000036}_{-0.00000035}$	$0.999843^{+0.000072}_{-0.000073}$	
K2-261	K2 C14	0.474 ± 0.031	0.208 ± 0.046	$0.00000000157^{+0.00000000065}_{-0.00000000057}$	0.9999974 ± 0.0000059	
	TESS S9	0.363 ± 0.027	0.257 ± 0.027	$0.000000106^{+0.000000050}_{-0.000000047}$	1.000048 ± 0.000034	0.0002 ± 0.0021
	TESS S35			$0.00000388^{+0.00000018}_{-0.00000017}$	1.000253 ± 0.000041	
	TESS S45			$0.000000017^{+0.000000054}_{-0.000000051}$	0.999950 ± 0.000035	
	TESS S46			$0.000000004^{+0.000000050}_{-0.000000046}$	1.000102 ± 0.000034	
K2-277	K2 C6	$0.419^{+0.055}_{-0.054}$	0.250 ± 0.052	$0.00000000110^{+0.00000000033}_{-0.00000000028}$	$0.9999913^{+0.0000046}_{-0.0000045}$	
	TESS S10	0.322 ± 0.040	$0.270^{+0.036}_{-0.037}$	$-0.000000010^{+0.000000044}_{-0.000000041}$	1.000020 ± 0.000034	-0.0000 ± 0.0021
	TESS S37			$0.000000024^{+0.000000012}_{-0.000000011}$	1.0000220 ± 0.0000080	
K2-321	K2 C14	$0.41^{+0.16}_{-0.17}$	$0.33^{+0.17}_{-0.18}$	$0.0000000045^{+0.0000000025}_{-0.0000000023}$	1.000003 ± 0.000010	
	TESS S8	0.38 ± 0.17	$0.30^{+0.17}_{-0.18}$	$0.00000023 \pm 0.00000012$	1.000003 ± 0.000028	0.0001 ± 0.0037
	TESS S35			$-0.000000009^{+0.000000044}_{-0.000000042}$	0.999998 ± 0.000025	

Table 2A.7 Median values and 68% confidence intervals for the radial velocity parameters.

K2-97					
Telescope Parameters:		HIRES	LEVY		
$\gamma_{\rm rel}$.	Relative RV Offset (m/s).	-5.2 ± 1.6	12^{+16}_{-19}		
σ_J .	RV Jitter (m/s).....	$5.8^{+1.6}_{-1.2}$	26^{+35}_{-27}		
σ_J^2 .	RV Jitter Variance	33^{+21}_{-12}	720^{+3100}_{-900}		
K2-98					
Telescope Parameters:		FIES	HARPS	HARPS-N	
$\gamma_{\rm rel}$.	Relative RV Offset (m/s).	$76612.0^{+4.5}_{-4.3}$	76747.7 ± 3.3	76740.8 ± 4.0	
σ_J .	RV Jitter (m/s).....	$7.03^{+0.94}_{-2.2}$	$1.55^{+0.12}_{-0.43}$	$0.00^{+1.6}_{-0.00}$	
σ_J^2 .	RV Jitter Variance	5^{+58}_{-41}	$0.1^{+2.7}_{-2.8}$	$-0.1^{+2.8}_{-2.7}$	
K2-114					
Telescope Parameters:		HIRES			
$\gamma_{\rm rel}$.	Relative RV Offset (m/s).	$-40.8^{+6.7}_{-6.8}$			
σ_J .	RV Jitter (m/s).....	$11.9^{+3.8}_{-4.9}$			
σ_J^2 .	RV Jitter Variance	141^{+100}_{-93}			
K2-115					
Telescope Parameters:		HIRES			
$\gamma_{\rm rel}$.	Relative RV Offset (m/s).	25^{+12}_{-13}			
σ_J .	RV Jitter (m/s).....	26^{+21}_{-10}			
σ_J^2 .	RV Jitter Variance	710^{+1600}_{-440}			
K2-180					
Telescope Parameters:		HARPS-N			
$\gamma_{\rm rel}$.	Relative RV Offset (m/s).	$-76614.40^{+0.58}_{-0.62}$			
σ_J .	RV Jitter (m/s).....	0.00			
σ_J^2 .	RV Jitter Variance	$-3.6^{+3.2}_{-1.0}$			
K2-182					
Telescope Parameters:		HIRES			
$\gamma_{\rm rel}$.	Relative RV Offset[4] (m/s)	-1.8 ± 1.6			
σ_J .	RV Jitter (m/s).....	$4.6^{+1.9}_{-1.2}$			
σ_J^2 .	RV Jitter Variance	$21.6^{+21}_{-9.8}$			
K2-237					
Telescope Parameters:		CORALIE	FIES	HARPS (Smith)	HARPS (Soto)
$\gamma_{\rm rel}$.	Relative RV Offset (m/s).	-22252 ± 40	-22507^{+15}_{-16}	$-22325.7^{+9.0}_{-9.4}$	-22252 ± 14
σ_J .	RV Jitter (m/s).....	110^{+49}_{-31}	$0.00^{+39}_{-0.00}$	18^{+22}_{-16}	$6.0^{+8.8}_{-6.0}$
σ_J^2 .	RV Jitter Variance	12200^{+13000}_{-5800}	-70^{+1600}_{-520}	340^{+1300}_{-330}	40^{+180}_{-220}
K2-260					
Telescope Parameters:		FIES			
$\gamma_{\rm rel}$.	Relative RV Offset (m/s).	29072^{+22}_{-24}			
σ_J .	RV Jitter (m/s).....	$0.00^{+60}_{-0.00}$			
σ_J^2 .	RV Jitter Variance	-600^{+4200}_{-2000}			
K2-261					
Telescope Parameters:		FIES	HARPS	HARPS-N	
$\gamma_{\rm rel}$.	Relative RV Offset (m/s).	$-13.5^{+2.7}_{-2.8}$	$3340.2^{+2.3}_{-2.4}$	$3335.3^{+2.1}_{-2.6}$	
σ_J .	RV Jitter (m/s).....	$4.6^{+4.0}_{-4.6}$	$6.6^{+2.7}_{-1.8}$	$5.6^{+4.2}_{-2.4}$	
σ_J^2 .	RV Jitter Variance	20^{+53}_{-25}	43^{+43}_{-20}	31^{+64}_{-21}	
K2-265					
Telescope Parameters:		HARPS			
$\gamma_{\rm rel}$.	Relative RV Offset (m/s).	$-18185.56^{+0.52}_{-0.53}$			
σ_J .	RV Jitter (m/s).....	$5.71^{+0.43}_{-0.39}$			
σ_J^2 .	RV Jitter Variance	$32.6^{+5.1}_{-4.3}$			

Notes. σ_J^2 was bound to ±300 m/s for K2-114 and the Soto et al. (2018) RVs for K2-237. For K2-98 σ_J^2 was bound to ±100 m/s for the FIES RVs and ±4 m/s for HARPS and HARPS-N. See §2.3.3 for discussion.

CHAPTER 3

K2-2

This section reviews the published work Thygesen et al. (2024).

3.1 Abstract

K2-2 b/HIP 116454 b, the first exoplanet discovery by K2 during its Two-Wheeled Concept Engineering Test, is a sub-Neptune (2.5 ± 0.1 $R_\oplus$, 9.7 ± 1.2 $M_\oplus$) orbiting a relatively bright (K_S = 8.03) K-dwarf on a 9.1 day period. Unfortunately, due to a spurious follow-up transit detection and ephemeris degradation, the transit ephemeris for this planet was lost. In this work, we recover and refine the transit ephemeris for K2-2 b, showing a $\sim 40\sigma$ discrepancy from the discovery results. To accurately measure the transit ephemeris and update the parameters of the system, we jointly fit space-based photometric observations from NASA's K2, TESS, and Spitzer missions with new photometric observations from the ground, as well as radial velocities from HARPS-N that are corrected for stellar activity using a new modeling technique. Ephemerides becoming lost or significantly degraded, as is the case for most transiting planets, highlights the importance of systematically updating transit ephemerides with upcoming large efforts expected to characterize hundreds of exoplanet atmospheres. K2-2 b sits at the high-mass peak of the known radius valley for sub-Neptunes, and is now well-suited for transmission spectroscopy with current and future facilities. Our updated transit ephemeris will ensure no more than a 13-minute uncertainty through 2030.

3.2 Introduction

In the era of cutting-edge atmospheric characterization of transiting exoplanets, precise and accurate ephemerides are crucial for efficiently scheduling these expensive observations. However, over 80% of transiting exoplanets will have uncertainties on their future transit times greater than 30 minutes by the end of the decade (see Thygesen et al. 2023), rendering these systems extremely challenging to observe with JWST (Gardner et al., 2006; Beichman et al., 2020), major upcoming facilities such as the Atmospheric Remote-sensing Infrared Exoplanet Large-survey (ARIEL; Tinetti et al. 2018, 2021), and 30m class telescopes like the Thirty Meter Telescope (TMT; Sanders 2013),

Giant Magellan Telescope (Johns et al., 2012), and the 39 m European Southern Observatory Extremely Large Telescope (ELT; Udry et al. 2014). This problem can be solved by observing new transits of these planets with current facilities. Fortunately, NASA's Transiting Exoplanet Survey Satellite (TESS) mission (Ricker et al., 2015) is observing the entire sky, providing a valuable opportunity to refine the transit ephemeris for most known planets.

After a successful 4-year nominal mission, discovering thousands of exoplanets, the Kepler mission (Borucki et al., 2010) was repurposed due to a mechanical issue. Using the solar pressure to stabilize pointing of the Kepler spacecraft, the K2 mission was able to survey the ecliptic plane, finding hundreds of exciting new systems that are well-suited for detailed characterization (Howell et al., 2012; Vanderburg et al., 2016; Zink et al., 2021; Kruse et al., 2019; Pope et al., 2016; Livingston et al., 2018a; Crossfield et al., 2016; Dattilo et al., 2019). The K2 mission ended in 2019, with many of its newly-detected planets never being reobserved since their discovery campaign(s). The K2 & TESS Synergy project is an effort to provide the community with updated and accurate transit times and system parameters for exoplanets originally discovered by the K2 mission that have been recently observed by TESS (Ricker et al., 2015). Following a successful pilot study (Ikwut-Ukwa et al., 2020), the second paper in this series revisited 26 K2 single-planet systems that TESS reobserved during its prime mission (Thygesen et al., 2023). This work improved the average ephemeris uncertainties by multiple orders of magnitude due to the addition of new TESS transits. Additionally, we identified systems where the original ephemeris has been completely lost (See K2-260; Thygesen et al. 2023), which is similar to this work on K2-2 b, K2's first exoplanet discovery.

K2-2 b was identified during the Two-Wheeled Concept Engineering Test (campaign 0) of the K2 mission. K2-2 b is a sub-Neptune ($2.5 \pm 0.1\ R_\oplus$, $9.7 \pm 1.2\ M_\oplus$) on a 9.1-day orbit around a bright ($V = 10.2$, $J = 8.6$, HIP 116454) K-dwarf (Vanderburg et al., 2015). At discovery, a single clear transit was detected in the K2 observations, along with a marginal ($\sim 3\sigma$) detection from the Microvariablity and Oscillations of Stars (MOST) Space Telescope (Walker et al., 2003). Follow-up observations were scheduled with Spitzer (P.I. Werner, AOR 57185280) and the Hubble

Space Telescope (P.I. Bourrier, proposal I.D. 15127), however, the transit was not seen during the predicted window from the discovery ephemeris. It was then determined that the MOST transit was likely not a real transit of K2-2 b, having skewed the period enough to cause subsequent transits to be missed.

In this work, we combine the discovery observations from Vanderburg et al. (2015) with new observations from NASA's TESS mission, follow up ground-based photometry, and improved radial velocities to accurately measure the ephemeris of K2-2 b for the first time, proving the original detection from MOST to be a false positive. In Section 3.3 we describe the observations used and the relevant reduction and analysis methods, including the reanalysis of radial velocities from the High Accuracy Radial Velocity Planet Searcher-North (HARPS-N; Cosentino et al. (2012)) on the 3.58m Telescopio Nazionale Galileo at the Roque de los Muchachos Observatory. Section 3.4 outlines the methodology used in running the `EXOFASTv2` global fit of all observations and archival information. We present our results and discuss the importance of ephemeris refinement in the context of future characterization of K2-2 b in Section 3.5.

3.3 Observations and Archival Data

The discovery analysis for K2-2 b included a 47 day long light curve from MOST (Walker et al., 2003), which was thought to contain a marginal $\sim 3\sigma$ detection of the transit, but future follow up attempts to reobserve the transit with Spitzer and HST showed no transit during or near the predicted window. This ultimately led to the idea that the MOST observations were not reliably constraining the transit ephemeris. While it is not clear why this happened, it is possible that Gaussian noise or satellite systematics caused an already marginal detection to be anchored to a different time of transit. Our new observations from MEarth, ULMT, Spitzer and TESS (Figure 3.1) confirm this hypothesis. In the near decade since its discovery, a variety of follow up observations have been conducted to better characterize the K2-2 system and to recover the transit ephemeris. In the following sections, we describe the new and archival observations used in our analysis. The magnitudes and literature values for K2-2 are listed in Table 3.1, and the photometric data sets we used are outlined in Table 3.2.

3.3.1 Ground-based archival imaging

At the discovery of of K2-2 b, Vanderburg et al. (2015) used multiple archival from the National Geographic Society–Palomar Observatory Sky Survey (POSS-I, van Leeuwen 2007) and Sloan Digital Sky Survey (SDSS, Abazajian et al. 2009), and newly acquired images from Robo-AO on Palomar (Baranec et al., 2014; Law et al., 2014) and Natural Guide Star Adaptive Optics (NGSAO) system on Keck to rule out nearby close companions that might be contaminating the K2 aperture. A nearby white dwarf with a separation of around 8″ was identified to share a similar proper motion to K2-2, suggesting that they exist in a gravitationally bound system (this is discussed more in Section 3.5.2). The white dwarf is within the K2 aperture, but is 6-7 magnitudes dimmer than K2-2, which would not affect the final transit depth of K2-2 b. No other nearby companions were found to a 7σ significance in the H band to the limits of 3.0 mag at 0″.1 separation, 9.2 mag at 1″.0 and 12.7 mag at 5″.0.

3.3.2 K2 Photometry

A single transit of K2-2 b was observed at 30-minute cadence during the Kepler Two-Wheel Concept Engineering Test during February 2014. Due to the loss of two of the four reaction wheels on the spacecraft, significant systematics were introduced to the light curves of the K2 mission. We corrected for these using the methods described in Vanderburg & Johnson (2014) and Vanderburg et al. (2016), which utilize a series of 20 apertures to extract raw light curves used to perform the corrections. Short timescale variations in each of these light curves are correlated with the roll angle of the spacecraft, with the latter being subtracted from the light curves. This process is repeated iteratively until the light curve is free of any variations associated with the roll of the spacecraft. The most precise light curve out of the 20 following the corrections is selected for final analysis. We performed further corrections by fitting the transit and correcting for the systematics and any low-frequency stellar variability, prior to the global fit.

3.3.3 MEarth

MEarth was used to initially recover the transit of K2-2 b and constrain the ephemeris, observing multiple partial and full transits. MEarth consists of 16 separate 0.4 m telescopes using

custom 715 nm longpass filters designed to find Earth-sized planets around M dwarfs (Nutzman & Charbonneau, 2008; Irwin et al., 2015). Telescopes 1-8 are a part of the MEarth-North Observatory at Fred Lawrence Whipple Observatory (FLWO) on Mount Hopkins, Arizona, while the other eight telescopes (numbered as 11-18) are part of the MEarth-South Observatory located at Cerro Tololo Inter-American Observatory (CTIO) on Cerro Tololo, Chile. K2-2 was observed using a subset of four telescopes from each observatory (see Table 3.2) with 1 minute cadence on UT 2016 September 21 and 30, and UT 2016 October 09. Light curves from MEarth are automatically extracted through a pipeline (see Irwin et al. 2007; Berta et al. 2011) that calibrates the images using flat fields, dark current frames and bias exposures. We combined the light curves across multiple nights for each telescope, so within the global fit the variance can be determined independently for each instrument. We sliced the light curves such that we only included one full transit duration before and after the transit, and detrended against airmass in the global fit. While the original observations also included telescopes 4, 5 and 8, we did not use these in our analysis as the light curves did not contain full transits and would not contribute significant value to the global fit. The transit was also missed during the night of UT 2016 September 11 due to the incorrect ephemeris.

These observations were the first use of the defocus observing mode of MEarth for transit follow-up, and served as the prototype for a large number of observations of TESS objects of interest done in later years. Here we describe the modifications made to the system to implement this mode. Prior to implementation of defocus, MEarth observations of bright stars were limited by scintillation noise due to the short maximum exposure times possible before detector saturation, combined with high overheads (approximately 15s, most of which was consumed by CCD readout and download over USB2 connection to the host computer), resulting in a low duty cycle. For scintillation limited observations of events of fixed duration such as transits, the overall transit-averaged photometric noise is determined by the duty cycle (e.g. Young 1967) so the goal of implementing defocus was to improve this by substantially lengthening the exposure times possible before saturation.

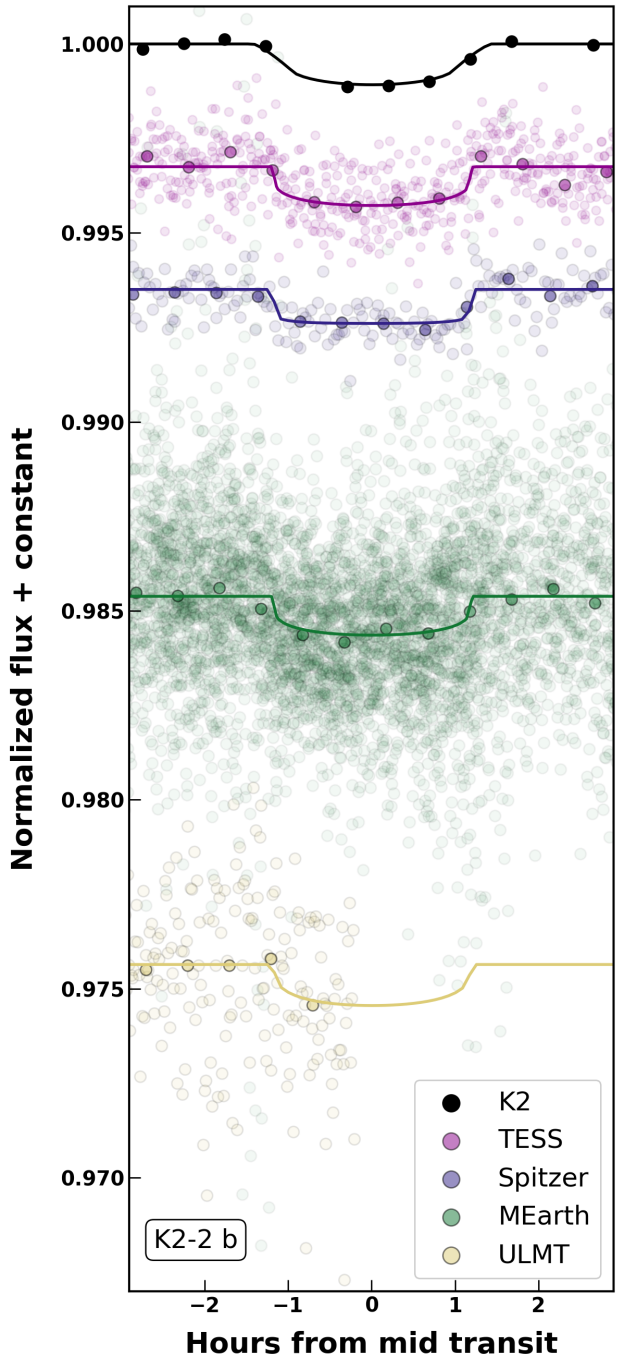

Figure 3.1 The discovery and follow up phase-folded transits of K2-2 b used in the EXOFASTv2 (see Section 3.4) analysis. The observations from K2 (black), TESS (purple), Spitzer (blue), MEarth (green), and ULMT (yellow) are shown in open colored circles with the solid colored line representing the EXOFASTv2 model for that dataset. The closed colored circles represent 30-minute bins. East transit is offset by a constant for clarity.

The scheduling and telescope control software were modified to allow each observation request to specify defocus as half flux diameter (HFD), in pixels. For these first observations of K2-2, we used HFD = 6.0 pixels, where the pixel scales are 0.76 arcsec/pix for MEarth-North and 0.84 arcsec/pix for MEarth-South. The telescope focus was offset by the scheduler prior to commencing observations of each target by the appropriate number of focus encoder counts, where the scaling factor was determined from the calibration curve of HFD versus focus encoder counts used by the standard automatic focus routine (normally used for focusing the telescope at the start of the night).

MEarth did not have autoguiders, and guiding to stabilize the target star position on the detector (vital for precise transit work) had to be done using the science exposures themselves, which were 36s for K2-2. The standard MEarth target acquisition and guiding system for normal in-focus images consisted of astrometric analysis of the images after readout to determine their center in celestial coordinates, followed by offsetting of the telescope to center the target based on its calculated position. Target acquisition was done by applying the full offset, and guiding by passing these measurements into a standard proportional-integral-derivative (PID) control loop with an overall gain less than unity to provide damping and avoid overshoot and oscillation during guiding.

To implement the defocus observing mode, the image analysis part of this astrometric routine was replaced with a custom source detection routine using a standard matched filter approach (e.g. Irwin 1985), where in the case of defocused images, rather than using a standard approximately Gaussian filter kernel, the filter kernel was instead a model of the defocused telescope PSF. This technique is appropriate for analysis of images with mild amounts of defocus, such as needed on MEarth. Previous work (e.g. McCormac et al. 2013) has usually concentrated on the case of severe defocus, where different analysis techniques are needed.

The PSF model was constructed by approximating the telescope entrance pupil as a circular annulus, and introducing defocus by setting the complex phase of this function to a multiple of the Z_2^0 Zernike mode. The resulting PSF was computed by taking the inverse Fourier transform of this function. In practice, it was also convolved by a Moffat profile (Moffat, 1969) with parameters chosen based on standard in-focus MEarth observations to approximate seeing and any effects other

than diffraction that contribute to the system's normal in-focus PSF spot size. The relationship between the Z_2^0 Zernike coefficient and HFD was determined empirically.

The PSF model was also used to compute exposure times and set photometric aperture radii for the automatic extraction pipeline. We found that these theoretical estimates of exposure times based on the idealised PSF models were rather optimistic, and in practice it was necessary to use shorter exposures (or equivalently, somewhat more defocus for a given desired exposure time) to avoid the risk of saturation due to non-uniformity of the resulting defocused star image. This can be caused by atmospheric turbulence (particularly in short exposures), but also other optical aberrations affecting the defocused star image, such as coma, which causes an asymmetric distribution of brightness around the resulting ring shaped PSF, and can cause one side of the ring to become too bright. Being remotely operated robotic telescopes, it was not always possible to maintain optimal collimation of the MEarth telescope optics, and while this had minimal effect on the normal in-focus images used for the majority of the survey, it did noticeably affect the defocused PSFs.

With an appropriate detection threshold, this source detection procedure was found to produce quite robust results, albeit at reduced sensitivity to faint sources, and with a practical upper limit to the defocus HFD of approximately 15 pixels. Given the field of view of the MEarth telescopes of approximately 27x27 arcmin the number of detected sources was found to still be sufficient for accurate multi-star guiding using the astrometric solutions on nearly all of the targets observed over several years of observations, including hundreds of TESS objects of interest.

3.3.4 ULMT

Once the ephemeris was refined from the MEarth observations, an ingress of K2-2 b was observed using the University of Louisville Manner Telescope (ULMT; formerly MVRC) at the Mt. Lemmon summit of Steward Observatory, Arizona. The observation was made in the r' band with 50 second exposure time on UT 2016 October 10. The setup used for the observation included a 0.6 m f/8 RC Optical Systems Ritchey–Chrétien telescope and SBIG STX-16803 CCD camera with a 4k×4k array of 9 μm pixels, which yielded a 26.6' × 26.6' field of view and 0.39 pixel-1 plate scale. The images were calibrated and photometric data were extracted using

Table 3.1 Literature values for K2-2.

Other Identifiers		
TIC 422618449		
2MASS J23354927+0026436		
EPIC 60021410		
WISE J233549.11+002641.9		
Parameter	Description	Value
$\alpha_{\rm J2000}$	Right ascension (R.A.)	23:35:49.29
$\delta_{\rm J2000}$	Declination (Dec.)	00:26:43.84
G	Gaia EDR3 G mag	9.932 ± 0.020
$G_{\rm Bp}$	Gaia EDR3 B_P mag	10.393 ± 0.020
$G_{\rm Rp}$	Gaia EDR3 R_P mag	9.317 ± 0.020
T	*TESS* mag	9.374 ± 0.006
J	2MASS J mag	8.604 ± 0.021
H	2MASS H mag	8.140 ± 0.033
K_S	2MASS K_S mag	8.029 ± 0.021
WISE1	WISE1 mag	7.996 ± 0.030
WISE2	WISE2 mag	8.078 ± 0.030
WISE3	WISE3 mag	8.019 ± 0.030
WISE4	WISE4 mag	7.878 ± 0.199
μ_α	Gaia p.m. in R.A.	-232.90 ± 0.019
μ_δ	Gaia p.m. in Dec.	-187.± 0.017
π	Gaia parallax (mas)	16.004 ± 0.046

Notes. The uncertainties of the photometry have a systematic error floor applied. Proper motions taken from the Gaia EDR3 archive and are in J2016. Parallaxes from Gaia EDR3 have a correction applied according to Lindegren et al. (2021).

`AstroImageJ` (Collins et al., 2017), and the light curves were detrended against airmass in the global fit.

3.3.5 Spitzer

With the ephemeris more precisely constrained from the MEarth and ULMT transits, Spitzer was used to observe a single transit of K2-2 b on UT 2017 April 1 (P.I. M. Werner, observing program 13052, AOR 62428416; Werner et al., 2016). The observation was 10.5 hours long, and was taken with the InfraRed Array Camera (IRAC; Fazio et al. 2004) channel 2 (4.5 μm) with a 2-second exposure time. We used the technique described in Livingston et al. (2018c) to extract

the light curve. In brief, we extracted an optimal light curve by selecting the photometric aperture that minimized both white and red noise, and then corrected for systematics using pixel-level decorrelation (PLD; Deming et al. 2015).

As Spitzer can have correlated noise due to spacecraft systematics, we scaled the per point errors so that we did not underestimate the uncertainties. We followed the procedure from Winn et al. (2008), where a scaling factor, β, is applied to the measured standard deviation to account for time-correlated noise. We first calculated the out-of-transit standard deviation for the unbinned data, σ_1 (for this calculation we conservatively defined out-of-transit as being outside of a full transit duration centered at the transit midpoint). We then binned the out-of-transit data points to a series of 10 temporal bin widths ranging from 4.2 minutes to 8.8 minutes, increasing in equal steps of 0.46 minutes. The limits on the bin widths correspond to the 1σ range of the ingress/egress duration based on a preliminary fit using K2 and TESS light curves.

We then calculated the standard deviation for each set of binned data. In general, this should be equivalent to $\sigma_N = \sigma_1/\sqrt{N} \times \sqrt{M/(M-1)}$, where M is number of bins and N is data points per bin, if there is no time-correlated noise. However, the measured σ_N can be larger than the expected value (by the factor β). We calculated this factor for each bin width, then used the mean value across all widths as the final value for β. Finally, we scaled the original unbinned, out-of-transit error bars by the factor $\beta = 1.19$, which is used as the per point uncertainty in our global fit.

3.3.6 TESS Photometry

A single transit was observed by the Transiting Exoplanet Survey Satellite (TESS) in each of Sectors 42 and 70. We used the 120 second cadence lightcurves in our global fits. We retrieved the light curve through the Python package *Lightkurve* (Lightkurve Collaboration et al., 2018), selecting the light curve processed through the Science Processing Operations Center (SPOC) pipeline at the NASA Ames Research Center (Jenkins et al., 2016), which corrects for various systematics and identifies transits. The light curves were created from the Pre-search Data Conditioned Simple Aperture Photometry (PDCSAP) flux, which uses the optimal TESS aperture to extract the flux and corrects the target for systematics using the PDC module (Stumpe et al., 2012, 2014; Smith et al.,

Table 3.2 Photometry used in this analysis.

Observatory	Date	Filter	Cadence
K2	February 6 2014	*Kepler*	30 min
MEarth South	September 21 2016	i'	1 min
MEarth South, North	September 30 2016	i'	1 min
MEarth North	October 9 2016	i'	1 min
ULMT	October 10 2016	r'	50 sec
Spitzer	April 1 2017	4.5μm	2 sec
TESS	August 21 2021	*TESS*	2 min
TESS	September 21 2023	*TESS*	2 min

Notes: Each telescope caught one full transit, except for ULMT which observed the ingress and partial transit. Observations with MEarth North used Telescopes 1, 2, 3 and 6, while MEarth South included Telescopes 11, 12, 16 and 18.

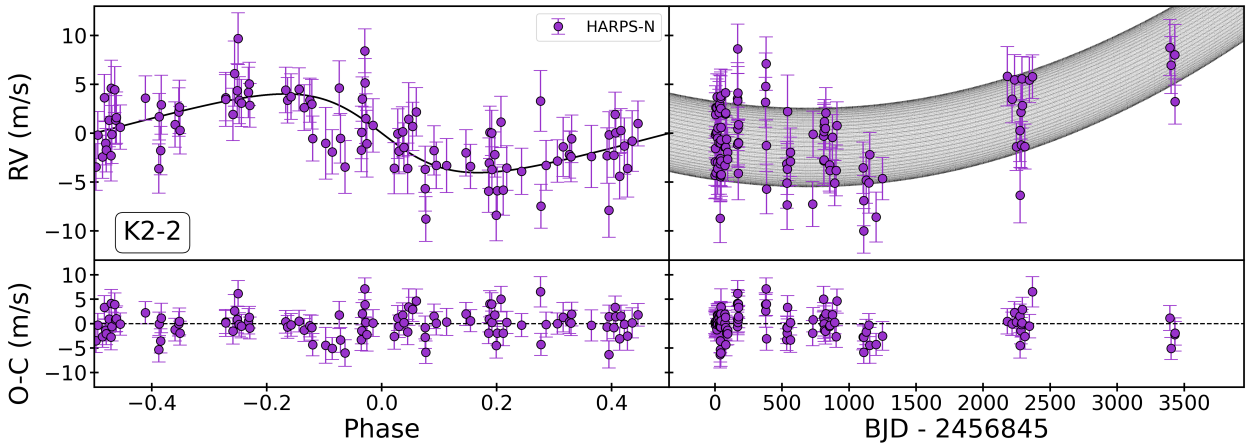

Figure 3.2 Archival HARPS-N radial velocities for K2-2 from Vanderburg et al. (2015) and Bonomo et al. (2023). The left panel shows the phased-folded RVs, and the right panel shows the long-term trend in the unphased RVs.

2012). To correct for stellar variability and any remaining systematics based on the out-of-transit photometry, we used the spline-fitting routine `keplerspline`[1] (Vanderburg & Johnson, 2014). We applied an initial estimate on the per-point errors for the corrected light curves as being the median absolute deviation of the out-of-transit photometry. We note that the per-point error is optimized through a fitted jitter term in the `EXOFASTv2` global fit (See Section 3.4).

[1]https://github.com/avanderburg/keplerspline

3.3.7 Archival Spectroscopy

We included archival spectroscopy to determine the host star properties and to refine the mass measurement of K2-2 b. In particular, to better characterize the host star in the global fit, we used metallicity measurements of K2-2 from the Tillinghast Reflector Echelle Spectrograph (TRES; Fűrész 2008) on the 1.5m Tillinghast Reflector at the Fred L. Whipple Observatory (FLWO). This is in keeping with our procedure for the larger Synergy catalog, where we are using TRES metallicities where available. The stellar parameters using TRES spectra were derived using the Stellar Parameter Classification (SPC; Buchhave et al. 2012). Three measurements from TRES ([M/H] = -0.193 ± 0.086, -0.191 ± 0.08, 0.009 ± 0.08) were available through the ExoFOP website[2]. We used the mean value to place a Gaussian prior on metallicity ([Fe/H]) of -0.125 ± 0.08.

We used a total of 105 spectra of K2-2, including those used in Vanderburg et al. (2015) and Bonomo et al. (2023), acquired using the High Accuracy Radial velocity Planet Searcher for the Northern hemisphere (HARPS-N) on the 3.6m Telescopio Nazionale Galileo (TNG) at the Roque de los Muchachos Observatory (Cosentino et al., 2012), in order to better characterize the mass of K2-2 b (Figure 3.2). Each observation had either 15 or 30 minutes exposure time, with a resolving power of R = 115,000. We followed the procedure of Dumusque et al. (2021) to reduce the RVs that were used in our global fits. The observations occurred in two main blocks, separated by $\sim$ 2.5 years; the first run was from UT 2014 July 7 to December 6 2017, and the second from UT 2020 June 25 to 2023 November 27. The second series of RVs was significantly offset to the earlier measurements, which led us to apply post-processing systematics corrections to investigate whether the offset was instrumental or physical in nature.

3.3.7.1 YARARA processing to correct remaining systematics

YARARA (Cretignier et al., 2021) is a post-processing methodology that aims to perform correction of the spectra by the analysis of the spectra time-series. While a more advanced version of the pipeline has been presented recently in Cretignier et al. (2023) (sometimes referred to as the YARARA V2 or YV2 datasets), the SNR of the target was too low to apply those advanced

[2]https://exofop.ipac.caltech.edu/tess/target.php?id=422618449

methods of correction (such as the SHELL presented in Cretignier et al. (2022)) and we remained with the YARARA V1 or YV1 version of the products.

The corrections available in YARARA cover as much as the telluric lines, as instrumental systematics or stellar activity. The pipeline usually starts from the S1D order-merged spectra produced by official DRS that have been continuum normalized by RASSINE (Cretignier et al., 2020b). The method then consists of a multi-linear decorrelation by fitting a basis of vectors that are designed to correct for some dedicated effects, either obtained by optimized extraction (see e.g. Stalport et al. (2023)) or by principal component analysis (PCA) as initially presented in Cretignier et al. (2021). For a dataset around SNR ~50, the main corrections that are possible to perform consist of removing cosmic, telluric lines, and the change of the instrumental PSF (Stalport et al., 2023). Even if a clear and strong emission is detected in the core of the CaII H&K lines, no reliable and precise extraction of the signal could be achieved and the stellar activity correction that mainly relies on this proxy (which contains most of the information from active regions (Cretignier et al., 2024)) was therefore skipped. The RVs were obtained with a cross-correlation function (CCF) on the corrected spectra using a line list optimised for the star following the line centre procedure described in Cretignier et al. (2020a).

After the application of YARARA, we still detect the long-trend signal which discards any potential effects from telluric or change of the instrumental PSF at the precision level of our data.

3.3.7.2 CCF Activity Linear Model (CALM) to model stellar variability

To model stellar variability in the radial velocities, we used activity indicators derived using the CCF Activity Linear Model (CALM) (de Beurs et al., 2024). CALM is a linear regression method which exploits the shape changes that stellar variability introduces into the cross-correlation functions (CCFs) computed from stellar spectra. Since CCFs represent an average of all line shapes in a star's spectrum, CALM is especially sensitive to line shape changes that persist in most spectral lines. In this method, we do not include the entire CCF in our model since CCFs are comprised of 49-element arrays and we only have 105 RVs. Including the entire CCF would lead to overfitting. We experimented with sampling various fractions of the CCFs and across random locations within

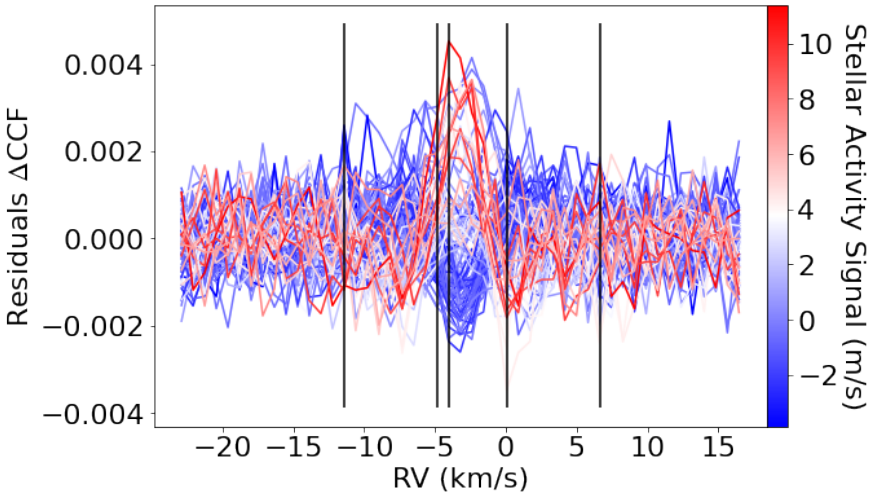

Figure 3.3 Residual CCFs (ΔCCFs) computed from HARPS-N spectra. The residual CCFs are computed by subtracting a median CCF. The CALM model-predicted stellar activity signal is indicated by the color (red = redshifted RVs, blue = blue-shifted RVs). The 5 CCF indexes used in our stellar activity model are indicated by black lines.

the CCF. We found that using 5 CCF locations provides a balance between preventing overfitting and optimizing goodness-of-fit. These 5 CCF locations are then used to decorrelate against in the global fit performed using `EXOFASTv2`. We visualize the CCFs for K2-2 and the specific 5 CCF locations in Figure 3.3, where we observe a clear pattern in the stellar variability and the CCF shape changes. This pattern allows us to use CALM to probe and predict stellar activity contributions to the RVs. In Figure 3.4, we plot the CALM model predicted stellar activity contributions to the RVs both in time and in the fourier domain. These activity indexes are able to probe both short- and long-term activity signals while preserving the planetary reflex motion. The ~270 day signal that is predicted by the CCF4 parameter was also found by Bonomo et al. (2023) and they noted that this signal is also seen in the periodograms of s-index and FWHM. This suggests that this signal corresponds to stellar variability and may be on a timescale longer than the stellar rotation period for K2-2.

3.4 Global Fits

Following the method described in Thygesen et al. (2023), we used the differential evolution Markov Chain Monte Carlo (DE-MCMC) exoplanet fitting software `EXOFASTv2` (Eastman et al., 2013, 2019) to simultaneously fit the parameters of K2-2 b and its host star. For a global fit to

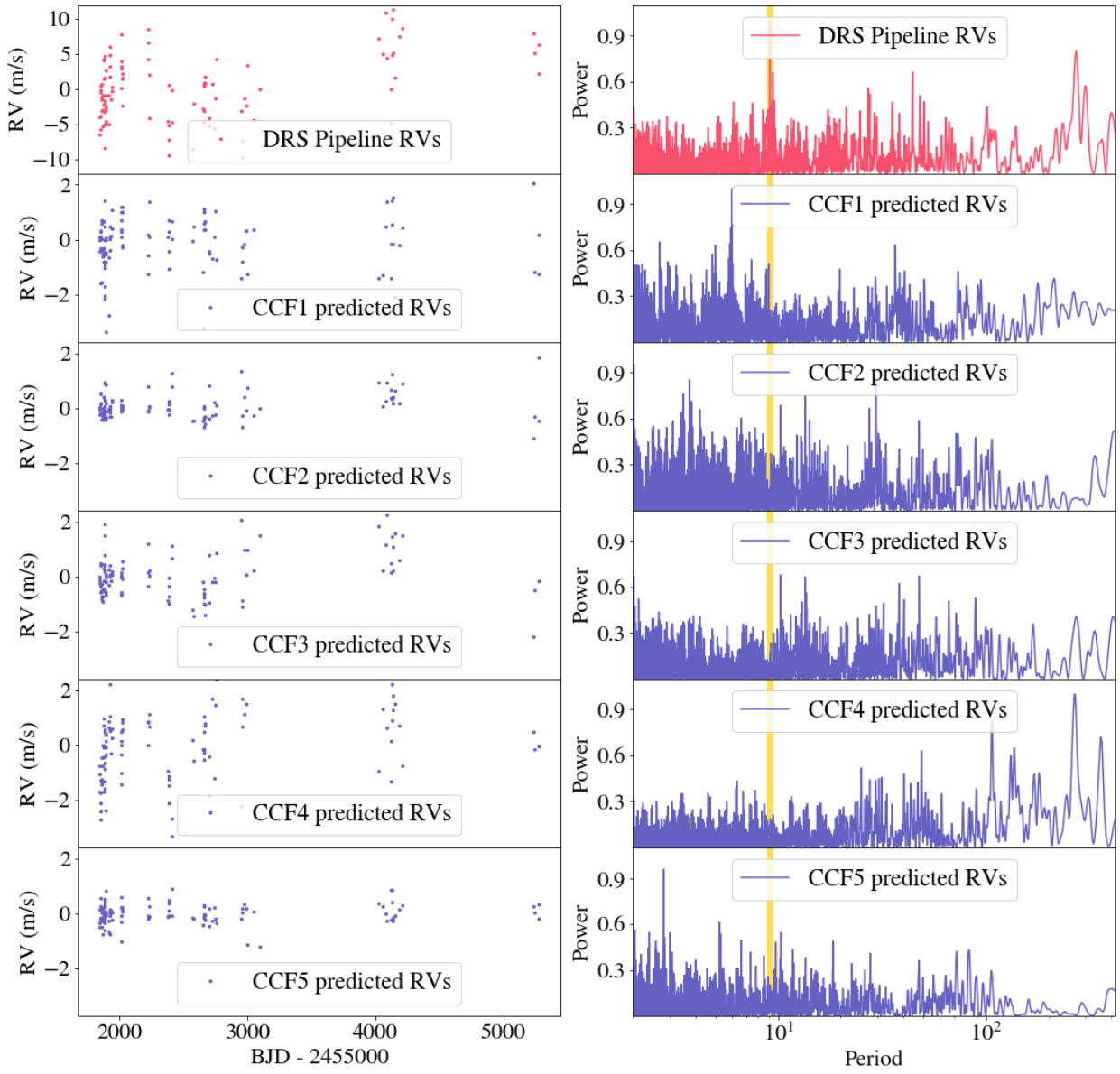

Figure 3.4 Timeseries and periodograms of the CALM predicted stellar variability. In the left panels, the DRS pipeline radial velocities and the stellar variability predictions from CCF index 1, 2, 3, 4, and 5 are plotted as a function of time. The location of these CCF indexes are indicated in Figure 3.3. On the right panel, the Lomb-Scargle periodograms of the corresponding RV timeseries are plotted. In yellow, the Keplerian period of K2-2 is indicated in the periodograms. We do not see signals at this planetary period, which provides reassurance that CALM is not absorbing or creating planetary signals.

be accepted as converged, we required that the Gelmin-Rubin statistic be less that 1.01 and the number of independent draws, T_z, greater than 1000. The global fits use MCMC sampling to find the best fit parameters for the system based on the photometric and spectroscopic data. We placed priors on several parameters as follows: a uniform prior from 0 to an upper bound of 0.09858 on the line-of-sight extinction (A_v) from Schlegel et al. (1998) and Schlafly & Finkbeiner (2011); a Gaussian prior on parallax of 16.0044 ± 0.0456 from Gaia Early Data Release 3 (accounting for the small systematic offset; EDR3; Gaia Collaboration et al. 2016, 2021; Lindegren et al. 2021); and a Gaussian prior on metallicity ([Fe/H]) of -0.125 ± 0.08 based on measurements from TRES (see Section 3.3.7). The fit also included the spectral energy distribution (SED) photometry as reported by Gaia EDR3 (Gaia Collaboration et al., 2021), WISE (Cutri et al., 2012) and 2MASS (Cutri et al., 2003) (see Table 3.1). To better characerize the host star, the MESA Isochrones and Stellar Tracks (MIST) stellar evolution models (Paxton et al., 2011, 2013, 2015; Choi et al., 2016; Dotter, 2016) were used within the `EXOFASTv2` fits. Within `EXOFASTv2`, limb darkening is constrained via priors derived from models by Claret & Bloemen (2011) and Claret (2017), with physical bounds from Kipping (2013) (see Section 3 of Eastman et al. (2019) for more details on how `EXOFASTv2` constrains limb darkening).

Although the TESS PDCSAP light curves generally have a correction applied for any contaminating sources, we fitted for a dilution term in case of any sources that may have been missed, based on the contamination ratio (CR) for K2-2 of 0.002101 as reported in the TESS input catalog (TICv8, Stassun et al., 2018). We used placed a 10% Gaussian prior on the dilution centered about CR/(1+CR) = 0.0021. However, the fitted dilution was consistent with zero in all the fits we ran.

To account for any residual correlated noise in the systematics-corrected Spitzer data within the `EXOFASTv2` fit (see Section 3.3.5), we followed the procedure outlined in §3 of Rodriguez et al. (2020). We scaled the uncertainties by the factor $\beta = 1.19$ before using the light curve in the global fit. To ensure `EXOFASTv2` did not reduce the per-point uncertainties on the Spitzer photometry within the fit, we enforced a lower bound on the variance of zero, otherwise the global fit could over-correct the scaled uncertainties to be consistent with pure white noise.

Table 3.3 Models tested for long-term RV trend.

Model	Description	ΔBIC
(i)	One RV season, linear and quadratic trend with time	0.0
(ii)	One RV season, linear trend with time	0.72
(iii)	Two RV seasons, no long-term trend	49.75
(iv)	Two RV seasons, linear trend with time	55.15
(v)	Two RV seasons, linear and quadratic trend with time	68.21

3.4.1 RV model selection

As the RVs still exhibited an offset in the second observing block after all processing (see Section 3.3.7), we compared five different models that attempt to model this long-term change and evaluated their goodness-of-fit with `EXOFASTv2`, while keeping all other inputs and priors the same. For each of these models, we first performed a fit using CALM since these long-term trends could be caused by stellar variability. We then took the initial CALM fit to the RVs for each model and ran a global fit with `EXOFASTv2`. The five models are listed in Table 3.3 and each include the CALM model, but differ in their modeling of the long-term trends where they include some combination of a linear ($\dot{\gamma}$) trend with time, a quadratic ($\ddot{\gamma}$) trend with time, and/or an offset D between the two observing blocks. In particular, our models include (i) a CALM model with a linear and quadratic trend with time that treats the RV timeseries as one RV observing season without an offsets between the two observing blocks, (ii) a CALM and linear trend model that treats the RV timeseries as one RV observing season without an offset, (iii) a CALM model with an offset D between the two observing blocks, (iv) a CALM model with a linear trend and an offset D, and (v) a CALM model with a linear and quadratic trend and an offset D . For the models where we treated the two observing blocks as separate seasons, this allows for different zero-points to be determined for each season. Comparing the Bayesian Information Criterion (BIC) of the models, we found that those including an offset component (i.e. two observing seasons) are heavily disfavored as seen in Table 3.3. The single-season models perform comparabley and we adopt the quadratic-trend model as it has the lowest BIC.

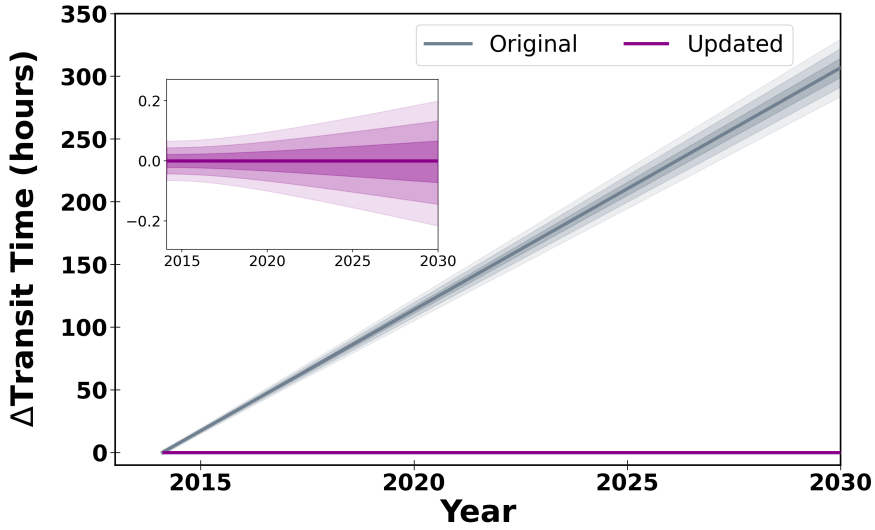

Figure 3.5 Projected difference in the time of transit for K2-2 b to the year 2030 using the original ephemeris (gray) and the new ephemeris from this work (purple). Shaded regions indicating up to the 3σ level uncertainty are shown. The inset shows the updated ephemeris, zoomed in for clarity.

3.5 Results and Discussion

In this work, we have combined multiple new observations with existing data available for K2-2 b to produce the most accurate and precise system parameters and transit ephemeris (transit time uncertainty <13 minutes in 2030). The period of K2-2 b has been updated to $9.1004157^{+4.1E-06}_{-4.5E-05}$ days and T_0 to $2458072.29291^{+0.00062}_{-0.00061}$ BJD (Figure 3.5). The solutions for the stellar and planetary parameters are shown in Tables 3.4 and 3.5, respectively. Table 3.6 contains the radial velocity parameters, including the detrending parameters we used, and Table 3.7 lists the parameters of the photometric models for each light curve. We included the MOST light curve in a preliminary fit, as the transit window was observed four times in the full light curve. However, this did not add value to the fit, and the transit was not detectable even with the updated ephemeris, so we did not include the MOST data in the final global fit. The discovery period (Vanderburg et al., 2015) we determined to be 28.8 minutes (~40 σ) from the true period. For context, if someone attempted an observation in 2025 of a K2-2 b transit using the original ephemeris, it would be ~200 hours from the correct time. We note that this would only result in an offset of ~18 hours from a transit of K2-2 b since the offset would be quite close to the orbital period of the planet by then, resulting in catching the next adjacent transit.

Table 3.4 Median values and 68% confidence interval for K2-2 stellar parameters from the EXOFASTv2 global fit.

Parameter	Units	Values
Priors:		
π	Gaia parallax (mas).....	$\mathcal{G}[16.0044, 0.0465]$
[Fe/H]	Metallicity (dex)	$\mathcal{G}[-0.125, 0.080]$
A_V	V-band extinction (mag)	$\mathcal{U}[0, 0.0985]$
M_*	Mass ($M_\odot$)	$0.800^{+0.033}_{-0.030}$
R_*	Radius ($R_\odot$)	$0.758^{+0.024}_{-0.022}$
L_*	Luminosity ($L_\odot$)	$0.3364^{+0.0100}_{-0.0096}$
F_{Bol} ...	Bolometric Flux $\times 10^{-9}$ (cgs) .	$2.757^{+0.081}_{-0.076}$
ρ_*	Density (cgs)	$2.59^{+0.26}_{-0.24}$
$\log g$ ...	Surface gravity (cgs)	$4.582^{+0.030}_{-0.031}$
$T_{\rm eff}$	Effective Temperature (K)....	5048^{+79}_{-78}
[Fe/H]	Metallicity (dex)	$0.000^{+0.045}_{-0.039}$
$[Fe/H]_0$	Initial Metallicity[1]	0.000 ± 0.055
Age ...	Age (Gyr)	$5.5^{+5.0}_{-3.9}$
EEP ..	Equal Evolutionary Phase[2] ..	335^{+16}_{-34}
A_V	V-band extinction (mag)	$0.045^{+0.035}_{-0.031}$
σ_{SED} ..	SED photometry error scaling	$0.76^{+0.32}_{-0.19}$
ϖ	Parallax (mas)	16.004 ± 0.046
d	Distance (pc)	62.48 ± 0.18

Notes. See Table 3 in Eastman et al. (2019) for a detailed description of all parameters. Gaussian and uniform priors are indicated as $\mathcal{G}[\text{mean}, \sigma]$ and $\mathcal{U}[\text{lower bound, upper bound}]$, respectively. The metallicity prior is adopted from the average of three TRES measurements: [M/H] = -0.193, -0.191, 0.009 (see Section 3.3.7 for details). [1]The metallicity of the star at birth. [2]Corresponds to static points in a star's evolutionary history. See §2 in Dotter (2016).

K2-2 b has a radius of $2.47^{+0.10}_{-0.09}$ $R_\oplus$ and a mass of 9.7 ± 1.2 $M_\oplus$. This yields a bulk density of $3.53^{+0.63}_{-0.57}$ g cm^{-3}, which is twice that of Neptune (1.638 g cm^{-3}). According to the composition models from Zeng et al. (2016), it is likely K2-2 b has a high water content (Figure 3.6). While it is consistent with 100% water, a more physically motivated solution would be a rocky core with an extended envelope of volatiles including a H/He envelope. More observations are needed to place further constraints on the planetary composition.

The mass of K2-2 b was updated in a recent in-depth radial velocity study of Kepler and K2 systems (Bonomo et al., 2023) to refine planet masses and identify cold Jupiters in systems containing small planets. Bonomo et al. (2023) refined important planetary parameters such as the

Table 3.5 Median values and 68% confidence interval for K2-2 b planetary parameters from the EXOFASTv2 global fit.

Parameter	Units	Values
P	Period (days)	$9.1004157^{+0.0000041}_{-0.0000045}$
R_P	Radius (R_E)	$2.469^{+0.10}_{-0.091}$
M_P	Mass (M_E)	9.7 ± 1.2
T_0	Optimal conjunction Time[1] (BJD_{TDB}) ..	$2458072.29291^{+0.00062}_{-0.00061}$
a	Semi-major axis (AU)	$0.0792^{+0.0011}_{-0.0010}$
i	Inclination (Degrees)	$88.91^{+0.68}_{-0.45}$
e	Eccentricity[2]	$0.215^{+0.056}_{-0.094}$
ω_*	Argument of Periastron (Degrees)	88^{+19}_{-20}
T_{eq}	Equilibrium temperature[3] (K)	$753.2^{+7.1}_{-6.9}$
$\tau_{\rm circ}$	Tidal circularization timescale (Gyr) ...	1310^{+540}_{-430}
K	RV semi-amplitude (m/s)	3.54 ± 0.42
R_P/R_* .	Radius of planet in stellar radii	$0.02981^{+0.00079}_{-0.00061}$
a/R_* ...	Semi-major axis in stellar radii	22.46 ± 0.72
δ	$(R_P/R_*)^2$	$0.000889^{+0.000048}_{-0.000036}$
$\delta_{\rm Kepler}$ ..	Transit depth in Kepler (fraction)	$0.001186^{+0.000052}_{-0.000050}$
$\delta_{\rm i'}$	Transit depth in i' (fraction)	$0.001092^{+0.000035}_{-0.000034}$
$\delta_{\rm r'}$	Transit depth in r' (fraction)	$0.001171^{+0.000056}_{-0.000051}$
$\delta_{4.5\mu{\rm m}}$ ..	Transit depth in $4.5\mu m$ (fraction)	$0.000922^{+0.000046}_{-0.000040}$
$\delta_{\rm TESS}$ ...	Transit depth in TESS (fraction)	$0.001092^{+0.000039}_{-0.000038}$
τ	Ingress/egress transit duration (days) ...	$0.00329^{+0.00088}_{-0.00036}$
T_{14}	Total transit duration (days)	$0.1013^{+0.0015}_{-0.0014}$
T_{FWHM} .	FWHM transit duration (days)	0.0978 ± 0.0013
b	Transit Impact parameter	$0.34^{+0.20}_{-0.22}$
b_S	Eclipse impact parameter	$0.51^{+0.15}_{-0.31}$
τ_S	Ingress/egress eclipse duration (days) ...	$0.00540^{+0.00074}_{-0.00051}$
$T_{S,14}$ ...	Total eclipse duration (days)	$0.141^{+0.027}_{-0.028}$
$T_{S,FWHM}$	FWHM eclipse duration (days)	$0.135^{+0.027}_{-0.028}$
$\delta_{S,2.5\mu m}$.	Blackbody eclipse depth at 2.5μm (ppm)	$0.912^{+0.083}_{-0.073}$
$\delta_{S,5.0\mu m}$.	Blackbody eclipse depth at 5.0μm (ppm)	$15.33^{+1.00}_{-0.85}$
$\delta_{S,7.5\mu m}$.	Blackbody eclipse depth at 7.5μm (ppm)	$34.9^{+2.2}_{-1.7}$
ρ_P	Density (cgs)	$3.53^{+0.63}_{-0.57}$
$logg_P$ ..	Surface gravity	$3.192^{+0.061}_{-0.065}$
Θ	Safronov Number	$0.0274^{+0.0035}_{-0.0034}$
$\langle F \rangle$	Incident Flux (10^9 erg s^{-1} cm^{-2})	$0.0698^{+0.0032}_{-0.0029}$
T_P	Time of Periastron (BJD_{TDB})	$2456689.01^{+0.30}_{-0.34}$
T_S	Time of eclipse (BJD_{TDB})	$2456693.61^{+0.35}_{-0.36}$
T_A	Time of Ascending Node (BJD_{TDB})	$2456705.54^{+0.20}_{-0.28}$
T_D	Time of Descending Node (BJD_{TDB}) ...	$2456690.73^{+0.32}_{-0.22}$
V_c/V_e ..	.....	$0.810^{+0.086}_{-0.047}$
$e\cos\omega_*$	See footnote[4]	$0.004^{+0.059}_{-0.060}$
$e\sin\omega_*$.	See footnote[5]	$0.205^{+0.057}_{-0.098}$
M_P/M_* .	Mass ratio	$0.0000365^{+0.0000044}_{-0.0000043}$
d/R_* ...	Separation at mid transit	$17.9^{+2.3}_{-1.7}$

Notes. See Table 3 in Eastman et al. (2019) for a detailed description of all parameters.

Table 3.6 Median values and 68% confidence interval for radial velocity parameters.

Telescope Parameters:		HARPS-N
$\gamma_{\rm sys}$ . .	Systemic velocity (km/s)	-2.91
$\gamma_{\rm rel}$ . .	Relative RV Offset (m/s)	0.02 ± 0.63
$\dot{\gamma}$	RV slope (m/s/day)	0.00239 ± 0.00039
$\ddot{\gamma}$	RV quadratic term (m/s/day^2)	$0.00000133 \pm 0.00000036$
σ_J . . .	RV Jitter (m/s)	$2.30^{+0.24}_{-0.22}$
σ_J^2 . .	RV Jitter Variance	$5.27^{+1.2}_{-0.98}$
CCF_0	Additive detrending coeff. . .	-3.23 ± 0.92
CCF_1	Additive detrending coeff. . .	3.4 ± 2.6
CCF_2	Additive detrending coeff. . .	2.0 ± 2.0
CCF_3	Additive detrending coeff. . .	-6.6 ± 1.5
CCF_4	Additive detrending coeff. . .	1.3 ± 1.0

Notes. Reference epoch = 2458561.069744 BJD. Five additive detrending parameters were included to account for stellar activity (see Section 3.4).

Table 3.7 Median values and 68% confidence intervals for the photometric models.

Telescope	Wavelength Parameters		Transit Parameters		Additive detren
	$u_1^\dagger$	$u_2^\ddagger$	$\sigma^{2\star}(10^{-9})$	F_0^*	C_0
K2	0.57 ± 0.052	0.171 ± 0.051	$2.45^{+0.56}_{-0.50}$	0.9999999 ± 0.0000047	—
MEarth (i') Tel. 1	$0.426^{+0.022}_{-0.023}$	0.205 ± 0.020	2360^{+320}_{-290}	$1.00042^{+0.000096}_{-0.000097}$	$-0.00026 \pm$
MEarth (i') Tel. 2	$0.426^{+0.022}_{-0.023}$	0.205 ± 0.020	2220^{+290}_{-270}	1.000525 ± 0.000093	0.00001 ± 0
MEarth (i') Tel. 3	$0.426^{+0.022}_{-0.023}$	0.205 ± 0.020	4830^{+510}_{-470}	1.00033 ± 0.00012	$-0.00142 \pm$
MEarth (i') Tel. 6	$0.426^{+0.022}_{-0.023}$	0.205 ± 0.020	4700^{+460}_{-430}	1.00053 ± 0.00012	$-0.00076 \pm$
MEarth (i') Tel. 11	$0.426^{+0.022}_{-0.023}$	0.205 ± 0.020	1310^{+200}_{-190}	$1.000213^{+0.000076}_{-0.000077}$	$-0.00147 \pm$
MEarth (i') Tel. 12	$0.426^{+0.022}_{-0.023}$	0.205 ± 0.020	2060^{+230}_{-210}	1.000355 ± 0.000080	$-0.00091 \pm$
MEarth (i') Tel. 16	$0.426^{+0.022}_{-0.023}$	0.205 ± 0.020	940^{+160}_{-150}	1.000344 ± 0.000070	$-0.00003 \pm$
MEarth (i') Tel. 18	$0.426^{+0.022}_{-0.023}$	0.205 ± 0.020	1530^{+200}_{-180}	1.000253 ± 0.000077	$-0.00098 \pm$
ULMT (r')	0.551 ± 0.054	0.183 ± 0.052	$3150.0^{+430.0}_{-380.0}$	0.99957 ± 0.00014	0.00041 ± 0
Spitzer ($4.5\mu m$)	$0.077^{+0.047}_{-0.043}$	0.146 ± 0.050	$5.7^{+9.2}_{-4.3}$	1.000003 ± 0.000036	—
TESS Sector 42	0.428 ± 0.038	0.21 ± 0.036	$28.3^{+8.1}_{-8.0}$	1.0000131 ± 0.0000073	—
TESS Sector 70	0.428 ± 0.038	0.21 ± 0.036	6.1 ± 7.1	1.0000099 ± 0.0000065	—

Notes. †Linear limb-darkening coefficient. ‡Quadratic limb-darkening coefficient. *Added variance. * Baseline flux.

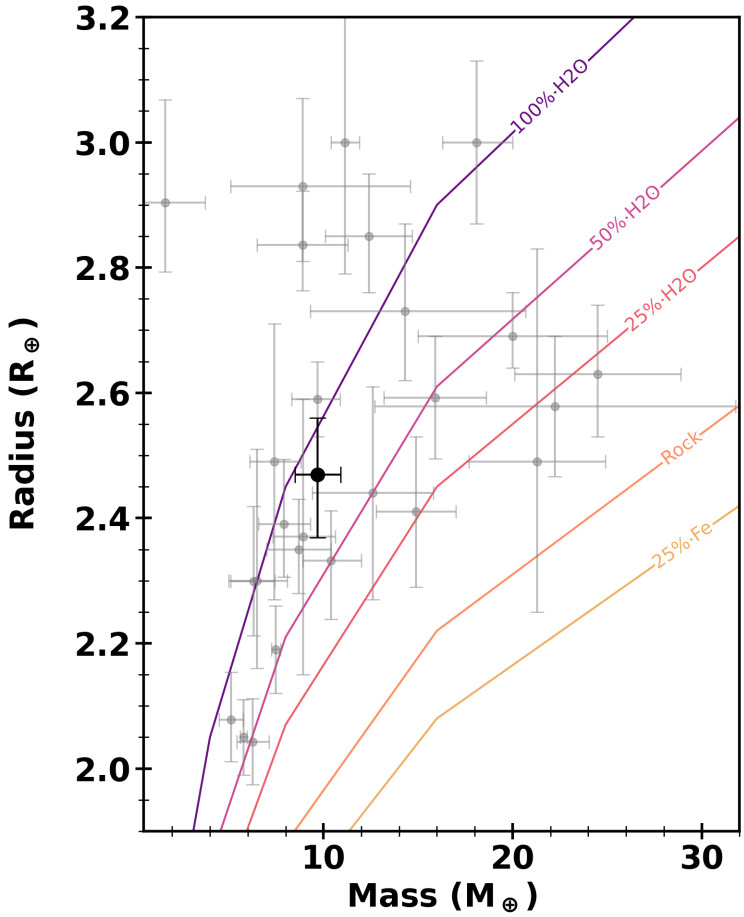

Figure 3.6 Mass-radius diagram for K2 sub-Neptunes ($R_P = 2.0-3.0\ R_\oplus$). The large black circle is K2-2 b, while the small gray circles are other sub-Neptunes with measured masses from the NASA Exoplanet Archive. The lines represent composition tracks from Zeng et al. (2016).

period (to 9.0949 ± 0.0026 days) and mass (to $10.1\ ^{+1.2}_{-1.1}\ M_\oplus$), and did not find any long-term trends in the RVs that could correspond to a long-period companion. We used the same RV observations from this work (in addition to those from Vanderburg et al. 2015) but with improved precision from improved modeling of the stellar activity using the CALM technique (see Section 3.3.7.2) in our global fit, and when combined with the other photometric and spectroscopic data, we were able to refine these measurements and uncover a potential outer companion due to a long-term trend in the RVs.

3.5.1 RV trend

As mentioned in Section 3.3.7, there is a long-term trend in the radial velocities (see Figure 3.2) after correcting for stellar variability. To test the possibility of a second planet or star within the

system, we reran the fit described in Section 3.4 but allowed `EXOFASTv2` to fit for a second planet within the RVs only. We note that there is no additional transit signal detected in any photometric data sets used in this analysis. However, preliminary fits did not converge nor provide any useful constraint on the period of a potential companion, even with improved constraints on K2-2 b. Figure 3.2 shows the long-term trend in the RVs, and our resulting best-fit model from `EXOFASTv2`. It is clear that the period of this secondary companion is much longer term than the extent of our RV data set from HARPS-N (~2500 days). We instead model the long-term trend with a quadratic acceleration term. Our best-fit results find a linear slope in the RVs of 0.0024 ± 0.0004 m s^{-1} with a quadratic term of $1.33E-06 \pm 3.6E-07$ m s^{-1} day^{-2} to best represent the long-term RV trend.

The observed RV trend may correspond to an additional companion to K2-2 with an orbital separation of several AU. Vanderburg et al. (2015) acquired high-resolution imaging observations of the star and did not detect any stellar companions between $0.1 - 5.0$" ($\approx 6 - 310$ AU). This non-detection, combined with the relatively small amplitude of the RV acceleration, suggests that this outer companion could be a planet or a brown dwarf.

As K2-2 was observed by *Hipparcos*, it is possible to place additional constraints on any outer companions using *Hipparcos-Gaia* astrometry (Brandt, 2018, 2021). If a massive companion exists at a separation of several AU from K2-2, it would likely generate a significant astrometric acceleration between *Hipparcos* and *Gaia*. However, no significant acceleration is detected in the *Hipparcos-Gaia* astrometry, with $\chi^2 = 2.3$ for a constant proper motion (Brandt, 2021). The astrometric precision for K2-2 is ~0.07 mas yr^{-1}, equivalent to ~20 m s^{-1} at the 62.48 ± 0.18 pc distance of the system. This means that a net *Hipparcos-Gaia* velocity change greater than $\gtrsim$100 m s^{-1} can be excluded at 5σ confidence. This non-detection largely excludes the existence of massive companions ($\gtrsim 10\ M_J$) orbiting K2-2 within several AU. However, a planetary-mass companion could be reconciled with the astrometric non-detection.

Continued RV monitoring of the K2-2 system is needed to constrain the further evolution of the RV trend, providing some constraints on the fundamental parameters of the possible second planet in the system.

Table 3.8 Stellar parameters for the white dwarf companion of K2-2 from Gentile Fusillo et al. (2021).

Composition	$T_{\rm eff}$ (K)	$\log g$ (cgs)	Mass ($M_\odot$)
H	7519 ± 195	7.88 ± 0.08	0.52 ± 0.04
He	7395 ± 189	7.82 ± 0.06	0.47 ± 0.02
H+He	7083 ± 167	7.71 ± 0.07	0.44 ± 0.03

3.5.2 Future work

The K2 mission was driven by the community, which led to planets orbiting much brighter host stars than the original Kepler mission, targets well suited for detailed characterization. Although characterization might be challenging with current facilities, K2-2 b is a worthwhile target for ongoing monitoring and targeted observations. Following the Kempton et al. (2018) prescription for the transmission spectroscopy metric (TSM), we find that K2-2 b has a TSM of $50.0^{9.2}_{8.7}$, which falls just below the lowest value suggested for target prioritization for JWST. However, when compared to the other $\sim$ 160 sub-Neptunes ($R_P = 2.0 - 3.0\ R_\oplus$) in the K2 catalog, the TSM of K2-2 b is the fifth highest, suggesting that it is a suitable candidate for studying sub-Neptunes in closer detail. Monitoring the radial velocities of K2-2 would allow for more refined constraints on the stellar activity, and possibly uncover additional long-period and/or low-mass candidates in the system.

The co-moving white dwarf (WD) companion to K2-2 provides an avenue to measure a precise age for the system if the mass and age for the WD can be determined. The stellar parameters were calculated as part of a catalog of all WDs within Gaia EDR3[3] by Gentile Fusillo et al. (2021). The mass, effective temperature, and surface gravity were determined for three different atmospheric compositions: pure H, pure He, and a mix of H and He (see Table 3.8). Assuming the highest mass value from the models (pure-H, 0.52 ± 0.04 $M_\odot$), we find a lower limit on the cooling age of 1.13±0.13 Gyr. While this current age estimate does not constrain the system age further, more precise photometry and measuring the spectrum of the WD would constrain the mass (and system age) more reliably than Gaia photometry alone.

[3]Gaia EDR3 source_id 2645940445519931520

3.6 Conclusion

With thousands of exoplanets discovered to date, some will inevitably be “lost" (unconstrained ephemerides) or forgotten as newer discoveries peak the interest of the community. Unfortunately, these lost planets may be excellent targets for detailed characterization with JWST (Gardner et al., 2006), but are not accessible due to large uncertainties in future transit times. K2-2 b was the first planet discovered during the Two-Wheeled Concept Engineering Test of the K2 mission (Howell et al., 2014), showing very quickly that K2 would be a successful repurposing of the Kepler spacecraft. By combining observations from multiple NASA missions along with key ground-based follow up that span nearly a decade, we have recovered the lost transit ephemeris of K2-2 b. In addition to being the first K2 planet, it is also well-suited for studying the atmosphere of a hot sub-Neptune as it orbits a bright (K∼8.03) K-dwarf. This would be a valuable measurement since it sits on the high-mass peak of the sub-Neptune radius valley (Owen & Jackson, 2012; Fulton et al., 2017) and could provide insight to the formation and evolution of sub-Neptunes. Our updated ephemeris ($P = 9.1004157^{+4.1E-06}_{-4.5E-06}$ days, $T_0 = 2458072.29291^{+0.00062}_{-0.00061}$ BJD) confirms the false detection from the MOST satellite (Vanderburg et al., 2015) that led to a ∼40σ offset to the true period. Systems like K2-2 show the importance of continued monitoring of exoplanet systems and dedicated ephemeris refinement efforts like the K2 & TESS Synergy project (Ikwut-Ukwa et al., 2020; Thygesen et al., 2023), ExoClock (Kokori et al., 2021, 2022, 2023), Exoplanet Watch (Zellem et al., 2019, 2020), and ORBYTS (Edwards et al., 2019, 2020, 2021).

CHAPTER 4

SYNERGY 4

This chapter presents the ongoing work for the fourth paper in the K2 & TESS Synergy series, which is expected to be submitted for publishing before Summer 2025.

4.1 Introduction

Within its first few years of operations, JWST has already revolutionized the field of exoplanet atmospheres through the success of its Early Release Science Program that targets a handful of well-studied systems with prior facilities like HST and Spitzer. The first release of JWST data was with the Early Release Observations (EROs; Pontoppidan et al. 2022), which contained images and spectra intended for public outreach purposes and to showcase the capabilities of the telescope. This was followed by several months dedicated to the Director's Discretionary Early Release Science Programs (DD-ERS), a small selection of observations utilizing all the instruments on board JWST that would produce science-quality data. Included in these programs were transmission spectra that have paved the way for transmission spectroscopy going forward.

The first JWST transmission spectrum was of WASP-96 b, a puffy hot Jupiter ($\sim 0.48 M_J$, $\sim 1.20 R_J$) that had previous well-studied transmission spectra (McGruder et al., 2022; Nikolov et al., 2018; Yip et al., 2021). The new JWST spectrum was able to significantly constrain elemental abundances, particularly for H_2O, CO_2, and K (Pontoppidan et al., 2022; Taylor et al., 2023), showcasing the capabilities of JWST for atmospheric characterization. Expand

One of the keystone systems in the first few years of exoplanetary science with JWST is WASP-39 b, a hot Jupiter that has become the poster child for the cutting-edge science that can be done with JWST. This targeted WASP-39 b, a Hot Jupiter ($\sim 0.28 M_J$, $\sim 1.27 R_J$) on a 4.06 day period around a G-type star. The spectrum contained significant features of CO_2, H_2O, and SO_2, with possible minor contributions from CO, H_2S, OCS, K, and CH_4 (Ahrer et al., 2022; Alderson et al., 2022; Feinstein et al., 2022; Rustamkulov et al., 2022). Atmospheric models fit to the transmission spectrum indicated a metallicity of $3 - 10\times$ Solar, which was a major improvement from previous estimates that ranged anywhere from 0.003-300$\times$ Solar (Alderson et al., 2022). The

models also resulted in an upper limit for the C/O ratio of ≤ 1. The combination of these constraints suggest that WASP-39 b formed via core accretion within the CO_2 snowline where it accreted it gaseous atmosphere, or alternatively accreted planetesimals high in oxygen content that enriched the atmosphere (Alderson et al., 2022). Furthermore, the previously undetected SO_2 feature is the first-ever convincing evidence of photochemical processes in an exoplanet atmosphere (Tsai et al., 2022; Polman et al., 2022). Expand

The interpretation of JWST results has not been without controversy. The transmission spectrum for K2-18 b showed an abundance of CH_4 and CO_2, and sparked debate with the reported detection of dimethyl sulfide (DMS; Madhusudhan et al. 2023), a molecule currently known to be a product only of biological activity. However, a second, less contentious scenario that also fits the data is that K2-18 b is a mini-Neptune without a well-defined surface (Wogan et al., 2024). Expand

While JWST has targeted many gas giants with large atmospheres that lend themselves to transmission spectra, a series of Earth-like planets orbiting M dwarfs have also been observed with the hope to characterize atmospheres on rocky planets. JWST was used to validate the Earth-sized planet LHS 475 b (Lustig-Yaeger et al., 2023), which was found to have a featureless spectrum consistent with that of Venus, Mars, or Titan. The transmission spectrum of super-Earth GJ 486 b was found to contain water vapor, but it is not clear whether this originates from unocculted star spots from the host or the planet itself (Moran et al., 2023). Transmission and emission spectroscopy of TRAPPIST-1 b have not detected a significant atmosphere (Greene et al., 2023; Lim et al., 2023; Ih et al., 2023). For planets like these, more JWST observations may increase the signal enough to resolve spectroscopic features of a present atmosphere, or rule out an atmosphere altogether. The super-Earth 55 Cancri e ($1.95M_\oplus$, $8.8M_\oplus$), orbiting a K-type star, was found to have an atmosphere with abundant CO_2 or CO, which could potentially be attributed to outgassing from a magma ocean (Hu et al., 2024).

Previously well-studied systems have been a major part of early JWST targets. These are planets with extremely precise ephemerides, and sometimes previous transmission spectra with facilities like HST. We would be remiss to limit observations to planets that have already been well-studied,

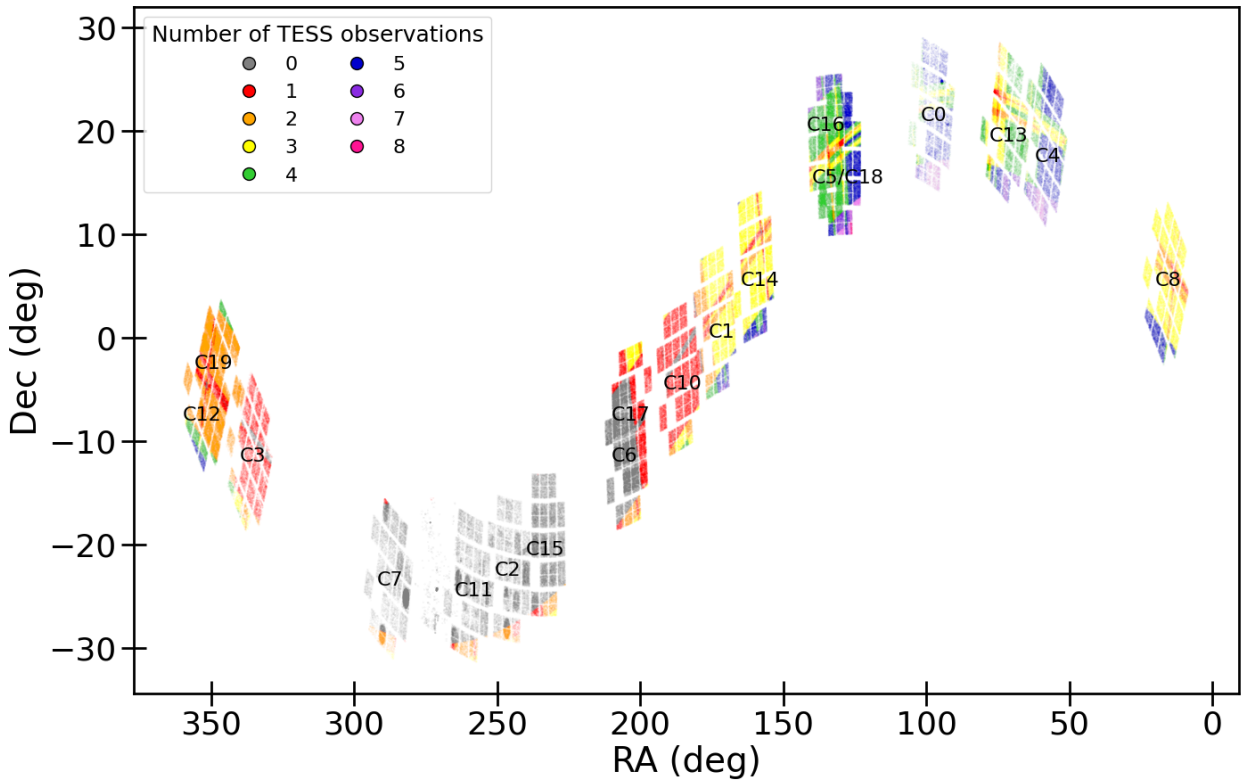

Figure 4.1 Overlap between K2 campaigns and TESS sectors. Each point represents a K2 target, which are colored by the number of times they have been reobserved by TESS up to and including Sector 84.

considering there are also a finite number of these. There remain hundreds of planets that could be prime targets for JWST if only their future transit times could be accurately predicted. With this in mind, we continue the K2 & TESS Synergy while prioritizing planets that are more likely to produce high signal-to-noise JWST transmission spectra.

In this chapter, we reanalyze 32 of the best planets for atmospheric observations within the K2 catalog. The TESS sectors used in this work are up to and including Sector 72 (December 7, 2023). Section 4.2 explains the selection process for the target list, and we summarize the analysis process in Section 4.3, which is for the most part the same as described in Chapter 2. We present our results in Section 4.4, highlighting targets of particular interest and comparing our current sample to planets observed by JWST, and conclude in Section 4.6.

4.2 Target Selection

To identify the top 50 exoplanet systems discovered by K2 that are most well-suited for atmospheric studies, we used the confirmed catalog in the NASA Exoplanet Archive (add date retrieved and footnote) and ranked them by transmission spectroscopy metric (TSM; Kempton et al. 2018). The TSM provides an estimate of the planet's accessibility for transmission spectroscopy based on the planet's mass, radius, and equilibrium temperature, and the host star's radius and apparent J magnitude. We scaled the TSM value of all confirmed K2 planets to the highest, K2-135 d. As the TSM calculation is only valid for planets up to 10 Earth radii, we also included planets with radii above this cutoff, as the scale height of the atmospheres are likely to be large enough for high S/N transmission spectroscopy.

To converge on a feasible list for this batch, we made some alterations to the TSM list. Some systems ranked highly have not yet been observed by TESS, so we excluded these from the list. For multiplanet systems, we included all planets within the system as long as one planet made the TSM threshold. However, we excluded three multiplanet systems that each have more than three planets (K2-135, K2-138, and K2-266), due to the complexity of the systems and high computational cost. These will be included in a future Synergy paper. Eight planets from the previous Synergy papers are above the TSM cut (K2-2, K2-97, K2-114, K2-115, K2-237, K2-260, K2-261, K2-277). We included these systems in the current sample for completeness, and ran new global fits to ensure the inclusion of any new TESS sectors. The final list for this sample is shown in Table 4.1.

4.3 Data and Global Fits

We followed the same general process for data preparation and analysis as outlined in Chapters 2.3 and 2.4, and Thygesen et al. (2023), which is briefly summarized here. We used the methods described in Vanderburg & Johnson (2014) and Vanderburg et al. (2016) to process the K2 light curves, and account for any major contamination from other stars within the K2 aperture. For TESS light curves, we prioritized short-cadence observations when available, otherwise using FFIs, and used the PDCSAP flux (Stumpe et al., 2012, 2014; Smith et al., 2012) processed through the SPOC pipeline (Jenkins et al., 2016; Caldwell et al., 2020). We ran the TESS light curves through

Table 4.1 Target list and data used in this analysis.

TIC ID	TOI	EPIC ID	KID	K2 Campaign	TESS Sector	RV Ref.	K2 Discovery Ref.
307733361	5071	211990866	K2-100	5,18	44, 45, 46, 72		
6892385	5164	211525389	K2-105	5,18	44, 45, 46, 71, 72		
366576758	514	211418729	K2-114	5, 18	7, 44, 45, 46, 72		
7020254	4316	211442297	K2-115	5, 18	7, 34, 45, 46, 71, 72		
7059054	5072	211818569	K2-121	5, 16	44, 45, 46, 71, 72		
422618449	6836	60021410	K2-2	-1	42, 70		
68577662	4606	247098361	K2-232	13	43, 44, 71		
350020859	5141	248777106	K2-234	14	45, 46		
243244680	5065	211945201	K2-236	5,16	44, 45, 46, 72		
16288184	1049	229426032	K2-237	11	12, 39		
293612446	2466	246911830	K2-260	13	5, 32, 43, 71		
281731203	685	201498078	K2-261	14	9, 35, 45, 46, 72		
411839167	2461	246851721	K2-267	13	32, 43, 44, 71		
404421005	4628	212357477	K2-277	6	10, 37		
39926974	4526	206318379	K2-28[†]	3	42		
380884458	-	220522262	K2-281	8	42, 70		
26017005	4535	210957318	K2-30	4	42, 43, 44, 70, 71		
203214081	5097	212048748	K2-313[†]	16	44, 45, 46, 72		
301258470	-	201205469	K2-329	12, 19	42		
330687113	5089	211730024	K2-334	16	44, 45, 46, 72		
178217113	5086	212110888	K2-34	5,16,18	44, 45, 46, 71, 72		
203289099	5111	212081533	K2-344[†]	16	44, 45, 46, 72		
456945304	5559	210797580	K2-370	13	43, 44, 70, 71		
366622912	515	211399359	K2-371	5,18	7, 34, 44, 45, 46, 72		
250977648	-	206247743	K2-39	3	42		
9030119	4549	245995977	K2-390	12	2, 29, 42, 70		
365007485	-	248758353	K2-403	14	45, 46, 72		
149496868	5116	248874928	K2-405	14	45, 46, 72		
443616612	5523	201205469	K2-43[†]	1	36, 45, 46, 63, 72		
366568760	5121	211351816	K2-97	5, 18	7, 44, 45, 46, 61, 72		
380907135	4536	220303276	WASP-118	8	42, 43, 70		

[†] The host stars in these systems were classed as low mass ($\lesssim 0.6\ M_{\odot}$), so we did not include the SEDs in the global fits. See Section 4.3 and 2.4 for details.

`keplerspline` to correct for remaining stellar variability (Vanderburg & Johnson, 2014). For systems with a quoted contamination ratio on ExoFOP we allowed for a dilution term to be fitted. We scoured the literature for any previously published RVs for each system, only including data sets that have at least four measurements to protect from overfitting.

For the global fits with `EXOFASTv2` (Eastman et al., 2013; Eastman, 2017; Eastman et al., 2019), we placed Gaussian priors on stellar metallicity, preferentially using measurements from TRES (Fűrész, 2008) for consistency within our catalog. Extinction was taken into account by including uniform priors with bounds from 0 to an upper limit taken from Schlegel et al. (1998) and Schlafly & Finkbeiner (2011), and Gaussian priors for parallax were used from Gaia EDR3 (Gaia Collaboration et al., 2016, 2021), accounting for the small systematic offset from Lindegren et al. (2021). Each host star was modeled via MIST evolution models (Paxton et al., 2011, 2013, 2015; Choi et al., 2016; Dotter, 2016), except in the cases of low-mass stars ($\sim 0.6 M_{\odot}$) where these models are not reliable (Mann et al., 2015). For these stars, we excluded the SED from the fit, set 5% Gaussian priors on M_* and R_* from their relationship with K_S(Mann et al., 2015, 2019), and placed a Gaussian prior of 0.2 on the limb darkening coefficients (Patel & Espinoza, 2022). We consider a fit to be converged once it reaches the thresholds of $T_Z > 1000$ and a Gelmin-Rubin value < 1.02, as well as passing visual inspections of the resulting models, PDFs, and MCMC chains.

One major difference in this sample compared to the previous batches is the inclusion of multiplanet and binary systems, the latter being a recent addition to the capabilities of `EXOFASTv2`. To account for multiple planets in a light curve, we masked all transits for all planets before flattening the light curve as described previously. For binary systems that are blended, the combined SED is modeled by including the broadband photometry for both stars in the global fit, allowing for parameters for each star to be modeled.

4.4 Results and Discussion

add plots: transits, rvs, side by side plot showing ephemeris improvement for all targets. add tables: literature, ephemeris, all exofast output

The updated parameters for all systems can be found in Tables 4.3-4.9. On average, we were able to improve the average $3\sigma_{2030}$ uncertainties on the ephemerides from 9.34 hours to 26 minutes (Figures 4.2-4.5). We compare the ephemerides to those from the discovery data sets from NEA to highlight the severity of ephemeris degradation when left unchecked. The significantly improved ephemerides mean these planets are accessible for JWST observations throughout the expected mission lifetime.

An advantage of the K2 catalog is the diversity of the systems that it targeted. The sample in this analysis consists of 32 systems with host stars ranging from M dwarfs through FGK spectral types, and planets ranging from Earth-like rocky planets all the way to gas giants (Figure 4.6). In this sense, the K2 & TESS Synergy will result in a self-consistent catalog of a plethora of system architectures (wrong word but i'm falling asleep).

4.4.1 Notes on the sample

None of the planets in the current Synergy sample have been observed for transmission spectroscopy, but there are a number of unique systems that would benefit from atmospheric characterization. Figure 4.7 shows the TSM for JWST transmission spectroscopy targets and Synergy planets as a function of orbital period. The TSM values for Synergy systems are relatively high in this distribution, showing that these planets are as well-suited to characterization efforts as current JWST targets.

Below, we briefly discuss individual and groups of systems of note within the sample. A more in-depth evaluation of the giant planets in the sample is given in Section 4.5.

4.4.1.1 Bimodal stellar masses

K2-234 and K2-261 both have bidmodal solutions for stellar mass, which is likely a result of the host stars being in a transitional point between their main-sequence and red giant phases. For both of these systems, we adopt the stellar mass with the higher likelihood going forward, but present both results and their respective probabilities in the exofast tables.

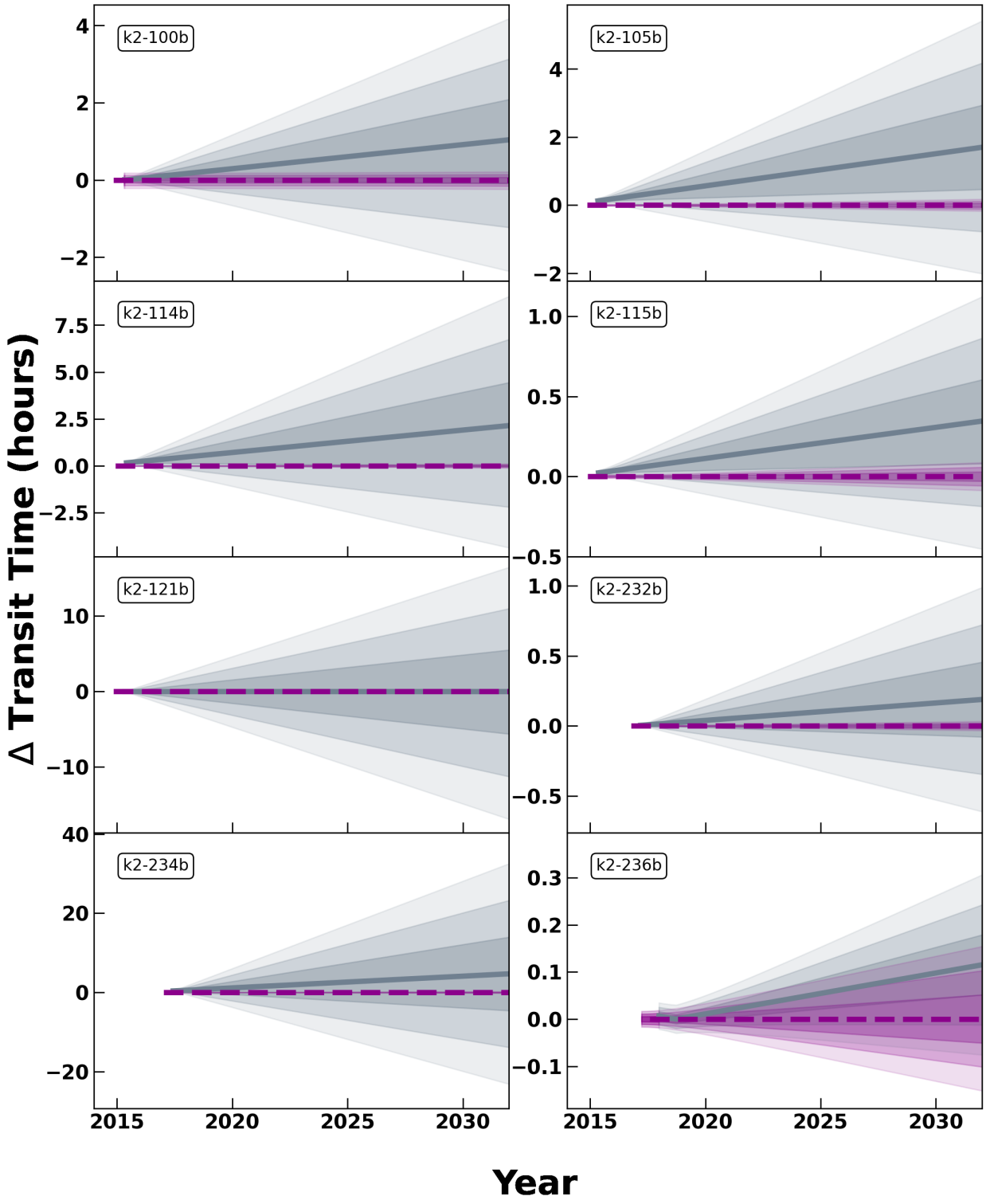

Figure 4.2 Projected uncertainties for the transits in the current sample. The shaded regions represent up to the 3σ level of uncertainty, which are shown for the discovery ephemeris (gray) and our updated ephemeris (purple).

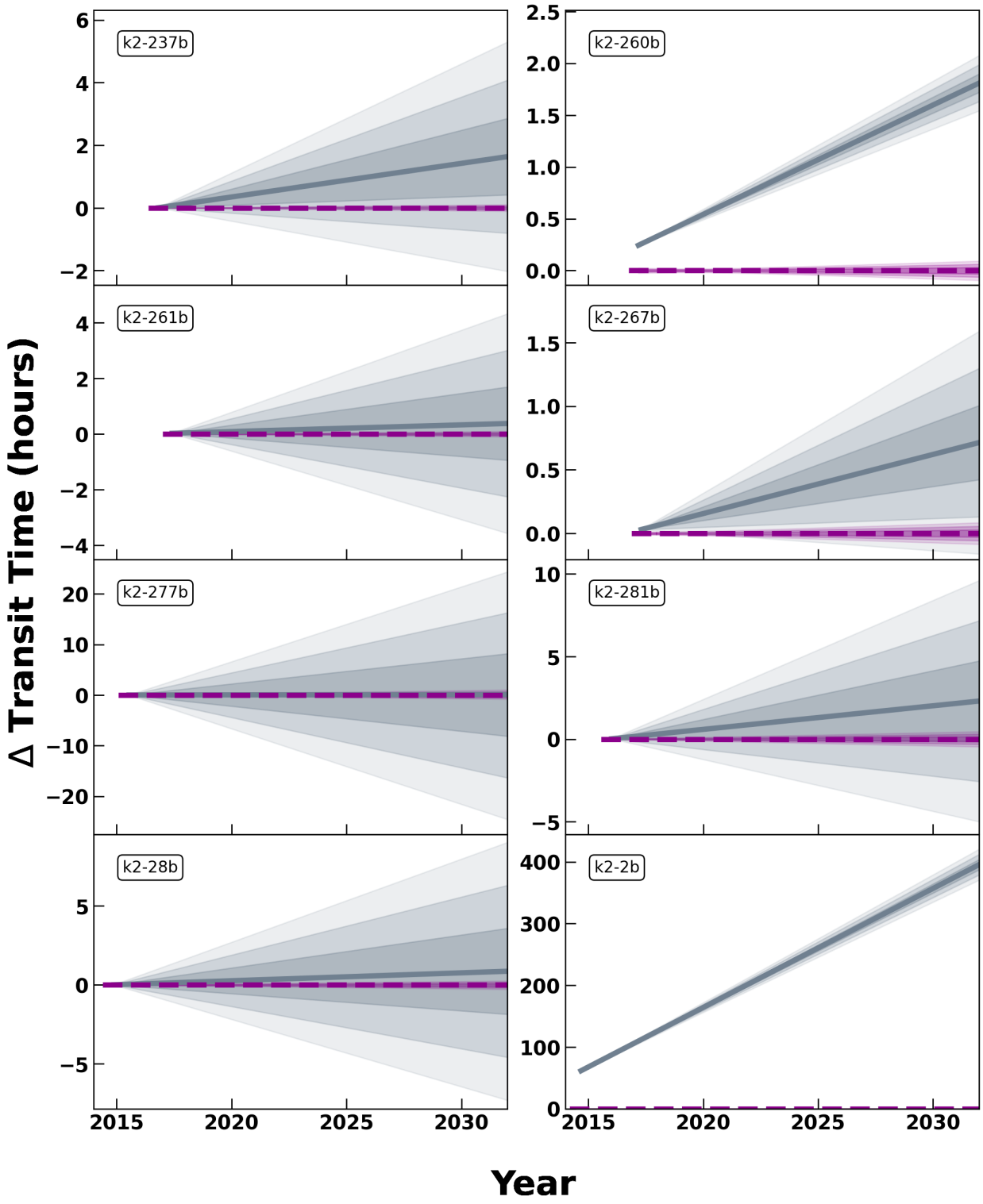

Figure 4.3 Continuation of ephemeris plots.

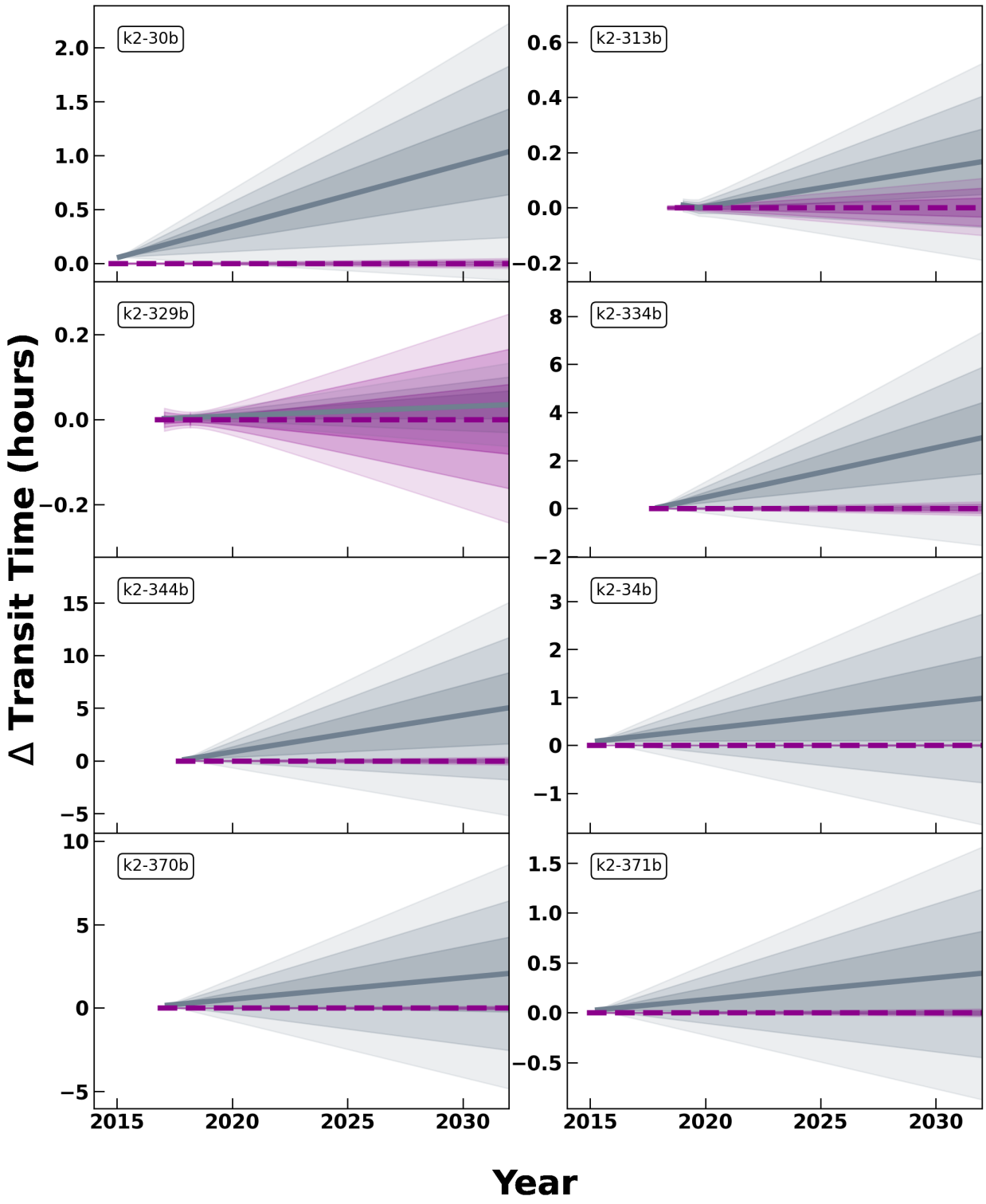

Figure 4.4 Continuation of ephemeris plots.

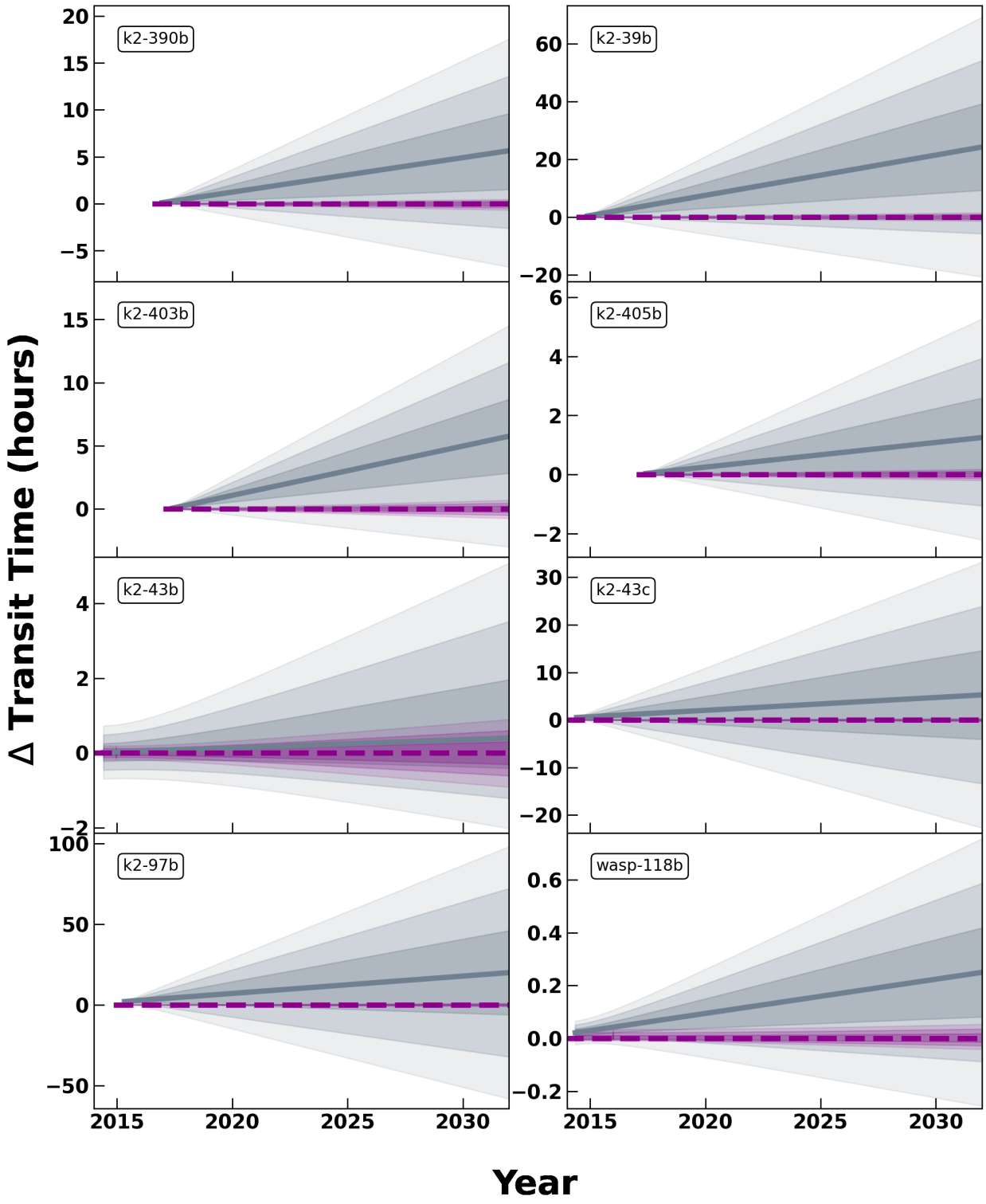

Figure 4.5 Continuation of ephemeris plots.

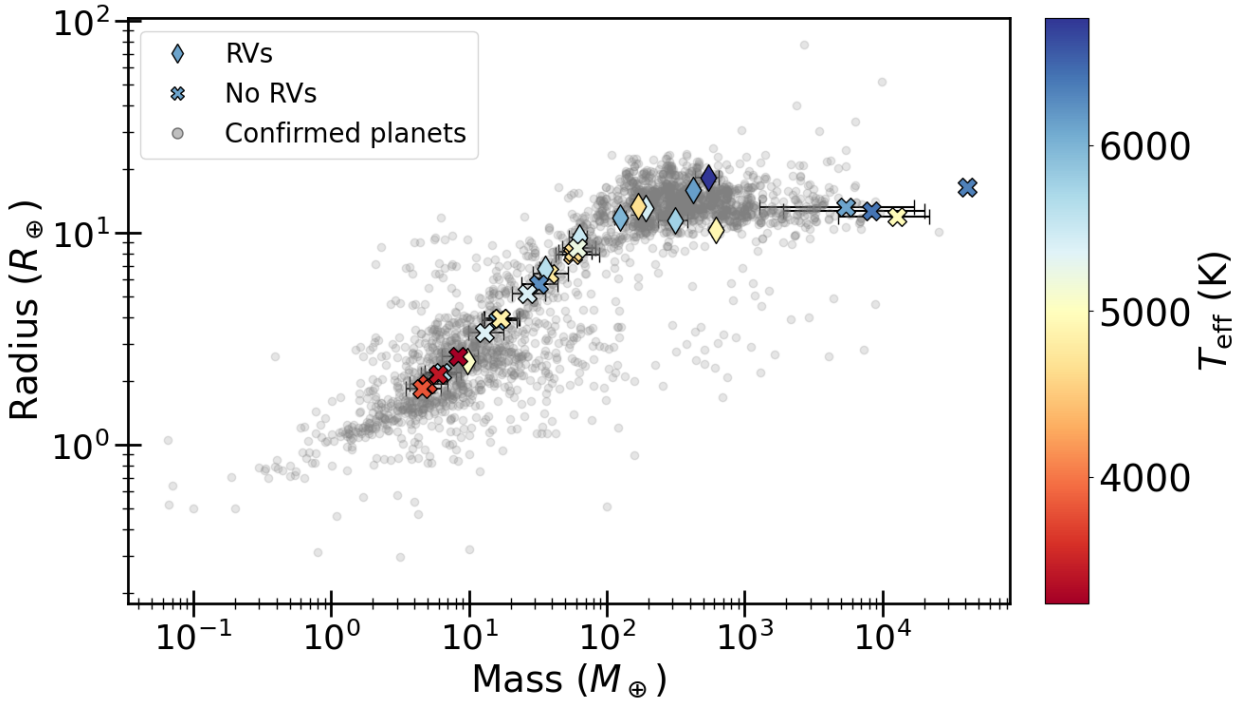

Figure 4.6 Radius versus mass for all confirmed exoplanets (gray; values taken from the NEA, accessed 12 January, 2025) and those in the Synergy sample with completed fits. Systems with measured masses are represented by diamonds, while those with masses from the Chen & Kipping (2017) mass-radius relations are shown as crosses. The markers are colored by the host star temperature.

4.4.1.2 Recently validated planets

While the K2 mission was retired seven years ago, there are still 975 planet candidates that are yet to be validated[1]. K2-344 b was recently validated by de Leon et al. (2021), and Christiansen et al. (2022) validated K2-370 b, K2-371 b, K2-390 b, K2-403 b, and K2-405 b. As the validation process involves using photometric data only from K2, these planets suffer from high ephemeris uncertainties (Figure 4.4 and 4.5), despite being fairly recent discoveries. The fact that six recently-validated planets are amongst the top atmospheric targets in the K2 catalog suggests there are more hidden gems in the K2 candidate list.

4.4.1.3 Low-mass ($< 4R_\oplus$) planets

Several super-Earths and sub-Neptunes in the sample would be interesting targets for follow-up. K2-313 b ($5.9M_\oplus$, $2.1R_\oplus$) and K2-344 b ($4.5M_\oplus$, $1.8R_\oplus$) are both sub-Neptunes on a 5.75 and

[1]From the NEA, accessed January 26, 2025. https://exoplanetarchive.ipac.caltech.edu/

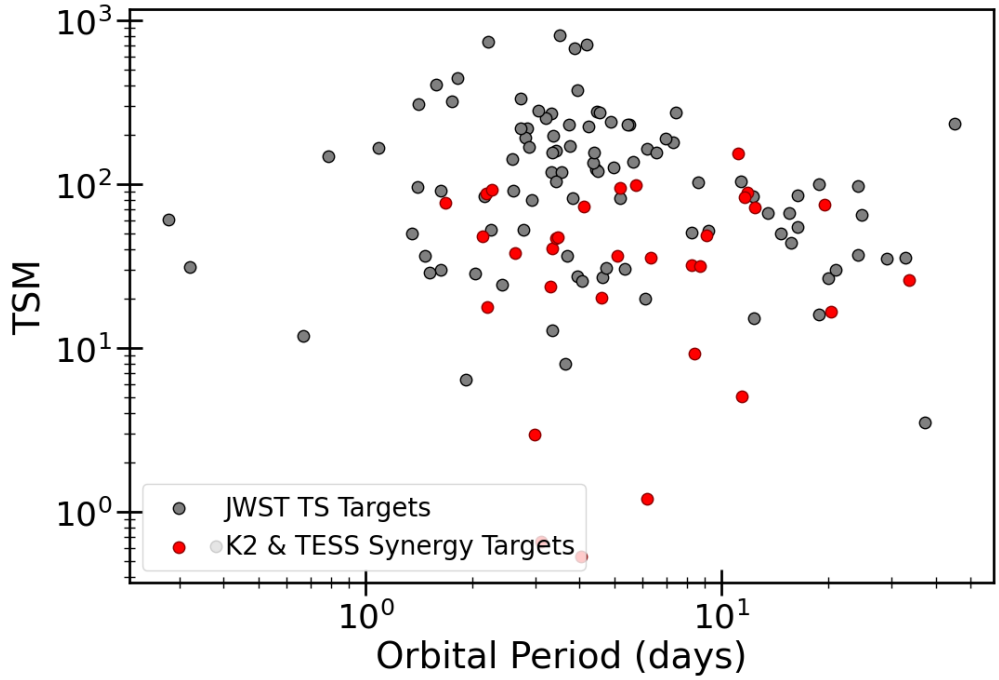

Figure 4.7 TSM versus orbital period for all transmission spectroscopy targets with JWST as of the end of Cycle 3 (gray) and the current batch of planets in the Synergy sample (red).

3.4 day period, respectively. They both orbit M dwarfs, and sit in the radius valley - an empirical sparsity of planets with radii $\sim 1.5 - 2R_{\oplus}$ (Fulton et al., 2017), thought to be a result of mass loss from photoevaporation. K2-313 b has a high TSM of 97.9, making it a prime candidate for JWST observations, while K2-344 has a lower TSM of 40.6, which is still higher than multiple JWST targets.

K2-43 is an M dwarf that is host to two sub-Neptunes (with another planet candidate to be confirmed) that straddle the higher-mass distribution of the radius valley. K2-43 c is on a 2.2 day period and is the inner planet of the system as it was validated more recently than K2-43 b, which has a 3.5 day period. K2-43 c ($5.0M_{\oplus}$, $1.9R_{\oplus}$) is in the radius valley, while K2-43 b ($14.6M_{\oplus}$, $3.6R_{\oplus}$) sits on the high-radius tail. Studying the atmospheres of these planets would allow for a unique comparison between sub-Neptune compositions that have likely undergone similar evolutionary histories.

K2-2 b was part of a previous K2 & TESS Synergy paper (Chapter 3; Thygesen et al. 2024), and originally had an incorrect ephemeris due to a spurious transit in a second light curve used

during validation. It sits at the peak of the sub-Neptune distribution of the radius valley (Fulton et al., 2017), and has the fifth highest TSM (48.7) of all K2 sub-Neptunes ($R_P = 2.0 - 3.0 R_\oplus$).

K2-100 b ($16.2 M_\oplus$, $3.9 R_\oplus$) and K2-105 b ($12.9 M_\oplus$, $3.4 R_\oplus$) are hot Neptunes with orbital periods of 1.7 days and 8.3 days, respectively. They both orbit G dwarf host stars. Due to its close proximity to the host star, K2-100 b is experiencing mass loss via to photoevaporation (Barragán et al., 2019). Its TSM is 76.3, which makes in an ideal candidate for studying planets undergoing rapid mass loss. K2-105 b has a lower TSM of 31.9, but this is still higher than many current JWST targets.

4.5 Example of Detailed Characterization Using the K2 & TESS Synergy

One aspect of exoplanet evolution that can be studied with the aid of the K2 & TESS Synergy is giant planet migration. While not a focus of this thesis, this is an example of a pertinent question that can be investigated using our sample. Below, we discuss giant planet formation and evolution, and present a key scientific question and how updated results from the Synergy survey allow us to pursue future characterization.

4.5.1 Hot Jupiter Formation and Evolution

Giant planets make up a third of all currently confirmed exoplanets, but there are still many open questions surrounding their origins and evolutionary mechanisms. Of the ~1500 known giant planets, ~550 are hot Jupiters (HJs), giant planets that orbit their host stars with periods of ≤ 10 days. These are widely thought to have formed outside of the ice line, then migrated inward to their current short-period orbits. Two predominant theories for the facilitation of migration are dynamical interactions and gas-disk migration. Gas giants that have experienced dynamical or secular interactions with other stars or planets will have their eccentricities increased, such that their periastron distances become small enough to be affected by tides, and thus get placed on short periods as their orbits circularize over time (this is known as "High Eccentricity Migration [HEM], Rasio & Ford, 1996; Fabrycky & Tremaine, 2007; Wu & Lithwick, 2011). HJs that have undergone these violent interactions tend to be the only known planets on short periods in their systems (Huang et al., 2016), having disrupted planet formation and existing inner planets as they

moved inward. In contrast, planetary migration through the gas disk is generally predicted to be smooth, maintaining fairly circular orbits throughout the process, and is expected to result in low eccentricity close-in orbits (D'Angelo et al., 2003).

Using a combination of photometric and spectroscopic results, we can look for evidence that a planet has undergone HEM (e.g. high eccentricity, short orbital period, orbital misalignment), but since many mechanisms can influence these properties, it is not typically conclusive for any individual system. For example, high primordial eccentricities—evidence of dynamical migration—can be erased as tidal interaction circularizes the short-period ($\lesssim$ 5-day) orbit(Adams & Laughlin, 2006). At longer periods ($\gtrsim$5 days), circularization timescales would be a few billion years, up to even longer than the age of the Universe. Therefore, the presence of highly-eccentric (e>0.3) hot Jupiters with periods longer than about 5 days would indicate that HEM is important for migration. Interestingly, recent work looking at the hot Jupiter population from NASA's TESS mission is consistent with HEM as the dominant migration method (Rodriguez et al., 2021, 2022b; Yee et al., 2022a,b; Rice et al., 2022a,b). However, understanding the evolutionary history of any individual system has been a challenge.

Although the population of hot Jupiters shows characteristics of being dominated by HEM, comparative studies of specific systems may distinguish individual evolutionary histories that can be informative for modeling planetary migration. Specifically, the atmospheric composition of a planet can provide constraints on the planet's formation location, which, combined with its orbital architecture, can lead to a detailed understanding of a planet's evolutionary pathway. A popular diagnostic that is feasible with current instrumentation is to measure the carbon-to-oxygen ratio (C/O) of the planetary atmosphere. Carbon and oxygen-bearing molecules (particularly CO, CO_2, H_2O and CH_4) have readily observable line features and will freeze out at different distances from their host star (Figure 4.8). Therefore, the abundance of these molecules in the gas state within the atmosphere of the planet can place constraints on where the planet formed in relation to the respective snowlines, potentially suggesting some systems may have formed in-situ. Although absolute measurements of carbon and oxygen do not entirely uncover the planet's

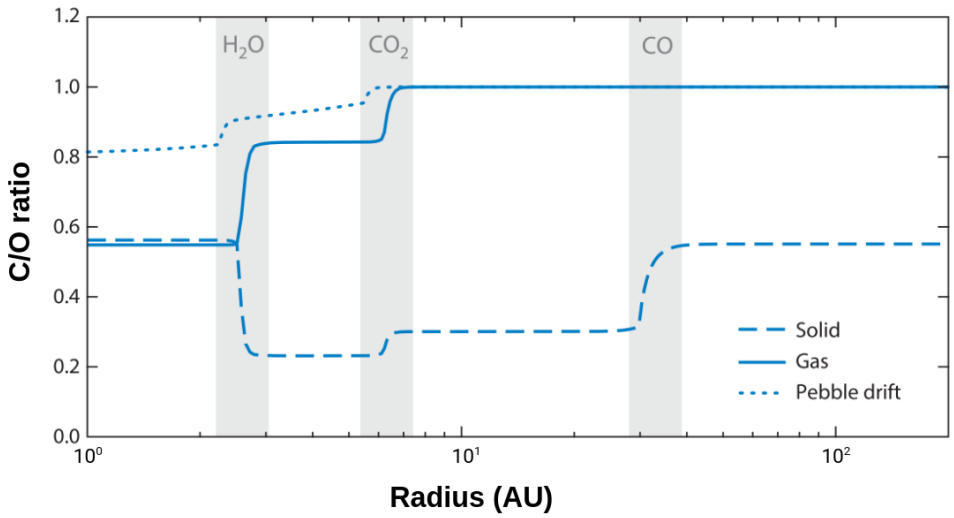

Figure 4.8 The predicted C/O ratios as a function of distance from the host star for a migrating giant planet (Figure 8a from Madhusudhan 2019). The C/O ratio is shown for the abundance in the gas phase (solid line) and solid phase (dashed line), as well as enhancement due to pebble drift (dotted line). The shaded regions represent snowlines. Planets that form within or migrate through different regions of the disk should possess distinct C/O ratios.

formation history, as they can depend on evolution models that are not yet well defined, we can now start to systematically compare these measurements for planets with different migration histories, as many HJs have been or are scheduled to be observed by JWST. Comparison of the atmospheric chemical composition of highly eccentric HJs to circular ones or those with nearby small companions can detect differences indicative of changes in their evolutionary history.

Over the past decade, there have been many studies into the possible interpretations of different C/O ratios. The strength of the C/O ratio and the abundances of C and O compared to Solar (C/O=0.54; Asplund et al. 2009), along with metallicity (C/H and C/O, typically associated with the abundance of CO_2 and H_2O; Lodders & Fegley 2002; Zahnle et al. 2009; Moses et al. 2013; Madhusudhan & Seager 2011), are thought to be linked to the initial formation mechanism (core accretion or gravitational instability) paired with when and whether migration occurred (e.g. whether the protoplanetary disk still existed at the time of migration; Madhusudhan et al. 2014). Accretion of pebbles and planetesimals can also affect the atmospheric composition, as the molecules originally locked in the solid phase sublimate, while the planet migrates through

successive snowlines.

A planet that formed through core accretion and then migrated through the disk, subsequently accreting planetesimals that enriched the atmosphere, is expected to have a subsolar C/O ratio and supersolar metallicity (Madhusudhan et al., 2014; Öberg et al., 2011). Formation beyond the CO and CO_2 snowlines followed by migration after the disk has dissipated is likely to result in C/O$\sim$1 and subsolar metallicity (Madhusudhan et al., 2017). If gas accretion occurred close to the CO or CO_2 snowlines, or if a significant amount of carbon-bearing grains was accumulated, both the resulting C/O ratio and metallicity are expected to be supersolar (Öberg et al., 2011). However, planets that underwent significant pebble accretion during disk migration, e.g. those that may have formed via gravitational instability far from the host star ($\gtrsim$20 AU), can display a range of both metallicity and C/O (Madhusudhan et al., 2014; Mordasini et al., 2016; Helled & Bodenheimer, 2010). Finally, hot Jupiters that formed within the H_2O snowline and carbon-grain evaporation line would likely have compositions reflecting that of the host star Öberg et al. (2011).

4.5.2 K2 & TESS Synergy Jupiters in the context of migration

The K2 & TESS Synergy sample contains several ideal targets for future JWST observations with the goal of studying giant planet migration. There are 19 giant planets ($> 4R_\oplus$) in the present K2 & TESS Synergy sample (Table 4.2). Four of these (K2-97 b, K2-232 b, K2-234 b, K2-261 b) have significant non-zero eccentricities considering the Lucy-Sweeney bias (Lucy & Sweeney, 1971), and have <12-day periods. Comparing the atmospheric compositions of the eccentric planets, which are likely undergoing HEM, to ones on circular orbits could potentially identify characteristics indicative of the differing migration histories. Figure 4.9 shows the eccentricity-period distribution of all planets with radii $> 4R_\oplus$ that will be observed for transmission spectra by JWST the end of Cycle 3, compared to those in the K2 & TESS Synergy.

Systems like TOI-1130 are ideal for the comparison between eccentric and circular HJs, as it is host to a sub-Neptune (0.06 M_J, 0.3 R_J) on a 4.1 day period, with an outer Jupiter (1.0 M_J, 1.2 R_J) on an 8.4 day period (Huang et al., 2020; Korth et al., 2023). The existence of two differently sized planets both on short-period, low-eccentricity (<0.2) orbits has the implication of a dynamically

System	M_* ($M_\odot$)	R_* ($R_\odot$)	$T_{\rm eff,*}$ (K)	[Fe/H]$_*$ (dex)	Period (days)	M_p (M_J)	R_p (R_J)	e	$T_{{\rm eq},p}$ (K)
K2 & TESS Synergy giants									
K2-30 b	0.94	0.94	5432	0.18	4.10	0.60	1.17	0	1144
K2-34 b	1.12	1.37	6110	0.01	3.0	1.70	1.17	0.11	1670
K2-39 b	1.14	3.09	4766	0.43	4.60	0.12	0.57	0.18	1722
K2-97 b	1.11	4.15	4664	0.33	8.41	0.53	1.19	0.21	1577
K2-114 b	0.86	0.82	4919	0.42	11.39	1.94	0.92	0.05	700
K2-115 b	0.87	0.87	5770	-0.23	20.27	0.98	1.02	0.07	695
K2-121 b	0.69	0.68	4551	-0.17	5.19	0.18	0.71	0.19	794
K2-232 b	1.06	1.24	5990	0.03	11.17	0.40	1.04	0.28	1017
K2-234 b	1.23	1.71	5620	0.47	11.81	0.11	0.61	0.26	1072
K2-236 b	1.13	1.38	6070	0.06	19.49	0.09	0.57	0.12	893
K2-237 b	1.22	1.23	6160	0.32	2.18	1.34	1.42	0.04	1761
K2-260 b	1.60	1.79	6770	0.33	2.63	1.71	1.62	0.04	2088
K2-261 b	1.11	1.66	5490	0.37	11.63	0.19	0.86	0.33	1058
K2-267 b	1.38	1.65	6420	0.12	6.18	3.0	1.13	0.26	1469
K2-281 b	0.79	0.75	4682	0.23	8.69	0.18	0.73	0.28	706
K2-329 b	0.85	0.83	5211	0.14	12.46	0.19	0.76	0.19	723
K2-334 b	1.30	1.47	6250	0.23	5.11	0.10	0.51	0.49	1453
K2-371 b	0.76	0.73	4958	-0.02	3.11	40	1.06	0.09	1035
K2-403 b	0.93	0.90	5396	0.20	33.59	0.08	0.46	0.25	554
WASP-118 b	1.43	1.84	6340	0.14	4.05	0.51	1.46	0.35	1728
JWST targets									
WASP-39 b	0.90	0.91	5470	0.02	4.06	0.28	1.27	<0.048	1166
WASP-127 b	1.02	1.33	5920	-0.12	4.18	0.16	1.31	0	1400
TOI-1130 c	0.68	0.69	4250	0.2	8.35	0.97	1.5	0.05	637
KELT-7 b	1.76	1.81	6768	0	2.73	1.39	1.6	0	1801
TRES-4 b	1.08	1.66	6200	0.14	3.55	0.78	1.61	0.02	1761
WASP-15 b	1.18	1.48	6300	-0.17	3.75	0.54	1.41	0.04	1512
NGTS-2 b	1.64	1.70	6478	-0.06	4.51	0.74	1.60	0	1468
HAT-P-30 b	1.55	1.31	6304	0.13	4.81	0.83	1.44	0.04	1487

Table 4.2 Key parameters for giant planets in the K2 & TESS Synergy sample (bold) and potential comparison targets that have or will observed with JWST for transmission spectra. Values for non-Synergy systems are taken from the NASA Exoplanet Archive.

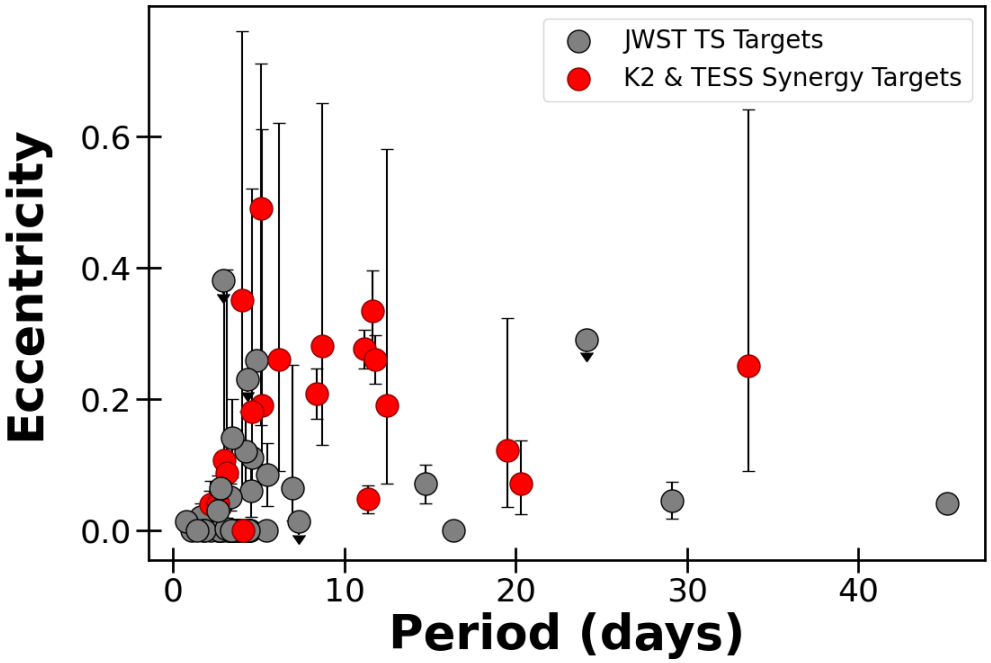

Figure 4.9 Eccentricity as a function of orbital period for giant planets that will have JWST transmission spectra by the end of Cycle 3 (gray) and targets in the K2 & TESS Synergy (red). Circles with error bars have eccentricities measured through RVs, while those with arrows are upper limits. Values for JWST targets are adopted from the NASA Exoplanet Archive.

quiet migration history, as any major interactions should have disrupted this configuration.

We can also compare eccentric HJs (without companions) that are currently on circular orbits, but that likely underwent some form of migration earlier in their life. While high eccentricity is a sign of current HEM, planets on circular orbits that are misaligned with the rotation axis of their host star are candidates for HJs that have completed their HEM, as the misalignment may have been caused by prior dynamical interactions. Therefore, comparing eccentric HJs to ones with different alignments could confirm whether the misaligned planets show signatures of HEM. JWST has observed at least five low-eccentricity HJs with various alignments (see Table 4.2), providing a growing sample of HJs that have undergone different migration mechanisms that could be used to test this theory.

Beyond migration histories, the effects of parameters like stellar metallicity, insolation, and atmospheric inflation may influence the chemical abundances of HJs. JWST HJs in conjunction with the Synergy giant planets span a range of these parameter spaces (see Table 4.2), which adds

to the value of future characterization of these planets. K2-39 b and K2-97 b provide a further point of comparison as the hosts are evolved stars, meaning the effects of late stellar evolution on the planetary atmosphere could be investigated.

4.6 Conclusion

In this chapter, we presented the fourth installment of the K2 & TESS Synergy, reanalyzing 32 K2-discovered systems observed by TESS. These systems were ranked among the highest in terms of their TSM values, making it a timely effort to ensure the most up-to-date ephemerides for characterization observations. Through running global fits for each system including photometry, spectroscopy, and stellar data, we improved the $3\sigma_{2030}$ uncertainties on the ephemerides for these planets from 9.34 hours to 26 minutes.

We highlighted some of the most unique cases in this sample of planets that would be significant additions to planets with JWST transmission spectra. We also discussed a potential avenue for investigating the effects of migration on giant planets via atmospheric compositions, utilizing the updated parameters from the K2 & TESS Synergy and comparing these systems to those already observed using JWST. With so much yet to uncover about the formation and evolution of exoplanets, it is vital that we have up-to-date ephemerides for the planets that are most amenable to atmospheric characterization so that minimal resources are wasted during targeted observations.

Table 4.3 Median values and 68% confidence intervals.

Priors:		k2-100	k2-105	k2-114	k2-115	k2-121
Gaussian	π Gaia Parallax (mas)					
Gaussian	[Fe/H] Metallicity (dex)					
Upper Limit	A_V V-band extinction (mag)					
Gaussian′	D_T Dilution in TESS					
Parameter	**Units**	**Values**				
Stellar Parameters:						
M_*	Mass ($M_\odot$)	$1.15^{+0.062}_{-0.076}$	$0.916^{+0.043}_{-0.036}$	$0.856^{+0.033}_{-0.028}$	$0.87^{+0.048}_{-0.043}$	$0.692^{+0.023}_{-0.022}$
R_*	Radius ($R_\odot$)	$1.199^{+0.054}_{-0.046}$	$0.909^{+0.029}_{-0.027}$	$0.822^{+0.022}_{-0.021}$	$0.871^{+0.032}_{-0.027}$	$0.681^{+0.02}_{-0.019}$
L_*	Luminosity ($L_\odot$)	$1.663^{+0.065}_{-0.062}$	$0.621^{+0.021}_{-0.02}$	$0.356^{+0.016}_{-0.015}$	$0.753^{+0.089}_{-0.059}$	$0.1792^{+0.006}_{-0.0059}$
$F_{\rm Bol}$	Bolometric Flux (cgs)	$1.609e-09^{+4.6e-11}_{-4.8e-11}$	5.06 ± 0.15	5.17 ± 0.15	$1.5^{+0.18}_{-0.11}$	$2.016^{+0.063}_{-0.062}$
ρ_*	Density (cgs)	$0.94^{+0.14}_{-0.15}$	$1.72^{+0.18}_{-0.16}$	$2.18^{+0.17}_{-0.16}$	$1.87^{+0.19}_{-0.21}$	$3.09^{+0.27}_{-0.25}$
$\log g$	Surface gravity (cgs)	$4.342^{+0.045}_{-0.058}$	4.483 ± 0.032	4.541 ± 0.024	$4.499^{+0.032}_{-0.039}$	$4.612^{+0.026}_{-0.025}$
$T_{\rm eff}$	Effective Temperature (K)	$5980.0^{+120.0}_{-130.0}$	$5372.0^{+79.0}_{-81.0}$	4919.0 ± 63.0	$5770.0^{+150.0}_{-130.0}$	$4551.0^{+65.0}_{-63.0}$
[Fe/H]	Metallicity (dex)	$0.245^{+0.078}_{-0.079}$	$0.261^{+0.076}_{-0.078}$	$0.417^{+0.036}_{-0.037}$	$-0.228^{+0.04}_{-0.042}$	-0.071 ± 0.027
$[{\rm Fe/H}]_0$	Initial Metallicity[2]	$0.244^{+0.07}_{-0.074}$	$0.257^{+0.074}_{-0.077}$	$0.392^{+0.044}_{-0.046}$	$-0.196^{+0.052}_{-0.054}$	$-0.052^{+0.044}_{-0.045}$
Age	Age (Gyr)	$3.2^{+3.3}_{-2.2}$	$8.0^{+3.6}_{-3.9}$	$8.5^{+3.5}_{-3.4}$	$6.4^{+4.2}_{-3.4}$	$9.7^{+2.8}_{-4.0}$
EEP	Equal Evolutionary Phase[3]	$362.0^{+49.0}_{-41.0}$	$365.0^{+26.0}_{-25.0}$	$350.0^{+21.0}_{-16.0}$	$352.0^{+35.0}_{-18.0}$	$338.7^{+6.8}_{-14.0}$
A_V	V-band extinction (mag)	$0.05^{+0.023}_{-0.031}$	$0.045^{+0.027}_{-0.03}$	$0.051^{+0.027}_{-0.033}$	$0.119^{+0.13}_{-0.084}$	0.054 ± 0.037
$\sigma_{\rm SED}$	SED photometry error scaling	$0.7^{+0.29}_{-0.18}$	$0.67^{+0.27}_{-0.17}$	$1.09^{+0.49}_{-0.29}$	$3.15^{+1.1}_{-0.71}$	$1.14^{+0.49}_{-0.29}$
ϖ	Parallax (mas)	5.498 ± 0.068	5.048 ± 0.039	2.129 ± 0.035	2.496 ± 0.025	5.931 ± 0.036
d	Distance (pc)	$181.9^{+2.3}_{-2.2}$	198.1 ± 1.5	$469.8^{+7.7}_{-7.5}$	$400.6^{+4.0}_{-3.9}$	168.6 ± 1.0
Planetary Parameters:						
P	Period (days)	$1.67390408^{+4.1e-07}_{-4e-07}$	$8.2669911^{+3.6e-06}_{-3.5e-06}$	$11.3909346 \pm 3.2e-06$	$20.2729891 \pm 4.3e-06$	$5.18575418 \pm 3.2e$
R_P	Radius ($R_{\rm J}$)	$0.346^{+0.024}_{-0.025}$	$0.301^{+0.013}_{-0.01}$	$0.922^{+0.027}_{-0.024}$	$1.021^{+0.038}_{-0.033}$	$0.705^{+0.022}_{-0.021}$
M_P	Mass ($M_{\rm J}$)	$0.051^{+0.019}_{-0.012}$	$0.0405^{+0.015}_{-0.0094}$	1.94 ± 0.12	$0.98^{+0.22}_{-0.24}$	$0.177^{+0.1}_{-0.043}$
T_C	Time of conjunction[4] ($\rm BJD_{TDB}$)	$2457140.7192^{+0.0025}_{-0.003}$	$2457147.99024 \pm 0.00048$	$2457140.32391 \pm 0.00022$	$2458495.17362 \pm 0.00027$	$2457143.5602^{+0.000}_{-0.00}$
T_T	Time of minimum projected separation[5] ($\rm BJD_{TDB}$)	$2457140.71924 \pm 0.00019$	$2457635.74272 \pm 0.00033$	$2457675.69783 \pm 0.00017$	$2457582.88915 \pm 0.00015$	$2457641.392634^{+5.4e}_{-4.7}$
T_0	Optimal conjunction Time[6] ($\rm BJD_{TDB}$)	$2457137.3714^{+0.0025}_{-0.003}$	$2457635.74315 \pm 0.00032$	$2457675.69837 \pm 0.00017$	$2457582.88991 \pm 0.00015$	$2457641.392895^{+4.1e}_{-4.4}$
a	Semi-major axis (AU)	$0.02891^{+0.00051}_{-0.00065}$	$0.0777^{+0.0012}_{-0.001}$	$0.0941^{+0.0012}_{-0.001}$	$0.1389^{+0.0025}_{-0.0023}$	$0.05193^{+0.00077}_{-0.00061}$
i	Inclination (Degrees)	$81.2^{+1.2}_{-1.9}$	$89.07^{+0.62}_{-0.66}$	$89.64^{+0.24}_{-0.27}$	$88.822^{+0.078}_{-0.1}$	$87.74^{+0.18}_{-0.5}$
e	Eccentricity	$0.34^{+0.29}_{-0.22}$	$0.17^{+0.37}_{-0.14}$	0.047 ± 0.021	$0.07^{+0.066}_{-0.046}$	$0.19^{+0.42}_{-0.12}$
ω_*	Argument of Periastron (Degrees)	$-131.0^{+110.0}_{-91.0}$	$-131.0^{+110.0}_{-65.0}$	$-6.0^{+43.0}_{-34.0}$	$135.0^{+50.0}_{-87.0}$	$-204.0^{+64.0}_{-120.0}$
T_{eq}	Equilibrium temperature[7] (K)	$1859.0^{+25.0}_{-22.0}$	$885.9^{+9.0}_{-9.1}$	700.8 ± 7.6	$695.0^{+18.0}_{-14.0}$	$794.2^{+7.5}_{-7.9}$
$\tau_{\rm circ}$	Tidal circularization timescale (Gyr)	$0.085^{+0.18}_{-0.081}$	$280.0^{+210.0}_{-270.0}$	$295.0^{+46.0}_{-45.0}$	$1030.0^{+390.0}_{-410.0}$	1.9 ± 1.8
K	RV semi-amplitude (m/s)	$8.8^{+3.7}_{-3.3}$	$4.6^{+2.1}_{-1.2}$	$194.0^{+10.0}_{-11.0}$	$79.0^{+17.0}_{-19.0}$	$29.4^{+25.0}_{-8.1}$
R_P/R_*	Radius of planet in stellar radii	$0.0297^{+0.0014}_{-0.0018}$	$0.03383^{+0.00094}_{-0.0004}$	$0.11519^{+0.001}_{-0.00073}$	0.1204 ± 0.0011	0.1064 ± 0.0011
a/R_*	Semi-major axis in stellar radii	$5.19^{+0.24}_{-0.29}$	18.4 ± 0.61	$24.65^{+0.62}_{-0.63}$	$34.4^{+1.1}_{-1.4}$	$16.43^{+0.46}_{-0.44}$
δ	$(R_P/R_*)^2$	$0.000882^{+8.2e-05}_{-0.0001}$	$0.001145^{+6.5e-05}_{-2.7e-05}$	$0.01327^{+0.00023}_{-0.00017}$	0.0145 ± 0.00027	$0.01133^{+0.00023}_{-0.00024}$
$\rm Depth_{K2}$	Flux decrement at mid transit for K2	$0.000846^{+1.5e-05}_{-2.1e-05}$	$0.001469 \pm 2.7e-05$	0.01856 ± 0.00027	$0.01549^{+0.00029}_{-0.00028}$	$0.01435^{+0.00031}_{-0.0003}$
$\rm Depth_{TESS}$	Flux decrement at mid transit for TESS	$0.000855^{+2.3e-05}_{-2e-05}$	$0.001386^{+2.5e-05}_{-2.7e-05}$	0.0172 ± 0.00029	0.01524 ± 0.00027	0.01334 ± 0.0002
τ	Ingress/egress transit duration (days)	$0.0056^{+0.003}_{-0.0026}$	$0.00508^{+0.0015}_{-0.0004}$	$0.01712^{+0.0011}_{-0.00041}$	$0.0303^{+0.0014}_{-0.0015}$	$0.01243^{+0.0008}_{-0.00082}$
T_{14}	Total transit duration (days)	0.0696 ± 0.0024	$0.1435^{+0.0016}_{-0.0012}$	$0.16241^{+0.00098}_{-0.00085}$	$0.1617^{+0.001}_{-0.0011}$	$0.08865^{+0.00058}_{-0.00062}$
b	Transit Impact parameter	$0.809^{+0.068}_{-0.18}$	$0.28^{+0.23}_{-0.19}$	$0.15^{+0.12}_{-0.1}$	$0.681^{+0.016}_{-0.019}$	$0.584^{+0.03}_{-0.036}$
ρ_P	Density (cgs)	$1.54^{+0.56}_{-0.36}$	$1.83^{+0.65}_{-0.42}$	$3.07^{+0.34}_{-0.32}$	$1.13^{+0.3}_{-0.31}$	$0.63^{+0.36}_{-0.15}$
$\log g_P$	Surface gravity	$3.02^{+0.11}_{-0.11}$	$3.04^{+0.13}_{-0.11}$	$3.753^{+0.036}_{-0.038}$	$3.366^{+0.095}_{-0.13}$	$2.95^{+0.19}_{-0.12}$
T_S	Time of eclipse ($\rm BJD_{TDB}$)	$2457139.87^{+0.37}_{-0.44}$	2457143.9 ± 1.5	$2457134.92^{+0.13}_{-0.16}$	$2458505.01^{+0.69}_{-0.93}$	$2457146.11^{+0.93}_{-1.4}$
$T_{S,14}$	Total eclipse duration (days)	$0.0685^{+0.0058}_{-0.012}$	$0.132^{+0.016}_{-0.036}$	$0.1613^{+0.008}_{-0.0084}$	$0.1647^{+0.0028}_{-0.0037}$	$0.0914^{+0.0049}_{-0.021}$
$e\cos\omega_*$		$-0.01^{+0.34}_{-0.41}$	$-0.0^{+0.28}_{-0.29}$	$0.04^{+0.018}_{-0.022}$	$-0.023^{+0.053}_{-0.072}$	$-0.01^{+0.29}_{-0.43}$

Table 4.4 Median values and 68% confidence intervals.

Priors:		k2-2	k2-232	k2-234	k2-236	k2-237
Gaussian	π Gaia Parallax (mas)					
Gaussian	[Fe/H] Metallicity (dex)					
Upper Limit	A_V V-band extinction (mag)					
Gaussian′	D_T Dilution in TESS					
Parameter	Units	Values				
Stellar Parameters:						
M_*	Mass ($M_\odot$)	$0.8^{+0.033}_{-0.03}$	$1.057^{+0.073}_{-0.069}$	$1.255^{+0.074}_{-0.12}$	$1.132^{+0.076}_{-0.078}$	$1.215^{+0.058}_{-0.064}$
R_*	Radius ($R_\odot$)	$0.758^{+0.024}_{-0.022}$	$1.236^{+0.04}_{-0.039}$	$1.706^{+0.067}_{-0.062}$	$1.378^{+0.053}_{-0.051}$	$1.231^{+0.043}_{-0.036}$
L_*	Luminosity ($L_\odot$)	$0.3364^{+0.01}_{-0.0095}$	$1.77^{+0.17}_{-0.14}$	$2.624^{+0.088}_{-0.087}$	$2.321^{+0.095}_{-0.097}$	$1.97^{+0.25}_{-0.2}$
$F_{\rm Bol}$	Bolometric Flux (cgs)	$2.757e-09^{+8.1e-11}_{-7.6e-11}$	$3.39^{+0.32}_{-0.27}$	$4.91e-09 \pm 1.5e-10$	$2.298^{+0.088}_{-0.092}$	$6.88^{+0.83}_{-0.65}$
ρ_*	Density (cgs)	$2.59^{+0.26}_{-0.24}$	$0.789^{+0.099}_{-0.087}$	$0.353^{+0.051}_{-0.053}$	$0.609^{+0.093}_{-0.081}$	$0.918^{+0.078}_{-0.088}$
$\log g$	Surface gravity (cgs)	$4.582^{+0.03}_{-0.031}$	4.278 ± 0.041	$4.071^{+0.044}_{-0.059}$	$4.213^{+0.048}_{-0.049}$	$4.342^{+0.024}_{-0.032}$
$T_{\rm eff}$	Effective Temperature (K)	$5048.0^{+79.0}_{-78.0}$	$5990.0^{+150.0}_{-130.0}$	5620.0 ± 110.0	6070.0 ± 120.0	$6160.0^{+160.0}_{-140.0}$
[Fe/H]	Metallicity (dex)	$-0.0^{+0.045}_{-0.039}$	$0.032^{+0.063}_{-0.05}$	$0.469^{+0.046}_{-0.059}$	$0.063^{+0.07}_{-0.059}$	0.322 ± 0.076
$[Fe/H]_0$	Initial Metallicity[2]	0.0 ± 0.055	$0.084^{+0.059}_{-0.053}$	$0.449^{+0.036}_{-0.054}$	$0.127^{+0.06}_{-0.056}$	0.307 ± 0.068
Age	Age (Gyr)	$5.5^{+5.0}_{-3.9}$	$6.3^{+3.2}_{-2.6}$	$5.3^{+2.8}_{-1.3}$	$5.2^{+2.7}_{-2.0}$	$2.1^{+1.8}_{-1.1}$
EEP	Equal Evolutionary Phase[3]	$335.0^{+16.0}_{-34.0}$	$410.0^{+19.0}_{-35.0}$	$421.0^{+34.0}_{-20.0}$	$415.0^{+21.0}_{-39.0}$	$345.0^{+37.0}_{-25.0}$
A_V	V-band extinction (mag)	$0.045^{+0.035}_{-0.031}$	$0.18^{+0.11}_{-0.1}$	$0.06^{+0.034}_{-0.039}$	$0.075^{+0.035}_{-0.046}$	$0.22^{+0.14}_{-0.13}$
$\sigma_{\rm SED}$	SED photometry error scaling	$0.76^{+0.32}_{-0.19}$	$0.68^{+0.32}_{-0.2}$	$0.88^{+0.31}_{-0.2}$	$0.58^{+0.22}_{-0.14}$	$1.83^{+0.73}_{-0.46}$
ϖ	Parallax (mas)	16.004 ± 0.046	7.739 ± 0.02	7.646 ± 0.045	5.563 ± 0.039	$3.304^{+0.068}_{-0.067}$
d	Distance (pc)	62.48 ± 0.18	129.22 ± 0.33	$130.79^{+0.78}_{-0.77}$	$179.8^{+1.3}_{-1.2}$	$302.6^{+6.3}_{-6.1}$
Planetary Parameters:						
P	Period (days)	$9.1004157^{+4.1e-06}_{-4.5e-06}$	$11.1684381 \pm 9.7e-07$	$11.8143898^{+6.2e-06}_{-6e-06}$	$19.4921493^{+7.7e-06}_{-7.6e-06}$	$2.18053328^{+5.8e-0}_{-5.7e-0}$
R_P	Radius (R_J)	—	$1.047^{+0.034}_{-0.033}$	$0.605^{+0.026}_{-0.023}$	$0.568^{+0.024}_{-0.023}$	$1.42^{+0.05}_{-0.044}$
M_P	Mass (M_J)	—	$0.395^{+0.038}_{-0.037}$	0.113 ± 0.011	$0.087^{+0.031}_{-0.033}$	$1.336^{+0.12}_{-0.092}$
T_C	Time of conjunction[4] (BJD_{TDB})	$2456698.13016^{+0.00092}_{-0.0009}$	$2457825.350977^{+5.2e-05}_{-5.4e-05}$	$2459556.00422^{+0.00075}_{-0.0007}$	$2459575.85066^{+0.00097}_{-0.0012}$	$2457656.463919 \pm 3.3e$
T_T	Time of minimum projected separation[5] (BJD_{TDB})	$2456698.13016^{+0.00092}_{-0.0009}$	$2457948.203818 \pm 4.6e-05$	$2459556.0041^{+0.00072}_{-0.00069}$	$2457841.04982 \pm 0.00024$	$2457704.435649 \pm 2.9e$
T_0	Optimal conjunction Time[6] (BJD_{TDB})	$2458072.29291^{+0.00062}_{-0.00061}$	$2457948.20434 \pm 3.5e-05$	$2458374.56525^{+0.0004}_{-0.00039}$	$2457841.05067 \pm 0.00023$	$2457704.435844 \pm 2.8e$
a	Semi-major axis (AU)	$0.0792^{+0.0011}_{-0.001}$	$0.0996^{+0.0023}_{-0.0022}$	$0.1095^{+0.0021}_{-0.0035}$	$0.1477^{+0.0032}_{-0.0035}$	$0.03513^{+0.00055}_{-0.00063}$
i	Inclination (Degrees)	$88.91^{+0.68}_{-0.45}$	$89.67^{+0.23}_{-0.27}$	$89.01^{+0.68}_{-0.83}$	$87.86^{+0.2}_{-0.25}$	$88.53^{+0.96}_{-0.89}$
e	Eccentricity	$0.215^{+0.056}_{-0.094}$	$0.276^{+0.029}_{-0.03}$	$0.259^{+0.038}_{-0.036}$	$0.122^{+0.2}_{-0.087}$	$0.039^{+0.036}_{-0.027}$
ω_*	Argument of Periastron (Degrees)	$88.0^{+19.0}_{-20.0}$	$176.0^{+7.8}_{-7.0}$	$33.9^{+9.5}_{-10.0}$	$-160.0^{+85.0}_{-50.0}$	72.0 ± 43.0
T_{eq}	Equilibrium temperature[7] (K)	$753.2^{+7.1}_{-6.9}$	$1017.0^{+20.0}_{-18.0}$	$1072.0^{+16.0}_{-14.0}$	$893.0^{+13.0}_{-12.0}$	$1761.0^{+47.0}_{-40.0}$
$\tau_{\rm circ}$	Tidal circularization timescale (Gyr)	$1310.0^{+540.0}_{-430.0}$	$14.2^{+4.3}_{-3.6}$	$98.0^{+49.0}_{-37.0}$	$1260.0^{+870.0}_{-840.0}$	$0.023^{+0.0041}_{-0.0043}$
K	RV semi-amplitude (m/s)	3.54 ± 0.42	$36.0^{+3.7}_{-3.5}$	$9.05^{+0.65}_{-0.64}$	$6.2^{+2.2}_{-2.4}$	$184.0^{+15.0}_{-12.0}$
R_P/R_*	Radius of planet in stellar radii	$0.02981^{+0.00079}_{-0.00061}$	$0.08701^{+0.00027}_{-0.00026}$	$0.0364^{+0.00041}_{-0.00026}$	$0.04239^{+0.00049}_{-0.00058}$	$0.11838^{+0.00063}_{-0.00039}$
a/R_*	Semi-major axis in stellar radii	22.46 ± 0.72	$17.33^{+0.7}_{-0.67}$	$13.77^{+0.64}_{-0.72}$	23.0 ± 1.1	$6.14^{+0.17}_{-0.2}$
δ	$(R_P/R_*)^2$	$0.000889^{+4.8e-05}_{-3.6e-05}$	$0.00757^{+4.7e-05}_{-4.5e-05}$	$0.001325^{+3e-05}_{-1.9e-05}$	$0.001797^{+4.2e-05}_{-4.9e-05}$	$0.014015^{+0.00015}_{-9.1e-05}$
$\text{Depth}_{\rm K2}$	Flux decrement at mid transit for K2	$0.001186^{+5.2e-05}_{-5e-05}$	$0.009495^{+8.8e-05}_{-8.7e-05}$	$0.001691^{+3.4e-05}_{-3.3e-05}$	$0.001625^{+1.5e-05}_{-1.7e-05}$	0.01677 ± 0.0001
$\text{Depth}_{\rm TESS}$	Flux decrement at mid transit for TESS	$0.001092^{+3.9e-05}_{-3.8e-05}$	$0.008712^{+9.6e-05}_{-9.3e-05}$	$0.001573^{+3.3e-05}_{-3.2e-05}$	$0.001667^{+2.2e-05}_{-2.1e-05}$	$0.01591^{+0.00029}_{-0.00028}$
τ	Ingress/egress transit duration (days)	$0.00329^{+0.00088}_{-0.00036}$	$0.0169^{+0.00036}_{-0.00014}$	$0.00848^{+0.00099}_{-0.00031}$	$0.023^{+0.003}_{-0.0031}$	$0.01328^{+0.00056}_{-0.0003}$
T_{14}	Total transit duration (days)	$0.1013^{+0.0015}_{-0.0014}$	$0.20937^{+0.00029}_{-0.00025}$	$0.2328^{+0.0013}_{-0.0012}$	$0.1621^{+0.0021}_{-0.0023}$	$0.1219^{+0.00036}_{-0.00028}$
b	Transit Impact parameter	$0.34^{+0.2}_{-0.22}$	$0.092^{+0.075}_{-0.062}$	$0.19^{+0.16}_{-0.13}$	$0.859^{+0.016}_{-0.022}$	$0.152^{+0.092}_{-0.099}$
ρ_P	Density (cgs)	$3.53^{+0.63}_{-0.57}$	$0.426^{+0.051}_{-0.047}$	$0.63^{+0.12}_{-0.11}$	$0.58^{+0.24}_{-0.23}$	$0.58^{+0.063}_{-0.06}$
$\log g_P$	Surface gravity	$3.192^{+0.061}_{-0.065}$	$2.95^{+0.042}_{-0.044}$	$2.883^{+0.06}_{-0.066}$	$2.82^{+0.14}_{-0.21}$	3.216 ± 0.037
T_S	Time of eclipse (BJD_{TDB})	$2456693.61^{+0.35}_{-0.36}$	$2457829.01^{+0.2}_{-0.19}$	2459551.7 ± 0.23	$2459584.8^{+1.1}_{-2.8}$	$2457655.384^{+0.035}_{-0.02}$
$T_{S,14}$	Total eclipse duration (days)	$0.141^{+0.027}_{-0.028}$	$0.217^{+0.016}_{-0.015}$	$0.304^{+0.033}_{-0.029}$	$0.1671^{+0.0097}_{-0.019}$	$0.1292^{+0.0092}_{-0.0066}$
$e\cos\omega_*$		$0.004^{+0.059}_{-0.06}$	$-0.273^{+0.03}_{-0.028}$	$0.212^{+0.031}_{-0.03}$	$-0.064^{+0.088}_{-0.23}$	$0.007^{+0.025}_{-0.017}$

Table 4.5 Median values and 68% confidence intervals.

Priors:		k2-260	k2-261	k2-267	k2-277	k2-28
Gaussian	π Gaia Parallax (mas)					
Gaussian	[Fe/H] Metallicity (dex)					
Upper Limit	A_V V-band extinction (mag)					
Gaussian′	D_T Dilution in TESS					
Parameter	**Units**	**Values**				
Stellar Parameters:						
M_*	Mass ($M_\odot$)	$1.598^{+0.068}_{-0.076}$	$1.12^{+0.13}_{-0.057}$	$1.38^{+0.13}_{-0.16}$	$0.938^{+0.052}_{-0.043}$	0.318 ± 0.016
R_*	Radius ($R_\odot$)	$1.785^{+0.056}_{-0.059}$	$1.651^{+0.067}_{-0.062}$	$1.653^{+0.097}_{-0.084}$	$0.973^{+0.034}_{-0.032}$	0.317 ± 0.016
L_*	Luminosity ($L_\odot$)	$6.02^{+0.55}_{-0.62}$	$2.258^{+0.092}_{-0.088}$	$4.19^{+1.2}_{-0.81}$	$0.869^{+0.048}_{-0.043}$	$0.21^{+1.5}_{-0.21}$
$F_{\rm Bol}$	Bolometric Flux (cgs)	$4.26^{+0.26}_{-0.38}$	$1.588^{+0.058}_{-0.055}$	$1.01^{+0.25}_{-0.17}$	$2.21^{+0.12}_{-0.11}$	—
ρ_*	Density (cgs)	$0.394^{+0.042}_{-0.032}$	$0.353^{+0.065}_{-0.047}$	0.429 ± 0.076	$1.44^{+0.18}_{-0.16}$	$14.1^{+2.4}_{-2.0}$
$\log g$	Surface gravity (cgs)	$4.137^{+0.03}_{-0.027}$	$4.052^{+0.063}_{-0.045}$	$4.14^{+0.053}_{-0.068}$	$4.434^{+0.039}_{-0.038}$	$4.938^{+0.049}_{-0.047}$
$T_{\rm eff}$	Effective Temperature (K)	$6770.0^{+140.0}_{-170.0}$	$5510.0^{+100.0}_{-110.0}$	$6420.0^{+380.0}_{-310.0}$	5650.0 ± 110.0	$1.24^{+0.86}_{-0.85}$
[Fe/H]	Metallicity (dex)	$0.327^{+0.049}_{-0.062}$	$0.379^{+0.069}_{-0.073}$	0.116 ± 0.081	$0.08^{+0.071}_{-0.065}$	0.26 ± 0.05
$[Fe/H]_0$	Initial Metallicity[2]	$0.439^{+0.04}_{-0.056}$	$0.375^{+0.064}_{-0.069}$	$0.217^{+0.078}_{-0.081}$	$0.099^{+0.07}_{-0.066}$	—
Age	Age (Gyr)	$0.99^{+0.49}_{-0.33}$	$8.3^{+2.0}_{-3.2}$	$2.4^{+2.4}_{-1.3}$	7.6 ± 3.7	—
EEP	Equal Evolutionary Phase[3]	$339.2^{+9.2}_{-11.0}$	$453.9^{+5.4}_{-36.0}$	$363.0^{+56.0}_{-25.0}$	$377.0^{+26.0}_{-33.0}$	—
A_V	V-band extinction (mag)	$0.737^{+0.062}_{-0.1}$	0.063 ± 0.043	$0.44^{+0.26}_{-0.23}$	$0.093^{+0.066}_{-0.062}$	—
$\sigma_{\rm SED}$	SED photometry error scaling	$0.56^{+0.23}_{-0.15}$	$0.81^{+0.33}_{-0.2}$	$5.12^{+1.4}_{-0.98}$	$0.64^{+0.23}_{-0.15}$	—
ϖ	Parallax (mas)	$1.484^{+0.04}_{-0.039}$	4.689 ± 0.043	2.75 ± 0.13	8.914 ± 0.058	—
d	Distance (pc)	673.0 ± 18.0	$213.3^{+2.0}_{-1.9}$	$364.0^{+18.0}_{-16.0}$	$112.19^{+0.73}_{-0.72}$	—
Planetary Parameters:						
P	Period (days)	$2.62669736^{+7.2e-07}_{-7.4e-07}$	$11.633472^{+3.1e-06}_{-3.2e-06}$	$6.1802678 \pm 1.4e-06$	$6.326767^{+1.5e-05}_{-1.2e-05}$	$2.2604421^{+1.3e-06}_{-1.4e-06}$
R_P	Radius ($R_{\rm J}$)	$1.621^{+0.062}_{-0.059}$	$0.848^{+0.035}_{-0.032}$	$1.128^{+0.066}_{-0.058}$	$0.195^{+0.018}_{-0.011}$	$0.233^{+0.018}_{-0.016}$
M_P	Mass ($M_{\rm J}$)	1.71 ± 0.34	$0.197^{+0.027}_{-0.03}$	$26.0^{+37.0}_{-20.0}$	$0.0198^{+0.0076}_{-0.0049}$	$0.0263^{+0.01}_{-0.0065}$
T_C	Time of conjunction[4] ($\rm BJD_{TDB}$)	$2457820.7375^{+0.00034}_{-0.00035}$	$2457906.84112^{+0.00025}_{-0.00029}$	$2457865.10994^{+0.0019}_{-0.00098}$	$2458575.1575^{+0.0034}_{-0.003}$	$2457931.89649 \pm 0.00065$
T_T	Time of minimum projected separation[5] ($\rm BJD_{TDB}$)	$2458663.90734^{+0.00024}_{-0.00025}$	$2458279.11235 \pm 0.00019$	$2458106.14035^{+0.0002}_{-0.00017}$	$2457309.804^{+0.0006}_{-0.00059}$	2457057.10538 ± 0.0002
T_0	Optimal conjunction Time[6] ($\rm BJD_{TDB}$)	$2458663.9076^{+0.00024}_{-0.00025}$	$2458279.11279 \pm 0.00019$	$2458106.1407^{+0.00018}_{-0.00016}$	$2457309.80425^{+0.0006}_{-0.00059}$	$2457057.10549^{+0.00019}_{-0.0002}$
a	Semi-major axis (AU)	$0.04357^{+0.00061}_{-0.0007}$	$0.1043^{+0.0038}_{-0.0018}$	$0.0739^{+0.0023}_{-0.0028}$	$0.0655^{+0.0012}_{-0.001}$	$0.023^{+0.00038}_{-0.00039}$
i	Inclination (Degrees)	$88.89^{+0.77}_{-1.1}$	$88.71^{+0.84}_{-0.8}$	$86.11^{+0.58}_{-1.1}$	$86.71^{+1.6}_{-0.95}$	$87.92^{+1.1}_{-0.59}$
e	Eccentricity	$0.041^{+0.042}_{-0.028}$	$0.333^{+0.062}_{-0.064}$	$0.26^{+0.36}_{-0.17}$	$0.52^{+0.24}_{-0.27}$	$0.28^{+0.37}_{-0.19}$
ω_*	Argument of Periastron (Degrees)	$-47.0^{+79.0}_{-110.0}$	$137.0^{+13.0}_{-15.0}$	$10.0^{+110.0}_{-180.0}$	$52.0^{+97.0}_{-100.0}$	$-36.0^{+97.0}_{-130.0}$
T_{eq}	Equilibrium temperature[7] (K)	$2088.0^{+39.0}_{-47.0}$	$1054.0^{+14.0}_{-17.0}$	$1469.0^{+76.0}_{-59.0}$	$1049.0^{+15.0}_{-14.0}$	22000.0 ± 15000.0
$\tau_{\rm circ}$	Tidal circularization timescale (Gyr)	$0.04^{+0.012}_{-0.011}$	$16.6^{+15.0}_{-7.9}$	$38.0^{+200.0}_{-37.0}$	$30.0^{+210.0}_{-30.0}$	$0.69^{+1.1}_{-0.68}$
K	RV semi-amplitude (m/s)	184.0 ± 36.0	$17.3^{+2.1}_{-2.5}$	$2700.0^{+3600.0}_{-2000.0}$	$2.8^{+1.4}_{-0.76}$	$9.8^{+4.9}_{-2.7}$
R_P/R_*	Radius of planet in stellar radii	0.0934 ± 0.0018	$0.05272^{+0.00059}_{-0.00046}$	$0.07023^{+0.00082}_{-0.00091}$	$0.02051^{+0.0019}_{-0.00081}$	$0.0756^{+0.004}_{-0.0032}$
a/R_*	Semi-major axis in stellar radii	$5.24^{+0.18}_{-0.14}$	$13.62^{+0.79}_{-0.63}$	$9.6^{+0.55}_{-0.62}$	$14.49^{+0.58}_{-0.55}$	$15.61^{+0.85}_{-0.77}$
δ	$(R_P/R_*)^2$	$0.00872^{+0.00034}_{-0.00032}$	$0.002779^{+6.2e-05}_{-4.8e-05}$	$0.00493^{+0.00012}_{-0.00013}$	$0.000421^{+8.3e-05}_{-3.3e-05}$	$0.00571^{+0.00062}_{-0.00048}$
$\rm Depth_{K2}$	Flux decrement at mid transit for K2	$0.00982^{+0.00042}_{-0.0004}$	$0.003585^{+8.1e-05}_{-7.9e-05}$	$0.00539^{+0.00012}_{-0.00011}$	$0.000482^{+1.8e-05}_{-1.9e-05}$	$0.00675^{+0.00047}_{-0.00034}$
$\rm Depth_{TESS}$	Flux decrement at mid transit for TESS	$0.00959^{+0.00038}_{-0.00037}$	$0.003353^{+5.5e-05}_{-5.4e-05}$	$0.005289^{+9.9e-05}_{-9.6e-05}$	$0.000469^{+1.6e-05}_{-1.7e-05}$	$0.00667^{+0.0017}_{-0.00076}$
τ	Ingress/egress transit duration (days)	$0.01539^{+0.00051}_{-0.00037}$	$0.0112^{+0.0013}_{-0.00053}$	$0.0158^{+0.0019}_{-0.002}$	$0.00236^{+0.0032}_{-0.00074}$	$0.0039^{+0.0021}_{-0.001}$
T_{14}	Total transit duration (days)	$0.17569^{+0.00084}_{-0.00082}$	$0.21319^{+0.0012}_{-0.00087}$	$0.1694^{+0.0016}_{-0.0018}$	$0.082^{+0.0028}_{-0.0023}$	$0.0414^{+0.002}_{-0.0016}$
b	Transit Impact parameter	$0.102^{+0.1}_{-0.069}$	0.22 ± 0.15	$0.561^{+0.058}_{-0.088}$	$0.56^{+0.27}_{-0.37}$	$0.52^{+0.19}_{-0.32}$
ρ_P	Density (cgs)	$0.5^{+0.12}_{-0.11}$	$0.399^{+0.085}_{-0.077}$	$23.0^{+35.0}_{-18.0}$	$3.17^{+1.2}_{-0.75}$	$2.56^{+0.94}_{-0.61}$
$\log g_P$	Surface gravity	$3.206^{+0.081}_{-0.1}$	$2.831^{+0.071}_{-0.082}$	$4.72^{+0.39}_{-0.65}$	$3.1^{+0.13}_{-0.11}$	$3.08^{+0.13}_{-0.11}$
T_S	Time of eclipse ($\rm BJD_{TDB}$)	$2457819.434^{+0.076}_{-0.051}$	$2457910.89^{+0.6}_{-0.61}$	$2457868.3^{+1.8}_{-1.2}$	$2458574.9^{+2.3}_{-2.4}$	$2457933.03^{+0.57}_{-0.54}$
$T_{S,14}$	Total eclipse duration (days)	$0.1731^{+0.0089}_{-0.012}$	$0.319^{+0.047}_{-0.042}$	$0.176^{+0.018}_{-0.035}$	$0.082^{+0.059}_{-0.046}$	$0.0403^{+0.0095}_{-0.012}$
$e\cos\omega_*$		$0.006^{+0.046}_{-0.031}$	$-0.235^{+0.081}_{-0.085}$	$0.02^{+0.49}_{-0.31}$	$0.0^{+0.56}_{-0.54}$	$0.0^{+0.4}_{-0.38}$

Table 4.6 Median values and 68% confidence intervals.

Priors:		k2-281	k2-30	k2-313	k2-329	k2-334
Gaussian	π Gaia Parallax (mas)					
Gaussian	[Fe/H] Metallicity (dex)					
Upper Limit	A_V V-band extinction (mag)					
Gaussian′	D_T Dilution in TESS					
Parameter	Units	Values				
Stellar Parameters:						
M_*	Mass ($M_\odot$)	$0.787^{+0.031}_{-0.028}$	$0.936^{+0.047}_{-0.044}$	0.346 ± 0.017	$0.85^{+0.036}_{-0.032}$	$1.296^{+0.066}_{-0.071}$
R_*	Radius ($R_\odot$)	$0.749^{+0.024}_{-0.023}$	$0.936^{+0.02}_{-0.019}$	0.341 ± 0.017	$0.825^{+0.026}_{-0.025}$	$1.473^{+0.065}_{-0.059}$
L_*	Luminosity ($L_\odot$)	$0.243^{+0.011}_{-0.01}$	$0.69^{+0.029}_{-0.037}$	$0.26^{+1.8}_{-0.25}$	0.453 ± 0.017	$2.98^{+0.16}_{-0.15}$
$F_{\rm Bol}$	Bolometric Flux (cgs)	$3.583e-11^{+9.8e-13}_{-9.7e-13}$	$2.051^{+0.078}_{-0.11}$	—	2.688 ± 0.087	$6.78^{+0.26}_{-0.25}$
ρ_*	Density (cgs)	$2.65^{+0.26}_{-0.24}$	$1.611^{+0.096}_{-0.089}$	$12.3^{+2.1}_{-1.7}$	$2.14^{+0.21}_{-0.19}$	$0.571^{+0.085}_{-0.08}$
$\log g$	Surface gravity (cgs)	4.586 ± 0.029	$4.467^{+0.021}_{-0.02}$	$4.91^{+0.049}_{-0.047}$	$4.535^{+0.03}_{-0.029}$	$4.214^{+0.044}_{-0.049}$
$T_{\rm eff}$	Effective Temperature (K)	4682.0 ± 72.0	$5432.0^{+70.0}_{-77.0}$	1.25 ± 0.85	$5211.0^{+79.0}_{-78.0}$	6250.0 ± 130.0
[Fe/H]	Metallicity (dex)	$0.233^{+0.051}_{-0.05}$	0.175 ± 0.08	0.04 ± 0.11	$0.141^{+0.077}_{-0.078}$	0.233 ± 0.077
$[Fe/H]_0$	Initial Metallicity[2]	$0.216^{+0.057}_{-0.058}$	0.181 ± 0.076	—	$0.142^{+0.077}_{-0.078}$	0.281 ± 0.069
Age	Age (Gyr)	$6.5^{+4.8}_{-4.4}$	$7.0^{+3.4}_{-3.1}$	—	$8.1^{+3.7}_{-4.0}$	$2.8^{+1.5}_{-1.2}$
EEP	Equal Evolutionary Phase[3]	$334.0^{+14.0}_{-32.0}$	$362.0^{+26.0}_{-21.0}$	—	$350.0^{+23.0}_{-17.0}$	$362.0^{+41.0}_{-23.0}$
A_V	V-band extinction (mag)	$0.057^{+0.033}_{-0.038}$	$0.654^{+0.038}_{-0.077}$	—	$0.061^{+0.029}_{-0.038}$	0.054 ± 0.036
$\sigma_{\rm SED}$	SED photometry error scaling	$1.15^{+0.52}_{-0.3}$	$1.05^{+0.46}_{-0.28}$	—	$1.22^{+0.49}_{-0.29}$	$0.86^{+0.34}_{-0.21}$
ϖ	Parallax (mas)	2.149 ± 0.036	$3.047^{+0.027}_{-0.026}$	—	$4.309^{+0.042}_{-0.041}$	2.67 ± 0.046
d	Distance (pc)	$465.4^{+7.9}_{-7.6}$	328.2 ± 2.8	—	232.1 ± 2.2	$374.6^{+6.6}_{-6.3}$
Planetary Parameters:						
P	Period (days)	$8.6878627^{+9.5e-06}_{-9.6e-06}$	$4.09847594 \pm 4.6e-07$	$5.7459981^{+1.7e-06}_{-1.6e-06}$	$12.4551256^{+8.5e-06}_{-8.3e-06}$	$5.1138606^{+3.9e-06}_{-4.1e-06}$
R_P	Radius (R_J)	$0.728^{+0.029}_{-0.026}$	$1.17^{+0.033}_{-0.032}$	$0.191^{+0.012}_{-0.011}$	$0.759^{+0.025}_{-0.024}$	$0.513^{+0.036}_{-0.03}$
M_P	Mass (M_J)	$0.181^{+0.063}_{-0.042}$	$0.604^{+0.039}_{-0.031}$	$0.0186^{+0.0069}_{-0.0045}$	$0.193^{+0.065}_{-0.044}$	$0.1^{+0.037}_{-0.024}$
T_C	Time of conjunction[4] (BJD_{TDB})	$2457393.8811^{+0.00029}_{-0.00028}$	$2457063.80699 \pm 0.00011$	$2458497.77675^{+0.0002}_{-0.00019}$	$2457773.15638^{+0.00041}_{-0.0004}$	$2458209.316^{+0.0014}_{-0.0017}$
T_T	Time of minimum projected separation[5] (BJD_{TDB})	$2457393.88111 \pm 0.00022$	2457436.7683 ± 0.0001	$2458250.69884 \pm 0.00012$	$2458184.17553^{+0.00026}_{-0.00027}$	2458168.40516 ± 0.000
T_0	Optimal conjunction Time[6] (BJD_{TDB})	$2457446.00828^{+0.00029}_{-0.00028}$	2457436.76858 ± 0.0001	$2458250.69905 \pm 0.00011$	$2458184.17603^{+0.00025}_{-0.00026}$	2458168.40541 ± 0.000
a	Semi-major axis (AU)	$0.07637^{+0.00098}_{-0.00093}$	$0.04904^{+0.00081}_{-0.00077}$	$0.04406^{+0.00072}_{-0.00075}$	$0.0996^{+0.0014}_{-0.0013}$	$0.0633^{+0.0011}_{-0.0012}$
i	Inclination (Degrees)	$88.91^{+0.69}_{-0.45}$	86.26 ± 0.14	$88.83^{+0.57}_{-0.34}$	$89.49^{+0.35}_{-0.39}$	$84.6^{+2.0}_{-1.5}$
e	Eccentricity	$0.28^{+0.37}_{-0.15}$	—	$0.29^{+0.36}_{-0.19}$	$0.19^{+0.39}_{-0.12}$	$0.49^{+0.22}_{-0.33}$
ω_*	Argument of Periastron (Degrees)	$30.0^{+110.0}_{-180.0}$	—	$10.0^{+120.0}_{-160.0}$	$-200.0^{+170.0}_{-130.0}$	$-230.0^{+80.0}_{-93.0}$
T_{eq}	Equilibrium temperature[7] (K)	$706.7^{+7.8}_{-7.7}$	$1144.0^{+14.0}_{-15.0}$	17000.0 ± 11000.0	723.1 ± 7.7	$1453.0^{+21.0}_{-19.0}$
$\tau_{\rm circ}$	Tidal circularization timescale (Gyr)	$9.9^{+12.0}_{-9.7}$	$0.365^{+0.056}_{-0.047}$	$76.0^{+110.0}_{-75.0}$	$68.0^{+52.0}_{-66.0}$	$0.89^{+6.1}_{-0.86}$
K	RV semi-amplitude (m/s)	$23.4^{+11.0}_{-6.0}$	$79.7^{+4.6}_{-2.9}$	$4.8^{+2.4}_{-1.3}$	$20.5^{+8.8}_{-5.1}$	$11.9^{+5.2}_{-3.1}$
R_P/R_*	Radius of planet in stellar radii	$0.0996^{+0.003}_{-0.0017}$	$0.1284^{+0.0027}_{-0.0025}$	$0.0574^{+0.002}_{-0.0016}$	$0.09439^{+0.0013}_{-0.00085}$	$0.0357^{+0.0022}_{-0.0016}$
a/R_*	Semi-major axis in stellar radii	$21.94^{+0.7}_{-0.68}$	$11.27^{+0.22}_{-0.21}$	$27.8^{+1.5}_{-1.4}$	$25.98^{+0.83}_{-0.8}$	$9.24^{+0.44}_{-0.45}$
δ	$(R_P/R_*)^2$	$0.00993^{+0.00061}_{-0.00034}$	$0.01648^{+0.00069}_{-0.00064}$	$0.00329^{+0.00023}_{-0.00018}$	$0.00891^{+0.00025}_{-0.00016}$	$0.00127^{+0.00016}_{-0.00011}$
$\text{Depth}_{\rm K2}$	Flux decrement at mid transit for K2	$0.01379^{+0.00032}_{-0.00031}$	$0.01698^{+0.00075}_{-0.0007}$	$0.00391^{+0.00023}_{-0.00018}$	0.01163 ± 0.0002	$0.001373 \pm 1.9e-05$
$\text{Depth}_{\rm TESS}$	Flux decrement at mid transit for TESS	0.01279 ± 0.00032	$0.01688^{+0.00073}_{-0.00068}$	$0.00375^{+0.00053}_{-0.00035}$	$0.01093^{+0.00033}_{-0.00032}$	$0.001353^{+3.5e-05}_{-4.1e-05}$
τ	Ingress/egress transit duration (days)	$0.0114^{+0.0027}_{-0.0012}$	0.0225 ± 0.0011	$0.00379^{+0.0014}_{-0.00081}$	$0.0136^{+0.0017}_{-0.00051}$	$0.006^{+0.0056}_{-0.0024}$
T_{14}	Total transit duration (days)	$0.1138^{+0.0021}_{-0.0015}$	$0.09943^{+0.00076}_{-0.00075}$	$0.05502^{+0.0014}_{-0.00096}$	$0.1526^{+0.0014}_{-0.0011}$	$0.1049^{+0.0043}_{-0.0026}$
b	Transit Impact parameter	$0.32^{+0.19}_{-0.21}$	$0.735^{+0.013}_{-0.014}$	$0.47^{+0.17}_{-0.27}$	$0.19^{+0.17}_{-0.13}$	$0.64^{+0.18}_{-0.4}$
ρ_P	Density (cgs)	$0.58^{+0.2}_{-0.13}$	$0.469^{+0.048}_{-0.041}$	$3.32^{+1.2}_{-0.77}$	$0.55^{+0.18}_{-0.12}$	$0.91^{+0.33}_{-0.21}$
$\log g_P$	Surface gravity	$2.92^{+0.13}_{-0.11}$	$3.04^{+0.034}_{-0.03}$	$3.1^{+0.13}_{-0.11}$	$2.92^{+0.12}_{-0.11}$	$2.97^{+0.13}_{-0.11}$
T_S	Time of eclipse (BJD_{TDB})	2457389.5 ± 2.3	$2457065.85623 \pm 0.00011$	2458494.9 ± 1.5	2457779.4 ± 2.6	$2458211.8^{+1.6}_{-1.7}$
$T_{S,14}$	Total eclipse duration (days)	$0.128^{+0.027}_{-0.036}$	—	$0.057^{+0.015}_{-0.014}$	$0.16^{+0.019}_{-0.041}$	$0.104^{+0.057}_{-0.1}$
$e\cos\omega_*$		-0.0 ± 0.43	—	$0.0^{+0.43}_{-0.42}$	$0.0^{+0.34}_{-0.33}$	$-0.01^{+0.48}_{-0.53}$

Table 4.7 Median values and 68% confidence intervals.

Priors:		k2-34	k2-344	k2-370	k2-371	k2-39
Gaussian	π Gaia Parallax (mas)					
Gaussian	[Fe/H] Metallicity (dex)					
Upper Limit	A_V V-band extinction (mag)					
Gaussian′	D_T Dilution in TESS					
Parameter	Units	Values				
Stellar Parameters:						
M_*	Mass ($M_\odot$)	$1.12^{+0.074}_{-0.073}$	0.588 ± 0.029	$0.916^{+0.055}_{-0.041}$	$0.762^{+0.032}_{-0.028}$	$1.141^{+0.15}_{-0.099}$
R_*	Radius ($R_\odot$)	1.365 ± 0.043	$0.564^{+0.028}_{-0.027}$	$0.956^{+0.034}_{-0.032}$	$0.728^{+0.019}_{-0.018}$	$3.19^{+0.13}_{-0.12}$
L_*	Luminosity ($L_\odot$)	$2.35^{+0.11}_{-0.1}$	$0.69^{+4.9}_{-0.68}$	$0.804^{+0.1}_{-0.082}$	0.288 ± 0.011	4.72 ± 0.21
$F_{\rm Bol}$	Bolometric Flux (cgs)	$6.41^{+0.27}_{-0.25}$	—	$1.31^{+0.16}_{-0.13}$	4.78 ± 0.15	$1.613^{+0.055}_{-0.056}$
ρ_*	Density (cgs)	$0.619^{+0.082}_{-0.067}$	$4.6^{+0.76}_{-0.65}$	$1.48^{+0.18}_{-0.16}$	$2.79^{+0.21}_{-0.2}$	$0.0502^{+0.0095}_{-0.0076}$
$\log g$	Surface gravity (cgs)	$4.216^{+0.042}_{-0.04}$	4.704 ± 0.047	$4.44^{+0.039}_{-0.036}$	4.597 ± 0.023	$3.491^{+0.065}_{-0.057}$
$T_{\rm eff}$	Effective Temperature (K)	$6110.0^{+110.0}_{-100.0}$	1.25 ± 0.85	$5590.0^{+170.0}_{-150.0}$	4958.0 ± 66.0	4766.0 ± 87.0
[Fe/H]	Metallicity (dex)	$0.005^{+0.058}_{-0.05}$	-0.95 ± 0.08	$0.034^{+0.073}_{-0.067}$	$-0.015^{+0.13}_{-0.057}$	$0.427^{+0.084}_{-0.091}$
$[{\rm Fe/H}]_0$	Initial Metallicity[2]	$0.08^{+0.054}_{-0.051}$	—	$0.06^{+0.072}_{-0.069}$	$0.002^{+0.12}_{-0.073}$	$0.356^{+0.077}_{-0.085}$
Age	Age (Gyr)	$5.3^{+2.5}_{-1.9}$	—	$8.2^{+3.6}_{-4.1}$	$8.3^{+3.6}_{-4.0}$	$8.6^{+3.4}_{-3.2}$
EEP	Equal Evolutionary Phase[3]	$415.0^{+19.0}_{-36.0}$	—	$379.0^{+23.0}_{-34.0}$	$342.5^{+8.6}_{-17.0}$	$489.2^{+6.3}_{-7.1}$
A_V	V-band extinction (mag)	0.057 ± 0.038	—	$0.29^{+0.16}_{-0.15}$	$0.066^{+0.027}_{-0.039}$	$0.089^{+0.042}_{-0.055}$
$\sigma_{\rm SED}$	SED photometry error scaling	$0.65^{+0.27}_{-0.17}$	—	$1.06^{+0.43}_{-0.26}$	$0.81^{+0.45}_{-0.24}$	$0.82^{+0.3}_{-0.19}$
ϖ	Parallax (mas)	2.924 ± 0.026	—	$7.126^{+0.056}_{-0.057}$	2.275 ± 0.025	3.267 ± 0.048
d	Distance (pc)	341.9 ± 3.1	—	140.3 ± 1.1	$439.6^{+4.9}_{-4.8}$	306.1 ± 4.5
Planetary Parameters:						
P	Period (days)	$2.99563577 \pm 1.5e-07$	$3.3557162^{+3.3e-06}_{-3.6e-06}$	$2.14080859^{+7.6e-07}_{-6.8e-07}$	$3.11489718 \pm 3e-07$	$4.604697^{+1.6e-05}_{-1.4e-05}$
R_P	Radius ($R_{\rm J}$)	1.174 ± 0.038	$0.1632^{+0.0093}_{-0.0088}$	$0.2227^{+0.0097}_{-0.0083}$	$1.061^{+0.028}_{-0.026}$	$0.57^{+0.03}_{-0.026}$
M_P	Mass ($M_{\rm J}$)	$17.0^{+36.0}_{-13.0}$	$0.0143^{+0.0053}_{-0.0034}$	$0.0243^{+0.0088}_{-0.0056}$	$40.0^{+29.0}_{-25.0}$	$0.12^{+0.044}_{-0.028}$
T_C	Time of conjunction[4] ($\rm BJD_{TDB}$)	2457141.351 ± 0.0015	$2458095.74934^{+0.00051}_{-0.00052}$	$2457822.18415^{+0.0005}_{-0.00052}$	$2457141.417386^{+8.9e-05}_{-8.6e-05}$	$2456980.8291^{+0.0032}_{-0.0026}$
T_T	Time of minimum projected separation[5] ($\rm BJD_{TDB}$)	$2457749.46504^{+3.9e-05}_{-3.5e-05}$	$2458219.91084 \pm 0.00041$	$2458299.58448 \pm 0.00031$	$2457611.766862^{+6.9e-05}_{-6.7e-05}$	$2457086.7371^{+0.002}_{-0.0018}$
T_0	Optimal conjunction Time[6] ($\rm BJD_{TDB}$)	$2457749.465275^{+3.5e-05}_{-3.3e-05}$	2458219.91104 ± 0.0004	2458299.5846 ± 0.00031	$2457611.767066^{+6.6e-05}_{-6.5e-05}$	$2457086.7374^{+0.002}_{-0.0018}$
a	Semi-major axis (AU)	$0.04254^{+0.00093}_{-0.00096}$	$0.03674^{+0.0006}_{-0.00062}$	$0.03157^{+0.00062}_{-0.00048}$	$0.03879^{+0.0006}_{-0.00058}$	$0.0566^{+0.0024}_{-0.0017}$
i	Inclination (Degrees)	$82.84^{+0.57}_{-0.81}$	$88.52^{+0.96}_{-0.84}$	$86.8^{+2.2}_{-2.3}$	$89.47^{+0.37}_{-0.49}$	$85.6^{+3.0}_{-3.1}$
e	Eccentricity	$0.106^{+0.26}_{-0.079}$	$0.2^{+0.39}_{-0.14}$	$0.42^{+0.24}_{-0.12}$	$0.087^{+0.31}_{-0.068}$	$0.18^{+0.34}_{-0.13}$
ω_*	Argument of Periastron (Degrees)	$-34.0^{+65.0}_{-130.0}$	$-146.0^{+130.0}_{-93.0}$	$99.0^{+73.0}_{-77.0}$	$-20.0^{+76.0}_{-150.0}$	$-10.0^{+100.0}_{-150.0}$
T_{eq}	Equilibrium temperature[7] (K)	$1670.0^{+25.0}_{-24.0}$	24000.0 ± 16000.0	$1482.0^{+41.0}_{-37.0}$	1035.0 ± 12.0	$1722.0^{+32.0}_{-36.0}$
$\tau_{\rm circ}$	Tidal circularization timescale (Gyr)	$1.7^{+5.6}_{-1.5}$	$28.0^{+26.0}_{-27.0}$	$0.47^{+0.92}_{-0.44}$	$7.1^{+11.0}_{-6.2}$	$3.0^{+2.5}_{-2.7}$
K	RV semi-amplitude (m/s)	$2300.0^{+4600.0}_{-1700.0}$	$3.01^{+1.4}_{-0.79}$	$4.7^{+2.0}_{-1.2}$	$6800.0^{+4600.0}_{-4200.0}$	$14.1^{+5.7}_{-3.6}$
R_P/R_*	Radius of planet in stellar radii	$0.08846^{+0.00045}_{-0.00044}$	0.02972 ± 0.0007	$0.02387^{+0.0006}_{-0.00035}$	$0.14973^{+0.00083}_{-0.00067}$	$0.01834^{+0.00055}_{-0.00034}$
a/R_*	Semi-major axis in stellar radii	$6.69^{+0.3}_{-0.25}$	$13.99^{+0.73}_{-0.69}$	$7.11^{+0.28}_{-0.26}$	$11.47^{+0.29}_{-0.3}$	$3.83^{+0.23}_{-0.2}$
δ	$(R_P/R_*)^2$	$0.007825^{+7.9e-05}_{-7.8e-05}$	$0.000884^{+4.2e-05}_{-4.1e-05}$	$0.00057^{+2.9e-05}_{-1.6e-05}$	$0.02242^{+0.00025}_{-0.0002}$	$0.000336^{+2e-05}_{-1.2e-05}$
$\rm Depth_{K2}$	Flux decrement at mid transit for K2	$0.007369^{+8.1e-05}_{-8.3e-05}$	$0.000949^{+4.8e-05}_{-4.3e-05}$	$0.000721^{+2.1e-05}_{-2e-05}$	$0.03083^{+0.00043}_{-0.00042}$	$0.00049 \pm 1.7e-05$
$\rm Depth_{TESS}$	Flux decrement at mid transit for TESS	$0.007512^{+6.5e-05}_{-6.6e-05}$	$0.00111^{+0.00039}_{-0.00016}$	$0.000671 \pm 1.8e-05$	$0.02823^{+0.00039}_{-0.00038}$	$0.000431 \pm 1.7e-05$
τ	Ingress/egress transit duration (days)	$0.02339^{+0.00057}_{-0.00059}$	$0.00234^{+0.0007}_{-0.00024}$	$0.00171^{+0.00046}_{-0.0001}$	$0.01297^{+0.00043}_{-0.00013}$	$0.00715^{+0.0017}_{-0.00053}$
T_{14}	Total transit duration (days)	$0.10298^{+0.00027}_{-0.00032}$	$0.0729^{+0.0018}_{-0.0017}$	$0.06908^{+0.001}_{-0.00099}$	$0.09863^{+0.00044}_{-0.0004}$	$0.3627^{+0.0049}_{-0.0054}$
b	Transit Impact parameter	$0.8247^{+0.0047}_{-0.005}$	0.33 ± 0.22	$0.24^{+0.25}_{-0.17}$	$0.1^{+0.094}_{-0.07}$	$0.27^{+0.21}_{-0.18}$
ρ_P	Density (cgs)	$13.0^{+29.0}_{-10.0}$	$4.07^{+1.5}_{-0.94}$	$2.7^{+0.97}_{-0.62}$	$42.0^{+30.0}_{-26.0}$	$0.8^{+0.28}_{-0.18}$
$\log g_P$	Surface gravity	$4.49^{+0.5}_{-0.65}$	$3.12^{+0.13}_{-0.11}$	$3.08^{+0.13}_{-0.11}$	$4.95^{+0.24}_{-0.43}$	$2.96^{+0.13}_{-0.11}$
T_S	Time of eclipse ($\rm BJD_{TDB}$)	2457139.85 ± 0.36	$2458097.43^{+0.66}_{-0.68}$	$2457821.1^{+0.64}_{-0.66}$	$2457142.97^{+0.39}_{-0.37}$	$2456983.16^{+1.1}_{-0.68}$
$T_{S,14}$	Total eclipse duration (days)	$0.1028^{+0.0012}_{-0.0057}$	$0.069^{+0.01}_{-0.02}$	$0.095^{+0.031}_{-0.026}$	$0.0967^{+0.0055}_{-0.014}$	$0.359^{+0.053}_{-0.075}$
$e\cos\omega_*$		0.0 ± 0.19	$-0.0^{+0.31}_{-0.32}$	$-0.01^{+0.48}_{-0.5}$	$0.0^{+0.2}_{-0.19}$	$0.01^{+0.37}_{-0.23}$

Table 4.8 Median values and 68% confidence intervals.

Priors:		k2-390	k2-403	k2-405	k2-97	wasp-118
Gaussian	π Gaia Parallax (mas)					
Gaussian	[Fe/H] Metallicity (dex)					
Upper Limit	A_V V-band extinction (mag)					
Gaussian′	D_T Dilution in TESS					
Parameter	Units	Values				
Stellar Parameters:						
M_*	Mass ($M_\odot$)	$0.915^{+0.05}_{-0.039}$	$0.932^{+0.047}_{-0.046}$	$0.817^{+0.034}_{-0.031}$	$1.111^{+0.17}_{-0.085}$	$1.429^{+0.075}_{-0.086}$
R_*	Radius ($R_\odot$)	$0.965^{+0.035}_{-0.033}$	$0.904^{+0.033}_{-0.03}$	$0.779^{+0.025}_{-0.023}$	$4.15^{+0.27}_{-0.25}$	$1.836^{+0.07}_{-0.068}$
L_*	Luminosity ($L_\odot$)	$0.727^{+0.031}_{-0.029}$	$0.624^{+0.021}_{-0.02}$	$0.3022^{+0.0099}_{-0.0096}$	$7.34^{+0.83}_{-0.72}$	$4.91^{+0.3}_{-0.31}$
$F_{\rm Bol}$	Bolometric Flux (cgs)	$1.14^{+0.038}_{-0.036}$	$3.37e-10^{+8.8e-12}_{-8.9e-12}$	$2.471e-10^{+6.2e-12}_{-6.1e-12}$	3.52 ± 0.11	$1.076^{+0.063}_{-0.066}$
ρ_*	Density (cgs)	$1.44^{+0.17}_{-0.15}$	1.78 ± 0.21	$2.44^{+0.24}_{-0.22}$	$0.0223^{+0.0056}_{-0.0042}$	$0.324^{+0.046}_{-0.043}$
$\log g$	Surface gravity (cgs)	$4.431^{+0.037}_{-0.033}$	$4.496^{+0.037}_{-0.041}$	$4.568^{+0.029}_{-0.03}$	$3.254^{+0.077}_{-0.067}$	$4.064^{+0.042}_{-0.047}$
$T_{\rm eff}$	Effective Temperature (K)	$5425.0^{+95.0}_{-93.0}$	$5396.0^{+91.0}_{-93.0}$	4848.0 ± 74.0	$4664.0^{+85.0}_{-83.0}$	6340.0 ± 140.0
[Fe/H]	Metallicity (dex)	$0.14^{+0.16}_{-0.14}$	$0.199^{+0.085}_{-0.083}$	$0.221^{+0.08}_{-0.078}$	$0.327^{+0.079}_{-0.081}$	$0.142^{+0.09}_{-0.086}$
$[{\rm Fe/H}]_0$	Initial Metallicity[2]	$0.16^{+0.14}_{-0.12}$	0.19 ± 0.082	0.207 ± 0.079	$0.262^{+0.075}_{-0.078}$	$0.231^{+0.092}_{-0.091}$
Age	Age (Gyr)	$9.6^{+2.8}_{-3.9}$	$5.4^{+5.0}_{-3.8}$	$6.7^{+4.7}_{-4.5}$	$9.2^{+3.1}_{-3.6}$	$2.47^{+0.98}_{-0.73}$
EEP	Equal Evolutionary Phase[3]	$388.0^{+17.0}_{-36.0}$	$347.0^{+37.0}_{-33.0}$	$339.0^{+14.0}_{-31.0}$	$502.5^{+6.7}_{-11.0}$	378.0 ± 27.0
A_V	V-band extinction (mag)	$0.048^{+0.024}_{-0.031}$	$0.048^{+0.022}_{-0.03}$	$0.027^{+0.015}_{-0.018}$	$0.09^{+0.035}_{-0.051}$	$0.132^{+0.064}_{-0.075}$
$\sigma_{\rm SED}$	SED photometry error scaling	$0.97^{+0.42}_{-0.25}$	$0.76^{+0.3}_{-0.19}$	$1.52^{+0.6}_{-0.37}$	$0.9^{+0.39}_{-0.24}$	$0.66^{+0.26}_{-0.16}$
ϖ	Parallax (mas)	2.214 ± 0.027	$4.109^{+0.041}_{-0.042}$	5.056 ± 0.052	$1.224^{+0.062}_{-0.061}$	$2.618^{+0.026}_{-0.025}$
d	Distance (pc)	$451.7^{+5.5}_{-5.4}$	$243.4^{+2.5}_{-2.4}$	$197.8^{+2.1}_{-2.0}$	$817.0^{+43.0}_{-39.0}$	$381.9^{+3.8}_{-3.7}$
Planetary Parameters:						
P	Period (days)	$3.3129312^{+3.9e-06}_{-5.9e-06}$	$33.591474^{+6.2e-05}_{-6.5e-05}$	$3.4355037^{+1.7e-06}_{-1.8e-06}$	$8.40713 \pm 2.1e-05$	$4.04604949^{+4e-07}_{-3.9e-07}$
R_P	Radius (R_J)	$0.353^{+0.02}_{-0.016}$	$0.46^{+0.022}_{-0.019}$	$0.351^{+0.016}_{-0.013}$	$1.186^{+0.11}_{-0.1}$	$1.461^{+0.056}_{-0.054}$
M_P	Mass (M_J)	$0.053^{+0.02}_{-0.013}$	$0.083^{+0.03}_{-0.019}$	$0.053^{+0.019}_{-0.012}$	$0.533^{+0.052}_{-0.037}$	$128.5^{+5.6}_{-5.4}$
T_C	Time of conjunction[4] ($\rm BJD_{TDB}$)	$2457739.90162^{+0.00089}_{-0.0009}$	$2457908.95869 \pm 0.00067$	$2457908.99553^{+0.00037}_{-0.00036}$	2457142.0531 ± 0.0032	$2456787.81502^{+0.00088}_{-0.00026}$
T_T	Time of minimum projected separation[5] ($\rm BJD_{TDB}$)	$2457839.28952 \pm 0.00064$	$2457908.95871^{+0.00058}_{-0.00059}$	$2457908.99553 \pm 0.00027$	$2457831.4339^{+0.0021}_{-0.002}$	$2457386.63024^{+0.00056}_{-0.00012}$
T_0	Optimal conjunction Time[6] ($\rm BJD_{TDB}$)	$2457839.28972 \pm 0.00064$	$2457976.14164 \pm 0.00065$	$2458073.89971^{+0.00036}_{-0.00034}$	$2457831.4343^{+0.0021}_{-0.002}$	$2457386.63053^{+0.00047}_{-0.00011}$
a	Semi-major axis (AU)	$0.04223^{+0.00075}_{-0.00061}$	$0.199^{+0.0033}_{-0.0034}$	$0.04165^{+0.00057}_{-0.00053}$	$0.0838^{+0.004}_{-0.0022}$	$0.05753^{+0.00091}_{-0.0011}$
i	Inclination (Degrees)	$86.9^{+2.0}_{-1.0}$	$89.38^{+0.35}_{-0.18}$	$88.42^{+1.0}_{-0.98}$	$75.2^{+1.5}_{-1.7}$	$88.38^{+1.0}_{-0.85}$
e	Eccentricity	$0.29^{+0.33}_{-0.17}$	$0.25^{+0.39}_{-0.16}$	$0.17^{+0.38}_{-0.13}$	$0.207^{+0.039}_{-0.038}$	$0.35^{+0.41}_{-0.3}$
ω_*	Argument of Periastron (Degrees)	$-200.0^{+170.0}_{-120.0}$	$-180.0^{+150.0}_{-120.0}$	$-40.0^{+70.0}_{-120.0}$	$68.5^{+9.0}_{-11.0}$	$-25.0^{+24.0}_{-120.0}$
T_{eq}	Equilibrium temperature[7] (K)	1249.0 ± 16.0	$554.4^{+6.2}_{-6.1}$	1010.9 ± 9.7	1577.0 ± 48.0	1728.0 ± 26.0
$\tau_{\rm circ}$	Tidal circularization timescale (Gyr)	$1.8^{+2.4}_{-1.7}$	$22000.0^{+23000.0}_{-21000.0}$	$3.5^{+2.6}_{-3.3}$	$4.5^{+2.9}_{-1.8}$	$9.3^{+28.0}_{-9.3}$
K	RV semi-amplitude (m/s)	$8.5^{+3.8}_{-2.2}$	$6.1^{+3.0}_{-1.6}$	$8.7^{+3.9}_{-2.2}$	$48.7^{+2.4}_{-2.3}$	$13600.0^{+5400.0}_{-1500.0}$
R_P/R_*	Radius of planet in stellar radii	$0.03744^{+0.0016}_{-0.00096}$	$0.0522^{+0.0017}_{-0.0013}$	$0.04615^{+0.0014}_{-0.00069}$	$0.02933^{+0.001}_{-0.00099}$	$0.08174^{+0.00035}_{-0.00034}$
a/R_*	Semi-major axis in stellar radii	$9.41^{+0.36}_{-0.34}$	$47.4^{+1.8}_{-1.9}$	11.51 ± 0.36	$4.37^{+0.34}_{-0.3}$	6.73 ± 0.29
δ	$(R_P/R_*)^2$	$0.001402^{+0.00012}_{-7.1e-05}$	$0.00272^{+0.00019}_{-0.00013}$	$0.00213^{+0.00013}_{-6.3e-05}$	$0.000861^{+6.1e-05}_{-5.7e-05}$	$0.006681^{+5.8e-05}_{-5.5e-05}$
$\rm Depth_{K2}$	Flux decrement at mid transit for K2	$0.001728^{+6.2e-05}_{-6.1e-05}$	$0.0034^{+7.9e-05}_{-7.4e-05}$	$0.002919 \pm 7.2e-05$	$0.000529^{+5.3e-05}_{-5.9e-05}$	$0.007898^{+9.3e-05}_{-9.2e-05}$
$\rm Depth_{TESS}$	Flux decrement at mid transit for TESS	$0.001648^{+5.3e-05}_{-5.4e-05}$	$0.003212^{+8.5e-05}_{-9.6e-05}$	$0.002709 \pm 6e-05$	$0.000645^{+3.1e-05}_{-3.3e-05}$	$0.007381^{+8.4e-05}_{-8.3e-05}$
τ	Ingress/egress transit duration (days)	$0.00397^{+0.0018}_{-0.00065}$	$0.012^{+0.0038}_{-0.0023}$	$0.0046^{+0.0013}_{-0.00041}$	$0.0359^{+0.0083}_{-0.0071}$	$0.01592^{+0.00073}_{-0.00041}$
T_{14}	Total transit duration (days)	$0.0929^{+0.0022}_{-0.0019}$	$0.1976^{+0.0035}_{-0.0026}$	$0.0955^{+0.0014}_{-0.0011}$	$0.2601^{+0.0075}_{-0.0071}$	$0.20491^{+0.00075}_{-0.0025}$
b	Transit Impact parameter	$0.4^{+0.23}_{-0.27}$	$0.44^{+0.17}_{-0.28}$	$0.3^{+0.22}_{-0.2}$	$0.901^{+0.017}_{-0.022}$	$0.161^{+0.092}_{-0.1}$
ρ_P	Density (cgs)	$1.48^{+0.53}_{-0.34}$	$1.05^{+0.37}_{-0.24}$	$1.49^{+0.53}_{-0.34}$	$0.398^{+0.13}_{-0.096}$	$51.1^{+3.7}_{-3.5}$
$\log g_P$	Surface gravity	$3.02^{+0.11}_{-0.11}$	$2.99^{+0.13}_{-0.11}$	$3.02^{+0.13}_{-0.11}$	$2.974^{+0.089}_{-0.084}$	5.174 ± 0.014
T_S	Time of eclipse ($\rm BJD_{TDB}$)	$2457741.56^{+0.83}_{-0.84}$	$2457925.7^{+8.2}_{-8.3}$	$2457910.72^{+0.66}_{-0.57}$	$2457138.26^{+0.14}_{-0.15}$	$2456787.05^{+0.47}_{-1.3}$
$T_{S,14}$	Total eclipse duration (days)	$0.098^{+0.03}_{-0.023}$	$0.201^{+0.047}_{-0.053}$	$0.089^{+0.01}_{-0.024}$	0.0 ± 0.0	$0.174^{+0.034}_{-0.074}$
$e \cos \omega_*$		$-0.0^{+0.4}_{-0.41}$	$-0.0^{+0.4}_{-0.39}$	$0.0^{+0.3}_{-0.26}$	$0.075^{+0.025}_{-0.027}$	$0.27^{+0.41}_{-0.31}$

Table 4.9 Median values and 68% confidence intervals.

Priors:		K2-43	
Gaussian	π Gaia Parallax (mas)		
Gaussian	[Fe/H] Metallicity (dex)		
Upper Limit	A_V V-band extinction (mag)		
Gaussian′	D_T Dilution in TESS		
Parameter	Units	Values	
Stellar Parameters:			
M_*	Mass ($M_\odot$)	0.553 ± 0.027	
R_*	Radius ($R_\odot$)	$0.575^{+0.024}_{-0.023}$	
L_*	Luminosity ($L_\odot$)	$0.74^{+5.1}_{-0.73} \times 10^5$	
ρ_*	Density (cgs)	$4.09^{+0.56}_{-0.49}$	
$\log g$	Surface gravity (cgs)	$4.661^{+0.039}_{-0.040}$	
$T_{\rm eff}$	Effective temperature (K)	$1.25 \pm 0.85 \times 10^5$	
[Fe/H]	Metallicity (dex)	-4.0 ± 4.1	
Planetary Parameters:		b	c
P	Period (days)	$2.1988785^{+0.0000043}_{-0.0000044}$	$3.4712470^{+0.0000024}_{-0.0000025}$
R_P	Radius (R_J)	$0.173^{+0.017}_{-0.015}$	$0.324^{+0.020}_{-0.019}$
M_P	Mass[1] (M_J)	$0.0158^{+0.0063}_{-0.0041}$	$0.046^{+0.017}_{-0.011}$
T_C	Observed Time of conjunction[2] (BJD_{TDB})	$2456810.4033^{+0.0027}_{-0.0026}$	2456809.8825 ± 0.0011
T_C	Model Time of conjunction[2,3] (TJD_{TDB})	$2456810.4032^{+0.0027}_{-0.0026}$	2456809.8823 ± 0.0011
T_T	Model time of min proj sep[3,4,5] (TJD_{TDB})	$2457010.5011^{+0.0026}_{-0.0025}$	$2457500.66042^{+0.00094}_{-0.00097}$
T_0	Obs time of min proj sep[4,6,7] (BJD_{TDB})	$2457010.5013^{+0.0026}_{-0.0025}$	$2457500.66063^{+0.00094}_{-0.00097}$
a	Semi-major axis (AU)	$0.02716^{+0.00044}_{-0.00046}$	$0.03682^{+0.00060}_{-0.00062}$
i	Inclination (Degrees)	$87.47^{+1.5}_{-1.00}$	$89.09^{+0.62}_{-0.70}$
e	Eccentricity	$0.094^{+0.089}_{-0.066}$	$0.055^{+0.064}_{-0.039}$
ω_*	Arg of periastron (Degrees)	60^{+100}_{-120}	-50^{+120}_{-100}
$\dot{\omega}_{\rm GR}$	Computed GR precession (°/century)	$3.66^{+0.14}_{-0.13}$	1.694 ± 0.058
$T_{\rm eq}$	Equilibrium temp[8] (K)	28000 ± 19000	24000 ± 16000
$\tau_{\rm circ}$	Tidal circ timescale (Gyr)	$5.3^{+3.2}_{-2.0}$	$5.3^{+2.3}_{-1.5}$
K	RV semi-amplitude[1] (m/s)	$3.70^{+1.5}_{-0.96}$	$9.1^{+3.4}_{-2.2}$
R_P/R_*	Radius of planet in stellar radii	$0.0310^{+0.0026}_{-0.0024}$	$0.0580^{+0.0026}_{-0.0025}$
a/R_*	Semi-major axis in stellar radii	$10.15^{+0.44}_{-0.42}$	$13.76^{+0.60}_{-0.58}$
δ	$(R_P/R_*)^2$	$0.00096^{+0.00017}_{-0.00014}$	$0.00337^{+0.00030}_{-0.00029}$
$\delta_{\rm Kepler}$	Transit depth in Kepler (frac)	$0.00119^{+0.00020}_{-0.00018}$	$0.00436^{+0.00056}_{-0.00048}$
$\delta_{\rm TESS}$	Transit depth in TESS (frac)	$0.00111^{+0.00018}_{-0.00016}$	$0.00399^{+0.00044}_{-0.00039}$
τ	In/egress transit duration (days)	$0.00230^{+0.00070}_{-0.00038}$	$0.00483^{+0.00061}_{-0.00033}$
T_{14}	Total transit duration (days)	$0.0619^{+0.0055}_{-0.0052}$	$0.0832^{+0.0029}_{-0.0027}$
T_{FWHM}	FWHM transit duration (days)	$0.0596^{+0.0056}_{-0.0055}$	$0.0783^{+0.0028}_{-0.0027}$
b	Transit impact parameter	$0.43^{+0.19}_{-0.27}$	$0.22^{+0.17}_{-0.15}$
b_S	Eclipse impact parameter	$0.45^{+0.16}_{-0.26}$	0.22 ± 0.15
τ_S	In/egress eclipse duration (days)	$0.00243^{+0.00053}_{-0.00037}$	$0.00473^{+0.00050}_{-0.00043}$
$T_{S,14}$	Total eclipse duration (days)	$0.0640^{+0.0095}_{-0.0077}$	$0.0815^{+0.0056}_{-0.0068}$
$T_{S,FWHM}$	FWHM eclipse duration (days)	$0.0616^{+0.0095}_{-0.0080}$	$0.0767^{+0.0054}_{-0.0065}$
$\delta_{S,2.5\mu m}$	BB eclipse depth at 2.5μm (ppm)	187^{+39}_{-42}	562^{+70}_{-110}
$\delta_{S,5.0\mu m}$	BB eclipse depth at 5.0μm (ppm)	198^{+38}_{-36}	595^{+65}_{-80}
$\delta_{S,7.5\mu m}$	BB eclipse depth at 7.5μm (ppm)	202^{+38}_{-35}	607^{+63}_{-71}
ρ_P	Density[1] (cgs)	$3.76^{+1.4}_{-0.92}$	$1.66^{+0.59}_{-0.38}$
$logg_P$	Surface gravity[1] (cgs)	$3.11^{+0.13}_{-0.11}$	$3.03^{+0.13}_{-0.11}$

CHAPTER 5

SUMMARY AND FUTURE WORK

5.1 Summary of work

As we enter an era of characterizing exoplanets in unprecedented detail, we need to prepare ahead of time for performing the required observations. The work in this thesis aims to provide a comprehensive, self-consistent catalog for K2-discovered planets that have been reobserved by TESS, prioritizing those that are more amenable to characterization efforts. This catalog provides renewed ephemerides for accurately predicting future transit times, and updated global parameters which will aid in the selection process for atmospheric characterization and allow for appropriate population studies within the K2 target list. In the following sections, we summarize each chapter and explore possibilities for the K2 & TESS Synergy project going forward.

5.1.1 Chapter 2: Reanalysis of 26 TESS Prime Mission Targets

In Chapter 2, we reanalyzed 26 single-planet systems that were observed during the TESS Prime Mission. Half of these had a transit S/N large enough to be detectable by TESS, which resulted in an average improvement on their ephemerides from 26.7 to 0.35 hours. The transits of the remaining 13 planets were not deep enough to be seen in the TESS light curves, but we were still able to reduce the average ephemeris uncertainties from 43.2 to 35.6 hours due to the light curve pipelines that we use and the nature of the global fits. We identified the inconsistency of the ephemeris for K2-260 b, where we believe an error was introduced for the literature transit time. This work was the first large batch to be published following the pilot study.

5.1.2 Chapter 3: Recovering K2's First Planet

Chapter 3 detailed our effort to recover the lost ephemeris of K2-2 b, which was the first planet discovery during the engineering phase of K2. The discovery of this planet included a spurious transit from a secondary light curve, which caused the calculated period to be 28.8 minutes ($\sim 40\sigma$) from the true period. This resulted in the transit being missed during targeted observations using HST and Spitzer, highlighting a real-world scenario where an inaccurate ephemeris led to the loss of data.

We used a series of ground- and space-based light curves from MEarth, ULMT, K2, TESS, and Spitzer to recover and refine the ephemeris of K2-2 b to within 13 minutes by 2030. Our analysis included new radial velocity measurements which were corrected for systematics with the YARARA post-processing tool, as well as using the new CALM method to remove any remaining stellar variability. The radial velocities of K2-2 showed a tentative long-term trend, suggesting there may be an outer companion in the system, and with astrometric analysis, we were able to constrain the potential planet to $\lesssim 10\ M_{\rm J}$.

Although challenging with current technology, K2-2 b would be a valuable addition to atmospheric characterization, as it has the fifth-highest TSM compared to all other K2 sub-Neptunes. K2-2 also has a comoving white dwarf companion, for which a spectrum would place significant constraints on the age of the entire system.

5.1.3 Chapter 4: K2's Top Atmospheric Candidates

Chapter 4 discussed the continuation of the K2 & TESS Synergy to 32 of the top K2 targets for characterization. We followed the same methods as in the previous chapters for analyzing the sample, with the addition of multiplanet and binary star systems. We improved the average $3\sigma_{2030}$ ephemeris uncertainties from 9.34 hours to 26 minutes. The planets in this sample have TSMs similar to current JWST targets, showing that the K2 & TESS Synergy catalog can be used in practicality. Eight systems previously analyzed as part of the K2 & TESS Synergy were included in this sample. Six planets in the sample had only been validated in the past four years, demonstrating that the K2 catalog still holds many candidate planets that are well-suited to atmospheric characterization.

The sample presented in this chapter consisted of multiple low- and high- mass planets that would make interesting targets for transmission spectroscopy. The low-mass sample ($< 4R_{\oplus}$) included sub-Neptunes that sit in the radius valley (K2-313 b and K2-344 b), hot Neptunes that are potentially losing their atmospheres due to photoevaporation (K2-100 b and K2-105 b), and a system with two sub-Neptunes on either side of the large-radius peak of the radius valley (K2-43). Each of these systems are pertinent in their own ways to the study of small planets with significant

atmospheres, and would make excellent targets for transmission spectroscopy.

The planets in the high mass regime ($> 4R_{\oplus}$) make an ideal selection of systems that could be used to study giant planet migration. We presented this as an example of how the K2 & TESS Synergy catalog can be used going forward to make significant contributions to the understanding of exoplanet evolution. The sample in this work consists of a variety of giant planets. The four planets with significantly eccentric orbits (K2-97 b, K2-232 b, K2-234 b, K2-261 b) are particularly interesting in terms of giant planet evolution, as they are likely actively undergoing high-eccentricity migration. Comparing the compositions of these planets to the giants on circular orbits could potentially uncover signatures of migration that are locked in the atmospheres of these planets.

5.2 Future Work

We have been able to update the global parameters for 31 exoplanet systems, but the work is far from over. The immediate goal is to extend the K2 & TESS Synergy to all 515 remaining K2 planets. The success of this will depend on their transit signal to noise, and as we have so far prioritized those with larger transit depths, this will become increasingly challenging with future batches. Ever-increasing TESS coverage will help in this regard, and future missions with higher photometric precision will be used to once again bring ephemerides into the current epoch.

The footprints of several K2 campaigns have not yet been covered by TESS at the time of writing. These will be a part of Sectors 91 and 92 (planned dates April 9 - June 3 2025; Figure 5.1), completing the TESS ecliptic plane sectors, and will thus allow the completion of the main target selection for the K2 & TESS Synergy with 68 new planetary overlaps.

Beyond refitting the remaining K2 systems, there are many paths this project could take going forward. We purposely did not fit for TTVs in the current work in order to reduce computation time for the global fits, however, `EXOFASTv2` has the capability of fitting for TTVs, making this a natural extension of the project. TTVs can uncover planets undergoing orbital decay, as well as indicate the existence of other planets in the system. Transit depth and duration variations can also tell us about the structure of the system, although this might be challenging with the precision of TESS

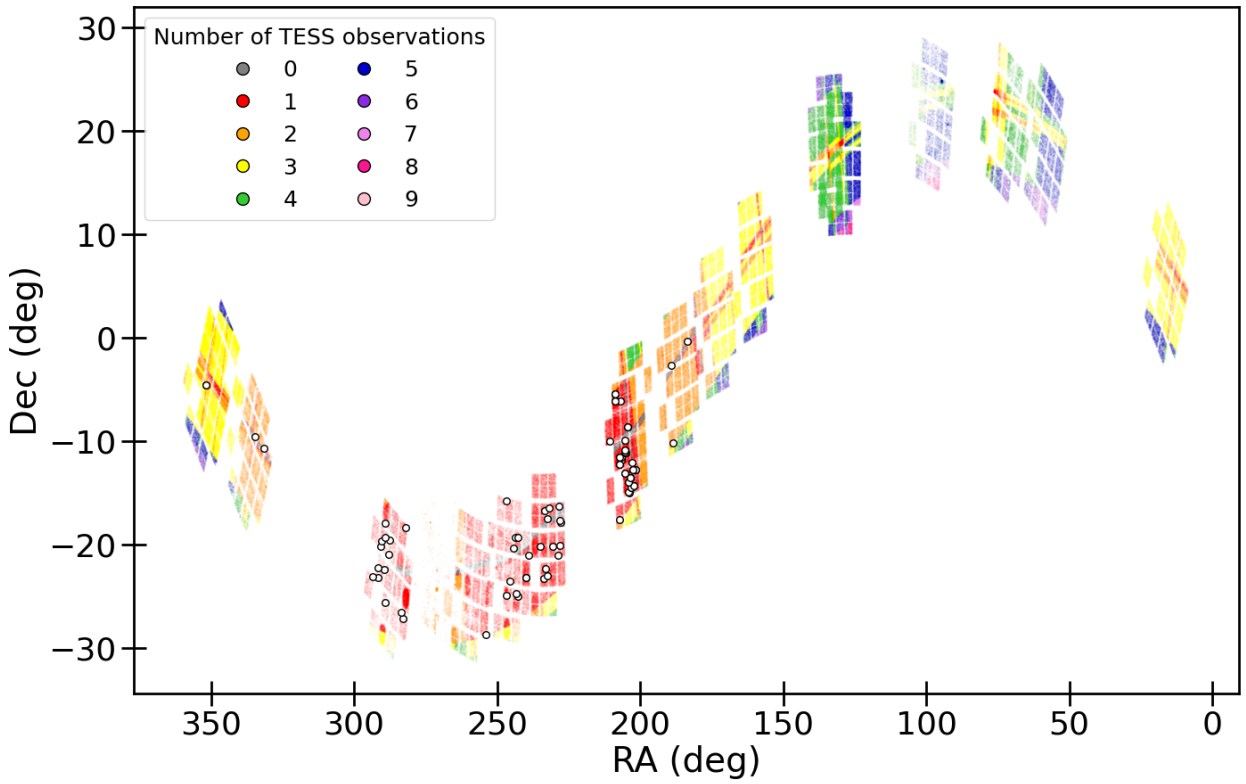

Figure 5.1 Overlap between K2 campaigns and TESS sectors. Each point represents a K2 target, which are colored by the number of times they have been reobserved by TESS up to and including Sector 92. Open circles are systems that will be observed for the first time in the upcoming ecliptic Sectors 91 and 92.

as the signal may be buried within the photometric noise. Another aspect for future study is the fitting of secondary eclipses (i.e. when a planet passes behind the host star), which can allow for the study of the temperature and brightness of the planet.

At the time of writing, there are 975 candidate planets in the K2 catalog. A systematic search for recurring transits within the TESS light curves could allow for assessment of the candidates, while providing immediately usable ephemerides for follow-up on interesting systems. A delve into single-transit K2 systems may also result in new exoplanet confirmations.

Another path forward would be to make use of the K2 & TESS Synergy catalog in terms of JWST spectroscopy. As presented in Chapter 4, the catalog contains a wide variety of planets that could be pursued for transmission spectroscopy to help answer certain aspects of planet formation and evolution. With the 51 planets from this work having up-to-date ephemerides,

detailed characterization can be the next step for systems that are key to answering lingering questions about exoplanet evolution.

Ephemeris renewal will be an ongoing necessity in the age of atmospheric characterization. The K2 & TESS Synergy has used the power of (nearly) all-sky TESS observations, but this is unfortunately not the final answer to ephemeris deterioration. Dragomir et al. (2020) performed a study on real and simulated TESS data to see how long after new TESS discoveries are made it takes for ephemerides to become stale. They found that merely a year after being first observed, 81% of TESS planets will have transit time uncertainties >30 minutes at a 1σ level, rendering them unfeasible for characterization. While this is alleviated somewhat by TESS revisiting the fields of previous sectors, it shows just how quickly planets can be lost, and missions that do not have the advantage of returning to the same fields years later will suffer more for this. Thousands more planets are expected to be discovered in the coming years with missions like the Nancy Grace Roman Space Telescope, Rubin Observatory, Plato, and ground-based ELTs, and it is imperative that we remember these planets will need to be reobserved to preserve their ephemerides. Ephemeris refinement may ultimately be a Sisyphean task, but it is a critical step in understanding the intricate details of exoplanets.

BIBLIOGRAPHY

Abazajian, K. N., Adelman-McCarthy, J. K., Agüeros, M. A., et al. 2009, ApJS, 182, 543, doi: 10.1088/0067-0049/182/2/543

Adams, E. R., Jackson, B., Johnson, S., et al. 2021, Planetary Science Journal, 2, 152, doi: 10.3847/PSJ/ac0ea0

Adams, F. C., & Laughlin, G. 2006, ApJ, 649, 1004, doi: 10.1086/506145

Ahrer, E.-M., Stevenson, K. B., Mansfield, M., et al. 2022, arXiv e-prints, arXiv:2211.10489, doi: 10.48550/arXiv.2211.10489

Aigrain, S., Parviainen, H., & Pope, B. J. S. 2016, MNRAS, 459, 2408, doi: 10.1093/mnras/stw706

Akana Murphy, J. M., Kosiarek, M. R., Batalha, N. M., et al. 2021, AJ, 162, 294, doi: 10.3847/1538-3881/ac2830

Alderson, L., Wakeford, H. R., Alam, M. K., et al. 2022, arXiv e-prints, arXiv:2211.10488, doi: 10.48550/arXiv.2211.10488

Asplund, M., Grevesse, N., Sauval, A. J., & Scott, P. 2009, ARA&A, 47, 481, doi: 10.1146/annurev.astro.46.060407.145222

Baranec, C., Riddle, R., Law, N. M., et al. 2014, ApJL, 790, L8, doi: 10.1088/2041-8205/790/1/L8

Barragán, O., Grziwa, S., Gandolfi, D., et al. 2016, AJ, 152, 193, doi: 10.3847/0004-6256/152/6/193

Barragán, O., Aigrain, S., Kubyshkina, D., et al. 2019, MNRAS, 490, 698, doi: 10.1093/mnras/stz2569

Barros, S. C. C., Demangeon, O., & Deleuil, M. 2016, A&A, 594, A100, doi: 10.1051/0004-6361/201628902

Bastien, F. A., Stassun, K. G., Basri, G., & Pepper, J. 2013, Nature, 500, 427, doi: 10.1038/nature12419

Beichman, C., Ygouf, M., Llop Sayson, J., et al. 2020, PASP, 132, 015002, doi: 10.1088/1538-3873/ab5066

Berger, T. A., Huber, D., Gaidos, E., van Saders, J. L., & Weiss, L. M. 2020a, AJ, 160, 108, doi: 10.3847/1538-3881/aba18a

Berger, T. A., Huber, D., van Saders, J. L., et al. 2020b, AJ, 159, 280, doi: 10.3847/1538-3881/159/6/280

Berta, Z. K., Charbonneau, D., Bean, J., et al. 2011, ApJ, 736, 12, doi: 10.1088/0004-637X/736/1/12

Bonomo, A. S., Dumusque, X., Massa, A., et al. 2023, A&A, 677, A33, doi: 10.1051/0004-6361/202346211

Borucki, W. J., Koch, D., Basri, G., et al. 2010, Science, 327, 977, doi: 10.1126/science.1185402

Brandt, T. D. 2018, ApJS, 239, 31, doi: 10.3847/1538-4365/aaec06

—. 2021, ApJS, 254, 42, doi: 10.3847/1538-4365/abf93c

Buchhave, L. A., Latham, D. W., Johansen, A., et al. 2012, Nature, 486, 375, doi: 10.1038/nature11121

Caldwell, D. A., Tenenbaum, P., Twicken, J. D., et al. 2020, Research Notes of the American Astronomical Society, 4, 201, doi: 10.3847/2515-5172/abc9b3

Carrión-González, Ó., García Muñoz, A., Santos, N. C., et al. 2021, A&A, 651, A7, doi: 10.1051/0004-6361/202039993

Castro González, A., Díez Alonso, E., Menéndez Blanco, J., et al. 2020, MNRAS, 499, 5416, doi: 10.1093/mnras/staa2353

Charbonneau, D., Brown, T. M., Latham, D. W., & Mayor, M. 2000, ApJL, 529, L45, doi: 10.1086/312457

Chen, J., & Kipping, D. 2017, ApJ, 834, 17, doi: 10.3847/1538-4357/834/1/17

Choi, J., Dotter, A., Conroy, C., et al. 2016, ApJ, 823, 102, doi: 10.3847/0004-637X/823/2/102

Christiansen, J. L., Bhure, S., Zink, J. K., et al. 2022, AJ, 163, 244, doi: 10.3847/1538-3881/ac5c4c

Claret, A. 2017, A&A, 600, A30, doi: 10.1051/0004-6361/201629705

Claret, A., & Bloemen, S. 2011, A&A, 529, A75, doi: 10.1051/0004-6361/201116451

Collins, K. A., Kielkopf, J. F., Stassun, K. G., & Hessman, F. V. 2017, AJ, 153, 77, doi: 10.3847/1538-3881/153/2/77

Collins, K. A., Collins, K. I., Pepper, J., et al. 2018, AJ, 156, 234, doi: 10.3847/1538-3881/aae582

Cosentino, R., Lovis, C., Pepe, F., et al. 2012, in Ground-based and Airborne Instrumentation for Astronomy IV, ed. I. S. McLean, S. K. Ramsay, & H. Takami, Vol. 8446, International Society for Optics and Photonics (SPIE), 657 – 676, doi: 10.1117/12.925738

Cretignier, M., Dumusque, X., Aigrain, S., & Pepe, F. 2023, A&A, 678, A2, doi: 10.1051/0004-6361/202347232

Cretignier, M., Dumusque, X., Allart, R., Pepe, F., & Lovis, C. 2020a, A&A, 633, A76, doi: 10.1051/0004-6361/201936548

Cretignier, M., Dumusque, X., Hara, N. C., & Pepe, F. 2021, A&A, 653, A43, doi: 10.1051/0004-6361/202140986

Cretignier, M., Dumusque, X., & Pepe, F. 2022, A&A, 659, A68, doi: 10.1051/0004-6361/202142435

Cretignier, M., Francfort, J., Dumusque, X., Allart, R., & Pepe, F. 2020b, A&A, 640, A42, doi: 10.1051/0004-6361/202037722

Cretignier, M., Pietrow, A. G. M., & Aigrain, S. 2024, MNRAS, 527, 2940, doi: 10.1093/mnras/stad3292

Crossfield, I. J. M., Ciardi, D. R., Petigura, E. A., et al. 2016, ApJS, 226, 7, doi: 10.3847/0067-0049/226/1/7

Cutri, R. M., Wright, E. L., T., C., & at al. 2012, VizieR Online Data Catalog, 2311, 0

Cutri, R. M., Skrutskie, M. F., van Dyk, S., et al. 2003, VizieR Online Data Catalog, 2246, 0

D'Angelo, G., Kley, W., & Henning, T. 2003, ApJ, 586, 540, doi: 10.1086/367555

Dattilo, A., Vanderburg, A., Shallue, C. J., et al. 2019, AJ, 157, 169, doi: 10.3847/1538-3881/ab0e12

de Beurs, Z. L., Vanderburg, A., Thygesen, E., et al. 2024, arXiv e-prints, arXiv:2401.12276, doi: 10.48550/arXiv.2401.12276

de Leon, J. P., Livingston, J., Endl, M., et al. 2021, MNRAS, 508, 195, doi: 10.1093/mnras/stab2305

Deming, D., Knutson, H., Kammer, J., et al. 2015, ApJ, 805, 132, doi: 10.1088/0004-637X/805/2/132

Dotter, A. 2016, ApJS, 222, 8, doi: 10.3847/0067-0049/222/1/8

Dragomir, D., Harris, M., Pepper, J., et al. 2020, AJ, 159, 219, doi: 10.3847/1538-3881/ab845d

Dumusque, X., Cretignier, M., Sosnowska, D., et al. 2021, A&A, 648, A103, doi: 10.1051/0004-6361/202039350

Eastman, J. 2017, EXOFASTv2: Generalized publication-quality exoplanet modeling code, Astrophysics Source Code Library. http://ascl.net/1710.003

Eastman, J., Gaudi, B. S., & Agol, E. 2013, PASP, 125, 83, doi: 10.1086/669497

Eastman, J. D., Rodriguez, J. E., Agol, E., et al. 2019, arXiv e-prints, arXiv:1907.09480. https://arxiv.org/abs/1907.09480

Edwards, B., Changeat, Q., Hou Yip, K., et al. 2019, in EPSC-DPS Joint Meeting 2019, Vol. 2019, EPSC–DPS2019–595

Edwards, B., Anisman, L., Changeat, Q., et al. 2020, Research Notes of the American Astronomical Society, 4, 109, doi: 10.3847/2515-5172/aba42b

Edwards, B., Ho, C., Osborne, H., et al. 2021, ATOM - Astronomy: Theory, 2, 25, doi: 10.32374/atom.2020.2.4

Espinoza, N., Kossakowski, D., & Brahm, R. 2019, MNRAS, 490, 2262, doi: 10.1093/mnras/stz2688

Fabrycky, D., & Tremaine, S. 2007, ApJ, 669, 1298, doi: 10.1086/521702

Fazio, G. G., Hora, J. L., Allen, L. E., et al. 2004, ApJS, 154, 10, doi: 10.1086/422843

Feinstein, A. D., Radica, M., Welbanks, L., et al. 2022, arXiv e-prints, arXiv:2211.10493, doi: 10.48550/arXiv.2211.10493

Fűrész, G. 2008, PhD thesis, University of Szeged, Hungary

Foreman-Mackey, D., Luger, R., Agol, E., et al. 2021, The Journal of Open Source Software, 6, 3285, doi: 10.21105/joss.03285

Frandsen, S., & Lindberg, B. 1999, in Astrophysics with the NOT, ed. H. Karttunen & V. Piirola, 71

Fulton, B. J., & Petigura, E. A. 2018, AJ, 156, 264, doi: 10.3847/1538-3881/aae828

Fulton, B. J., Petigura, E. A., Howard, A. W., et al. 2017, AJ, 154, 109, doi: 10.3847/1538-3881/aa80eb

Gaia Collaboration, Prusti, T., de Bruijne, J. H. J., et al. 2016, A&A, 595, A1, doi: 10.1051/0004-6361/201629272

Gaia Collaboration, Brown, A. G. A., Vallenari, A., et al. 2018, A&A, 616, A1, doi: 10.1051/0004-6361/201833051

—. 2021, A&A, 649, A1, doi: 10.1051/0004-6361/202039657

Gaidos, E., Mann, A. W., Rizzuto, A., et al. 2017, MNRAS, 464, 850, doi: 10.1093/mnras/stw2345

Gardner, J. P., Mather, J. C., Clampin, M., et al. 2006, SSRv, 123, 485, doi: 10.1007/s11214-006-8315-7

Gentile Fusillo, N. P., Tremblay, P. E., Cukanovaite, E., et al. 2021, MNRAS, 508, 3877, doi: 10.1093/mnras/stab2672

Greene, T. P., Bell, T. J., Ducrot, E., et al. 2023, Nature, 618, 39, doi: 10.1038/s41586-023-05951-7

Grunblatt, S. K., Huber, D., Gaidos, E. J., et al. 2016, AJ, 152, 185, doi: 10.3847/0004-6256/152/6/185

Grunblatt, S. K., Huber, D., Gaidos, E., et al. 2018, ApJL, 861, L5, doi: 10.3847/2041-8213/aacc67

Günther, M. N., & Daylan, T. 2021, ApJS, 254, 13, doi: 10.3847/1538-4365/abe70e

Helled, R., & Bodenheimer, P. 2010, Icarus, 207, 503, doi: 10.1016/j.icarus.2009.11.023

Henry, G. W., Marcy, G. W., Butler, R. P., & Vogt, S. S. 2000, ApJL, 529, L41, doi: 10.1086/312458

Hewitt, H. B., Simon, M. N., Mead, C., et al. 2023, Physical Review Physics Education Research, 19, 020156, doi: 10.1103/PhysRevPhysEducRes.19.020156

Hirano, T., Dai, F., Gandolfi, D., et al. 2018, AJ, 155, 127, doi: 10.3847/1538-3881/aaa9c1

Howell, S. B., Rowe, J. F., Bryson, S. T., et al. 2012, ApJ, 746, 123, doi: 10.1088/0004-637X/746/2/123

Howell, S. B., Sobeck, C., Haas, M., et al. 2014, PASP, 126, 398, doi: 10.1086/676406

Hu, R., Bello-Arufe, A., Zhang, M., et al. 2024, Nature, 630, 609, doi: 10.1038/s41586-024-07432-x

Huang, C., Wu, Y., & Triaud, A. H. M. J. 2016, ApJ, 825, 98, doi: 10.3847/0004-637X/825/2/98

Huang, C. X., Quinn, S. N., Vanderburg, A., et al. 2020, ApJL, 892, L7, doi: 10.3847/2041-8213/ab7302

Huber, D., Bryson, S. T., Haas, M. R., et al. 2016, ApJS, 224, 2, doi: 10.3847/0067-0049/224/1/2

Ih, J., Kempton, E. M. R., Whittaker, E. A., & Lessard, M. 2023, ApJL, 952, L4, doi: 10.3847/2041-8213/ace03b

Ikwut-Ukwa, M., Rodriguez, J. E., Bieryla, A., et al. 2020, AJ, 160, 209, doi: 10.3847/1538-3881/aba964

Irwin, J., Irwin, M., Aigrain, S., et al. 2007, MNRAS, 375, 1449, doi: 10.1111/j.1365-2966.2006.11408.x

Irwin, J. M., Berta-Thompson, Z. K., Charbonneau, D., et al. 2015, in Cambridge Workshop on Cool Stars, Stellar Systems, and the Sun, Vol. 18, 18th Cambridge Workshop on Cool Stars, Stellar Systems, and the Sun, 767–772, doi: 10.48550/arXiv.1409.0891

Irwin, M. J. 1985, MNRAS, 214, 575, doi: 10.1093/mnras/214.4.575

Jenkins, J. M., Twicken, J. D., McCauliff, S., et al. 2016, in Proc. SPIE, Vol. 9913, Software and Cyberinfrastructure for Astronomy IV, 99133E, doi: 10.1117/12.2233418

Johns, M., McCarthy, P., Raybould, K., et al. 2012, in Society of Photo-Optical Instrumentation Engineers (SPIE) Conference Series, Vol. 8444, Ground-based and Airborne Telescopes IV, ed. L. M. Stepp, R. Gilmozzi, & H. J. Hall, 84441H, doi: 10.1117/12.926716

Johnson, J. A. 2016, How Do You Find An Exoplanet?

Johnson, M. C., Dai, F., Justesen, A. B., et al. 2018a, MNRAS, 481, 596, doi: 10.1093/mnras/sty2238

Johnson, M. C., Rodriguez, J. E., Zhou, G., et al. 2018b, AJ, 155, 100, doi: 10.3847/1538-3881/aaa5af

Kane, S. R., Mahadevan, S., von Braun, K., Laughlin, G., & Ciardi, D. R. 2009, PASP, 121, 1386, doi: 10.1086/648564

Kempton, E. M. R., Bean, J. L., Louie, D. R., et al. 2018, PASP, 130, 114401, doi: 10.1088/1538-3873/aadf6f

Kipping, D. M. 2013, MNRAS, 435, 2152, doi: 10.1093/mnras/stt1435

Kokori, A., Tsiaras, A., Edwards, B., et al. 2021, Experimental Astronomy, doi: 10.1007/s10686-020-09696-3

—. 2022, ApJS, 258, 40, doi: 10.3847/1538-4365/ac3a10

—. 2023, ApJS, 265, 4, doi: 10.3847/1538-4365/ac9da4

Konacki, M., Torres, G., Jha, S., & Sasselov, D. D. 2003, Nature, 421, 507, doi: 10.1038/nature01379

Korth, J., Csizmadia, S., Gandolfi, D., et al. 2019, MNRAS, 482, 1807, doi: 10.1093/mnras/sty2760

Korth, J., Gandolfi, D., Šubjak, J., et al. 2023, A&A, 675, A115, doi: 10.1051/0004-6361/202244617

Kruse, E., Agol, E., Luger, R., & Foreman-Mackey, D. 2019, ApJS, 244, 11, doi: 10.3847/1538-4365/ab346b

Lam, K. W. F., Santerne, A., Sousa, S. G., et al. 2018, A&A, 620, A77, doi: 10.1051/0004-6361/201834073

Law, N. M., Morton, T., Baranec, C., et al. 2014, ApJ, 791, 35, doi: 10.1088/0004-637X/791/1/35

Lightkurve Collaboration, Cardoso, J. V. d. M. a., Hedges, C., et al. 2018, Lightkurve: Kepler and TESS time series analysis in Python. http://ascl.net/1812.013

Lim, O., Benneke, B., Doyon, R., et al. 2023, ApJL, 955, L22, doi: 10.3847/2041-8213/acf7c4

Lindegren, L., Hernández, J., Bombrun, A., et al. 2018, A&A, 616, A2, doi: 10.1051/0004-6361/201832727

Lindegren, L., Bastian, U., Biermann, M., et al. 2021, A&A, 649, A4, doi: 10.1051/0004-6361/202039653

Livingston, J. H., Crossfield, I. J. M., Petigura, E. A., et al. 2018a, AJ, 156, 277, doi: 10.3847/1538-3881/aae778

Livingston, J. H., Endl, M., Dai, F., et al. 2018b, AJ, 156, 78, doi: 10.3847/1538-3881/aaccde

Livingston, J. H., Dai, F., Hirano, T., et al. 2018c, AJ, 155, 115, doi: 10.3847/1538-3881/aaa841

Lodders, K., & Fegley, B. 2002, Icarus, 155, 393, doi: 10.1006/icar.2001.6740

Lucy, L. B., & Sweeney, M. A. 1971, AJ, 76, 544, doi: 10.1086/111159

Luger, R., Agol, E., Kruse, E., et al. 2016, AJ, 152, 100, doi: 10.3847/0004-6256/152/4/100

Lund, M. N., Handberg, R., Davies, G. R., Chaplin, W. J., & Jones, C. D. 2015, ApJ, 806, 30, doi: 10.1088/0004-637X/806/1/30

Lustig-Yaeger, J., Fu, G., May, E. M., et al. 2023, Nature Astronomy, 7, 1317, doi: 10.1038/s41550-023-02064-z

Madhusudhan, N. 2019, ARA&A, 57, 617, doi: 10.1146/annurev-astro-081817-051846

Madhusudhan, N., Amin, M. A., & Kennedy, G. M. 2014, ApJL, 794, L12, doi: 10.1088/2041-8205/794/1/L12

Madhusudhan, N., Bitsch, B., Johansen, A., & Eriksson, L. 2017, MNRAS, 469, 4102, doi: 10.1093/mnras/stx1139

Madhusudhan, N., Sarkar, S., Constantinou, S., et al. 2023, ApJL, 956, L13, doi: 10.3847/2041-8213/acf577

Madhusudhan, N., & Seager, S. 2011, ApJ, 729, 41, doi: 10.1088/0004-637X/729/1/41

Mann, A. W., Feiden, G. A., Gaidos, E., Boyajian, T., & von Braun, K. 2015, ApJ, 804, 64, doi: 10.1088/0004-637X/804/1/64

Mann, A. W., Dupuy, T., Kraus, A. L., et al. 2019, ApJ, 871, 63, doi: 10.3847/1538-4357/aaf3bc

Mayo, A. W., Vanderburg, A., Latham, D. W., et al. 2018, AJ, 155, 136, doi: 10.3847/1538-3881/aaadff

Mayor, M., & Queloz, D. 1995, Nature, 378, 355, doi: 10.1038/378355a0

Mayor, M., Pepe, F., Queloz, D., et al. 2003, The Messenger, 114, 20

Mazeh, T., Naef, D., Torres, G., et al. 2000, ApJL, 532, L55, doi: 10.1086/312558

McCormac, J., Pollacco, D., Skillen, I., et al. 2013, PASP, 125, 548, doi: 10.1086/670940

McGruder, C. D., López-Morales, M., Kirk, J., et al. 2022, AJ, 164, 134, doi: 10.3847/1538-3881/ac7f2e

Moffat, A. F. J. 1969, A&A, 3, 455

Montet, B. T., Morton, T. D., Foreman-Mackey, D., et al. 2015, ApJ, 809, 25, doi: 10.1088/0004-637X/809/1/25

Moran, S. E., Stevenson, K. B., Sing, D. K., et al. 2023, ApJL, 948, L11, doi: 10.3847/2041-8213/accb9c

Mordasini, C., van Boekel, R., Mollière, P., Henning, T., & Benneke, B. 2016, ApJ, 832, 41, doi: 10.3847/0004-637X/832/1/41

Moses, J. I., Line, M. R., Visscher, C., et al. 2013, ApJ, 777, 34, doi: 10.1088/0004-637X/777/1/34

Nikolov, N., Sing, D. K., Fortney, J. J., et al. 2018, Nature, 557, 526, doi: 10.1038/s41586-018-0101-7

Nutzman, P., & Charbonneau, D. 2008, PASP, 120, 317, doi: 10.1086/533420

Öberg, K. I., Murray-Clay, R., & Bergin, E. A. 2011, ApJL, 743, L16, doi: 10.1088/2041-8205/743/1/L16

Owen, J. E., & Jackson, A. P. 2012, MNRAS, 425, 2931, doi: 10.1111/j.1365-2966.2012.21481.x

Patel, J. A., & Espinoza, N. 2022, AJ, 163, 228, doi: 10.3847/1538-3881/ac5f55

Paxton, B., Bildsten, L., Dotter, A., et al. 2011, ApJS, 192, 3, doi: 10.1088/0067-0049/192/1/3

Paxton, B., Cantiello, M., Arras, P., et al. 2013, ApJS, 208, 4, doi: 10.1088/0067-0049/208/1/4

Paxton, B., Marchant, P., Schwab, J., et al. 2015, ApJS, 220, 15, doi: 10.1088/0067-0049/220/1/15

Poddaný, S., Brát, L., & Pejcha, O. 2010, NewA, 15, 297, doi: 10.1016/j.newast.2009.09.001

Polman, J., Waters, L. B. F. M., Min, M., Miguel, Y., & Khorshid, N. 2022, arXiv e-prints, arXiv:2208.00469, doi: 10.48550/arXiv.2208.00469

Pontoppidan, K. M., Barrientes, J., Blome, C., et al. 2022, ApJL, 936, L14, doi: 10.3847/2041-8213/ac8a4e

Pope, B. J. S., Parviainen, H., & Aigrain, S. 2016, MNRAS, 461, 3399, doi: 10.1093/mnras/stw1373

Pope, B. J. S., White, T. R., Farr, W. M., et al. 2019, ApJS, 245, 8, doi: 10.3847/1538-4365/ab3d29

Queloz, D., Mayor, M., Weber, L., et al. 2000, A&A, 354, 99

Rampalli, R., Vanderburg, A., Bieryla, A., et al. 2019, AJ, 158, 62, doi: 10.3847/1538-3881/ab27c2

Rasio, F. A., & Ford, E. B. 1996, Science, 274, 954, doi: 10.1126/science.274.5289.954

Rice, M., Wang, S., & Laughlin, G. 2022a, ApJL, 926, L17, doi: 10.3847/2041-8213/ac502d

Rice, M., Wang, S., Wang, X.-Y., et al. 2022b, AJ, 164, 104, doi: 10.3847/1538-3881/ac8153

Ricker, G. R., Winn, J. N., Vanderspek, R., et al. 2015, Journal of Astronomical Telescopes, Instruments, and Systems, 1, 014003, doi: 10.1117/1.JATIS.1.1.014003

Rodriguez, J. E., Vanderburg, A., Zieba, S., et al. 2020, AJ, 160, 117, doi: 10.3847/1538-3881/aba4b3

Rodriguez, J. E., Quinn, S. N., Zhou, G., et al. 2021, AJ, 161, 194, doi: 10.3847/1538-3881/abe38a

Rodriguez, J. E., Quinn, S. N., Vanderburg, A., et al. 2022a, arXiv e-prints, arXiv:2205.05709. https://arxiv.org/abs/2205.05709

—. 2022b, arXiv e-prints, arXiv:2205.05709, doi: 10.48550/arXiv.2205.05709

Rustamkulov, Z., Sing, D. K., Mukherjee, S., et al. 2022, arXiv e-prints, arXiv:2211.10487, doi: 10.48550/arXiv.2211.10487

Sanders, G. H. 2013, Journal of Astrophysics and Astronomy, 34, 81, doi: 10.1007/s12036-013-9169-5

Schlafly, E. F., & Finkbeiner, D. P. 2011, ApJ, 737, 103, doi: 10.1088/0004-637X/737/2/103

Schlegel, D. J., Finkbeiner, D. P., & Davis, M. 1998, ApJ, 500, 525, doi: 10.1086/305772

Sgro, L. A., Dalba, P. A., Esposito, T. M., et al. 2024, AJ, 168, 26, doi: 10.3847/1538-3881/ad5096

Shallue, C. J., & Vanderburg, A. 2018, AJ, 155, 94, doi: 10.3847/1538-3881/aa9e09

Shporer, A., Zhou, G., Fulton, B. J., et al. 2017, AJ, 154, 188, doi: 10.3847/1538-3881/aa8bb9

Smith, A. M. S., Csizmadia, S., Gandolfi, D., et al. 2019, AcA, 69, 135, doi: 10.32023/0001-5237/69.2.3

Smith, J. C., Stumpe, M. C., Van Cleve, J. E., et al. 2012, PASP, 124, 1000, doi: 10.1086/667697

Soto, M. G., Díaz, M. R., Jenkins, J. S., et al. 2018, MNRAS, 478, 5356, doi: 10.1093/mnras/sty1334

Stalport, M., Cretignier, M., Udry, S., et al. 2023, A&A, 678, A90, doi: 10.1051/0004-6361/202346887

Stassun, K. G., Oelkers, R. J., Pepper, J., et al. 2018, AJ, 156, 102, doi: 10.3847/1538-3881/aad050

Stumpe, M. C., Smith, J. C., Catanzarite, J. H., et al. 2014, PASP, 126, 100, doi: 10.1086/674989

Stumpe, M. C., Smith, J. C., Van Cleve, J. E., et al. 2012, PASP, 124, 985, doi: 10.1086/667698

Taylor, J., Radica, M., Welbanks, L., et al. 2023, MNRAS, 524, 817, doi: 10.1093/mnras/stad1547

Thygesen, E., Ranshaw, J. A., Rodriguez, J. E., et al. 2023, AJ, 165, 155, doi: 10.3847/1538-3881/acaf03

Thygesen, E., Rodriguez, J. E., de Beurs, Z. L., et al. 2024, AJ, 168, 161, doi: 10.3847/1538-3881/ad60bf

Tinetti, G., Drossart, P., Eccleston, P., et al. 2018, Experimental Astronomy, 46, 135, doi: 10.1007/s10686-018-9598-x

Tinetti, G., Eccleston, P., Haswell, C., et al. 2021, arXiv e-prints, arXiv:2104.04824. https://arxiv.org/abs/2104.04824

Tsai, S.-M., Lee, E. K. H., Powell, D., et al. 2022, arXiv e-prints, arXiv:2211.10490, doi: 10.48550/arXiv.2211.10490

Udalski, A., Zebrun, K., Szymanski, M., et al. 2002a, AcA, 52, 115, doi: 10.48550/arXiv.astro-ph/0207133

Udalski, A., Paczynski, B., Zebrun, K., et al. 2002b, AcA, 52, 1, doi: 10.48550/arXiv.astro-ph/0202320

Udry, S., Lovis, C., Bouchy, F., et al. 2014, arXiv e-prints, arXiv:1412.1048. https://arxiv.org/abs/1412.1048

van Leeuwen, F. 2007, A&A, 474, 653, doi: 10.1051/0004-6361:20078357

Vanderburg, A., & Johnson, J. A. 2014, PASP, 126, 948, doi: 10.1086/678764

Vanderburg, A., Montet, B. T., Johnson, J. A., et al. 2015, ApJ, 800, 59, doi: 10.1088/0004-637X/800/1/59

Vanderburg, A., Latham, D. W., Buchhave, L. A., et al. 2016, ApJS, 222, 14, doi: 10.3847/0067-0049/222/1/14

Vanderburg, A., Huang, C. X., Rodriguez, J. E., et al. 2019, ApJL, 881, L19, doi: 10.3847/2041-8213/ab322d

Vogt, S. S., Allen, S. L., Bigelow, B. C., et al. 1994, in Proc. SPIE, Vol. 2198, Instrumentation in Astronomy VIII, ed. D. L. Crawford & E. R. Craine, 362, doi: 10.1117/12.176725

Walker, G., Matthews, J., Kuschnig, R., et al. 2003, PASP, 115, 1023, doi: 10.1086/377358

Wang, J., Xie, J.-W., Barclay, T., & Fischer, D. A. 2014, ApJ, 783, 4, doi: 10.1088/0004-637X/783/1/4

Werner, M., Crossfield, I., Akeson, R., et al. 2016, Spitzer v. K2: Part II, Spitzer Proposal ID 13052

Winn, J. N., Holman, M. J., Torres, G., et al. 2008, ApJ, 683, 1076, doi: 10.1086/589737

Wogan, N. F., Batalha, N. E., Zahnle, K. J., et al. 2024, ApJL, 963, L7, doi: 10.3847/2041-8213/ad2616

Wolszczan, A., & Frail, D. A. 1992, Nature, 355, 145, doi: 10.1038/355145a0

Wu, Y., & Lithwick, Y. 2011, ApJ, 735, 109, doi: 10.1088/0004-637X/735/2/109

Yee, S. W., Winn, J. N., Hartman, J. D., et al. 2022a, AJ, 164, 70, doi: 10.3847/1538-3881/ac73ff

—. 2022b, arXiv e-prints, arXiv:2210.15473, doi: 10.48550/arXiv.2210.15473

Yip, K. H., Changeat, Q., Edwards, B., et al. 2021, AJ, 161, 4, doi: 10.3847/1538-3881/abc179

Young, A. T. 1967, AJ, 72, 328

Zahnle, K., Marley, M. S., Freedman, R. S., Lodders, K., & Fortney, J. J. 2009, ApJL, 701, L20, doi: 10.1088/0004-637X/701/1/L20

Zellem, R., Biferno, A., Ciardi, D. R., et al. 2019, BAAS, 51, 416. https://arxiv.org/abs/1903.07716

Zellem, R. T., Pearson, K. A., Blaser, E., et al. 2020, PASP, 132, 054401, doi: 10.1088/1538-3873/ab7ee7

Zeng, L., Sasselov, D. D., & Jacobsen, S. B. 2016, ApJ, 819, 127, doi: 10.3847/0004-637X/819/2/127

Zink, J. K., Hardegree-Ullman, K. K., Christiansen, J. L., et al. 2021, AJ, 162, 259, doi: 10.3847/1538-3881/ac2309